THE UNIVERSITY *of* EDINBURGH

Cortical Development & Plasticity in the FMRP KO Mouse

Chih-Yuan Chiang, MSc

Doctor of Philosophy – The University of Edinburgh – 2016

Doctor of Philosophy – The University of Edinburgh – 2016

Declaration

This work was carried out in the Centre for Integrative Physiology, School of Biomedical Sciences at the University of Edinburgh. I hereby certify that this thesis and its composition are entirely my own work, with the exception of the following:

1.) Most of the genotyping works were carried out by Mr. Mark Patrizio and Mr. Derek Thomson.

2.) Dr. Aleksander Domanski provided the MATLAB script used for VEP analysis (multi-taper Fast Fourier Transform), and he also assisted in setting up the simulation software NEURON which was used to model neuronal conduction velocity in Chapter 3.

3.) Ms. Ann Wright assisted with the sample preparation and image acquisition for the electron microscopy.

4.) Prof. Peter Kind and Dr. Emily Osterweil both assisted with the tissue dissection for Western blotting.

5.) Dr. Emily Osterweil also assisted with the purchase of the lovastatin-containing chows and control chows.

6.) Dr. Lynsey Meikle and Dr. Trudi Gillespie both assisted with some preliminary confocal imaging for dendritic spine analysis.

No part of the work contained in this thesis has been submitted for any other degree or professional qualification.

Signed: _____ Date: _____

Doctor of Philosophy – The University of Edinburgh – 2016

Contents

List of Figures

List of Tables

Abbreviations

4E-BP: eIF4E binding proteins

αCaMKII: Ca^{2+}/calmodulin-dependent protein kinase IIα

ABC: Autism Behaviour Checklist

ACSF: artificial cerebrospinal fluid

AD: Alzheimer's disease

ADHD: attention-deficit hyperactivity disorder

AGS: audiogenic seizure

AMPA: α-amino-3-hydroxy-5-methyl-4-isoxazolepropionic acid

ANOVA: analysis of variance

ASD: autism spectrum disorder

BDNF: brain-derived neurotrophic factor

bp: base pairs

BRR-HRB: Biomedical Research Resources at Hugh Robson Building

BOLD: blood-oxygen-level dependent

cAMP: cyclic adenosine monophosphate

CACNA1C: calcium channel, voltage-dependent, L type, alpha 1C subunit

CB1: cannabinoid receptor type 1

CB2: cannabinoid receptor type 2

CNS: central nervous system

CON: control chow

CPP: 3-(2-Carboxypiperazin-4-yl)propyl-1-phosphonic acid

CRT: cathode ray tube

CSPG: chondroitin sulfate proteoglycan

CT: computed tomography

Cx: cortex

DAB: 3,3'-diaminobenzidine

DBA: dilute brown non-agouti

ddH_2O: double-distilled water

DIV: days *in vitro*

dLGN: dorsal lateral geniculate nucleus

Dr.: Doctor

DSM: Diagnostic and Statistical Manual of Mental Disorders

DTI: diffusion tensor imaging

DZ: dizygotic

e.g.: *exempli gratia* (Latin; "for example")

ECoG: electrocorticogram

EDTA: ethylenediaminetetraacetic acid

EEG: electroencephalography

eIF4E: eukaryotic translation initiation factor 4E

EM: electron microscopy

ERK: extracellular signal-regulated kinase

etc.: *et cetera* (Latin; "and other things" or "and so forth")

[^{18}F]: fluorine-18

FA: fractional anisotropy

FDG: fluorodeoxyglucose

FITC: fluorescein isothiocyanate

FMR1: fragile X mental retardation 1

fMRI: functional magnetic resonance imaging

FMRP: fragile X mental retardation protein

FPP: farnesyl pyrophosphate

FTS: farnesylthiosalicylic acid

FXS: fragile X syndrome

FXTAS: fragile X-associated tremor/ataxia syndrome

G-proteins: guanine nucleotide-binding regulatory proteins

GABA: γ-aminobutyric acid

GFP: green fluorescent protein

GGPP: geranylgeranyl pyrophosphate

GluR1: glutamate receptor 1

GluR1-CT: C-terminal domain of GluR1

GMV: grey matter volume

HMG-CoA: 3-hydroxy-3-methyl-glutaryl-CoA

ICD: International Classification of Diseases

ID: intellectual disability

i.e.: *id est* (Latin; "that is")

IQ: intelligence quotient

K-S test: Kolmogorov-Smirnov test

KO: knock-out

LDL: low-density lipoprotein

LFP: local field potential

LOV: lovastatin-containing chows

MAPK: mitogen-activated protein kinases

MBP: myelin basic protein

MD: monocular deprivation

MeCP2: methyl-CpG-binding protein 2

MEK: mitogen-activated protein kinase kinase

mGluR: metabotropic glutamate receptor

MMP-9: matrix metalloproteinase-9

Mnk1: MAPK-interacting serine/threonine kinase 1

MPEP: 2-methyl-6-(phenylethynyl)-pyridine

MRI: magnetic resonance imaging

mRNA: messenger RNA

mTOR: mammalian target of rapamycin

MZ: monozygotic

n.s.: not significant

NaV channel: voltage-gated sodium channel

NES: nuclear export signal

NF1: neurofibromatosis type 1

NF1: neurofibromin 1

NLS: nuclear localisation signal

NMDA: *N*-Methyl-$_D$-aspartate (or *N*-Methyl-$_D$-aspartic acid)

OCD: obsessive compulsive disorder

OD: ocular dominance

PB: phosphate buffer

PBS: phosphate-buffered saline

PCR: polymerase chain reaction

PD: Parkinson's disease

PDD: pervasive developmental disorder

PDD-NOS: pervasive developmental disorder not otherwise specified

PET: positron emission tomography

PFA: paraformaldehyde

PI3K: phosphoinositide 3-kinase

PKA: protein kinase A

PNS: peripheral nervous system

PP: pyrophosphate

Prof.: Professor

PSD: post-synaptic density

PV^+: parvalbumin-positive

RIPA: radio-immunoprecipitation assay

RNA: ribonucleic acid

RNP: ribonucleoprotein

S6K1: p70 ribosomal S6 kinase 1

SC: subcutaneous

SDS: sodium dodecyl sulfate

SEM: standard error of the mean

SRP: stimulus-selective response potentiation

STDP: spike-timing-dependent plasticity

STED: stimulated emission depletion microscopy

SynGAP: synaptic Ras GTPase-activating protein

TNFα: tumour necrosis factor-α

TrkB: tropomyosin receptor kinase B

TSC: tuberous sclerosis complex

TTX: tetrodotoxin

UBE3A: ubiquitin-protein ligase E3A

UTR: untranslated region

VEP: visual evoked potential

WMV: white matter volume

WT: wild-type

XLID: X-linked intellectual disability

Acknowledgement

Time flies. Four years passed in a sudden and I hardly realised that…

To begin with, I would like to express my sincere gratitude to my supervisor Prof. Peter Kind for giving me this opportunity to start my Ph.D. in the University of Edinburgh. Peter is not only a great mentor who guides me through this journey, but he also offers assistance and advice which helps me get through these years. My sincere thanks also goes to my thesis examiners Prof. Frank Sengpiel and Prof. Mike Cousin, their valuable inputs are essential to me. Great thanks to my thesis committees Prof. David Wyllie and Prof. Giles Hardingham for all their suggestions during my PhD study.

I would like to give my special thanks to Dr. Aleksander Domanski, he and his scripts saved my thesis in many ways. "Phoenix rising from the ashes" was the exact term me and Peter used when Aleks pointed out a new way to analyse my data just before we were about to give up. I would also like to thank Dr. Nathalie Rochefort and Dr. Lynsey Meikle for training me how to perform animal surgeries. I still remember those days working with Lynsey till late night when the lights were off in the animal unit. I would like to thank Dr. Marc-André Martel for his endless patience in training me how to do cell culture, and I will always remember those days we've spent together working in the Laminar hoods. I thank Dr. Sally Till for her patience and detailed instructions in immunohistochemistry, PCR, and Western blotting. I also thank Dr. Lasani Wijetunge and Viktoria Lehner's assistance in intracellular filling and imaging.

I would like to thank Ann Wright and Steve Mitchell for their assistance in conducting those EM experiments. I thank Dr. Trudi Gillespie's assistance in confocal microscopy, and Dr. Sam Booker's assistance in electrophysiological recordings and data analysis. I am grateful to Evelyn Dylda for working with me closely in my final years and offered great help and support through that period. Dr. Janelle Pakan's assistance in data analysis is also greatly appreciated.

I would like to thank all the Kind, Wyllie, and Daw lab members and DBUG members for your support and feedbacks for my work. My special thanks goes to Dr. Sally Till, Dr. Owen Dando, and Danai Katsanevaki for your great help and company through my study. I thank all the staffs in the animal unit and all the animals that helped me complete this thesis through their sacrifice.

I would like to extend my deepest gratitude to my family. Your endless support (both mentally and physically) is the reason that I can pursuit my dream without hesitation.

Last but not the least, I would like to thank my wife who is always there when I need her. Thank you for taking good care of me, and your company is the main reason that keeps me moving forward. Thank you, Dr. Lai.

Abstract

Autism is one of the leading causes of human intellectual disability (ID). More than 1% of the human population has autism spectrum disorders (ASDs), and it has been estimated that over 50% of those with ASDs also have ID. Fragile X syndrome (FXS) is the most common inherited form of mental retardation and is the leading known genetic cause of autism, affecting approximately 1 in 4000 males and 1 in 8000 females. Approximately 30% of boys with FXS will be diagnosed with autism in their later lives.

The cause of FXS is through an over-expansion of the CGG trinucleotide repeat located at the 5' untranslated region of the *FMR1* gene, leading to hypermethylation of the surrounding sequence and eventually partially or fully silencing of the gene. Therefore, the protein product of the gene, fragile X mental retardation protein (FMRP), is reduced or missing.

As a single-gene disorder, FXS offers a scientifically tractable way to examine the underlying mechanism of the disease and also shed some light on understanding ASD and ID. The mouse model of FXS (*Fmr1*$^{-/y}$ mice) is widely accepted and used as a good model, offering good structural and face validity. Since a primary deficit of FXS is believed to be altered neuronal communication, in this thesis I examined white matter tract and dendritic spine abnormalities in the mouse model of FXS. Loss of FMRP does not alter the gross morphology of the white matter. However, recent brain imaging studies indicated that loss of FMRP could lead to some minute abnormalities in different major white matter tracts in the human

brain. The gross white matter morphology and myelination was unaltered in the *Fmr1*$^{-/y}$ mice, however, a small but significant increase of axon diameter in the corpus callosum (CC) was found compared to wild-type (WT) controls. Our computation model suggested that the increase of axon diameter in the *Fmr1*$^{-/y}$ mice could lead to an increase of conduction velocity in these animals.

One of the key phenotypes reported previously in the loss of FMRP is the increase of "immature" dendritic spines. The increase of long and thin spines was reported in several brain regions including the somatosensory cortex and visual cortex in both FXS patients and the mouse model of FXS. Although recent studies which employed state-of-the-art microscopy techniques suggested that only minute differences were noticed between the WT and *Fmr1*$^{-/y}$ mice. In agreement with previous findings, I found an increase of dendritic spine density in the visual cortex in the *Fmr1*$^{-/y}$ mice, and spine morphology was also different between the two genotypes. We found that the spine head diameter is significantly increased in the CA1 area of the apical dendrites of the *Fmr1*$^{-/y}$ mice compared to WT controls. Dendritic spine length is also significantly increased in the same region of the *Fmr1*$^{-/y}$ mice. However, apical spine head size does not alter between the two genotypes in the V1 region of the visual cortex, and spine length is significantly decreased in the *Fmr1*$^{-/y}$ mice compared to WT animals in this region.

Lovastatin, a drug known as one of the 3-hydroxy-3-methyl-glutaryl-CoA (HMG-CoA) reductase inhibitors, functions as a modulator of the mitogen-activated protein kinases (MAPK) pathway through inhibiting Ras farnesylation, was used in an attempt to rescue the dendritic spine abnormalities in the *Fmr1*$^{-/y}$ mice. Mice

lacking FMRP are susceptible to audiogenic seizure (AGS). Previous work has shown that 48 hr of lovastatin treatment reduced the incidence of AGS in the *Fmr1*$^{-/y}$ mice. However, chronic lovastatin treatment failed to rescue the spine density and morphology abnormalities in the *Fmr1*$^{-/y}$ mice.

Mouse models are invaluable tools for modelling human diseases. However inter-strain differences have often confounded results between laboratories. In my final Chapter of this thesis, I compared two commonly used C57BL/6 substrains of mice by recording their electrophysiological responses to visual stimuli *in vivo*. I found a significant increase of high-frequency gamma power in adult C57BL/6JOla mice, and this phenomenon was reduced during the critical period. My results suggested that the C57BL/6JOla substrain has a significant stronger overall inhibitory network activity in the visual cortex than the C57BL/6J substrain. This is in good agreement with previous findings showing a lack of open-eye potentiation to monocular deprivation in the C57BL/6JOla substrain, and highlights the need for appropriate choice of mouse strain when studying neurodevelopmental models. They also give valuable insights into the genetic mechanisms that permit experience-dependent developmental plasticity.

In summary, these findings give us a better understanding of the fine structure abnormalities of the *Fmr1*$^{-/y}$ mice, which in turn can benefit future discoveries of the underlying mechanisms of neurodevelopmental disorders such as ID and ASDs.

Lay summary

Intellectual disability (ID) and autism spectrum disorders (ASDs) are co-occurring developmental disorders. More than 1% of the human population have ASDs and approximately 2 – 3% have ID. Furthermore, it is estimated that over 50% of individuals with ASDs also have intellectual disability and 25 – 30% of people with ID have ASDs. ASDs are mainly diagnosed via three distinct behavioural deficits (namely the "triad" deficits), including impaired social interaction, impaired communication, and restrict interest or repetitive behaviours.

To date, the underlying developmental aetiology of most ASDs/ID remains unknown. However, studying other single-gene disorders that have high co-occurrence of ID and ASDs may offer a strategy to unravel the mystery of autism. Fragile X syndrome (FXS) is one of the single-gene disorders that among 30% of FXS patients will meet the diagnosis criteria for autism in their later lives and almost all boys presenting with ASDs. FXS also shares several behavioural phenotypes such as learning disability and impaired social interaction with autism. Because FXS is caused by the silencing of a single gene, it is relatively straightforward to study in animal models. In this thesis I therefore used a specific mouse line that modelled FXS. This model is widely used and accepted for studying key symptoms observed both in FXS patients and animal models.

The brain comprises two parts, so called white matter and grey matter. The white matter is mainly composed of nerve fibres known as "axons" that connect nearby and distal parts of the brain so they can effectively communicate. The grey

matter, on the other hand, is mainly composed of the brain cells known as “neurons” and “glia”. Furthermore, each one of the hundreds of billions neurons sends out axons that make thousands of contacts with other neurons. These contacts occur on tree-like extensions from the cell called “dendrites”. Alterations in these connections are believed to underlie many forms of ASDs/ID. To gain insights of the underlying mechanisms of FXS, I examined the white matter and grey matter abnormalities in the mouse model of FXS. My results indicated that no gross abnormalities of both the white matter and grey matter were noticed in the mouse model of FXS. An increase of axon diameter was found in the mouse model of FXS, suggesting that the conduction velocity might increase in these animals.

In good agreement with previous findings, I noticed an increase of dendritic spine density and altered spine morphology in two brain regions of the mouse model of FXS. Lovastatin, a well-known blood cholesterol lowering drug, was reported previously that it was effective in rescuing certain key phenotypes in the mouse model of FXS. However, chronic lovastatin treatment did not rescue the dendritic spine abnormalities in these animals.

Since ASDs/ID are developmental disorders that result from both genetic and environmental influences, I next studied the mechanism by which genetic predisposition affects experience-dependent brain development. Two distinct substrains of mice show very different responses to early visual deprivation. I found that mice that lack a particular response to visual deprivation show very different brain rhythms to those that have this response. This finding gives a vital glimpse

into the cellular mechanism that underlies this form of experience-dependent development in the cerebral cortex.

In summary, these findings regarding those fine structure abnormalities in the mouse model of FXS can provide some valuable insights to the underlying mechanisms of FXS, and therefore benefit the further understanding of ID and ASDs.

“The worst thing about a disability is that people see it before they see you.”

—Easter Seals

Chapter 1: General Introduction

1.1 Intellectual disability (ID)

Intellectual disability or mental retardation is defined as *"a condition of arrested or incomplete development of the mind, which is especially characterised by impairment of skills manifested during the developmental period, which contribute to the overall level of intelligence, i.e., cognitive, language, motor, and social abilities"* (World Health Organization, 1993). The prevalence of ID is estimated around 1% of the entire human population (Harris, 2006; Maulik et al., 2011). A strong sexual bias is noticed in the ID population. Approximately 30% more males are diagnosed with ID or mental retardation than females (Leonard and Wen, 2002; McLaren and Bryson, 1987). Among all the individuals with ID, different degrees of mental retardation ranging from mild, moderate, severe, and profound affects about 85%, 10%, 4%, and 2% of this population, respectively (King et al., 2009; Maulik et al., 2011).

1.1.1 Symptoms of ID

The core symptom of ID is a significant impairment in intellectual performance which is determined by scoring 70 or below in the intelligence quotient (IQ) test. Patients with ID are often being identified in early childhood due to the signs of developmental delay or the comorbidity with other early-onset

neurodevelopmental disorders such as epilepsy, autism/autism spectrum disorders (ASDs) or fragile X syndrome (FXS).

Comorbidity in ID patients is common. For example, 40 – 55% of children with autism have ID in a various degrees (Newschaffer et al., 2007), and nearly all patients with FXS have moderate to severe ID (O'Donnell and Warren, 2002). Epilepsy, language disorders, sleep disturbances, and other mental disorders are all common comorbid disorders seen in ID patients (Di Nuovo and Buono, 2007; Einfeld et al., 2011; Emerson and Hatton, 2007; Matson and Cervantes, 2013).

1.1.2 Diagnosis of ID

The diagnosis criteria for ID consists of an IQ test score of 70 or below, and deficits in at least two behaviours related to adaptive functioning by the age of 18 (American Psychiatric Association, 2000). ID is therefore most likely to be diagnosed in late childhood or until early adulthood due to the use of IQ test as its diagnostic tool. Based on the results of the IQ test, ID patients can further be divided into 4 groups: mild (IQ = 55 – 70), moderate (IQ = 40 – 55), severe (IQ = 25 – 40), and profound (IQ < 25) (American Psychiatric Association, 2013). However, the use of IQ test as the main diagnostic tool has been criticised as this cannot assess the actual adaptive functioning of the patients, which is crucial for care givers and social workers to evaluate the level of support the patients need. Moreover, IQ test becomes less valid toward the lower end of its range. Hence, in the latest version of the Diagnostic and Statistical Manual of Mental Disorders, 5th edition (DSM-V), the

severity of ID is now based on adaptive functioning rather than the IQ score, and is assessed in three domains including conceptual, social, and practical skills (American Psychiatric Association, 2013). Based on the DSM-V, ID is only diagnosed when all three of the following criteria are met:

1.) Deficit in intellectual functions (assessed through the IQ test).

2.) Deficit in adaptive functioning (assessed the patient's ability for daily living, e.g., communication, independent living, participation in social activities).

3.) Onset of both 1 and 2 during the developmental period.

1.1.3 Genetics of ID

Both environmental and genetic factors account for about 40% of all the currently known causes of ID, which leaves 60% of the ID population with unknown causes (Rauch et al., 2006). Maternal malnutrition, maternal psychiatric disorders, maternal alcohol abuse during pregnancy, and certain birth complications can all lead to ID in the new-borns (Morgan et al., 2012; Vissers et al., 2015). Moreover, ID is more likely to occur in patients with mental disorders such as schizophrenia, bipolar disorder, and major depression; patients with ID also have a higher risk (about 30%, which is 3 – 4 fold higher than healthy individuals) of developing mental disorders (Morgan et al., 2008; The WHO World Mental Health Survey Consortium, 2004).

Genetic causes of ID are extensively studied. Chromosomal abnormalities (Lubs et al., 2012), rare copy number variants (Girirajan et al., 2012), and *de novo* mutations (Hamdan et al., 2011b; The Deciphering Developmental Disorders Study, 2015; Vissers et al., 2010) have all been reported as a cause of ID. ID can be further subdivided into syndromic ID and non-syndromic ID; syndromic ID patients present at least one or more clinical features of other developmental disorders, whereas in non-syndromic ID patients intellectual disability is their sole clinical feature. Single-gene neurodevelopmental disorders such as FXS, neurofibromatosis type 1 (NF1), and tuberous sclerosis complex (TSC) are all examples of the coexistence between ID and other neurodevelopmental disorders. *De novo* mutations (e.g., *SYNGAP1* haploinsufficiency, *STXBP1*) have been suggested as a major cause of non-syndromic ID. And with the advancement of techniques (e.g., next-generation sequencing, genomic microarrays), more understandings regarding the cause of non-syndromic IDs would be expected.

Finally, X-linked intellectual disability (XLID) have been thoroughly studied in the past 40 years and it is estimated to account for 5 – 10% of ID in males (Lubs et al., 2012). In total, 102 genes has been described and are responsible for around 50% of the current known XLID syndromes (Lubs et al., 2012). Details of these genes and their mutation sites are summarised in Figure 1-1 (from Lubs et al., 2012).

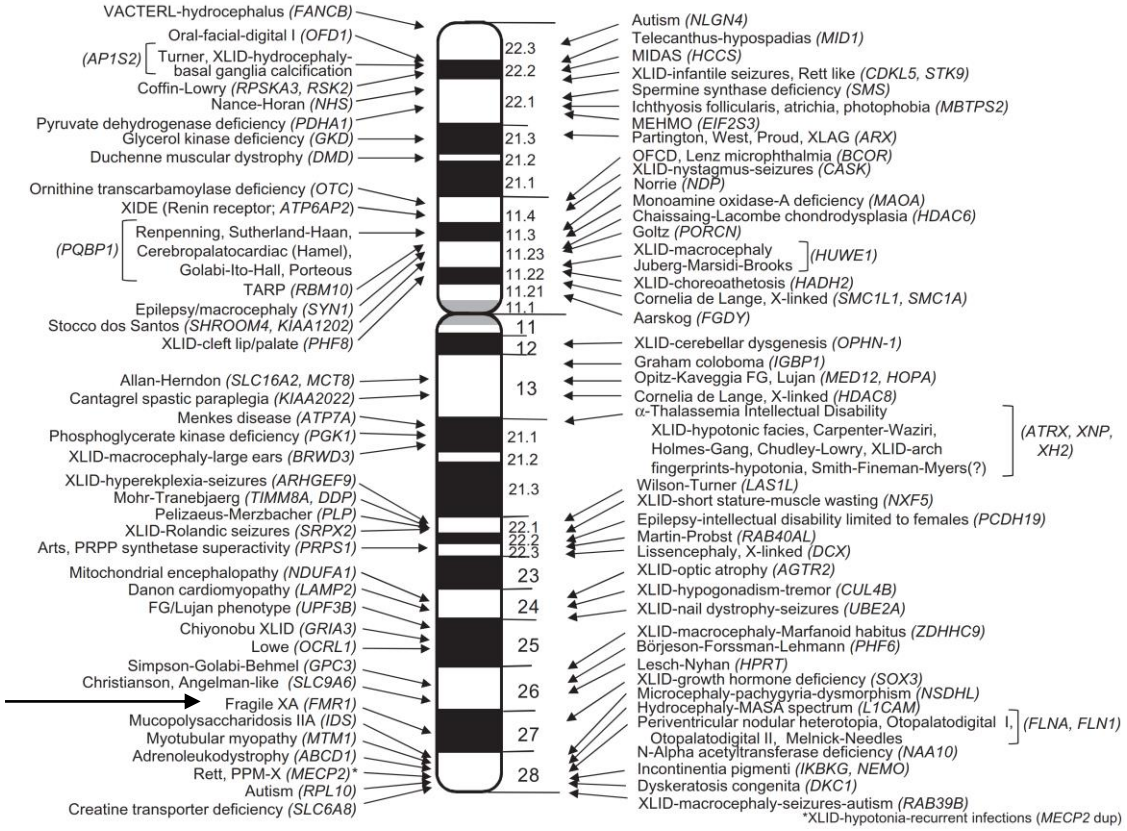

Figure 1-1. A detailed map of genes with identified mutations that cause syndromal X-linked intellectual disability and their locations on the chromosomal band.

Arrowhead indicates the location of the *FMR1* gene on the X-chromosome, which is considered as the leading cause of X-linked intellectual disability. Figure credit: (Lubs et al., 2012).

1.2 Autism and autism spectrum disorders (ASDs)

Autism is the most common ASD, and the latter has a prevalence of 1 in 68 children among the population of the United States and 1 in 160 children among the entire human population (U.S. Centers for Disease Control and Prevention, 2014;

World Health Organisation, 2016[1]). The prevalence of autism has increased dramatically since 1970, as children born before that with a prevalence rate of 2 – 5 cases per 10000 children; and children born after 1970 with a rate around 1 in 1000 (Gillberg and Wing, 1999). Although there is no precise explanation for this increase, it is believed that the improve of diagnostic and the awareness of the disease are the two main reasons (Gillberg and Wing, 1999).

Autism is first described by two psychiatrists, Dr. Leo Kanner and followed by Dr. Hans Asperger in the early 1940s (Asperger, 1944; Kanner, 1943). At that time Kanner's definition of autism was more "narrowed" compared to the current standards. He described 11 children with "extreme autistic aloneness," delayed echolalia, and an *"anxiously obsessive desire for the maintenance of sameness"*, and some of them may have extraordinary memory skills in his report published in 1943 (Baker, 2013; Kanner, 1943). This "strict" definition of autism provided by Kanner may count as one of the major factors that the prevalence of autism is far fewer of the children born before 1970, as most of the physicians use Kanner's definition as the diagnostic standard of autism at that time before the third version of the Diagnostic and Statistical Manual of Mental Disorders (DSM-III) was introduced.

ASDs are the leading cause of intellectual disability and affects around 1% of the entire human population (Baird et al., 2006; Chakrabarti and Fombonne, 2001; Elsabbagh et al., 2012; Kim et al., 2011; Levy et al., 2009; U.S. Centers for Disease Control and Prevention, 2014). Traditionally, ASDs comprise three different

[1] From the WHO website: http://www.who.int/mediacentre/factsheets/autism-spectrum-disorders/en/#

diagnoses: autism, Asperger's disorder, and pervasive developmental disorder not otherwise specified (PDD-NOS). All these three disorders overlap in a certain degree but meanwhile contain some distinct features. For example, patients with Asperger's disorder generally do not show signs of language delay in their early development, whereas most autistic patients would show different degrees of language delay and communication impairment. But repetitive/stereotyped behaviours and social deficits are core features in both of them. Details of each disorder will be discussed in the rest of this Chapter.

1.2.1 Symptoms and comorbidity

Autism stands for a disorder that covers a wide range of symptoms. It is mainly diagnosed via three distinct behavioural deficits (namely the "triad" deficits), including impaired social interaction, impaired communication, and restrict interest or repetitive behaviours (Belmonte and Bourgeron, 2006; Newschaffer et al., 2007). However, the diagnosis of autism is reduced to two main categories according to the latest version of DSM (DSM-V); namely the deficits in social communications and restricted/repetitive behaviours in early childhood.

From the developmental perspective, these symptoms mainly become obvious around 3 years of age. High risk infants (whose older siblings are diagnosed with autism) can show certain deficits in either communication, ways of play, or responsiveness to outer stimuli as early as 6 – 12 months of age (Volkmar and Chawarska, 2008). Less and limited eye contact, hypersensitivity to outer stimuli

such as touch, problems of sleep regulation, and less likely to engage in either motor or vocal imitations from these children have also been reported previously (Dawson et al., 2000; Maestro et al., 2002).

Around 50% of autistic patients also have intellectual disability/mental retardation (Levy et al., 2009; Newschaffer et al., 2007; Yeargin-Allsopp et al., 2003), but some patients tend to have normal or even above average IQ. Beyond that, some other symptoms are often seen in patients with ASD, such as seizure (Matson and Neal, 2009; Tuchman and Rapin, 2002; Tuchman et al., 2010; Viscidi et al., 2013), attention-deficit hyperactivity disorder (ADHD) (Levy et al., 2009), dysregulation of immune system (Warren et al., 1996), problems relating to gastrointestinal systems (Kuddo and Nelson, 2003), difficulties with feeding (Volkert and Vaz, 2010), and sleep disruption (Polimeni et al., 2005).

Comorbid psychiatric disorders in patients with autism are also mentioned in previous studies (Leyfer et al., 2006; Matson and Nebel-Schwalm, 2007; Simonoff et al., 2008). Among all of the comorbid psychiatric disorders, 44% of the children with autism meet the diagnostic criteria for specific phobias. Interestingly, children with autism tend to have uncommon phobias when comparing with normal developing children. For example, certain types of specific phobias are common in the normal children population, such as fears of tunnels and bridges; but for the children with autism, they rarely develop phobias to these. Instead, they tend to develop phobias to more than one object or situation, which normal children would not have phobias with, such as crowds and loud noises (Levy et al., 2009; Leyfer et al., 2006).

Obsessive compulsive disorder, or OCD, is another psychiatric disorder that patients with autism have high comorbidity with. Around 37% of children with autism were also diagnosed to have OCD (Levy et al., 2009; Leyfer et al., 2006). Other comorbid psychiatric disorders common in patients with autism are ADHD (up to 31%), anxiety, and depression (Kim et al., 2000).

1.2.2 Diagnosis of autism and ASDs

In the new online app version (2016) of the 10th International Statistical Classification of Diseases and Related Health Problems (ICD-10) (World Health Organization, 1993), autism is categorized under "Pervasive Developmental Disorders (PDDs)" which is then specified as:

"A group of disorders characterized by qualitative abnormalities in reciprocal social interactions and in patterns of communication, and by a restricted, stereotyped, repetitive repertoire of interests and activities. These qualitative abnormalities are a pervasive feature of the individual's functioning in all situations."

According to the previous edition of the DSM (DSM-IV), autism (autistic disorder is the term used in DSM-IV) is categorised as PDD along with other four disorders: Asperger's disorder, childhood disintegrative disorder, PDD-NOS, and Rett syndrome (American Psychiatric Association, 2000). However, in the latest version of the DSM (DSM-V), autism is no longer categorised under PDD but now it is an independent diagnosis category by the name of "Autism Spectrum Disorder"

(American Psychiatric Association, 2013). The introduction of ASD as an independent diagnosis in DSM-V is based on several considerations, one of them is the overlap between PDD-NOS and Asperger's disorder which needs to be clarified. Beyond this, the arguments that Asperger's disorder is just a group of "high-functioning" autistic patients (i.e., IQ > 70) also urges a better and clearer definition of these PDDs (Carpenter et al., 2009; Howlin, 2003; Sharma et al., 2011).

According to the definition of PDD-NOS in the DSM-IV, it has been described as the following:

"This category should be used when there is a severe and pervasive impairment in the development of reciprocal social interaction or verbal and nonverbal communication skills, or when stereotyped behaviour, interests, and activities are present, but the criteria are not met for a specific pervasive developmental disorder, schizophrenia, schizotypal personality disorder, or avoidant personality disorder. For example, this category includes "atypical autism"—presentations that do not meet the criteria for autistic disorder because of late age of onset, atypical symptomatology, or subthreshold symptomatology, or all of these."

Meanwhile, Asperger's disorder is only diagnosed when all six of the following criteria are met:

1.) Qualitative impairment in social interaction.

2.) Restricted, repetitive, and stereotyped patterns of behaviour, interests, and activities.

3.) The disturbance causes clinically significant impairment in social, occupational, or other important areas of functioning.

4.) There is no clinically significant general delay in language (e.g., single words used by age 2 years, communicative phrases used by age 3 years).

5.) There is no clinically significant delay in cognitive development or in the development of age-appropriate self-help skills, adaptive behaviour (other than in social interaction), and curiosity about the environment in childhood.

6.) Criteria are not met for another specific pervasive developmental disorder or schizophrenia. (American Psychiatric Association, 2000)

Thus, if one does not show obvious cognitive impairment but show some repetitive/restricted behaviours during childhood development, then the presence of delayed language development would be the main factor to assign this patient into the PDD-NOS group rather than the Asperger's disorder group. And depending on the severity of cognitive or language impairment, PDD-NOS can then be subdivided to three subgroups: 1) a high-functioning group that resembles Asperger's disorder but with mild cognitive impairment or language delay; 2) a subgroup that resembles autism but with either a relative late onset or too severe cognitive delays, or patients are too young to meet the full diagnostic criteria for autism; and 3) a subgroup that does not meet the full diagnostic criteria for autism due to having fewer repetitive/stereotyped behaviours (Walker et al., 2004). And with the newly introduced system there will be no Asperger's disorders nor PDD-NOS in the future.

To be more precise, autistic disorder, Asperger's disorder, and PDD-NOS are now collapsed into the "Autism Spectrum Disorder" described in the DSM-V (American Psychiatric Association, 2013).

With the new DSM-V, now the diagnosis criteria for autism is reduced to two main categories with two restrictions, and all criteria need to be fulfilled to meet the diagnosis. To summarise, patients show signs of A) persistent deficits in social communication and B) restricted and repetitive patterns of behaviour, interests, or activities; and C) all these symptoms are present in early childhood and D) these symptoms together limit and impair their everyday functioning can then be diagnosed as ASD (American Psychiatric Association, 2013).

1.2.2.1 Post-mortem diagnosis of autism.

In Darby's report dated back in 1976, he did not find any pathological evidence in two patients diagnosed with autism with mental retardation (Darby, 1976). One autistic patient was diagnosed with tuberous sclerosis after the autopsy (Darby, 1976). Even to date, the post-mortem studies for autism are still very limited compared to other neurodevelopmental disorders, fewer than 100 cases and approximately 5 autism cases per study (Amaral et al., 2008). Although no gross anatomical differences were reported, one most consistent finding among several previous studies suggested that an increase of head circumference was noticed in children with autism in their early lives, especially the 1st year after birth. This rapid increase of head circumference generally decelerate after the 1st year of life

(Courchesne et al., 2003, 2001; Dawson et al., 2007; Dementieva et al., 2005; Hazlett et al., 2005; Sparks et al., 2002).

1.2.3 Functional brain imaging findings in autism

The increased head circumference in the early ages of patients with autism reveals that there might be some brain anatomical and structural deficits among them. With the improved brain imaging techniques, scientists and physicians now can gather more information regarding our brain in a more efficient way. And more importantly, with the invention of magnetic resonance imaging (MRI) and positron emission tomography (PET), brain imaging can now not only give us detailed structural information about the brain but also evaluate its function. The advancement of brain imaging techniques is crucial as functional brain imaging can detect the minute brain activities during the time when subjects are performing tasks that designed to stimulate or require the activation of certain specific brain regions. Thus functional brain imaging can provide some invaluable information that cannot be obtained via traditional brain imaging such as X-ray computed tomography (CT).

To date, the primary use of PET is to detect the consumption of glucose in the blood flow. As glucose is the main source of energy consumption for all the organs in the body, through measuring the rate and amount of glucose consumption can therefore indicate the activity of organs or regions during the imaging process. To achieve this goal, subjects need to first receive an injection of a short-lived

radioactive tracer isotope, the most common one is the [^{18}F]-fluorodeoxyglucose[2] (FDG), which is an analogue of glucose (Boellaard et al., 2010). With its fine tissue metabolic mapping, FDG-PET is now greatly used in the field of oncology as tumour tissues consume more energy than normal tissues (Boellaard et al., 2010). Combining with CT scan, the PET-CT scanner can provide a thorough examination of the subject with the 3-dimential structural reconstruction via CT and tissue activity measured by PET. MRI, on the other hand, is mainly designed to detect the much smaller changes in the blood flow during energy consumption, which is the consumption of oxygen. Similar to PET, MRI scanning is also a non-invasive procedure. MRI can also be used to do functional mapping of the brain through its blood-oxygen-level dependent (BOLD) imaging, MRI can therefore measure brain activity and so called the functional MRI (fMRI) (Ogawa et al., 1992; Raichle, 2003).

In Courchesne's paper (Courchesne et al., 2001) dated back to 2001, using MRI to systematically analyse the brain structure abnormalities in 2 – 4-year-old children with autistic traits showed that over 90% of autistic boys had a significantly larger brain volume compared to normal controls. Meanwhile, 37% of these boys met the diagnostic criteria for developmental macrencephaly, a clinical symptom used to described an abnormally large brain (Courchesne et al., 2001). The increased overall cerebral volumes in children with ASDs were further confirmed in several other studies (Courchesne et al., 2003; Dawson et al., 2007; Dementieva et al., 2005; Hazlett et al., 2005; Sparks et al., 2002), the volume of amygdalae and hippocampi

[2] [^{18}F]: fluorine-18

were also significantly increased as indicated in some previous studies (Schumann et al., 2009, 2004; Sparks et al., 2002).

Several detailed studies indicated that besides a general increased head circumference, some sub-regional and cell-specific abnormalities were also noticed in the patients of autism. A case study composed of six autistic patients revealed an interesting results that all six patients showed increased cell packing density and reduced cell size in the hippocampus and amygdala regions, accompanying with reduced and limited dendritic arbors (Kemper and Bauman, 1993; Palman et al., 2004). A decreased Purkinje cell density in the cerebellum is also reported (Kemper and Bauman, 1993; Ritvo et al., 1986; Williams et al., 1980), which is surprisingly consistent among studies that it is observed in 12 out of 12 autistic patients examined by 4 different labs (Courchesne, 1997). Besides, reduced volume of grey matter is also noticed in the autistic patients (Courchesne et al., 2001). Abnormalities in the cerebral cortex is mostly sparse and not consistent between studies nor cases examined. One area worth mentioning is the anterior cingulate cortex, which is consistently reported that it is unusually coarse and poorly laminated among all cases examined (Kemper and Bauman, 1993).

A recent study examining the whole brain local network connectivity of autistic patients, unaffected siblings, and typically-developing controls showed that hypoconnectivity might be an endophenotype of autism (Moseley et al., 2015). Several diffusion tensor imaging (DTI) studies also suggested that the brain microstructures of autistic patients are affected such as the corpus callosum (CC) (Alexander et al., 2007; Barnea-Goraly et al., 2004; Hardan et al., 2000), brainstem

(Travers et al., 2015), bilateral anterior cingulate cortex (Barnea-Goraly et al., 2004), and the frontal lobe (Sundaram et al., 2008). Although overall in general myelination in patients with autism appears to be normal (Courchesne, 1997).

1.2.4 Underlying genetics of autism and ASDs

Although the discovery and diagnosis of autism can be traced back to the 1940s, its precise underlying mechanism remains unknown. One thing to be noted is that autism is highly genetic, sibling studies showed that the second child's chances of being diagnosed as autism or ASDs is up to 50 times higher than normal population if the first child is autistic (Levy et al., 2009; O'Roak and State, 2008; Rutter et al., 1999). Sex differences are also noticed in autism, where males tend to be affected four times more than females (Kogan et al., 2009). Further studies focusing on the monozygotic (MZ) and dizygotic (DZ) twin pairs yield some more intriguing results: the concordance in MZ ranges from 69% – 95% and in DZ is 0% in most cases reported, highlights the importance of genetic factors in autism but also raises the notion that other factors are involved in the cause of autism (Lauritsen and Ewald, 2001; Newschaffer et al., 2007; Ritvo et al., 1985; Steffenburg et al., 1989). Among 6 – 10% of children with autism, a medical disorder that might lead to autism is diagnosed (Fombonne, 2003; Fombonne et al., 1997). However, this leaves approximately 90% of the rest of the children belonging to idiopathic autism, and this urges the understanding of its underlying mechanisms.

Several genetic findings in the recent years shed a light on the underlying mechanisms of autism. Certain single-gene disorders such as FXS (*FMR1*), Rett syndrome (*MECP2*), neurofibromatosis type 1 (*NF1*), tuberous sclerosis complex (*TSC1/2*), Angelman syndrome (*UBE3A*: ubiquitin-protein ligase E3A) , and Timothy syndrome (*CACNA1C*: calcium channel, voltage-dependent, L type, alpha 1C subunit) are all known genetic risk factors for autism (Kelleher and Bear, 2008). FXS is the leading cause of human intellectual disability, up to 30% of patients with FXS would meet the diagnostic criteria for autism in their lives (Jacquemont et al., 2007; Kelleher and Bear, 2008).[3] Another X-linked single gene disorder, Rett syndrome, is almost exclusively occurs in females, with an incidence of 1 in 10000 – 15000. It is one of the most common causes of mental retardation in females, and it is caused via a loss-function mutation of the *MECP2* gene which encodes the methyl-CpG-binding protein 2 (MeCP2) (Amir et al., 1999). Nearly 100% of patients with Rett syndrome will develop autism in their later lives (Kelleher and Bear, 2008). Patients with TSC also have a very high incidence rate of autism, up to 60% of patients with TSC may develop autism in their later lives (Kelleher and Bear, 2008; Miles, 2011). NF1 is another common neurodevelopmental disorder which is caused by losing function of the neurofibromin 1 gene, or *NF1*. Neurofibromin is a tumour suppressor protein and is mainly found within neurons and oligodendrocytes in the central nervous system (CNS) or Schwann cells in the peripheral nervous system (PNS) (Daston et al., 1992; Wallace et al., 1990; Zhu et al., 2002). Patients with Angelman syndrome usually suffer from severe mental retardation, severe language

[3] FXS will be discussed in detail in an independent section (Chap. 1.3).

delay, and often show loud laughter or smiling, which is one of the characteristic of this disorder (Peters et al., 2004). Although the precise underlying mechanism is unclear, a single mutation or a deletion on chromosome 15 of the region which contains the *UBE3A* gene, is recognised as the main cause of this disorder. Up to 40% of children with Angelman syndrome also meet the diagnostic criteria for autism (Kelleher and Bear, 2008; Peters et al., 2004). A rarer disorder, Timothy syndrome, is also reported in several previous studies which suggest it might also lead to autism. Timothy syndrome was first reported in 1992, that some patients showed a novel arrhythmia syndrome which associated with syndactyly (webbing of fingers and toes). Beyond heart conditions, affected individuals also suffered from multiple organs/systems symptoms, including eyes, skin, gastrointestinal system, teeth, lungs, immune system, and the CNS (Splawski et al., 2004). Due to its severity, the average age of death among affected individuals is 2.5 years. Around 60% of surviving individuals will meet the diagnostic criteria for autism owing to the severe language and cognitive impairment of the disorder (Kelleher and Bear, 2008; Splawski et al., 2004). Besides these known single-gene disorders, novel *de novo* mutations that contribute to ASDs are also being noticed in recent years, since they offer more candidate genes that may have been neglected previously (Hamdan et al., 2011a, 2009; Iossifov et al., 2012; O'Roak et al., 2012, 2011; Ronemus et al., 2014; Sanders et al., 2012).

The intriguing fact that MZ twins do not have 100% concordance may suggest that other factors such as environmental factors would also contribute to ASDs. Most of the current predictable factors are involved in maternal behaviour,

such as the use of valproic acid, thalidomide and alcohol during maternity. Other factors like maternal hypothyroidism, congenital cytomegalovirus infection, and congenital rubella infection (for a detailed review, see Folstein and Rosen-Sheidley, 2001). Among this, congenital rubella infection is the most compelling evidence that links to either typical or atypical autism, roughly 10% children with congenital rubella meet the diagnostic criteria for autism (Chess, 1971; Desmond et al., 1967).

1.2.5 Current therapeutic strategies for autism and ASDs

As described above, ASD is a heterogeneous syndrome that its aetiology includes comorbidity with other neurodevelopmental disorders, genetic mutations, exposure to certain substances during maternity, and environmental factors. Thus, no cure has been found even to date, after the disorder has been identified 70 years ago.

There are only two approved pharmacological therapies for ASD currently, risperidone and aripiprazole, and both are designed to alleviate the irritability which is caused by ASD rather than targeting the core symptoms (Ghanizadeh et al., 2014). Other atypical antipsychotics may be used, such as drugs that alleviate ADHD symptoms in patients with autism, antidepressants, and antiepileptic drugs. However, only methylphenidate (Ritalin) has shown to be effective in improving ADHD symptoms in patients with autism, but many other antipsychotic drugs either did not differ from placebo or cause more adverse effects than improving the symptoms (Ji and Findling, 2015).

Thus, behavioural training sessions and language therapies are essential to improve patients communicating skills and allow them to learn how to interact with other individuals. Since most children are diagnosed at early childhood, parenting workshops and professional consultants also are key resources to help the whole family to understand and cope with autistic patients.

1.3 Fragile X syndrome (FXS)

FXS is the most common inherited form of human mental retardation and is the leading known genetic cause of autism, affecting approximately 1 in 4000 males and 1 in 8000 females (Crawford et al., 2001; O'Donnell and Warren, 2002; Turner et al., 1996). Moreover, approximately 30% of boys with FXS will meet the diagnostic criteria for autism in their lives (Jacquemont et al., 2007). The predominant cause of FXS is a trinucleotide (CGG) repeat expansion in the 5' untranslated region (UTR) of the fragile X mental retardation 1 (*FMR1*) gene. Humans without FXS normally have 6 – 54 CGG repeats, however the repeat length is much longer in individuals with FXS and cytosines in the region become hypermethylated when the number of repeats exceeds 200. This leads to silencing of *FMR1* and loss of the protein it encodes, fragile X mental retardation protein (FMRP) (Kooy, 2003; Krueger and Bear, 2011; Penagarikano et al., 2007; Verkerk et al., 1991). Whereas autism appears to involve multiple genetic factors, FXS is caused by mutations in one single gene. Therefore animal models of FXS are likely

to offer insights into symptoms shared between these related disorders (The Dutch-Belgian Fragile X Consortium, 1994).

1.3.1 Symptoms of FXS

The first FXS report was described by J. Purdon Martin and Julia Bell in 1943, the same year when Leo Kanner published the first report of autism (Martin and Bell, 1943). In this report, Martin and Bell examined a family in which 11 males within two generations showed abnormal signs including a severe degree of dementia, and their mental ages were between two to four years of age despite the fact that all of them were above age sixteen and some of them were in their fifties (Martin and Bell, 1943). Beyond mental retardation, patients of FXS often have some other clinical signs such as spontaneous epilepsy, autistic behaviours, hyperactivity, and macroorchidism (Bowen et al., 1978; Hatton et al., 2006; Kooy, 2003; Musumeci et al., 1991; Partington, 1984; Penagarikano et al., 2007; Turner et al., 1975). Some distinct facial characteristics were also noticed, an elongated, narrow face and prominent ears were the most commonly accepted facial features of FXS (Heulens et al., 2013; Penagarikano et al., 2007). A below-average IQ score is often noticed in affected individuals, in males IQ can range from 20 – 70 whereas in females IQ usually falls in the mildly retarded range (IQ: 50 – 70) (Terracciano et al., 2005).

1.3.2 Diagnosis of FXS

The term "fragile X syndrome" describes the nature of this disease; a fragile site on the X chromosome. This phenomenon was first reported by Lubs in 1969, when he identified a constriction of the long arm of the X chromosome from several mentally retarded individuals in a single family (Lubs, 1969). Years later Sutherland's work first established the concept that specific culture conditions (i.e., types of the tissue culture medium) would affect the frequency of lesions at the fragile site (Sutherland, 1977). And he concluded that the fragile site of FXS is likely located either in the Xq27 or Xq28 region (Sutherland, 1977). The fragile site was then further confirmed that it is located specifically to band Xq27.3 through using an electron microscope (Harrison et al., 1983).

Through years of research we now can conclude that the cause of FXS is through silencing of the *FMR1* gene and eventually lead to the loss of FMRP. The silencing process is called dynamic mutation (Richards and Sutherland, 1997), where the copy number of trinucleotide repeat exceeds to a certain degree that would lead to a disease and/or a fragile site of the gene. In the case of FXS, the length of the CGG trinucleotide repeat which is located in the 5' UTR is more than 200; whereas in unaffected individuals the length of the repeat is between 6 – 54. The expansion of the CGG repeat lead to hypermethylation to the surrounding sequence and silence the gene entirely or partially, therefore contribute to the absence of the protein product FMRP (Penagarikano et al., 2007; Pieretti et al., 1991; Verkerk et al., 1991). The CGG-repeat expansion mutation accounts for ~98% of all FXS patients,

however, about 1% of FXS patients are not caused by expansion of the CGG repeat but through rare single point mutations in the *FMR1* gene (Collins et al., 2010).

A diagnosis of FXS is often made in young children as some symptoms such as delayed or absent of language development are noticed around 3 years of age (Bailey et al., 2009). At the early developmental stage, children with FXS can be misdiagnosed as ASD due to sharing some common traits (e.g., irritability, symptoms of ADHD, social and language deficits) (Sullivan et al., 2006). Some facial characteristics like a narrow-long face, prominent ears, and highly arched palate combine with macroorchidism (can be noticed around 2 years of age) can assist physicians to better distinguish these children (Lachiewicz and Dawson, 1994). Beyond these behavioural traits and other symptoms, a genetic screening would be the most accurate way to confirm the diagnosis of FXS.

1.3.3 Functional brain imaging findings in FXS

A series of brain imaging studies reveal some minute differences between the FXS patients and healthy controls. To summarise, increased fractional anisotropy (FA) values and decreased radial diffusivity are noticed in the inferior longitudinal, inferior fronto-occipital, and uncinated fasciculi from both male and female patients with FXS based on DTI findings (Green et al., 2015). FA describes the degree of diffusivity and reports with a value between 0 and 1. A value of 0 represents that diffusion is unrestricted thus it can happen in any directions; whereas a value of 1 indicates that diffusion is highly restricted and can only diffuse along one axis. FA

values can be used to measure brain white matter (WM) integrity, especially axon fibre density and myelination. Thus, increased FA values in the FXS patients suggests increased fibre density and/or increased myelination in those areas. Lower FA values is reported in the fronto-striatal pathways and parietal sensory-motor tracts from female FXS patients (Barnea-Goraly et al., 2003). On the contrary, increased axon fibre density is reported in the left ventral fronto-striatal pathway from young boys with FXS (Haas et al., 2009).

Findings in MRI studies also reveal some microstructural alterations in patients with FXS. Functional connectivity and grey matter density are found decreased in the left insular cortex in both male and female patients compared to age-matched healthy controls (Hall et al., 2013). Enlarged grey matter volume (GMV) in the caudate, thalamus, and fusiform gyri is reported in young males with FXS (1 – 3 years old), and reduced GMV is noticed in the cerebellar vermis. Along with this, white matter volume (WMV) of the striatal-prefrontal regions was increased in FXS patients compared to controls (Hoeft et al., 2010). The decrease of posterior vermis size is also reported in another independent study focusing on both male and female FXS patients (Mostofsky et al., 1998). A summarised table is listed below.

Table 1-1. A brief summary of brain structural abnormalities in individuals with FXS.

DTI	Age	~20 y/o
	Gender	Males and females
	Findings	Increased FA and decreased radial diffusivity in the inferior longitudinal, inferior fronto-occipital, and uncinated fasciculi
	Ref.	(Green et al., 2015)

DTI	Age	13 – 22 y/o
	Gender	Females
	Findings	Lower FA values was reported in the fronto-striatal pathways and the parietal sensory-motor tracts
	Ref.	(Barnea-Goraly et al., 2003)
DTI	Age	1 – 3 y/o
	Gender	Males
	Findings	Increased fibre density in the left ventral fronto-striatal pathway
	Ref.	(Haas et al., 2009)
DTI	Age	7 – 14 y/o
	Gender	Females
	Findings	Higher diffusivity in the corpus callosum, parts of the internal and external capsules, occipital lobes, and central portions of the right thalamus
	Ref.	(Villalon-Reina et al., 2013)
MRI	Age	10 – 23 y/o
	Gender	Males and females
	Findings	Decreased functional connectivity and grey matter density in the left insular cortex
	Ref.	(Hall et al., 2013)
MRI	Age	1 – 3 y/o
	Gender	Males
	Findings	Enlarged GMV in the caudate, thalamus, and fusiform gyri; reduced GMV in the cerebellar vermis WMV of the striatal-prefrontal regions was greater over time
	Ref.	(Hoeft et al., 2010)
MRI	Age	Range from 1 – 43 y/o, with a mean age of 11 y/o

	Gender	Males and females
	Findings	Decreased posterior vermis size in the FXS patients
	Ref.	(Mostofsky et al., 1998)

1.3.4 Animal models of FXS

Animal models are essential for tackling the underlying mechanisms of human diseases. In the case of FXS, several animal models across different species were made in this regard, including *Drosophila* (Lee et al., 2003; McBride et al., 2005; Michel et al., 2004; Morales et al., 2002; Sekine et al., 2008), zebrafish (den Broeder et al., 2009; Tucker et al., 2006), mouse, and more recently rat (Hamilton et al., 2014; Till et al., 2015).

Drosophila contains a single, functionally conserved member of the *FMR1* family, the *dfmr1* gene (Wan et al., 2000). Zhang *et al*. and Morales *et al*. referred to the *dfmr1* gene as *Drosophila fragile X related* (*dfxr*) gene in their studies. Similar to mammals, *Drosophila* dFXR is highly expressed in both pre- and postsynaptic neurons, and *dfxr* mutants showed defects in the larval neuromuscular junction (NMJ) synaptic terminals compared to WT flies (Zhang et al., 2001). Further characterisation indicates that dFXR is ubiquitously expressed and cytoplasmically localised, and only exists in neurons but not in glia (Morales et al., 2002). dFXR was also highly expressed in dendritic arborisation neurons, and more dendritic process

(especially higher-order branches) was reported in the *dfxr* mutant larvae compared to the WT larvae (Lee et al., 2003).

Morpholino antisense oligonucleotide repression of *fmr1* mRNA translation (*fmr1*MO) was used to study the loss-of-function of *fmr1* in the zebrafish. The *fmr1*MO zebrafish showed a great reduction of protein levels of Fmr1, and a significant increase in neurite branching and an increase in neurite branch terminations in Rohon-Beard primary sensory neurons (Tucker et al., 2006). These defects can then be rescued by treating *fmr1*MO-injected embryos with a selective mGluR5 antagonist 2-methyl-6-(phenylethynyl)-pyridine (MPEP), indicating the branching defects caused by the loss of Fmr1 was mGluR-dependent. One characteristic phenotype of human patients with FXS is mild craniofacial abnormalities such as elongated face, prominent ears, and high-arched palate (Heulens et al., 2013). These facial features were not recapitulated in the mouse model of FXS as previously reported (Heulens et al., 2013). However, craniofacial defects were noticed in the *fmr1*MO zebrafish (abnormalities of the Meckel's cartilage) and can be rescued by MPEP treatment (Tucker et al., 2006).

Instead of using the knock-down approach, den Broeder and colleagues used the *fmr1* knock-out strategy to study the loss of Fmr1 in zebrafish (den Broeder et al., 2009). Strikingly, none of the previously characterised phenotypes (i.e., craniofacial defects and abnormal neurite branching) reported by using the *fmr1*MO zebrafish were found in the *fmr1* knock-out zebrafish. One possible explanation is that the morpholino-induced phenotypes may not be directly linked to the loss of Fmr1, as

morpholino oligonucleotides are known to cause phenotypes that are unrelated to the intended gene (Robu et al., 2007).

The first genetic mouse model of FXS was engineered in 1994 (The Dutch-Belgian Fragile X Consortium, 1994). Taking advantage of the fact that the mouse *Fmr1* gene has 98% homology with the human *FMR1* gene, the mouse model was engineered by introducing a neomycin cassette into exon 5 of the mouse *Fmr1* gene, to generate an *Fmr1* knock-out mouse. This mouse model of FXS successfully recapitulated some of the key phenotypes of the disease, including macroorchidism, learning deficits, and hyperactivity (The Dutch-Belgian Fragile X Consortium, 1994). Moreover, the brain of the *Fmr1* knock-out mouse did not differ from the WT mice, with normal myelination and no gross alterations were noted (The Dutch-Belgian Fragile X Consortium, 1994). And most importantly, no FMRP expression was found in the brains of the knock-out mice when examined with Western blotting (The Dutch-Belgian Fragile X Consortium, 1994).

The *Fmr1* knock-out mouse showed several behavioural phenotypes that can be related to FXS-like symptoms, including hyperactivity, seizures, cognitive impairments, increased anxiety/depression, and hyper-responsiveness to sensory stimulation (Bregman et al., 1988; Ding et al., 2014; Frankland et al., 2004; Kooy, 2003; Musumeci et al., 2000, 1991; Spencer et al., 2005; The Dutch-Belgian Fragile X Consortium, 1994). Some autistic-like phenotypes were also reported, such as repetitive/stereotypic behaviours and deficits in social interaction, which corresponded to the high co-occurrence of ASDs with FXS (Bailey et al., 2001;

Hatton et al., 2006; Kerby and Dawson, 1994; Rogers et al., 2001; Spencer et al., 2011).

Intriguingly, the cause of FXS is an expansion of the CGG trinucleotide repeat located in the promotor region of the *FMR1* gene, and eventually silence the gene through hypermethylation. Thus, the *Fmr1* knock-out mouse mentioned above only mimicked the result of losing FMRP, but did not completely reproduce the actual cause of FXS. Several studies therefore began to create mouse models of FXS via expanding the CGG repeat, which should be a more causative and precise model than the knock-out model.

The CGG repeat in the *FMR1* gene is well-conserved in most of the mammals with a variation of the number of copies of the repeat between species (Deelen et al., 1994). To replicate the expansion of CGG repeat in mice, a "knock-in" mouse model was engineered by replacing the endogenous mouse CGG repeat (~8 – 11 CGG) with a human CGG repeat which carried various numbers of CGG triplets varying from studies (Bontekoe et al., 2001; Lavedan et al., 1998, 1997; Ludwig et al., 2014; Van Dam et al., 2005). When numbers of CGG triplets of the inserted human CGG repeat ranging from 50 – 200 (i.e., in the permutation range), the knock-in mice recapitulated the fragile X-associated tremor/ataxia syndrome (FXTAS) and showed an elevation of *Fmr1* mRNA level and a slightly reduced FMRP level as well as some neuromotor disturbances and cognitive decline shown in humans with FXTAS (Ludwig et al., 2014; Tassone et al., 2000; Van Dam et al., 2005). Longer expansions (> 200 CGGs) would then be expected to mirror FXS in humans, which

would be more promising than previous knock-out models as this approach mimicked the actual mechanism that caused FXS.

However, a longer expansion of the CGG triplets did not silence the *Fmr1* gene in the knock-in mouse model and FMRP was still expressed, hence greatly reducing the possibility of using this knock-in model as a model of FXS (Brouwer et al., 2007). Similar to those knock-in models previously described, the longer expansion model also showed elevated *Fmr1* mRNA levels and reduced FMRP expression compared to the WT controls. Immunocytochemistry also indicated a significant reduction of FMRP in these mice, however, FMRP was still detectable and with the highest expression in the CA2 and CA3 regions of the hippocampus.

The absence of hypermethylation of the CpG island might be the explanation of why FMRP was still expressed in the knock-in mouse model. One possibility is that certain methyl transferases that are essential for methylating the *FMR1* promotor in humans might be missing in the mouse (Brouwer et al., 2007). This finding suggested that the knock-in mouse model could serve as an animal model for studying FXTAS, but not ideal for FXS. Thus, despite the fact that the knock-in model mimicked the causative mechanism of FXS in humans better than the knock-out model, the latter is still the most popular and widely accepted animal model of FXS.

1.3.5 Underlying mechanisms of FXS

Silence of the *FMR1* gene results in a partial or full reduction of its protein product FMRP. Although the relationship/causality between CGG expansion and methylation remains unclear, evidence suggests that both events lead to the reduction of FMRP (Jin and Warren, 2000). FMRP is expressed in most tissues, but most abundantly existed in neurons (particularly in the granular layers of hippocampus and cerebellum), and testes (Abitbol et al., 1993; Hinds et al., 1993). In the cell, FMRP is predominantly localised in the cytoplasm, but generally about 5% of the total amounts of FMRPs are localised in the nucleus. Evidence suggests that it can shuffle between the cytoplasm and nucleus owes to its nuclear localisation signal (NLS) and nuclear export signal (NES) (Eberhart et al., 1996; Fridell et al., 1996).

FMRP is a ribonucleic acid (RNA) binding protein, more specifically, it assembles with messenger RNAs (mRNA) into ribonucleoprotein (RNP) particles by entering the nucleus and then exports into the cytoplasm. Once in the cytoplasm, FMRP then associates with ribosomes and regulates downstream gene expression via posttranscriptional mechanisms (Eberhart et al., 1996; Schaeffer et al., 2003). More than 800 FMRP target mRNAs have been reported previously (Darnell and Klann, 2013). Among these mRNAs, about 30% of them are enriched in the post-synaptic density (PSD), such as the *N*-Methyl-$_{D}$-aspartate (NMDA) receptor subunits, mGluR5 receptor, and PSD-95; suggesting a regulatory role of FMRP in the PSD through coupling to different post-synaptic receptors. It is not surprising that FMRP targets the post-synaptic proteins as previous electron microscopic studies already indicated the localisation of FMRP in dendrites and PSD. However, FMRP has also

been found that it may regulate a great portion of pre-synaptic proteome (e.g., scaffolding proteins, synaptotagmins) (Darnell and Klann, 2013). A recent study indicated that enhanced vesicle recycling and enlarged readily-releasable and reserved vesicle pools were found in *Fmr1* knock-out mice further suggested the role of FMRP in repressing presynaptic protein synthesis (Deng et al., 2011).

Additionally, FMRP is one of the proteins that are synthesised in response of the mGluR pathway which in turn negatively regulate its downstream protein translation (Weiler and Greenough, 1999); loss of FMRP would therefore lead to an exaggerated mGluR signalling and an elevated downstream basal protein synthesis and this is thought of as the main underlying mechanism of FXS.

In 2004, the "mGluR theory" was proposed as one of the underlying mechanisms of FXS (Bear et al., 2004). It is based on the findings that several symptoms of patients with FXS and mouse model of the disease can be speculated as a consequence of group 1 metabotropic glutamate receptor (mGluR) activation (Fig. 1-2). The initial hypothesis was established on the findings from both human post-mortem results and mouse models of FXS that an immature dendritic spine phenotype stands as a hallmark of losing FMRP.[4] This may indicate that the dynamic equilibrium between spine formation and elimination (i.e., spine pruning) is disrupted in the case of FXS (Cruz-Martín et al., 2010). Notwithstanding the discrepancy in the literature concerning the spine data, long-term depression (LTD), a mechanism of spine pruning (Bian et al., 2015), is exaggerated in hippocampal

[4] Recent studies failed to recapitulate this finding. Detailed discussions can be found in Chapter 6.

CA1 neuronal responses to group 1 mGluR stimulation (mGluR-LTD) in mouse and rat models of FXS (Huber et al., 2002; Till et al., 2015). FMRP is then recognised as a translational repressor based on this phenomenon along with other studies (Laggerbauer et al., 2001; Li et al., 2001).

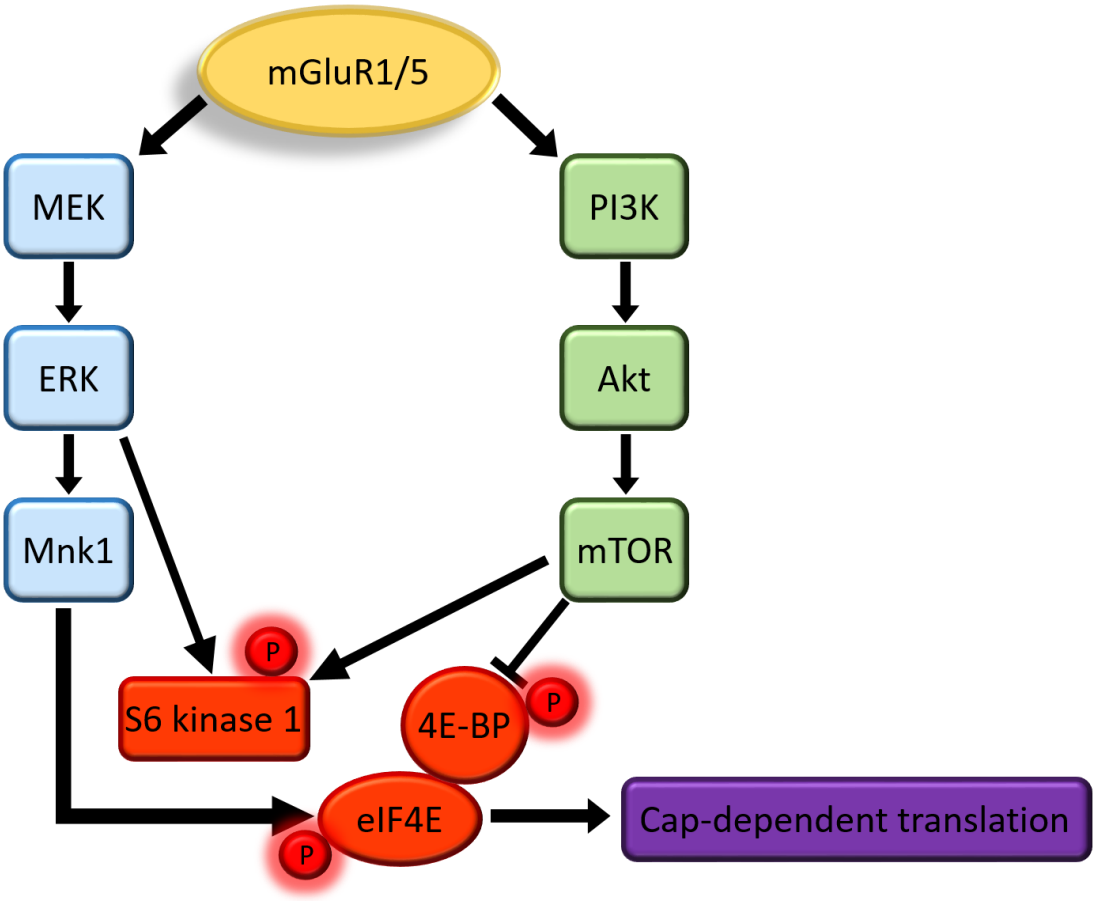

Figure 1-2. The mGluR signalling pathway.

Activation of group 1 mGluRs engages the MAPK-ERK and PI3K-mTOR pathways that involves in mRNA translation and local protein synthesis. MEK phosphorylates and activates ERK, and ERK activates and phosphorylates Mnk1 that phosphorylates eIF4E. PI3K phosphorylates and activates Akt, which then phosphorylates and activates mTOR. Both ERK and mTOR phosphorylate and activate S6 kinase 1, which in turn phosphorylate ribosomal protein S6 that enhance translation initiation. mTOR also activates and phosphorylates the eIF4E binding proteins (4E-BPs). Phosphorylation of 4E-BPs induces the release of 4E-BPs from eIF4E and results in promoting cap-dependent translation via the eIF4E complex. MEK: mitogen-activated protein kinase kinase; Mnk1: MAPK-interacting serine/threonine kinase 1; PI3K: phosphatidylinositol 3-kinase; Akt (also known as protein kinase B); eIF4E: eukaryotic translation initiation factor 4E. For review, see Klann and Dever, 2004.

A key reproducible hallmark of the *Fmr1* knock-out deletion is elevated basal protein synthesis and an exaggerated, protein synthesis-independent mGluR-LTD in the hippocampal region (Huber et al., 2002; Nosyreva and Huber, 2006; Osterweil et al., 2010; Till et al., 2015). There are two main signalling pathways downstream of mGluR that regulate protein synthesis, the mitogen-activated protein kinase kinase (MEK)-extracellular signal-regulated kinase (ERK) pathway and the phosphoinositide 3-kinase (PI3K)-Akt-mammalian target of rapamycin (mTOR) pathway (Banko et al., 2006; Gallagher et al., 2004). Thus, the MEK-ERK pathway and/or the PI3K-mTOR pathway are very likely to be involved in these alterations under the loss of FMRP. Genetically (Dölen et al., 2007) or pharmacologically (Gandhi et al., 2014; Michalon et al., 2012) reducing the activity of the mGluR pathway has rescued several key phenotypes in the mouse model of FXS. Meanwhile, reducing the activity of either the MEK-ERK pathway, the PI3K-mTOR pathway, or their shared downstream effector p70 ribosomal S6 kinase 1 (S6K1) have all been reported to reverse some key phenotypes in the mouse model of FXS (Auerbach et al., 2011; Bhattacharya et al., 2012; Osterweil et al., 2010).

An increase of activity of the PI3K-mTOR pathway is reported in the case of FXS (Hoeffer et al., 2012; Sharma et al., 2010). Similar findings focusing on the MEK-ERK pathway are also reported (Wang et al., 2012). However, a paper published in 2010 by Osterweil et al. suggests that the basal activity of either the MEK-ERK pathway or the PI3K-mTOR pathway are not greatly altered in FXS, and the increased basal protein synthesis is most likely due to an increased sensitivity of the protein synthetic machinery to mGluR-ERK signalling (Osterweil et al., 2010).

Moreover, inhibiting the MEK-ERK pathway via its inhibitor U0126 (but not the mTOR pathway inhibitor rapamycin) corrects the increased basal protein synthesis in the mouse model of FXS (Osterweil et al., 2010).

The mGluR theory of FXS led to the clinical trials for what would have been the first rational treatment for FXS, rather than symptom controls only.[5] Other studies also offer some possibilities and new strategies to unravel the underlying mechanism of FXS. Matrix metalloproteinase 9 (MMP-9) mRNA was recently identified as an FMRP target, it colocalised with FMRP in the dendrites and evidence suggests that MMP-9 mRNA translation is locally regulated by FMRP at synapses following neuronal stimulation (Janusz et al., 2013). Genetically removal of MMP-9 rescues several key phenotypes in the mouse model of FXS, including dendritic spine abnormalities, exaggerated mGluR-LTD, and non-neural features such as macroorchidism (Sidhu et al., 2014).

The endocannabinoid signalling has also recently been implicated in FXS because of the ability of group 1 mGluR stimulation to generate the release of endogenous cannabinoids that subsequently regulate synaptic transmission. Two types of cannabinoid receptors, CB1 and CB2, are predominantly expressed in the mammalian system; where CB1 mainly enriched in the CNS while CB2 in the PNS. However, recent studies also provide evidence that CB1 can be found in several peripheral organs and systems whereas CB2 can also be found in neurons and microglial cells (Svizenska et al., 2008). Both CB1 and CB2 are G-protein coupled

[5] Therapeutic strategies are discussed in the next section.

receptors, more specifically, they both couple with the $G_{i/o}$ subunit and therefore negatively regulate the activity of adenylyl cyclase, hence reduce the production of cyclic adenosine monophosphate (cAMP) (Svizenska et al., 2008). The decrease of cAMP leads to the inactivation of protein kinase A (PKA) as PKA activation is cAMP-dependent. Eventually, activation of presynaptic CB1 receptors leads to a reduction of PKA activity via a cAMP-dependent manner, and the reduction of PKA hence attenuates its downstream signalling such as the MEK-ERK pathway (Fig. 1-3) (Davis et al., 2003). Pharmacological and genetic blockade of CB1 but not CB2 in the mouse model of FXS rescues cognitive deficit, dendritic spine abnormality, and the susceptibility to audio-genic seizures (Busquets-Garcia et al., 2013).

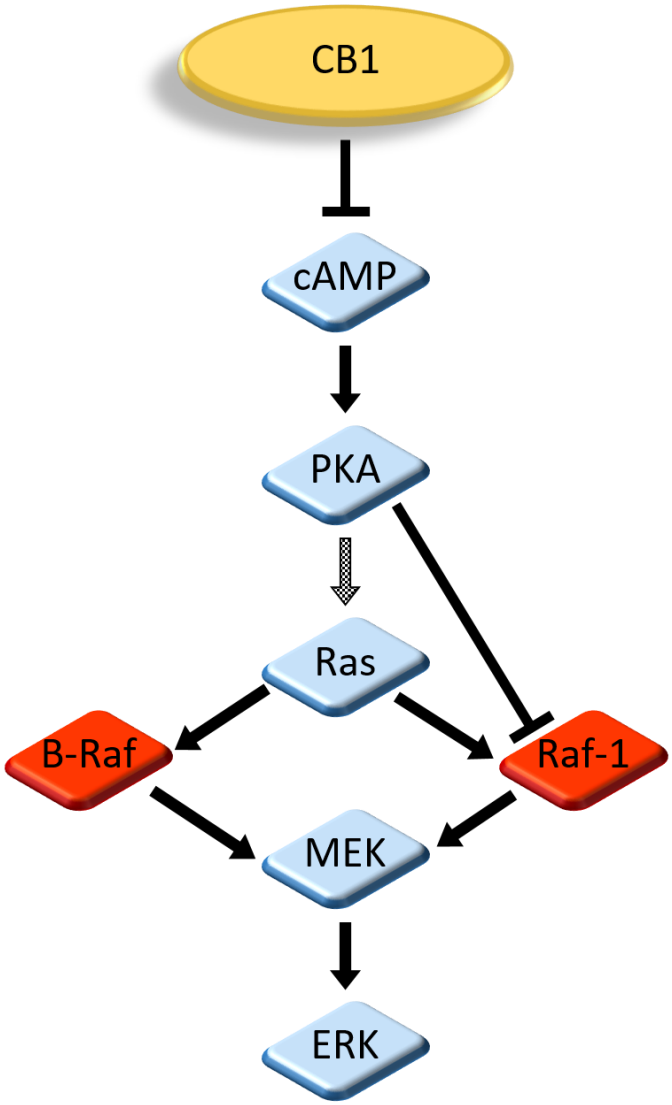

Figure 1-3. The CB1-cAMP-ERK pathway.

CB1 receptor activation inactivates cAMP, therefore negatively regulates the MAPK/ERK signalling pathway. cAMP-dependent PKA indirectly activates Ras and its subsequent MAPK/ERK signal transduction pathway. PKA also directly inactivates Raf-1, hence, depending on the expression of B-Raf, cAMP can either activate or deactivate the MAPK/ERK pathway (i.e., the ability of cAMP to activate the MAPK/ERK pathway correlates with the expression of B-Raf). Raf-1 and B-Raf are members of the Raf kinase family and they both can be activated and phosphorylated by Ras. Raf-1 knockout mice die *in utero*, however, Raf-1 knockout fibroblasts show no alterations in ERK activation and this is likely due to the compensation effect of B-Raf. Ref: (Bos, 2003; Roberson et al., 1999; Turu and Hunyady, 2010)

1.3.6 Current therapeutic strategies for FXS

The mGluR-theory points out a possible route of targeting the core symptoms of FXS, hence several studies using different approaches to target the mGluR-signalling flourished since then. mGluR antagonists shows promising results in the mouse model of FXS, thus several large scale clinical trials have been initiated in different countries all over the world. The first trial led by Berry-Kravis *et al*. in 2009 using a highly selective mGluR antagonist fenobam in patients of FXS. Their results suggests that a single dose of fenobam can improve the prepulse inhibition test and also rapidly reduce anxiety and hyperactivity in those patients, without any noticeable side effects (Berry-Kravis et al., 2009). However, the lack of a proper placebo controlled group and fail to conduct a double-blind design made this result problematic. Later, two new selective mGluR5 antagonists AFQ056 (Mavoglurant; Novartis pharmaceuticals) and RO491756 (Basimglurant; Hoffman-LaRoche pharmaceuticals) entered into phase II clinical trial, but both were stopped in 2014 as they failed to reach their efficacy criteria (Hagerman and Polussa, 2015).

As previously discussed, genetic or pharmacological removal of MMP-9 rescues some key phenotypes in the mouse model of FXS, suggesting that MMP-9 might serve as an important role in the underlying mechanism of FXS (Bilousova et al., 2009; Sidhu et al., 2014). A pilot study targeting young FXS patients (mean age: 10 – 11 y/o) indicates that the MMP-9 inhibitor minocycline can improve their performance in a task using quantitative electroencephalography (EEG) and event-related potentials approach after 3 months of drug treatment (Schneider et al., 2013).

Direct targeting of the mGluR-signalling pathway shows promising results in animal models of FXS, however, current clinical trials failed to reproduce the success in human patients. Thus, some attempts have been made to target the upstream or downstream of the mGluR-signalling pathway. The γ-aminobutyric acid (GABA) system is down-regulated in the case of FXS as noticed in many brain areas of the mouse model of FXS (D'Hulst and Kooy, 2007; Olmos-Serrano et al., 2010); thus agonists of the GABA receptors have been tested in both FXS patients and animal models of FXS to test if restoring the GABA-mediated inhibition can rescue FXS. Follow by getting promising results from the animal model (Henderson et al., 2012), a $GABA_B$ receptor agonist (STX209; arbaclofen) was then being used in a clinical trial that enrolled 63 FXS patients (Berry-Kravis et al., 2012). The outcome is encouraging, an improvement in the social impairments domain was noticed in patients received STX209 but not the placebo-treated group (Berry-Kravis et al., 2012). A larger STX209 clinical trial initiated by Seaside Therapeutics was discontinued in 2013. No official details have been released yet, but the company disclosed the closure was due to financial and resource limitations.

Lastly, in the light of the promising findings from a previous study focusing on the effect of lovastatin treatment on a mouse model of NF1 (Li et al., 2005), a new approach of targeting FXS has emerged. The underlying cause of NF1 is an exaggerated activity of p21Ras, thus inhibition of p21Ras activity would be beneficial and effective in treating NF1. Lovastatin belongs to the statin family and serves as a 3-hydroxy-3-methyl-glutaryl-CoA (HMG-CoA) reductase inhibitor, therefore its primarily role is to reduce cholesterol concentration in patients with

hypercholesterolemia (i.e., high blood cholesterol), as HMG-CoA reductase serves as a rate-limiting enzyme in cholesterol synthesis (Goldstein and Brown, 1990). Lovastatin was then recognised as a potent Ras inhibitor via inhibiting Ras farnesylation, which in turn limits its ability to attach to the inner cell membrane to trigger downstream signalling cascades (Downward, 2003; Johnson et al., 2002). Acute administration of lovastatin rescues the audio-genic seizure phenotype in the mouse model of FXS, and biochemical assays confirmed its ability to restore the excessive protein synthesis downstream of the mGluR-MEK-ERK signalling pathway to the WT animals level (Osterweil et al., 2013). This finding indicates the potential therapeutic effect of lovastatin in FXS. The first clinical trial of lovastatin (LovaX) indicates that after 12 weeks of lovastatin treatment, significant improvement in aberrant behaviours, communication, and socialisation were noticed among 80% of the participants and the treatment was well-tolerated (Caku et al., 2014). Meanwhile, lovastatin has been approved by the United States Food and Drug Administration for the long-term treatment of familial hypercholesterolemia in young children, to prevent the development of cardiovascular diseases in these children in their later adulthood (Descamps et al., 2011). The high tolerance and potential therapeutic effect hence makes lovastatin a valuable candidate in the treatment of FXS.

1.4 Aims of the thesis

Based on the clinical and animal models' findings, loss of FMRP does not cause gross abnormalities in the brain. However, fine structural abnormalities such as myelination and dendritic spine abnormalities are reported, but with some caveats. For example, no detailed EM data describing the axonal pathology in the mouse model of FXS has been published. Nevertheless, a great deal of the previous reports addressing spine abnormalities in FXS used Golgi staining as the way of spine visualisation, which was not ideal especially for spine morphological analysis. Hence, in this thesis I first examined the axonal profile in the *Fmr1*$^{-/y}$ mice using electron microscopy (Chapter 3).

Secondly, I used intracellular dye filling as the way of spine visualisation and examined the effect of lovastatin on dendritic spine abnormalities in the *Fmr1*$^{-/y}$ mice (Chapter 4). Lovastatin has been previously reported to rescue some key phenotypes in the *Fmr1*$^{-/y}$ mice, but the effect of lovastatin treatment on spine abnormalities has not been addressed previously.

Lastly, I examined the experience-dependent visual plasticity in two commonly used inbred mouse substrains (Chapter 5). This project is a pilot study to identify the visual responses in two C57BL/6 substrains for two reasons: 1) we kept the *Fmr1*$^{-/y}$ mice on these two backgrounds; it is therefore important to characterise the visual plasticity of this two substrains, especially since a lack of homeostatic plasticity has previously been reported in the C57BL/6JOla substrain. 2) We plan to examine the visual plasticity in other mouse models of neurodevelopmental disorders

such as *SYNGAP1* haploinsufficiency, but *SynGAP*$^{-/-}$ mice appeared to only breed on the C57BL/6JOla background.

Chapter 2: Materials and Methods

2.1 Animals

All animals were obtained from the animal unit located in the Hugh Robson Building (BRR-HRB, The University of Edinburgh) in accordance with the United Kingdom Animals (Scientific Procedures) Act 1986 under the authority of Project Licences (PPL 60/3631 and PPL 60/4290). Animals were housed under a 12 hr/12 hr light/dark cycle. All mice had *ad libitum* access to food and water at all times through the experiment unless otherwise specified. All experiments were performed blind to the genotype of the animal. Only males were used and they were generally housed in a group of 4 – 6 mice per cage.

2.2 Genotyping

Genotyping of animals was obtained by using a thermal cycler (MJ Mini™, Bio-Rad) for conducting polymerase chain reaction (PCR), specific custom-designed primers were purchased from MWG Operon (Eurofins, EU).[6] For DNA digestion, ear notches from experimental animals were put into 1.5 ml Eppendorf tubes and digested with 500 µl "tail buffer"[7] containing 20 mg/ml Proteinase K (10 µl per 1 ml tail buffer) overnight in a water bath with temperature set at 55°C.

[6]All primers are listed in the Appendix at the end of the thesis.

[7]Recipes for all buffers are listed in the Appendix at the end of the thesis.

Next day, digested tissues were pelleted at maximum speed in a microfuge for 10 – 15 min. Supernatant of each sample (400 µl) was then transferred to a new set of Eppendorf tubes containing 400 µl isopropanol, and then DNA of each sample was pelleted at maximum speed in a microfuge for 10 min. Supernatants were poured off in the sink, and tubes were then rinsed with 900 µl 70% ethanol. After removing all ethanol in the tubes, 150 µl double distilled water (ddH_2O) was added to each tube using filter tips. The lids remained open and samples were resuspended at room temperature overnight.

Next day, samples were then processed differently based on the targeted gene of interest. In general, 1 µl DNA from each sample was mixed with custom-designed oligonucleotide primers (1 µl of each primer), 6 µl of GoTaq® Green Master Mix (Promega, USA), and 2 µl of nuclease-free water, to make a 12 µl final product. All procedures were done on ice and once finished the tubes were then transferred to a pre-heated (95°C) thermal cycler for PCR reaction. For the *Fmr1*$^{-/y}$ mice four sets of primers were used to amplify both the WT allele and the neomycin cassette of the knock-out allele. Specifically, primer pairs 2009/2010 (2009: 5'—GTG GTT AGC TAA AGT GAG GAT GAT—3'; 2010: 5'—CAG GTT TGT TGG GAT TAA CAG ATC—3', Eurofins MWG Operons) were used to amplify the WT allele and primer pairs 162/163 (162: 5'—CCG GTT CTT TTT GTC AAG ACC G—3'; 163: 5'—CGG CAG GAG CAA GGT GAG AT—3', Eurofins MWG Operons) were used for the neomycin cassette of the knock-out allele. Details of PCR reaction and cycling settings can be found in the Appendix section. The final PCR products consisted of two bands; one band with the size around 197 base pairs

(bp) represented the *Fmr1* knock-out allele with the neomycin cassette, the other band with a size around 500 bp indicated the WT allele. The PCR products were separated on a 1.5% agarose gel containing 1 µl of SYBR® Safe DNA gel stain (Thermo Fisher Scientific #S33102) in 1X running buffer (TBE buffer, 50 – 60 ml) at 40 V for 35 – 40 min. A 100 bp ladder was used to mark the size of bands on the gel (New England BioLabs # N3231S). An ultraviolet-transilluminator was then used for visualisation of target DNAs.

2.3 Immunohistochemistry

Mice were anesthetized with sodium pentobarbital prior to transcardial perfusion with phosphate-buffered saline (PBS) followed by 4% paraformaldehyde (PFA) in 0.1 M phosphate buffer. Brains were removed and post-fixed in 4% PFA overnight at 4°C before being sectioned. Coronal sections were sliced at 50 µm using a vibrating microtome (Leica #VT1000 S) and sections containing the regions of interest were first washed with ice-cold PBS several times then incubated with blocking buffer containing 5% cold water fish gelatin and 0.5% Triton X-100 in PBS for 2 hr at room temperature. Sections were then washed several times with PBS and treated with primary antibodies in blocking buffer for the first day, and then reacted with secondary antibodies in blocking buffer on the second day. Details of antibodies used are listed in the corresponding Chapters.

After several washes with PBS containing 0.1% Triton X-100 (PBST), nuclei were counterstained by TO-PRO®-3 iodide (1:1000, Life Technologies #T3605) in

PBST. Finally, sections were mounted and coverslipped in VECTASHIELD® HardSet (Vector #H-1400, CA, USA) before imaging. For long-term storage and better reservation, sections can be incubated and stored in VECTASHIELD® (Vector #H-1000, CA, USA) prior and after confocal imaging.

2.4 Electron microscopy

Mice were anaesthetised with sodium pentobarbital prior to transcardial perfusion with ice-cold PBS followed by 2% PFA and 2.5% glutaraldehyde in 0.1 M PB. Brains were removed and post-fixed in 4% PFA for 2 – 4 h before being sectioned in the coronal plane. All sections were post-fixed in 1% osmium tetroxide in 0.1 M PB for 30 min, dehydrated in an ascending series of ethanol, followed by propylene oxide and embedded on glass slides in Durcupan resin. Area of interest was cut off from each section and put on a pre-made resin block, secured with superglue and left in the hood for 24 – 48 hr before use. Ultrathin sections (60 nm) were cut from regions of interest (1×1 mm^2) and collected on Formvar-coated grids (Agar Scientific), stained with lead citrate in a LKB-Wallac Ultrostainer (Gaithersburg, MD, USA) and imaged using a Philips CM120 BioTwin transmission electron microscope.

2.5 Stick and stain (intracellular dye filling)

Mice were sacrificed through transcardial perfusion with ice-cold PBS then followed by 4% PFA. The volume and concentration of PFA needed to be carefully monitored as this would affect the dye-filling process dramatically. Brains were then rinsed with ice-cold PBS several times next morning, and quickly sliced into 200 µm coronal sections with a vibratome. Sections containing the region of interest were collected into a 24-well plate pre-filled with ice-cold PBS.

Coronal sections containing the region of interest were placed in a chamber on a membranous filter (Millipore #HAWG04700, MA, USA), a "C" shaped weight was then put on top to ensure the section remained in position during dye-filling. The chamber was filled with ice-cold PBS and was put into a holding stage of the upright microscope. The section was imaged using a 20X water immersion objective in PBS. Microinjection pipettes were pulled from thin walled glass capillaries (1.5 mm O.D. × 1.17 mm I.D., Harvard Apparatus, MA, USA) and filled with fluorescent dyes (Alexa Fluor® 568 Hydrazide, 10 mM made up in ddH_2O, Life Technologies #A-10437). They were subsequently backfilled with a conducting solution (0.1 M KCl, pH 7.4). An $AgCl_2$ wire which connected to a pulse generator (Isolated Pulse Stimulator, A-M Systems Model 2100, WA, USA) was inserted in the electrode. An earth wire connecting the solution and the pulse generator was used to close the circuit. The electrode was checked to see if regular puffs of dye were emitted under fluorescence, then inserted carefully into a cell body without penetrating it. A given cell might require 15 – 20 min to fill depending on its size and fixation using a continuous square pulse at 1 Hz. Generally 3 – 5 cells were filled for each region

from a single animal. Cells after filling were post-fixed with 4% PFA for 1 hr then rinsed with PBS and stored in mounting medium (VECTASHIELD® antifade mounting medium, Vector # H-1000, CA, USA) at 4°C before imaging.

Sections were rinsed with PBS and nuclei were counterstained with TO-PRO®-3 iodide (1:1000, Life Technologies #T3605) before mounting with VECTASHIELD® HardSet (Vector # H-1400, CA, USA). An inverted laser-scanning confocal microscope (Zeiss Axiovert LSM510, Germany) was used to acquire images of filled cells.

2.6 Image acquisition and analysis of filled cells

All confocal images in this thesis were acquired by Nyquist sampling. Undersampling often fails to reconstruct the true information of the image. Although theoretically oversampling would have a better resolution to reconstruct the image, some obvious drawbacks such as the increase amounts of acquisition time and storage space are reported. Most importantly, oversampling often causes photobleaching and ultimately destroys the image. I used the commonly known Nyquist sampling (i.e., the sampling frequency is greater than twice the band width of the signal) method to acquire my confocal images in order to reconstruct all the information of the images without bleaching them (Nyquist 1928; Shannon 1949).

Confocal image Z-stacks (0.14 µm per stack) were first deconvolved by using the deconvolution software (Huygens Essential, The Netherlands) prior image analysis. NIH ImageJ was used to analyse dendritic spine density and characterise spine morphology. For more detailed spine measurement such as spine head diameter and spine length, a commercial image analysis software IMARIS® with FilamentTracer plugin (Bitplane, Zurich, Switzerland) was used in order to perform a more detailed dendritic structure analysis.

2.7 Western blotting

Animals were sacrificed via neck dislocation, brains were then quickly removed and the region of interest were dissected out from both hemispheres. All procedures were performed in a dissecting dish on ice and filled with ice-cold PBS with 10% sucrose. Dissected tissues were quickly put into 1.5 ml Eppendorf tubes which were pre-cooled with dry ice to "snap-freeze" before being stored in a −80°C freezer.

Tissues were homogenised with lysis buffer containing protease and phosphatase inhibitors (RIPA buffer: 50 mM Tris-HCl, 150 mM NaCl, 1% Triton X-100, 0.5% sodium deoxylcholate, 0.1% SDS, 1 mM EDTA, pH 7.4; protease inhibitor (EDTA free), Roche #11836170001; phosphatase inhibitor cocktail, Calbiochem #524625 (II) and #524628 (IV)). Protein concentration of homogenised tissues were checked by using a protein assay kit (Pierce™ BCA Protein Assay Kit, Thermo #23225, 23227) before running the Western blot. Briefly, for a microplate

(96 wells), pipette 10 µl of each standard or unknown sample replicate into each well, and then add 200 µl of the BCA working reagent into each well. The microplate was then put on a plate shaker to mix thoroughly for 30 seconds. The plate was then covered with tin foil and left in 37°C for 30 min for incubation. Finally, the microplate was allowed to cool to room temperature prior plate reading. Several loading stocks were made based on the plate reading results of protein concentration of each sample. A 50 µl loading stock with a protein concentration of 0.5 µg/µl (containing 25 µl of 2X Laemmli buffer) was made for each sample and all loading stocks were stored in a −80°C freezer prior gel running. Details of buffers used and buffers recipes can be found in the Appendix section (Chapter 8) at the end of the thesis.

Pre-cast gels (Mini-PROTEAN® TGX gels, Bio-Rad #456-1046; 12%) were used for all Western blotting experiments in this thesis. Those pre-made loading stocks were heated to 95°C on a heat plate for 5 min prior to gel running. The first and last lane of each gel were loaded with 5 µl of 2X Laemmli buffer only, and one lane was loaded with 5 µl of protein ladder (PageRuler® Plus Prestained Protein Ladder, 10 to 250 kDa, Thermo #26619) of each gel. The remaining lanes were then loaded with 10 µl loading stock to make the final protein concentration of each lane equal to 5 µg. Gels were running for about 100 min with 100 V before transferring to nitrocellulose membranes. All components were equilibrated in transfer buffer to reduce the risk of air bubbles which would impede protein transfer. The gels were transferred to nitrocellulose membranes for 1 hr with 100 mA, then membranes were washed thoroughly with PBS followed by incubating in the blocking buffer

(Odyssey® blocking buffer, Li-COR #927-40000, Cambridge, UK) for 45 min at room temperature. Primary antibodies against the proteins of interest were then added into the blocking buffer (with 0.1% Tween-20) at the desired concentration and gels were incubated at 4°C overnight. Membranes were washed thoroughly with PBS the next day and incubated with secondary antibodies for 1 hr at room temperature in a light-tight box to prevent fading. Membranes were then washed again with PBS for several times and were imaged with an Odyssey Infrared Imaging System (Li-COR Odyssey 9120, Cambridge, UK) which equipped with two infrared channels (700 nm and 800 nm). Images of Western blots were then quantified with a freeware provided by Li-COR (Image Studio™ Lite, Li-COR).

Some membranes were blotted several times with different antibodies, in this case membranes were incubated in 1X stripping buffer (ReBlot Plus stripping solution (10X), Millipore #2504) for 10 – 15 min at room temperature and rinsed thoroughly with PBS. After incubating in blocking buffer for 1 hr, a new primary antibody can then be introduced to the membrane following the above process.

For Western blot results, images gathered via Li-COR Odyssey were processed and quantified by using their own software Image Studio™ Lite. Two channels were analysed separately. For each channel, multiple size-fixed user-defined region of interests (ROIs) were put on top of each individual lane where proteins were shown. Along that, a small area surrounding each ROI was used as the background value for further readout adjustment. An absolute value was then shown for each ROI after subtracting its own background noise value. The value for β-actin

was used as a loading control and all values presented were shown as a ratio of protein : β-actin.

2.8 Visual evoked potential (VEP) recording in the mouse visual cortex

2.8.1 Electrode implantation

Mice were anesthetized by inhalation of isoflurane (1.5 – 2% in pure O_2). Depth of anaesthesia was carefully monitored throughout the whole surgery procedure via monitoring the respiration rate and hind-limb pinch withdrawal. A heating plate connected to a thermometer was used at all times during surgery to maintain the animal's body temperature. A subcutaneous injection of Buprenorphine (Vetergesic®; 0.05 mg/kg) was given prior to surgery. Surgical area was first cleaned with iodine and 70% ethanol, then the skull was exposed by removing the hair and skin above. For future head restraint purpose, a steel headpost was affixed to the skull at a position anterior to bregma with cyanoacrylate glue. Two small burr holes were drilled in the skull just anterior to bregma and overlaying the prefrontal cortex, and another two burr holes were drilled overlaying the binocular visual cortex (3.2 mm lateral of lambda; 3 mm was used for animals at P28). Two reference electrodes were implanted into the two burr holes anterior to bregma. Each one of the reference electrodes was custom made by soldering a silver wire with a gold wire contact (FST #19003-00). Two tungsten recording electrodes (FHC Tungsten Microelectrode, UEWSECSEBN1C, Ext. 2 mm/Epoxy 2 mm/7 mm Exp. w/ male pin, impedance

within 0.4 – 0.5 MΩ) were implanted into the two burr holes overlaying the binocular visual cortex at a depth of 470 μm (450 μm was used for animals at P28) below the cortical surface. All four electrodes were secured using cyanoacrylate glue and then reinforced with dental cement. Finally, the remaining skull was covered with dental cement to form a stable "head cap". Animals were put back to their home cages and kept warm with a thermal blanket to accelerate recovery and avoid death caused by loss of body heat. Jellies containing 0.5 mg/kg of Buprenorphine were given to animals for post-operative pain relief. Animals were monitored frequently for signs of discomfort or infection and allowed at least 24 hr recovery before proceeding to habituation and further training. Animals showing signs of infection or significant weight loss after surgery would be removed from further experiment and humanely culled.

2.8.2 Habituation and VEP recording

Animals were allowed to habituate to the head restrain apparatus for 30 min at the day prior to further chronic VEP recordings. To fit the animal into the restrain apparatus, its headpost was screwed tight with the apparatus and thus the head of the animal remained still but its body could move freely inside the holding cylinder. The animal and the apparatus were then put in front of a CRT monitor at a distance of 20 cm. Animals remained still but alert at all times during the recording procedure. An isolated room was used for the VEP recording to minimize the background noise, and all room lights were turned off during recording.

During the habituation process a grey screen was first presented to the animal for 100 phase reversals, followed by 300 phase reversals using 0° sine-wave gratings of 100% contrast. Animals showing signs of distress (e.g., squeak, running) were first checked and if the distress signs continued animals were returned to their home cages temporarily and tested later. Animals that successfully passed the habituation phase were further tested for their basal VEP response at the next day, which consisted of 300 phase reversals at a random orientation of 100% contrast. For long-term recordings, animals received one recording session per day (60 min maximum) for five consecutive days. Animals showing continuous distress signs during recordings were removed from the experiment.

2.8.3 Data acquiring and analysis

Electrical signals were amplified (1000×) and acquired via a USB board (NI USB-6251, National Instruments, TX, US). Data were first acquired and analysed using custom software written in LabView (National Instruments, TX, US) provided courtesy of the Maffei Lab (Pisa, Italy) and with the assistance of the Bear Lab (MIT, MA, US). Individual traces were then re-analysed and plotted with MATLAB with the script provided by Dr. Aleksander Domanski.

The amplitude of VEP was quantified by measuring the trough – peak response amplitude, as described previously (Frenkel and Bear, 2004; Sawtell et al., 2003). In general, animals were presented around 300 – 500 phase reversals of each oriented stimulus per day. The number of trials (1 trial contained 100 phase reversals

of a given contrast and orientation) varied depending on animals' response to the presentation. If VEP responses varied over 15% between trials then additional trials were performed until at least 3 successful trials were acquired for each animal.

2.8.4 Post-mortem histological verification

Animals were humanely culled via cervical dislocation and electrolytic lesions were conducted using a 9-V battery (Duracell®). Brains were quickly removed and stored in ice-cold 4% PFA overnight. Brains were sliced into 50 µm coronal sections and rinsed thoroughly with PBS. Slices were then put on pre-coated slides and left in room temperature overnight. Next day, slides were rinsed with ddH_2O several times and then put into Nissl staining solution[8] for 5 – 15 min followed by several rinses with 70% ethanol. Slides were then rinsed with 95% ethanol containing 0.1% glacial acetic acid, then dehydrated with 100% ethanol for 10 min. Finally, slides were rinsed with xylene and then coverslipped with DPX (Sigma-Aldrich). A Leica light microscope was then used for image acquisition.

2.9 Statistics

Data were analysed with GraphPad Prism (version 6th, GraphPad Software, CA, USA), presented as mean ± SEM unless otherwise specified. Student's unpaired

[8] The recipe of Nissl staining solution can be found in the Appendix.

t-test, Kolmogorov-Smirnov (K-S) test, or analysis of variance (ANOVA) were used for statistical analysis as appropriate. Specifically, Student's unpaired *t*-test was used when comparing two unpaired groups. K-S test is a non-parametric and distribution free (i.e., making no assumption about the distribution of data) statistical test. It was used when comparing two distribution datasets (e.g., cumulative frequency). ANOVA was used when comparing three or more means (groups or variable) for statistical significance. *p* values were reported and significance was set when $p < 0.05$ (marked as *; ** when $p < 0.01$ and *** when $p < 0.001$, respectively). A free statistical software G*Power was adopted to perform Power analysis where appropriate (Faul et al., 2007). Throughout the thesis, "*n*" equals the number of animals.

Chapter 3: White Matter Abnormalities in the *Fmr1*$^{-/y}$ Mice

3.1 Introduction

3.1.1 Evidence for a role of altered WM tracts in FXS

Brain white matter is made up of axon tracts that connect distant structures. The *white* appearance results from the axons being coated with myelin, which is essential for maintaining the stability and fidelity of signal conduction in the brain. For example, white matter abnormalities have been linked to seizures or altered sensory sensitivities, as well as altered cognitive capabilities—features commonly associated with FXS and autism (Fields, 2008; Levy et al., 2009). Yet, while numerous studies have focused on the effects of the loss of FMRP in brain grey matter, whether white matter abnormalities influence the fragile X pathophysiology remains unclear.

Altered brain connectivity is key to the pathophysiology of ASDs/ID and related neurodevelopmental disorders. Early brain imaging studies indicated white matter tract differences between autistic patients and age-matched normal controls. For example, one study using DTI showed that the FA values were reduced in several brain regions in young patients with autism (control group: 13.4 ± 2.8 years; autism group: 14.6 ± 3.4 years), including the anterior cingulate and subgenual area, the CC, and the superior temporal gyrus (Barnea-Goraly et al., 2004). Another study

targeting teenagers and young adults also found the volume of CC was significantly reduced in the autism group (Alexander et al., 2007).

Because most people with FXS also develop ASDs, researchers looked for white matter abnormalities in FXS using brain imaging and post-mortem autopsy. The Reiss laboratory published a series of brain imaging studies targeting different population of individuals with FXS to examine the white matter abnormalities in FXS compared to unaffected individuals. A longitudinal MRI study focusing on young boys (1 – 3 y/o) with FXS showed increased WMV in bilateral fronto-striatal and medial temporal regions, indicated an early onset white matter abnormalities in these areas in individuals with FXS (Hoeft et al., 2010). Intriguingly, WMV was significantly increased over time in some other regions including the ventral prefrontal tracts and posterior temporal regions (Hoeft et al., 2010). The increased WMV over time in these tracts along with the accumulating evidence showing that FMRP can regulate axonal development (Bureau et al., 2008; Tessier and Broadie, 2008) and myelination (Pacey et al., 2013; Wang et al., 2004), suggested that white matter abnormalities in these tracts in FXS were result from an axonal pathology due to the loss of FMRP in these areas rather than a secondary connectional dysregulation between brain regions. Meanwhile, the size of the posterior vermis was significantly reduced in both males and females with FXS compared to healthy controls (Mostofsky et al., 1998). The posterior vermis is located in the cerebellum and mainly involves in motor coordination and receives information from the spinal cord about proprioception. Moreover, recent studies identified the connection between cerebellum and the prefrontal cortex by using retrograde tracing, which

suggests a role of cerebellum in cognitive function (Middleton and Strick, 1994; Paul et al., 2009).

A further study using DTI, which examined females with FXS, revealed that the FA values in white matter in frontostriatal pathways and parietal sensory-motor tracts were reduced (Barnea-Goraly et al., 2003). Another DTI study in young males (range from 1 year 7 months to 3 year 10 months) indicated that the FXS patients had an increased relative fibre density after DTI reconstruction in the left ventral frontostriatal pathway, which the author claimed the greater relative fibre in this area was associated to lower IQ (Haas et al., 2009). Other labs also published some studies to explore the white matter abnormalities in FXS. For example, Villalon-Reina *et al*. reported that FA was lower in the internal capsule, posterior thalami, and precentral gyrus in girls with FXS (Villalon-Reina et al., 2013). Recently, a DTI study using individuals with FXS and IQ-matched controls (average IQ: 70, all FXS negative) showing that an increased FA and reduced radial diffusivity values were found in the inferior longitudinal, inferior fronto-occipital and uncinate fasciculi in FXS group. There was also an increased FA in the CC in FXS group (Green et al., 2015).

3.1.2 FMRP targets mRNAs encoding WM proteins

FMRP is an mRNA binding protein that has numerous functions, including transporting specific mRNAs from the nucleus to the cytoplasm as well as regulating their stability localisation and translation (Bagni and Greenough, 2005). One

example is the mRNA coding for MBP; FMRP binds MBP mRNA in its 3' UTR and suppresses its translation *in vitro,* suggesting that loss of FMRP could lead to alterations in myelination (Brown et al., 1998; Wang et al., 2004). Indeed, findings from several human brain imaging studies are consistent with this possibility. For example, one DTI study revealed a decrease in myelination in fronto-striatal pathways, as well as parietal sensory-motor tracts in female teenagers diagnosed with FXS compared to healthy controls (Barnea-Goraly et al., 2003). DTI showed an increase of white matter fibre density in left ventral fronto-striatal pathway, while the fractional anisotropy between individuals with FXS and control groups remained the same (Haas et al., 2009). However, due to the varieties of imaging techniques and different subject populations, the precise mechanism of white matter abnormalities in FXS still remains unclear.

3.1.3 Evidence for WM abnormalities in a mouse model of FXS

The *Fmr1*$^{-/y}$ mice does not show gross abnormalities regarding myelination of the white matter tract (The Dutch-Belgian Fragile X Consortium, 1994). Pacey *et al*. showed an early loss of MBP (up to 80%), reduced myelinated axons and thinner myelin sheaths in the cerebellum of the *Fmr1*$^{-/y}$ mice (Pacey et al., 2013). Although these phenomena seemed only to happen in early developmental stages (P7) as they were later corrected by P30 through development. The *Fmr1*$^{-/y}$ mice also showed a rightward shift in MBP expression over development, which might correlate with the

reduced myelination in early development. However, another study suggested that losing FMRP did not alter the gross MBP expression in cerebral hemisphere homogenates from P8, P12, and P15. MBP level in homogenates detected by Western blots was also not altered during active myelination period (P21) nor after active myelination (6 weeks, 5 months) between the *Fmr1*$^{-/y}$ and WT mice (Giampetruzzi et al., 2013). Ellegood *et al*. demonstrated that brain white matter of the *Fmr1*$^{-/y}$ mice was not significantly different compared to WT mice at P30 using both DTI and computed tomography (Ellegood et al., 2010). However, a decrease of cerebellum volume was reported by using MRI. More specifically, the volume of the arbor vita of the cerebellum was significantly reduced in the *Fmr1*$^{-/y}$ mice (Ellegood et al., 2010).

One consequence of abnormal white matter development could be impaired action potential propagation, possibly leading to alterations in the timing of synaptic signalling, a key regulator of spike-timing-dependent plasticity (STDP). This may explain numerous studies in the *Fmr1*$^{-/y}$ mice that suggest loss of FMRP leads to alterations in synaptic plasticity, including abnormal STDP (Bagni and Greenough, 2005; Comery et al., 1997; Desai et al., 2006; Harlow et al., 2010; Irwin et al., 2001; Meredith et al., 2007; Nimchinsky et al., 2001; Till et al., 2012).

To determine whether loss of FMRP in mice would lead to white matter or axon fibre abnormalities, I used MBP immunohistochemistry to examine the general distribution of MBP in the CC and the IC of the *Fmr1*$^{-/y}$ mice. CC and IC were chosen due to several previously mentioned imaging studies had already found differences in these areas between individuals with FXS and healthy controls (Green

et al., 2015; Villalon-Reina et al., 2013). Next, serial EM images were taken to examine the fine microstructures of axon fibres in the CC area to provide evidence of any myelination or axonal differences in the mouse model of FXS. Our data suggested that there was a mild but significantly increase of axon fibre diameter in the *Fmr1*$^{-/y}$ mice compared to WT controls. Thus, we then used a computer simulation software NEURON to predict the axonal conduction and tested whether the increase of axonal fibre diameter we observed in the *Fmr1*$^{-/y}$ mice would lead to an increase in axonal conduction velocity.

Table 3-1. Summary of myelin sheath detection through various methods during development.

	P3	P5	P7	P10	P14	P21	P28
LFB	−	−	−	−	+	+	+
MBP-OLGs	very few	↑	↑↑	↑↑	↑↑	↑↑	↑↑↑
EM	−	−	light and medium OLGs	early stages of myelination	compact myelin sheaths was first detected	thin, but mostly compacted myelin sheaths	thicker myelin sheaths

+: indicates myelin positive
−: indicates no signs of myelin sheaths
↑: indicates an increased number
LFB: Luxol fast blue stain; used to detect lipoproteins → demonstrate myelin under light microscopy
OLGs: oligodendrocytes
CC: corpus callosum
EM: electron microscopy
Reference: (Vincze et al., 2008)

3.2 Materials and methods

3.2.1 Animals

The *Fmr1*$^{-/y}$ mice originally obtained from Neuromice.org (Northwestern University, Evanston, IL, USA) were backcrossed more than twenty generations onto the C57BL/6JOla background (Harlan Labs, Bicester, UK). *Fmr1*$^{-/y}$ mice were used as experimental groups and WT littermates were used as controls in this Chapter. For the immunohistochemical staining experiments, animals at P14 – P15 and P20 – P21 were used; for the EM experiments, animals at P14 – P15 and P35 – P37 were used.

3.2.2 Immunohistochemistry

Mice were anesthetized with sodium pentobarbital prior to transcardial perfusion with phosphate-buffered saline (PBS) followed by 4% paraformaldehyde (PFA) in 0.1 M phosphate buffer. Brains were removed and post-fixed in 4% PFA overnight at 4°C before being sectioned. Coronal sections were sliced at 50 µm using a vibrating microtome (Leica #VT1000 S) and sections containing the dorsal hippocampus were first washed with ice-cold PBS several times then incubated with blocking buffer containing 5% cold water fish gelatin and 0.5% Triton X-100 in PBS for 2 hr at room temperature. Sections were then washed several times with PBS and treated with primary antibodies specific for MBP (1:400, rat anti-MBP, AbD Serotec #MCA409S) and neurofilament-heavy chain (NF-H) (1:3000, chicken anti-NF-H, Millipore #AB5539) in blocking buffer for the first day, and then reacted with

secondary antibodies (1:200, Alexa Fluor® 488 donkey anti-rat IgG, Life Technologies #A21208; 1:200, goat anti-chicken IgG biotin conjugated, Millipore) in blocking buffer on the second day. After several washes with PBS containing 0.1% Triton X-100 (PBST), sections were further treated with streptavidin-568 (1:200, Alexa Fluor® 568 conjugate, Life Technologies #S-11226) in blocking buffer and nuclei were counterstained by TO-PRO®-3 iodide (1:1000, Life Technologies #T3605) in PBST. Finally, sections were mounted and coverslipped in VECTASHIELD® HardSet (Vector #H-1400, CA, USA) before confocal imaging. For long-term storage and better section preservation, sections were incubated and stored in VECTASHIELD® (Vector #H-1000, CA, USA) prior and after confocal imaging.

3.2.3 Electron microscopy

Mice were anaesthetised with sodium pentobarbital prior to transcardial perfusion with ice-cold PBS followed by 2% PFA and 2.5% glutaraldehyde in 0.1 M PB. Brains were removed and post-fixed in 4% PFA for 2 – 4 h before being sectioned in the coronal plane. All sections were post-fixed in 1% osmium tetroxide in 0.1 M PB for 30 min, dehydrated in an ascending series of ethanol, followed by propylene oxide and embedded on glass slides in Durcupan resin. Area of interest (CC in this case) was cut off from each section and put on a pre-made resin block, secured with superglue and left it in the hood for 24 – 48 hr before use. Ultrathin sections (60 nm) were cut from regions of the CC (1×1 mm^2) where close to the midline of the two hemispheres and collected on Formvar-coated grids (Agar

Scientific), stained with lead citrate in a LKB-Wallac Ultrostainer (Gaithersburg, MD, USA) and imaged using a Philips CM120 BioTwin transmission electron microscope.

3.2.4 NEURON simulation

The free NEURON software was obtained through its official webpage (https://www.neuron.yale.edu/neuron/). Data simulation was conducted with Dr. Aleksander Domanski. Briefly, we generated a model neuron based on values acquired from our EM experiments, and the axonal conduction velocity and conduction latency were modelled by inputting axon fibre diameter and myelin sheath thickness into the model neuron.

3.2.5 Image analysis and statistics

NIH-ImageJ (NIH, Bethesda, USA) was used for general image analysis and axonal measurement. Six parameters were measured for each myelinated axon from the EM images taken, these parameters were axon diameter (AD), axon outer diameter (OD), axon inner diameter (ID), myelin sheath thickness, *g*-ratio, and X-ratio as shown in the following figure (Fig. 3-1).

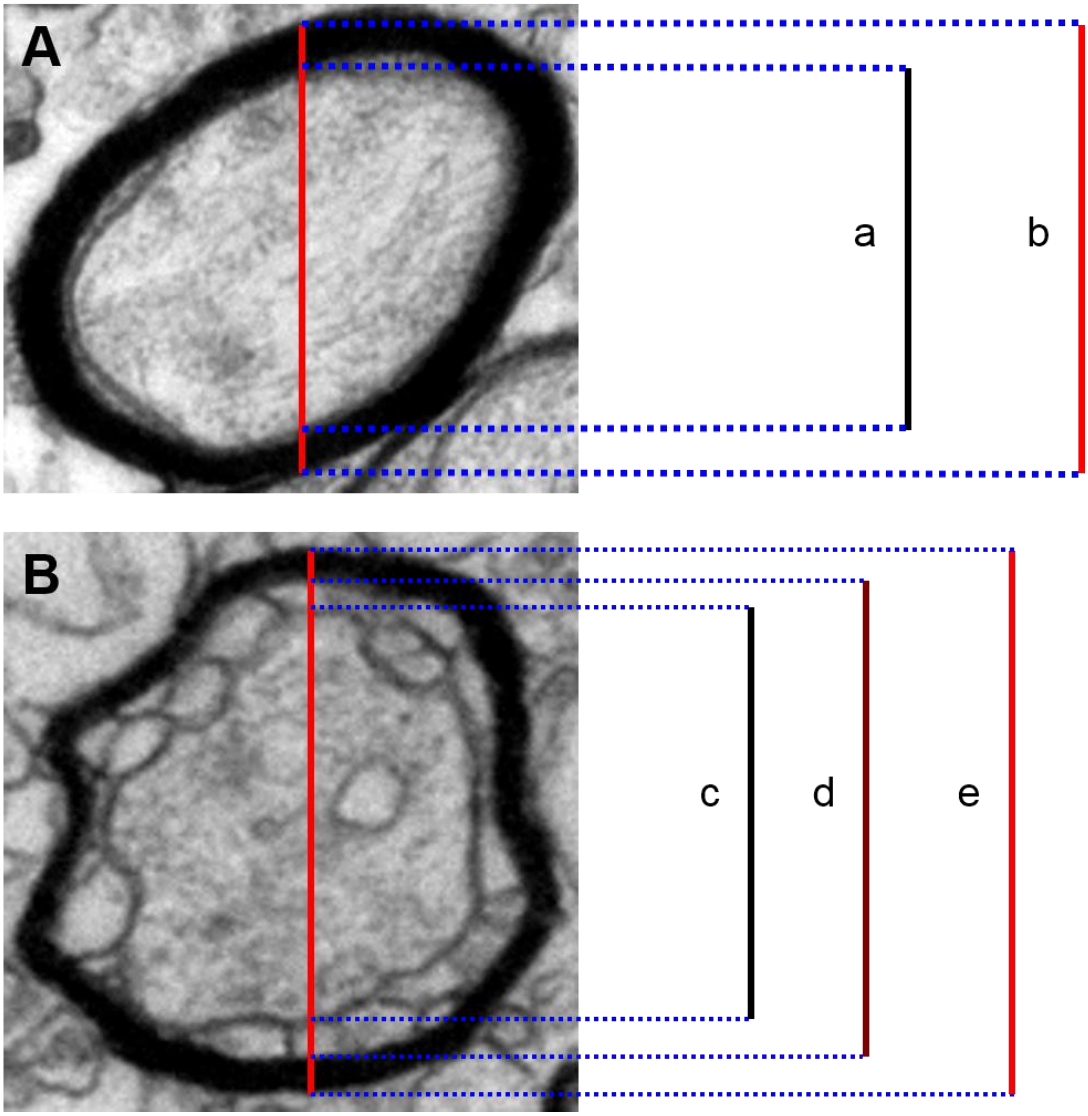

Figure 3-1. An example figure of how different axonal measurements were made.

A typical myelinated axon (without *gaps*) is shown in (A), where axon diameter is marked as (a) and axon outer diameter is marked as (b). An axon with *gaps* is shown in (B), where axon diameter is marked as (c), axon inner diameter is marked as (d), and axon outer diameter is marked as (e), respectively.

I specifically measured the "inner" and "outer" diameter of an axon (for a normal axon without any gaps, the inner axon diameter = 0) in order to get an accurate measurement for the *g*-ratio calculation. *g*-ratio of the axon was calculated as:

$$\frac{a}{b}$$

However, for those axons with gaps I needed to get around of those gaps so the modified *g*-ratio for the axon in (B) would be:

$$\frac{c}{[c + (e - d)]}$$

In order to separate this modified *g*-ratio I called it "X-ratio" in this thesis, for a normal axon without gaps the *g*-ratio and X-ratio would be the same. Finally, the myelin sheath thickness of the axon in (A) would be calculated as:

$$b - a$$

And for axon in (B), the myelin sheath thickness would be calculated as:

$$e - d$$

All statistics in this Chapter were conducted by using GraphPad Prism (version 6th, GraphPad Software, CA, USA), unpaired Student's *t*-test, K-S test, or ANOVA were used for statistical analysis as appropriate. Average data were presented as means ± SEM. Significance was set when $p < 0.05$ (marked as *; **

when $p < 0.01$ and *** when $p < 0.001$, respectively). A free statistical software G*Power was adopted to perform Power analysis as where appropriate (Faul et al., 2007). "*n*" equals to number of animals throughout this thesis unless otherwise specified.

3.3 Results

3.3.1 Loss of FMRP did not cause gross changes in MBP labelled structures in the mouse CNS.

To look at the effect of loss of FMRP on gross myelination I first compared the myelin basic protein (MBP) expression in the *Fmr1*$^{-/y}$ mice and its WT littermate controls using immunofluorescence staining at two developmental stages: juvenile (P14 – 15) and one week after that (P21 – 22). MBP expression was widely used as a way to examine the myelination process in the brain. In fact, the protein itself plays a very important role in myelination as it is a major constituent of the myelin sheath. Our first aim was to see whether MBP expressed differently due to the loss of FMRP in the *Fmr1*$^{-/y}$ mouse. Since MBP is the key component of myelination, we therefore chose two big white matter tracts in the brain to start with, in this case we started with the CC and the IC.

At the two developmental stages we chose, no gross MBP expression was changed in the area of CC or IC (Fig. 3-2). This agreed well with previous reports that the loss of FMRP did not cause a gross change of MBP expression nor changes

of white matter tract morphologies at these developmental stages (Giampetruzzi et al., 2013; Pacey et al., 2013).

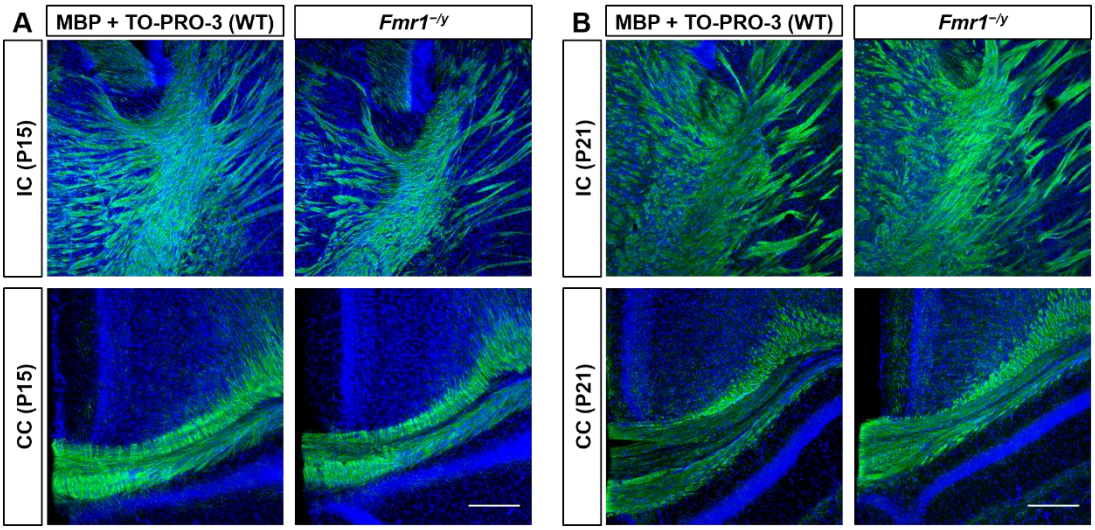

Figure 3-2. Representative MBP expression in the IC and CC area was identical between the *Fmr1*$^{-/y}$ mice and WT controls.

MBP expression in the IC and CC area at P15 (A) and P21 (B) of the *Fmr1*$^{-/y}$ mice and WT controls are shown. MBP was labelled in green and nuclei were counter-stained with blue TO-PRO-3 staining. The MBP-stained axon fibres did not show a gross difference between the two genotypes at both IC and CC. Note that MBP-labelled axon fibres were not only exist in the CC but also reach out to deep cortical layers in the CC area (bottom figures in both (A) and (B)). Scale bar: 200 μm.

I next examined MBP expression in the cortex at the above developmental stages, as a previous study reported changes in the pattern of cortical axonal arborisation and branching in the *Fmr1*$^{-/y}$ mice (Bureau et al., 2008). I found no evidence of gross changes of MBP expression in the WM beneath or within the somatosensory cortex between the *Fmr1*$^{-/y}$ and WT mice at the ages we examined

(Fig. 3-3), indicating no delay in the developmental progression of myelination in the cortex.

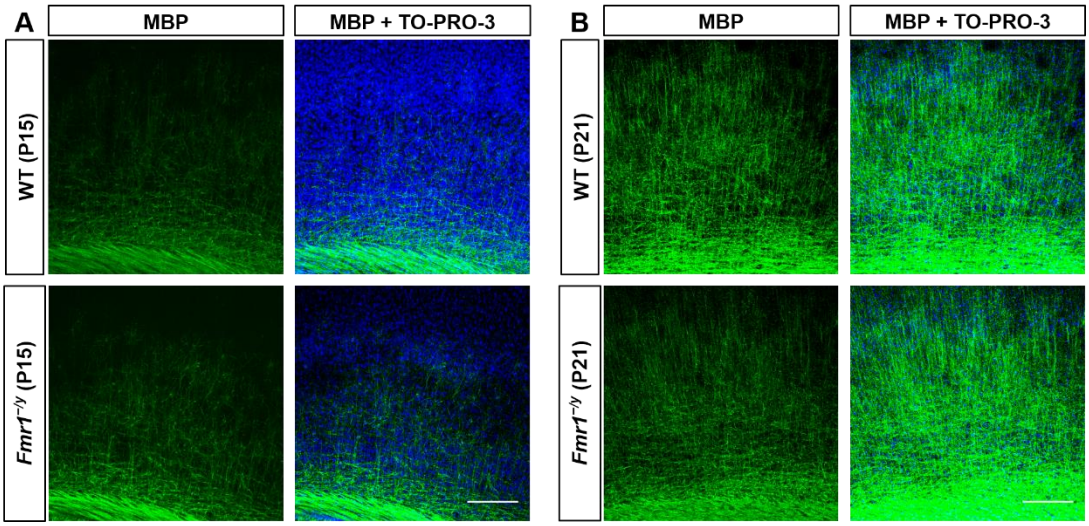

Figure 3-3. Representative MBP expression in the somatosensory cortex was identical between *Fmr1*$^{-/y}$ and WT mice.

MBP expression in the somatosensory cortex did not show gross changes between the *Fmr1*$^{-/y}$ mice and WT controls at P15 (A) and P21 (B). MBP was labelled in green and nuclei were counter-stained with blue TO-PRO-3 staining. MBP expression in the somatosensory cortex at P15 (A) showed a dense staining in layer VI and CC (at the bottom of the graph) and reach out to deeper layers and mostly stop at layer IV, no gross changes (qualitatively) were noticed between the two genotypes of animals. At P21 (B), the amount of MBP staining was increased and again denser staining was noticed in layer VI, however, MBP-stained fibres reached out to layer I in both genotypes, and occupied more spaces than P15. Scale bar: 200 µm.

3.3.2 Number of myelinated axons in the CC is comparable in the *Fmr1*$^{-/y}$ and WT mice.

I next performed electron microscopy on CC from WT and *Fmr1*$^{-/y}$ mice and to determine whether losing FMRP in mice at early developmental stages (P14 – P15) and young adulthood (P35 – P37) would lead to changes of white matter tracts or the myelination status of these tracts.

A series of EM images in the area of CC from both *Fmr1*$^{-/y}$ and WT mice were taken (Fig. 3-4) and the density of myelinated/unmyelinated axons and the myelin sheath thickness of myelinated axons were measured by using NIH-ImageJ. Our data showed that the density of myelinated axons were comparable between the two genotypes in the CC at P14 and P35 (Fig. 3-5B), however, the density of myelinated axons were significantly increased in both the *Fmr1*$^{-/y}$ and WT animals when they reached P35 (Fig. 3-5B).

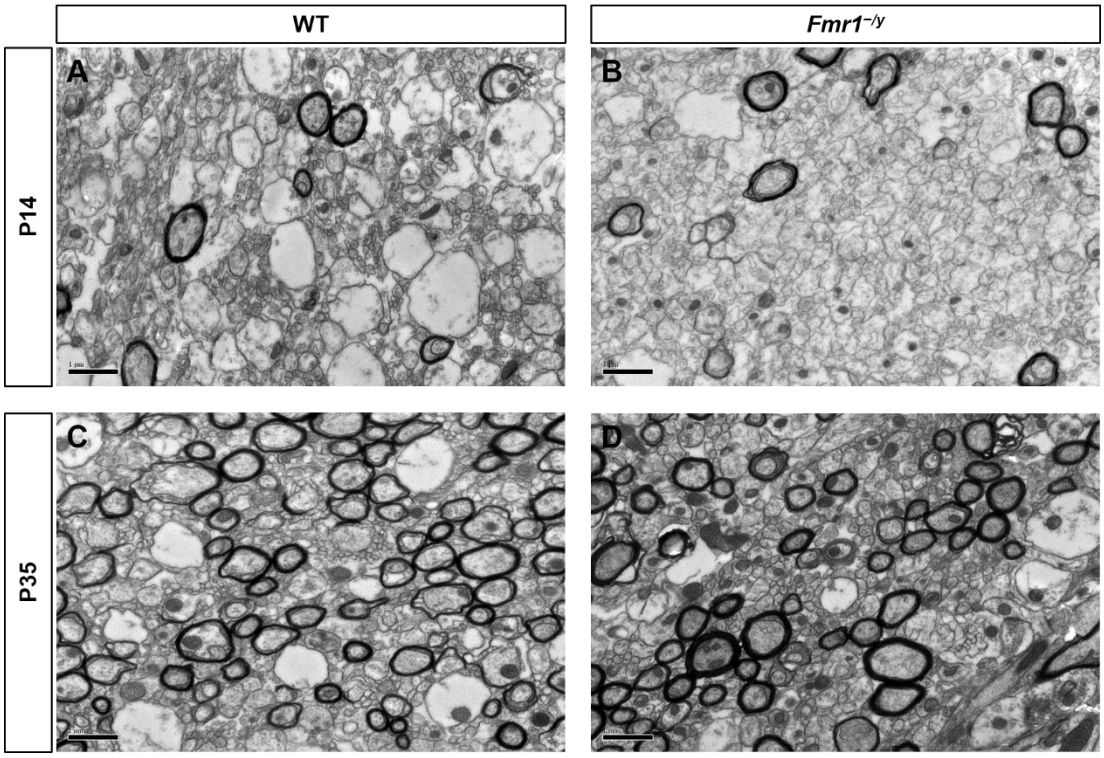

Figure 3-4. Representative EM images of myelinated/unmyelinated axons in the CC from the *Fmr1*$^{-/y}$ and WT animals at different developmental ages.

Representative EM images of axons in the CC from the *Fmr1*$^{-/y}$ and WT animals are shown here. Myelinated axons were surrounded with myelin sheaths (dark, ring-shape structures that surrounded the axons), and the number of myelinated axons were clearly more at P35 then P14 regardless of genotypes. Scale bar: 1 μm.

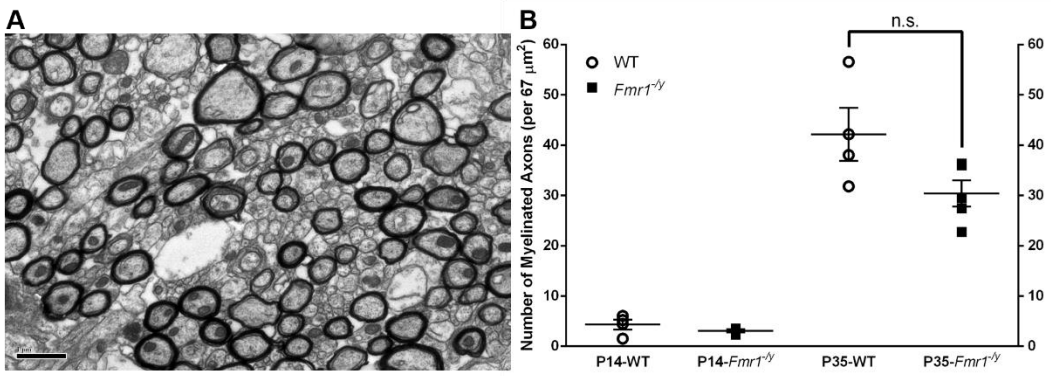

Figure 3-5. Density of myelinated axons remain unaltered in the *Fmr1*$^{-/y}$ and WT mice.

A representative EM image of myelinated axons in the CC from a WT mouse at P35 is shown here (A). The density of myelinated axons in the CC from *Fmr1*$^{-/y}$ mice and WT controls at P14 – 15 and P35 – 37 are shown in (B). WT: $n = 4$; *Fmr1*$^{-/y}$: $n = 5$. Scale bar in (A): 1 μm.

No significant differences in the number of myelinated axons were found between the two genotypes at P14 – 15 (Fig. 3-5B, $p = 0.2771$, unpaired two-tailed Student's *t*-test) nor at P35 (Fig. 3-5B, $p = 0.069$, unpaired two-tailed Student's *t*-test; Power = 0.46, at least 8 WT and 10 *Fmr1*$^{-/y}$ mice will be needed if aiming to reach 0.8 in Power). The density of myelinated axons was significantly increased for animals of both genotypes at the age of P35 than P14 (Fig. 3-5B, WT P14 and P35: $p = 0.0004$; *Fmr1*$^{-/y}$ P14 and P35: $p < 0.0001$, two-tailed Student's *t*-test).

3.3.3 The axons with "gaps" were identical between the *Fmr1*$^{-/y}$ mice and WT controls.

Interestingly, a subpopulation of the myelinated axons demonstrated clear "*gaps*" adjacent to the membrane of the axon or between the axon and its myelin sheath (Fig. 3-6). Thus, I first calculated the proportion of these gaps-containing axons to determine if there was a difference between the two genotypes. There was no significant difference between the *Fmr1*$^{-/y}$ mice and WT controls when comparing the percentage of gaps-containing axons (Fig. 3-7, $p = 0.4367$, unpaired two-tailed Student's *t*-test). Then I measured the size of these gaps and tried to determine whether these gaps would affect the actual size of the axons. I found these gaps were relatively consistent in size (Fig. 3-8C) and did not alter the overall distribution of the diameter of axon fibres in the *Fmr1*$^{-/y}$ mice and WT controls (Fig. 3-9).

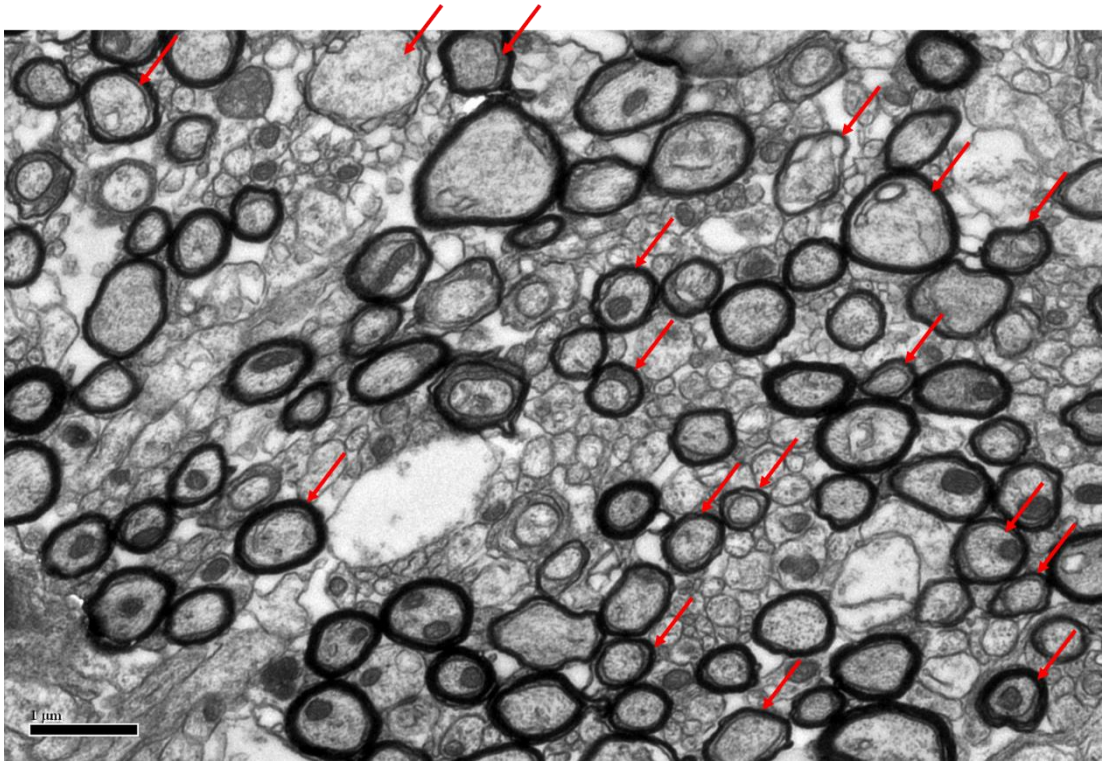

Figure 3-6. Representative EM images of myelinated axons (with or without gaps) in the CC from a WT mouse at P35.

Axons with gaps were noticed throughout the EM images I took regardless of genotypes. Gaps can happen inside an axon or sit between an axon and its myelin sheath. Axons with gaps are indicated by red arrows. Scale bar: 1 µm.

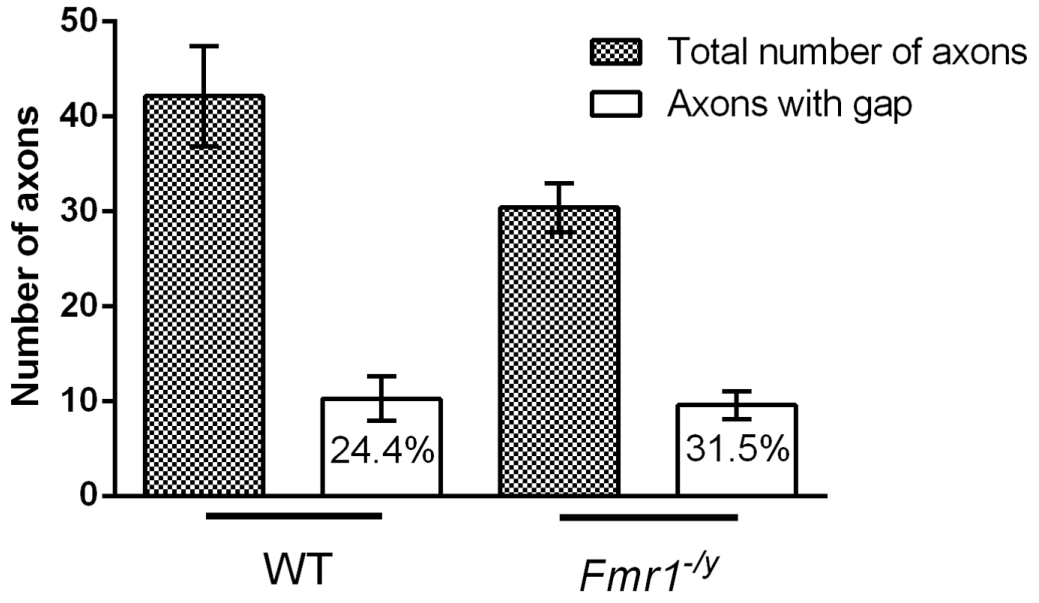

Figure 3-7. Percentage of axons containing gaps in the *Fmr1*$^{-/y}$ mice and WT controls.

No difference between the *Fmr1*$^{-/y}$ and WT mice was noticed regarding the constitution of axons with gaps among the total population of myelinated axons in the CC area. WT: $n = 4$; *Fmr1*$^{-/y}$: $n = 5$.

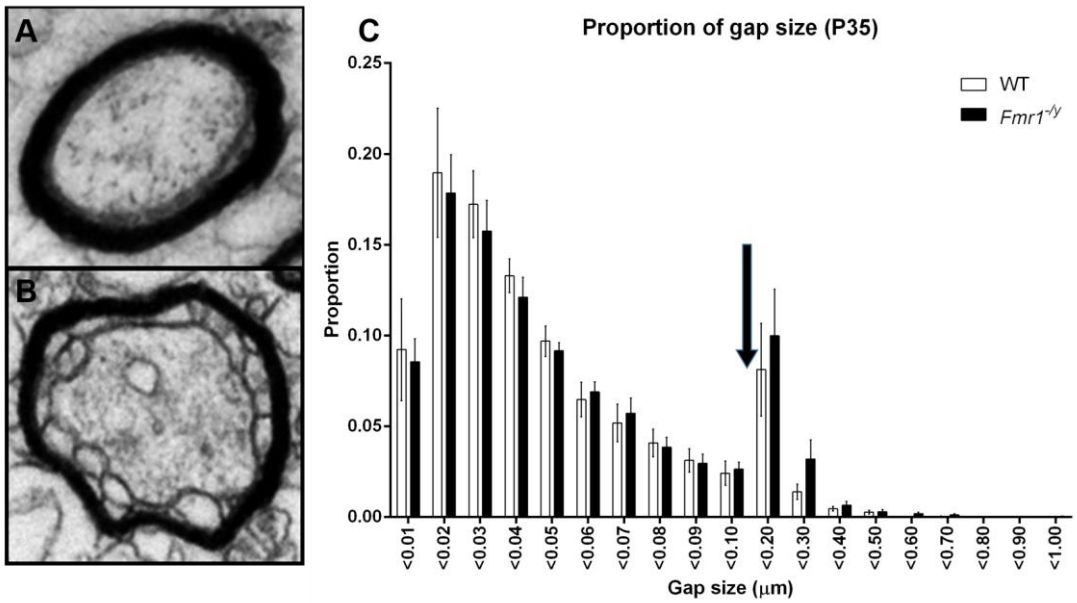

Figure 3-8. The gap sizes were identical between the *Fmr1*$^{-/y}$ mice and WT controls.

Two representative EM images showing an axon without gaps (A) and an axon with gaps (B) are presented, respectively. Note that these gaps can either sit inside the axon or in between the axon and its myelin sheath. The proportion of these gap size is presented in (C), and the arrow indicates a discontinued-break in the X axis between 0.1 μm and 0.2 μm. WT: $n = 4$; *Fmr1*$^{-/y}$: $n = 5$.

The cumulative frequency of axon diameter of both genotypes remained unaltered at P35 (Fig. 3-9B, $p = 0.3291$, K-S test). Similarly, the cumulative frequency of the gap size was also unaltered between the two genotypes (Fig. 3-9D, $p = 0.9718$, K-S test.).

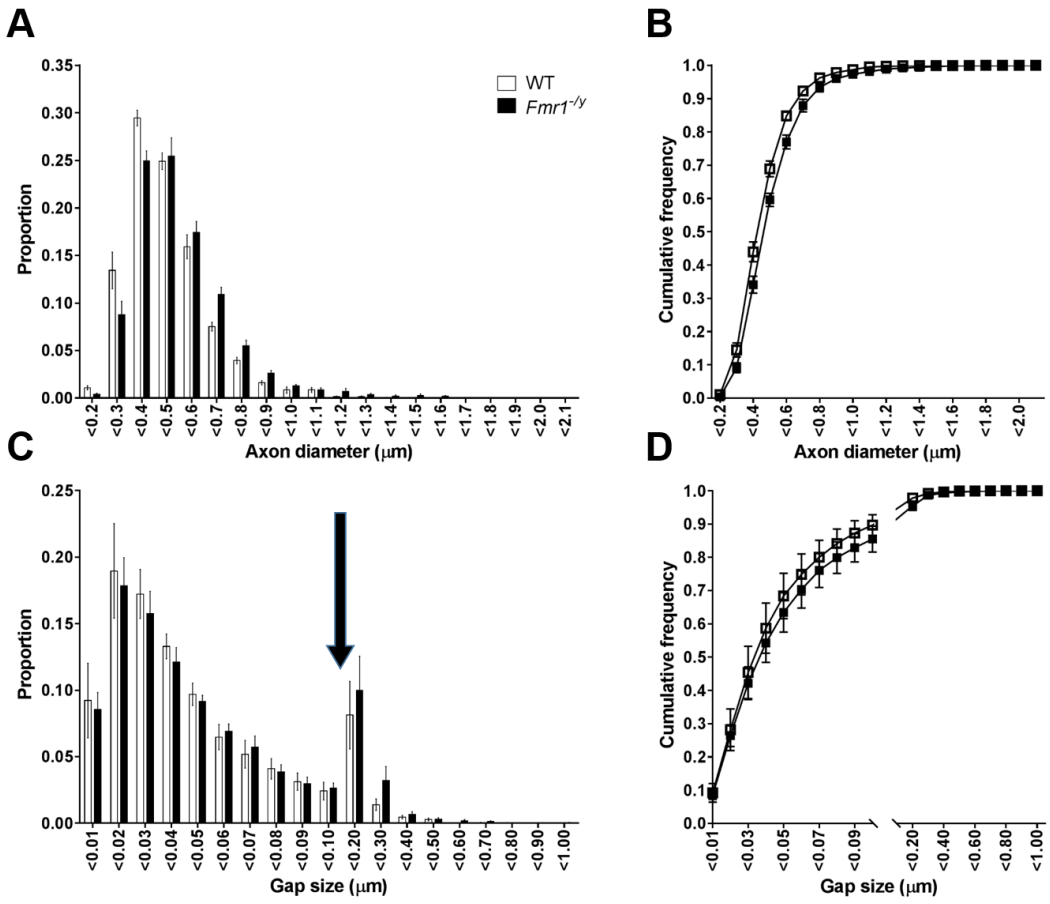

Figure 3-9. The gap size did not alter the overall distribution of the diameter of axon fibres in the *Fmr1*$^{-/y}$ mice and WT controls at P35.

The distribution of axon diameter in booth genotypes at P35 is shown in (A) and the cumulative frequency of the diameter of axon fibres of the *Fmr1*$^{-/y}$ mice and WT controls is shown in (B). The distribution of gap size in both genotypes is shown in (C) (the arrow indicates a discontinued-break in the X axis between 0.1 μm and 0.2 μm), and the cumulative frequency of the gap size of both genotypes is shown in (D). WT: $n = 4$; *Fmr1*$^{-/y}$: $n = 5$.

Since the gaps located between an axon and its myelin sheath would lead to an "increase" of estimates of axon outer diameter, and hence skew the estimates of the *g*-ratio, I devised a second ratio, here called the "X-ratio" to generate an alternative measurement of the ratio of myelin sheath thickness to axon diameter. Considering that the gap size could have a direct impact on several measurements especially the axon outer diameter and *g*-ratio, I calculated the correlation between the gap size and the axon diameter, myelin sheath thickness, *g*-ratio, and X-ratio. Our results suggested that the gap size was correlated with the axon diameter in both genotypes (Fig. 3-10A, WT: $p < 0.0001$, $R^2 = 0.26$; *Fmr1*$^{-/y}$: $p < 0.0001$, $R^2 = 0.16$), and was also correlated with the X-ratio in both genotypes (Fig. 3-10D, WT: $p < 0.0001$, $R^2 = 0.26$; *Fmr1*$^{-/y}$: $p < 0.0001$, $R^2 = 0.12$). However, the gap size was not correlated with either the myelin sheath thickness (Fig. 3-10B, WT: $p = 0.101$, $R^2 = 0.02$; *Fmr1*$^{-/y}$: $p = 0.2364$, $R^2 = 0.01$) or the *g*-ratio (Fig. 3-10C, WT: $p = 0.97$, $R^2 < 0.0001$; *Fmr1*$^{-/y}$: $p = 0.08$, $R^2 = 0.02$).

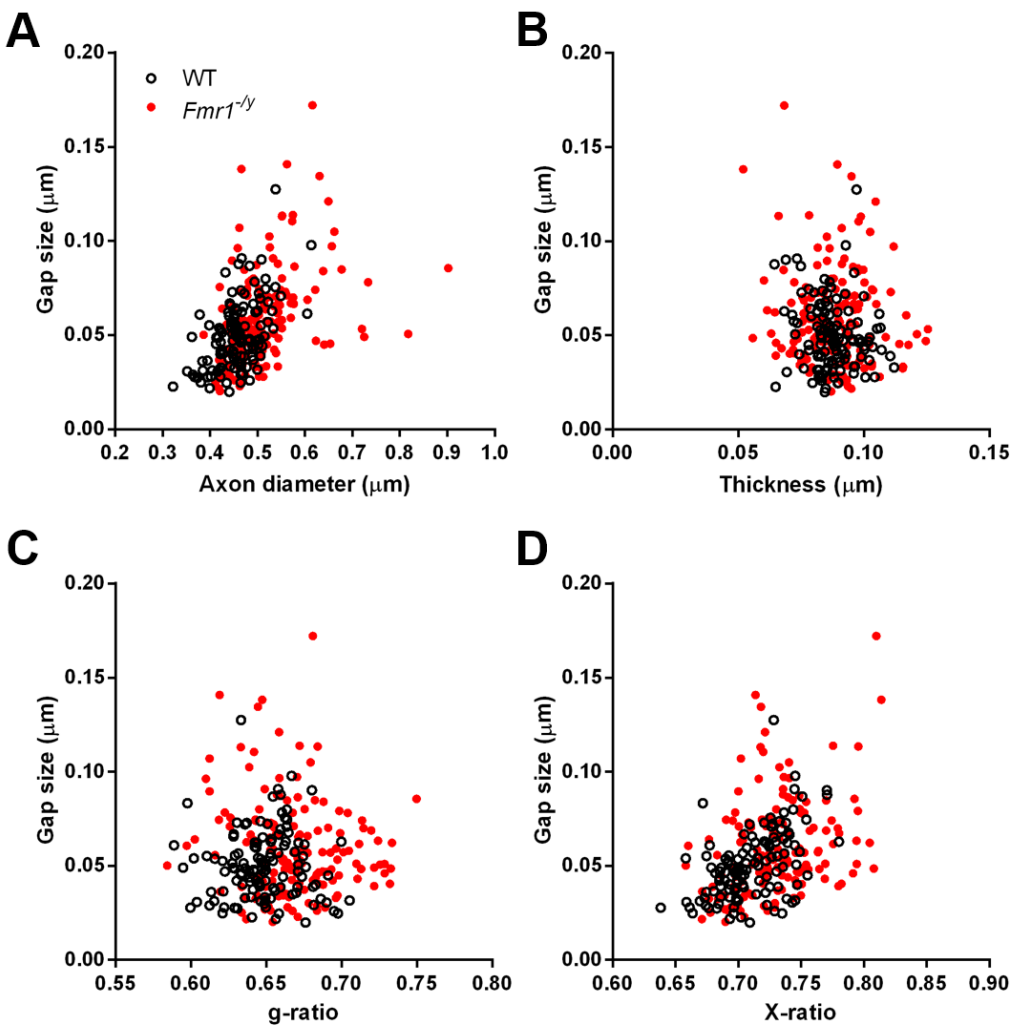

Figure 3-10. The correlation between the gap size and the axon diameter, myelin sheath thickness, *g*-ratio, and X-ratio.

A correlation was found between the gaps and axon diameter, and there was also a correlation between the gaps and the X-ratio in both genotypes. No correlation was found between the gaps and myelin sheath thickness nor between the gaps and *g*-ratio. WT: $n = 4$; *Fmr1*$^{-/y}$: $n = 5$.

3.3.4 No gross changes besides an increase in axon diameter in the CC of the *Fmr1*$^{-/y}$ mice at P35.

I next asked whether loss of FMRP would affect the diameter of axon fibres or the extent of myelination at P35. Animals at the age of P14 – P15 were not included as there were few myelinated axons at this age (Fig. 3-5B). I quantified the axon diameter, axon outer diameter (including the thickness of its myelin sheath), *g*-ratio, X-ratio, myelin sheath thickness, and gap size from EM images of CC from the *Fmr1*$^{-/y}$ and WT mice (Fig. 3-11). Comparison of the total number of myelinated axons between *Fmr1*$^{-/y}$ and WT littermates did not reveal any significant effects of genotype (Fig. 3-5B). Whereas axon diameter was significantly enlarged in the *Fmr1*$^{-/y}$ mice compared to WT controls at P35 (Fig. 3-11A, $p = 0.03$, unpaired two-tailed Student's *t*-test; Power = 0.68, at least 5 WT and 7 *Fmr1*$^{-/y}$ mice will be needed if aiming to reach 0.8 in Power), the outer diameter, myelin sheath thickness, and gap size of the axons remained unchanged between the two genotypes (Fig. 3-11B, $p = 0.084$; Fig. 3-11E, $p = 0.89$; Fig. 3-11F, $p = 0.396$, unpaired two-tailed Student's *t*-test). Interestingly, the difference in axon diameter resulting from the loss of FMRP did not affect the *g*-ratio or X-ratio of the *Fmr1*$^{-/y}$ mice (Fig. 3-11C, $p = 0.068$ and Fig. 3-11D, $p = 0.149$, unpaired two-tailed Student's *t*-test). The proportion of axons with gaps were also not different between the two genotypes (Fig. 3-11G, $p = 0.799$ and Fig. 3-11H, $p = 0.437$, unpaired two-tailed Student's *t*-test). Together, these findings indicate that loss of FMRP may not affect myelination in general but instead increases the axon diameter mildly at P35.

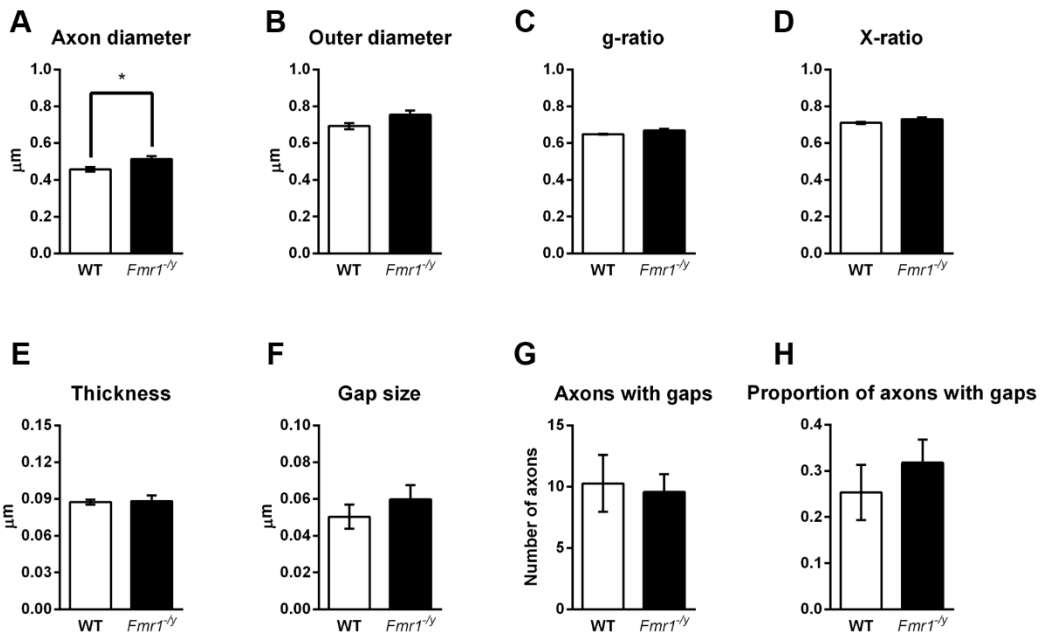

Figure 3-11. Different measurements of axons of the *Fmr1*$^{-/y}$ and WT mice at P35.

Several parameters of axonal measurement were plotted with the data obtained from EM images of both the *Fmr1*$^{-/y}$ and WT mice at P35. Axon diameter (A), outer diameter an axon (B), *g*-ratio (C), X-ratio (D), myelin sheath thickness (E), the size of a gap (F), number of axons with gaps (G), and the proportion of axons with gaps of all axons (H) are presented and unpaired Student's *t*-test was used for each individual graphs. $n = 4$ for WT and $n = 5$ for *Fmr1*$^{-/y}$.

3.3.5 Computational models of axonal transduction suggest that loss of FMRP might increase the conduction velocity of axons.

I then asked whether the increase in axon diameter in the *Fmr1*$^{-/y}$ mice might have a functional effect on axonal conductance. Setting the axon diameter parameter

in the simulation software NEURON to the values measured in the *Fmr1*$^{-/y}$ and control littermates I was able to predict conduction velocity in the myelinated axons of a model neuron (Fig. 3-12). This modelling predicted that the conduction latency in the *Fmr1*$^{-/y}$ mice would be significantly shorter than the WT animals (Fig. 3-13A, $p = 0.04$, unpaired two-tailed Student's *t*-test; Power = 0.63, at least 6 WT and 8 *Fmr1*$^{-/y}$ mice will be needed if aiming to reach 0.8 in Power), suggesting that the increase of axon diameter in the *Fmr1*$^{-/y}$ mice impacts axonal conduction. However, the axon conduction velocity simulated from the program was not significantly different between the *Fmr1*$^{-/y}$ and WT mice (Fig. 3-13B, $p = 0.073$, unpaired two-tailed Student's *t*-test). Since conduction latency and axon conduction velocity should be directly linked, I was surprised by this result as I would have predicted the velocity would also significantly increase in the *Fmr1*$^{-/y}$ animals compared to controls, although we did see that the simulated axon conduction velocity was increased (but not significantly) in the *Fmr1*$^{-/y}$ animals (Fig. 3-13B).

One thing that will also affect the axon conduction velocity is *g*-ratio, which indicates the myelination status of axons. We did not see any differences of *g*-ratio, X-ratio, and even myelin sheath thickness between the *Fmr1*$^{-/y}$ and WT animals (Fig. 3-11C, 3-11D, and 3-11E), suggesting that the increase of axon conduction velocity in the *Fmr1*$^{-/y}$ animals might be due to the increase of axon diameter only rather than changing with the myelination status.

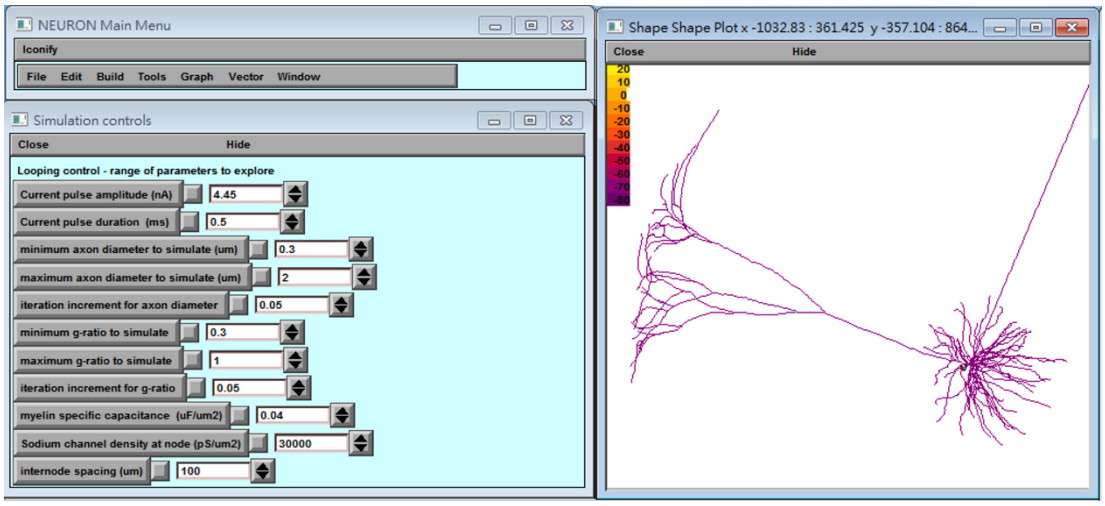

Figure 3-12. The working environment overview of the simulation software NEURON.

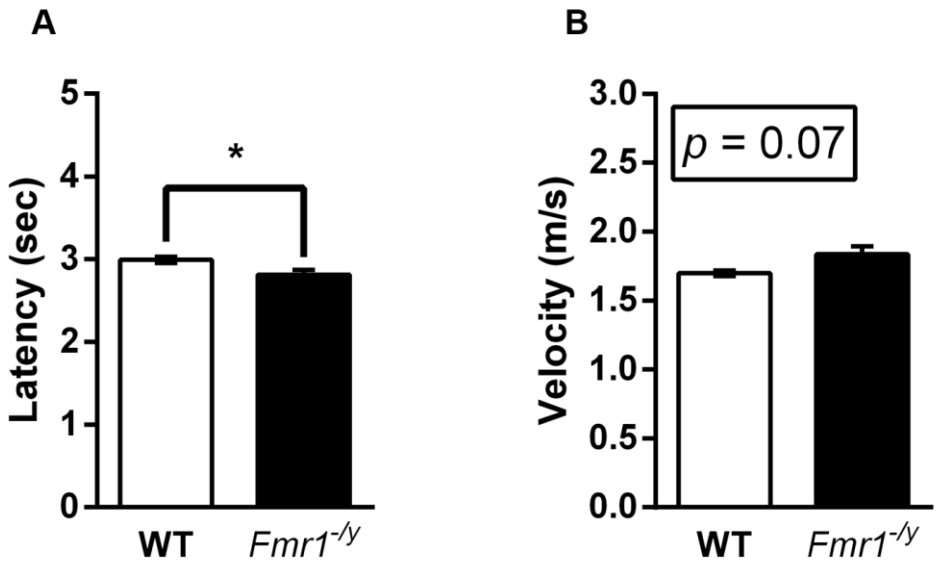

Figure 3-13. The NEURON simulation results of conduction latency and velocity of axons from the *Fmr1*$^{-/y}$ and WT animals at P35.

Simulation of axonal conduction latency from the *Fmr1*$^{-/y}$ and WT animals is shown in (A), axonal conduction latency in the *Fmr1*$^{-/y}$ mice is significantly shorter than the WT controls. Simulation

results of conduction velocity between the two genotypes is shown in (B), and there is no difference between the two genotypes. WT: $n = 4$; *Fmr1*$^{-/y}$: $n = 5$.

3.4 Discussion

3.4.1 No gross WM abnormalities in *Fmr1*$^{-/y}$ mice.

Together, my current data show that the axon diameter of the *Fmr1*$^{-/y}$ mice was mildly but significantly larger than WT control animals at P35, which could lead to an increase of axonal conduction velocity as suggested by our neuron modelling. This suggested a potential mechanism underlying the altered spike-timing-dependent plasticity (STDP) in the *Fmr1*$^{-/y}$ mice reported by other labs (Desai et al., 2006; Meredith et al., 2007) and offers a new perspective on the cause of intellectual disabilities in FXS and related disorders focusing on white matter.

From the immunohistochemical staining experiments I did not notice any gross changes of MBP expression in the somatosensory cortex, CC, nor IC; which agreed well with some previous reports suggesting that losing FMRP did not cause a fundamental change of white matter tract morphologies (Giampetruzzi et al., 2013; Pacey et al., 2013). However, some former MRI and DTI work did show some interesting findings (summarised in Table 1-1) when they examined the white matter tracts between individuals with FXS and healthy controls (Barnea-Goraly et al., 2003; Green et al., 2015; Haas et al., 2009; Hoeft et al., 2010; Mostofsky et al., 1998). Thus, losing FMRP might not alter the gross MBP expression but might have some

impact on the white matter tract morphologies or, more specifically, the axon fibre morphology of these tracts as suggested by my current findings.

We found that there was no difference of the total number of myelinated axons between the *Fmr1*$^{-/y}$ and WT mice at P35 through examining the EM images acquired from both genotypes (Fig. 3-5B). A previous report suggested that there was a delay in myelination in the cerebellum of the *Fmr1*$^{-/y}$ mice at early postnatal ages (P7), the *Fmr1*$^{-/y}$ mice then caught up with myelination at P15 and this delay between the *Fmr1*$^{-/y}$ and WT mice was no longer evident (Pacey et al., 2013). This may explain the result we observed in the CC, as by P35 the myelination process is mostly completed in the mouse CNS (Vincze et al., 2008).

3.4.2 An increase of axon diameter might lead to an increase of conduction velocity.

An increase of fibre diameter can be directly related to an increase of axonal conduction velocity, as for a given *g*-ratio in a group of myelinated axons, the bigger the axon diameter the faster the conduction velocity for that axon. This nearly linear relationship between the axon diameter and conduction velocity has been proposed and examined at the late 1930s by Hursh (Hursh, 1939) and later on Rushton (Rushton, 1951). However, in Rushton's work he suggests that "1 μm" is a critical number: for axon fibre diameter above 1 μm "myelination increases conduction velocity", below this value "conduction is faster without myelination". This may hold true for axon fibres in the PNS, but as most of the myelinated fibres in the CNS

are below 1 μm in diameter, therefore, there are likely other factors need to be taken into consideration when identifying the relationship between axon diameter and conduction velocity. Taking the CC as an example, axon diameter in mice callosal regions varies from 0.1 – 2 μm, in rabbits from 0.05 – 1.84 μm, in cats 0 – 3.5 μm, and 0.1 – 6 μm for monkeys (for a comprehensive review, see Olivares et al., 2001). The estimated conduction velocity is relatively similar between mice and rabbits (mice: 1.2 m/s; rabbits: 0.85 m/s), but it is faster in cats (12 m/s) than in monkeys (6.86 m/s) despite the observation that the axon diameter is larger in monkeys (Innocenti et al., 1995; Olivares et al., 2001). Thus, the size of axon diameter would not be the only factor that determines conduction velocity.

Our current simulation predicted that the conduction latency would be significantly reduced in the *Fmr1*$^{-/y}$ mice compared to the WT controls, however the conduction velocity would not be significantly different between the two genotypes, although it was slightly increased in the *Fmr1*$^{-/y}$ mice. The conduction velocity of a myelinated axon increases directly with the diameter of the fibre, doubling the diameter gives a doubling of the rate; in those unmyelinated axons, the velocity increases with the square root of the axon diameter (i.e., the rate would only be doubled if the axon is four times larger) (Hildebrand et al., 1993). However, numerous factors should be taken into account when calculating the conduction velocity besides axon diameter and myelination. The intermodal distance, *g*-ratio, and nodal properties will also affect the conduction velocity, however not as dramatically as the previous two parameters (Waxman, 1980). One thing might also worth noticing is that the fibre size in the CC will vary depending the sub-regions of

sampling (Aboitiz and Montiel, 2003; Olivares et al., 2001). Interestingly, axons connecting to higher order brain regions such as the prefrontal and frontal areas tend to be smaller in size, poorly myelinated and with a slow conduction speed and are mainly concentrated in the genu part of the CC (i.e., anterior pole of the CC); on the contrary, axons with larger calibre, highly myelinated and with a fast conduction speed are concentrated in the body part of the cerebellum, which is consisted of fibres that connect visual and somatosensory cortices (Aboitiz and Montiel, 2003; Aboitiz et al., 1992). These regional differences in the CC are best characterised in primates. In rodents, no gross changes of fibre calibre of the CC was noticed, at least not in the posterior part of the CC (Olivares et al., 2001). All the tissues we sampled for EM were acquired from the CC close to the midline margin with a size of 1×1 mm^2. In this case we would expect most of the axons we measured would be originated from the same region of the CC.

3.4.3 The gaps were unlikely to be artefacts, but more likely to be some yet-unknown microstructures.

The gaps we observed in many myelinated axons were unusual and have not been reported previously (Fig. 3-6). These gaps are unlikely to be an artefact during our EM preparation or the imaging process for mainly two reasons: 1) 50% of the tissues were handled and processed by me, and one senior EM technician assisted me with the rest. We were both blind to the genotypes and these gap-containing axons were found in both mine and her images; 2) we have discussed with several experts

in this field, unfortunately none of them could give us a clue about these gaps, but they all agreed these were not artefacts. Finally, if these gaps were artefacts, we would expect they expressed evenly in the same batch of samples; however, our data showed that only some of the images contained these gap-containing axons, again suggested that these gaps were not artefacts.

The fact that these gaps spread either inside the axon or sit between the axon and its myelin sheath makes it hard to interpret what is their function and physiological role, especially when it is not mentioned in literatures previously. Our best assumption of this gap-like structure is the Schmidt-Lanterman clefts (also known as myelin incisures or Schmidt-Lanterman incisures) as the morphology looks similar and the fact that it forms a connection between the cell cytoplasm internal and external to the myelin sheath. However, the Schmidt-Lanterman clefts only persists in the PNS (for a detailed review, see Ghabriel and Allt, 1981). We have no clue whether the gaps we observed are the counterparts of the Schmidt-Lanterman clefts in the CNS. And the physiological roles of these gaps and the developmental distributions of them remains unclear. Despite of our lack of understanding of the gaps, the increase of axon diameter in the *Fmr1*$^{-/y}$ mice was independent of the gaps as we found no significant differences of myelin sheath thickness, *g*-ratio, and the X-ratio between the two genotypes (Fig. 3-11). And the gap-containing axons were no difference between the *Fmr1*$^{-/y}$ and WT mice, suggesting that these gaps were some yet-unknown structures during normal white matter development in the CNS.

In summary, we found no gross changes of myelination and the number of myelinated axons between the *Fmr1*$^{-/y}$ mice and WT controls in the CC. This agreed

well with previous findings that losing FMRP did not alter myelination in the brain. Further analysis revealed an increase of axon diameter in the *Fmr1*$^{-/y}$ mice, and our simulation model suggested that the magnitude of the increase could lead to a higher conduction velocity in the *Fmr1*$^{-/y}$ mice. These current findings offered a new insight into how STDP was altered in the loss of FMRP, possibly through an alteration of the axon diameter and eventually resulted in a disrupted conduction velocity in certain brain regions such as the CC. In the near future, I plan to measure the latency between stimulation and the elicited afferent fibre volley, and with a known distance between the stimulation site and recording site (marked with biocytin) I will be able to estimate the conduction velocity of the CC in the *Fmr1*$^{-/y}$ mice *in vitro*.

Chapter 4: The Effects of Lovastatin on Dendritic Spine Abnormalities in FXS

4.1 Introduction

4.1.1 Dendritic spine abnormalities in FXS

Fragile X syndrome was first described by Martin and Bell in 1943 (Martin and Bell, 1943). Seventy years of clinical research has described several key FXS phenotypes which are commonly expressed among most of the affected individuals, such as an elongated face, macroorchidism, intellectual disability, epilepsy, and autistic behaviours (Bowen et al., 1978; Hatton et al., 2006; Kooy, 2003; Musumeci et al., 1991; Penagarikano et al., 2007; Turner et al., 1975). Post-mortem examination of FXS patients did not reveal any gross changes in the brain compared to healthy individuals (Reyniers et al., 1999). Several human post-mortem studies indicated that there was an increase of immature long/thin dendritic spines in the individuals with FXS (Hinton et al., 1991; Irwin et al., 2001, 2000; Rudelli et al., 1985; Wisniewski et al., 1991). However, the small sample size in some studies and various developmental stages and brain areas of sampling made the results hard to interpret.

The FXS mouse model recapitulates most of these phenotypes (Comery et al., 1997; Irwin et al., 2002; Nimchinsky et al., 2001; The Dutch-Belgian Fragile X Consortium, 1994), which offers a great opportunity for researchers to explore the pathological symptoms and the underlying mechanisms of FXS. Early reports

revealed an excessively long and immature dendritic spine morphology appeared in the *Fmr1*$^{-/y}$ mice compared to WT controls (Comery et al., 1997; Irwin et al., 2002; Nimchinsky et al., 2001). Increased spine density across different neocortical layers in various brain regions have also been reported in the *Fmr1*$^{-/y}$ mice (Dölen et al., 2007; Hayashi et al., 2007; Liu et al., 2011). However, most of these studies used the Golgi method for spine visualisation, which was a method known to have poor morphological information of spines and easy to get random and unpredictable staining, therefore might yield inconsistent results between different labs (Buell, 1982; Mancuso et al., 2013; Rosoklija et al., 2003). Thus, I chose to use the intracellular fluorescent dye-filling technique as the method of spine visualisation, which can give a better morphological information and less distortion of the spine morphology (Trommald et al., 1995).

4.1.2 The development and function of spines

Dendritic spines are where the excitatory synapses going to form, and thus these "protrusions" alongside the dendritic tree play a crucial role in regulating the excitability of a given cell. Dendritic spines are dynamic, formation of a spine only takes several minutes (Bhatt et al., 2009; Yuste and Bonhoeffer, 2004; Ziv and Smith, 1996); while some spines are forming, other spines are being eliminated, a process called "spine pruning". This dynamic process of spine formation has been proposed as one of the important potential mechanisms of learning and memory (Knafo et al., 2004; Maletic-Savatic et al., 1999; Moser et al., 1994; Segal, 2005; Yuste and Bonhoeffer, 2001). Dendritic spines can also be classified as either "mature" or

"immature" based on their morphology (Harris et al., 1992). However, due to the variety of cell composition in different brain areas, some spines considered "mature" in a designated brain region may become less mature or "immature" in another brain area. Spine morphology is also highly regulated by development (Wijetunge et al., 2014). The current well-accepted concept of spine formation is that neurons will generate spines in excess during development which is followed by a period of "pruning". Eventually a dynamic equilibrium will be achieved where the loss and gain of spine formation is balanced (Segal, 2005).

4.1.3 The mGluR theory of FXS

Since the paper proposing the "mGluR theory of FXS" came out in 2004 (Bear et al., 2004), FXS became one of the very first developmental brain disorders where therapies were being developed to treat "core deficits" (as opposed to symptoms) based on a rational hypothesis. The mGluR theory is based on the observation that the symptoms/phenotypes of losing FMRP in patients/mouse models are very similar as a result of exaggerated mGluR signalling. For example, mGluR hypersensitivity specifically in the CA1 region of the hippocampus leads to an enhanced LTD (mGluR-LTD), one of the most consistent phenotypes reported in the *Fmr1*$^{-/y}$ mice (Bhattacharya et al., 2012; Huber et al., 2002). Thus, to physiologically reduce the activity of mGluR-signalling seems to be a promising route to alleviate the symptoms of FXS. Several attempts have been made, including large-scale clinical trials and animal studies (Berry-Kravis et al., 2009; Gantois et al., 2013; Pop et al., 2014). However, Novartis and Roche announced earlier last year

that their mGluR antagonists AFQ056 and RG7090 (RO4917523) failed to show beneficial therapeutic effects in their clinical trials. The results were disappointing to the whole FXS community, and the withdrawal of these pharmaceutical companies may imply that the mGluR theory is no longer a favourable target in treating FXS. Despite the unsuccessful attempts from these trials, we may want to ask ourselves whether these trials were actually "testing" the mGluR theory or not, before we jump to the conclusions that mGluR antagonists were ineffective. First of all, both trials used the Autism Behaviour Checklist (ABC) and IQ as their primary and secondary outcome measures, respectively. However, none of them could be used to measure "synaptic plasticity" in those individuals with FXS, therefore it was hard to interpret the effect of these drugs when the improvement of synaptic plasticity was a major outcome in animal studies (Dölen et al., 2007; Michalon et al., 2012; Pop et al., 2014). More importantly, it was the caregivers or parents who scored the ABC for those participants but not clinicians, and this would only add more variability for the outcome measure.

Second, most of the core symptoms of FXS can be found in early development (i.e., 3 – 5 y/o) and we can easily focus on such an early stage of development to examine the effects of drugs in animal models, but not humans. In both clinical trials, the age of the participants were mostly teenagers and adults, which had already passed the developmental stage when mGluR antagonists showed positive effects in animal studies. Third, the required dosage for these drugs to effectively target the mGluR signalling in humans still remains unclear. And

whether the 3-month trials were long enough to observe the positive outcome was also hard to know.

While attempts were made targeting the mGluR-signalling, other studies targeted the upstream or downstream targets of mGluR5 activation/signalling, including inhibitory control (i.e., the GABA signalling) in both FXS patients and mouse models were also conducted and the results looked promising (Berry-Kravis et al., 2012; Henderson et al., 2012).

4.1.4 Disrupted Ras-ERK signalling in FXS and the potential therapeutic effect of lovastatin

An excessive protein synthesis downstream of the mGluR pathway has been reported in the *Fmr1*$^{-/y}$ mice (Osterweil et al., 2010; Qin et al., 2005). The Ras-ERK pathway is one of the downstream signalling of mGluR that involves protein translation, and inhibiting this pathway has rescued the excessive protein synthesis in the mouse model of FXS (Osterweil et al., 2013, 2010). Like FXS, another single-gene neurodevelopmental disorder called neurofibromatosis type 1 (NF1), for which an increase of Ras activity has been proposed as its main underlying pathological mechanism (Basu et al., 1992; DeClue et al., 1992) might shed a light on the FXS treatment. Li *et al*. published a paper in 2005 suggesting the HMG-CoA reductase inhibitor lovastatin is able to reduce certain cognitive and behavioural deficits in the mouse model of NF1 (Li et al., 2005). Followed by that, Osterweil *et al*. published a study in 2013 using lovastatin as a mGluR-signalling modulator and they

successfully rescued several key phenotypes of the *Fmr1*$^{-/y}$ mice, including excessive protein synthesis, mGluR-induced epileptogenesis, hyperexcitability in the visual cortex, and reduced the susceptibility to audio-genic seizures (Osterweil et al., 2013). Lovastatin itself is a natural compound which can be found in food such as oyster mushrooms and red yeast rice, and was initially used as a treatment for hyperlipidemia as it acts as an inhibitor of the HMG-CoA reductase, which is a key enzyme of cholesterol synthesis. Lovastatin is well-tolerated and can be prescribed to young children and elderly people (Descamps et al., 2011; Tobert, 1988), making it an ideal drug for FXS as most patients develop their symptoms in their childhood (Bailey et al., 2009)

In this Chapter, I tested whether lovastatin would rescue the altered dendritic spine density and morphology in *Fmr1*$^{-/y}$ mice. Statins are known to suppress the expression of chondroitin sulfate proteoglycans (CSPGs) (Holmberg et al., 2008). CSPGs are extracellular matrix molecules that are essential in glial scar formation and neural development. Previous reports also point out the importance of CSPGs in inhibiting axon regeneration (for review, see Yiu and He, 2006). CSPGs down-regulate spine formation by dephosphorylating tropomyosin receptor kinase B (TrkB), the receptor of brain-derived neurotrophic factor (BDNF) (Kurihara and Yamashita, 2012). Hence, lovastatin treatment is likely to rescue the dendritic spine abnormalities in *Fmr1*$^{-/y}$ mice.

A treatment-oriented, oral route of administering lovastatin was used in the current study, by supplying animals the rodent chows that pre-mixed with lovastatin. *Fmr1*$^{-/y}$ mice and WT controls were randomly assigned to either lovastatin-

containing chows (lovachows, LOV), or control chows (CON) treatment for 10 days during early development (P25) and detailed spine analysis was conducted afterwards. This age was chosen as spine turnover rate decreased and the overall circuit towards maturation around this time point (Holtmaat et al., 2005). Spine density and morphology was assessed using confocal microscopy with a resolution of approximately 180 nm.

4.2 Materials and methods

4.2.1 Animals

All animals were obtained from the animal unit located in the Hugh Robson Building (BRR-HRB, The University of Edinburgh) in accordance with the United Kingdom Animals (Scientific Procedures) Act 1986 under the authority of Project Licences (PPL 60/3631 and PPL 60/4290). Animals were housed under a 12 hr/12 hr light/dark cycle. The *Fmr1*$^{-/y}$ mice used in this Chapter were originally purchased from the Jackson Labs and then backcrossed and maintained onto the C57BL/6J substrain purchased from Charles River UK. Male *Fmr1*$^{-/y}$ mice and their WT littermates were first weighted and then assigned randomly to receive either lovastatin-containing chows or control chows as their source of food. All mice have *ad libitum* access to the designated food and water at all times through the experiment.

4.2.2 Lovastatin treatment

LOV and CON were purchased from Bio-Serv (Flemington, NJ, USA). LOV were regular rodent chows pre-mixed with 0.01 % (w/w) lovastatin, which was a dose equivalent to 10 – 25 mg/kg daily (Osterweil et al., 2013; Yamada et al., 2000). All experimental mice were first weighted at P25 and then randomly assigned to either the LOV group or the CON group. The drug treatment lasted for 10 days and the weights of all mice were monitored daily for the first 3 days then every 3 days afterwards. All mice were sacrificed at the age between P35 and P37 through transcardial perfusion and their brains were removed and stored overnight at 4°C for future experiments.

4.2.3 Stick and stain

Mice were sacrificed through transcardial perfusion with ice-cold PBS then followed by 4% PFA. The volume and concentration of PFA needed to be carefully monitored as this would affect the dye-filling process dramatically. For filling cells in the hippocampal CA1 and V1 in the visual cortex, I used 6 – 7 ml of 4% PFA for perfusion and then post-fixed with 2% PFA overnight at 4°C. Brains were then rinsed with ice-cold PBS several times next morning, and quickly sliced into 200 µm coronal sections with a vibratome. Sections containing CA1 or V1 were used in this experiment.

Coronal sections containing either CA1 or V1 were placed in a chamber on a membranous filter (Millipore #HAWG04700, MA, USA), a “C” shaped weight was

then put on top to ensure the section remain in position during dye-filling. The chamber was filled with ice-cold PBS and was put into a holding stage of the upright microscope. The section was imaged using a 20X water immersion objective in PBS. Microinjection pipettes were pulled from thin walled glass capillaries (1.5 mm O.D. × 1.17 mm I.D., Harvard Apparatus, MA, USA) and filled with fluorescent dye (Alexa Fluor® 568 Hydrazide, 10 mM made up in ddH_2O, Life Technologies #A-10437). They were subsequently backfilled with a conducting solution (0.1 M KCl, pH 7.4). An $AgCl_2$ wire which connected to a pulse generator (Isolated Pulse Stimulator, A-M Systems Model 2100, WA, USA) was inserted in the electrode. An earth wire connecting the solution and the pulse generator was used to close the circuit. The electrode was checked to see if regular puffs of dye were emitted under fluorescence, then inserted carefully into a cell body without penetrating it. I focused on pyramidal cells located in the CA1 and layer II/III of the visual cortex. A given cell might require 15 – 20 min to fill depending on its size and fixation using a continuous square pulse at 1 Hz. Generally 3 – 5 cells were filled for each region (i.e., CA1 and V1) from a single animal. Cells after filling were post-fixed with 4% PFA for 1 hr then rinsed with PBS and stored in mounting medium (VECTASHIELD® antifade mounting medium, Vector # H-1000, CA, USA) at 4°C before imaging.

Before imaging, sections were rinsed with PBS and counterstained with TO-PRO®-3 iodide (1:1000, Life Technologies #T3605) then mounted with VECTASHIELD® HardSet (Vector # H-1400, CA, USA). An inverted laser-

scanning confocal microscope (Zeiss Axiovert LSM510, Germany) was used to acquire images of filled cells. All images were acquired by Nyquist sampling.

4.2.4 Image analysis

Confocal image Z-stacks (0.14 µm per stack) were first deconvolved by using the deconvolution software (Huygens Essential, The Netherlands) prior image analysis. NIH ImageJ was used to analyse dendritic spine density and characterise spine morphology. For more detailed spine measurement such as spine head diameter and spine length, a commercial image analysis software IMARIS® with FilamentTracer plugin (Bitplane, Zurich, Switzerland) was used in order to perform a more detailed dendritic structure reconstruction (Fig. 4-1 – 4-3).

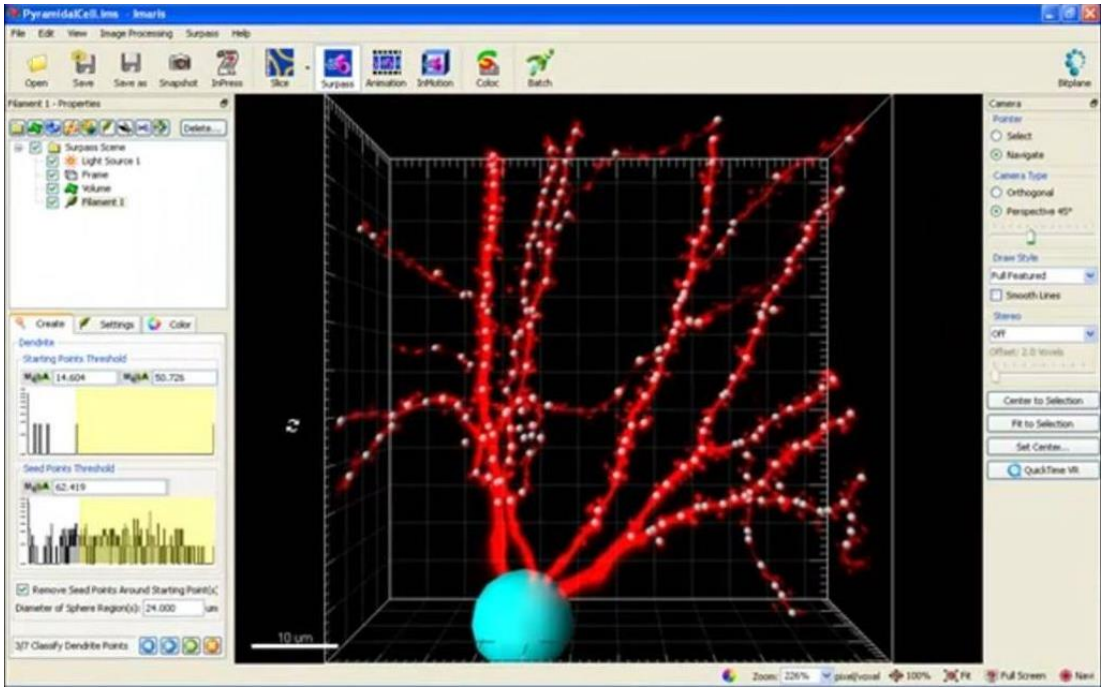

Figure 4-1. A representative figure showing the dendritic structure reconstruction process using IMARIS.

To reconstruct a dendrite, I first set-up "seeds" along the dendrites of interest to tell IMARIS which dendrite needed to be reconstructed. For most of the situations IMARIS would mark more than one dendrite which, in our case, was not ideal as I only wanted one dendrite to be reconstructed at a time to prevent oversampling from certain neurons over the others. Those excess dendrites were trimmed manually. I only analysed one of the secondary apical dendrites (apical obliques) and one of the secondary basal dendrites for each neuron for the dendritic spine analysis.

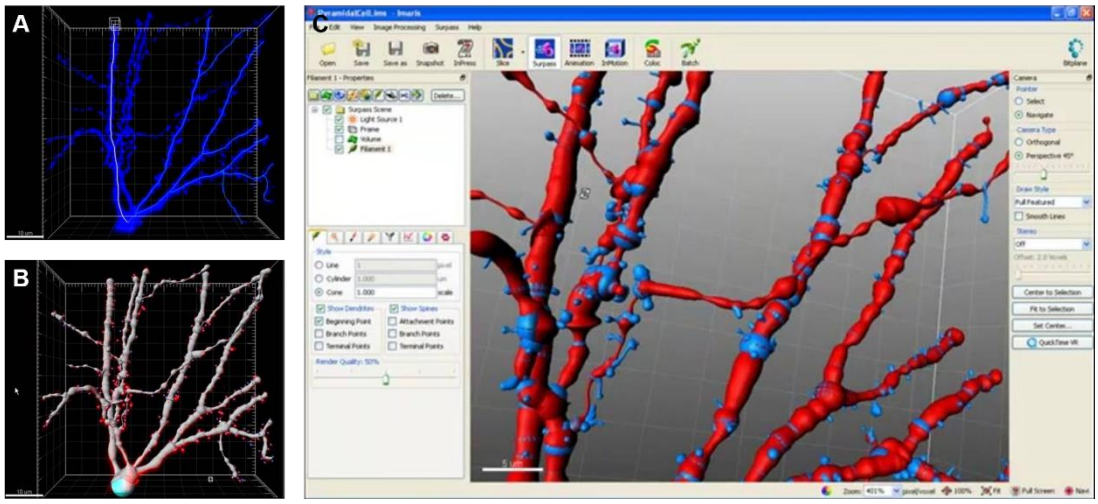

Figure 4-2. A representative image showing the dendrite reconstruction process using IMARIS is presented here.

Here in (A) a dendrite of interest was selected and reconstructed in (B) and (C), however almost every other dendrite in the same region was also reconstructed at the same time. Manually trimming was done at this stage to delete those dendrites that were out of focus.

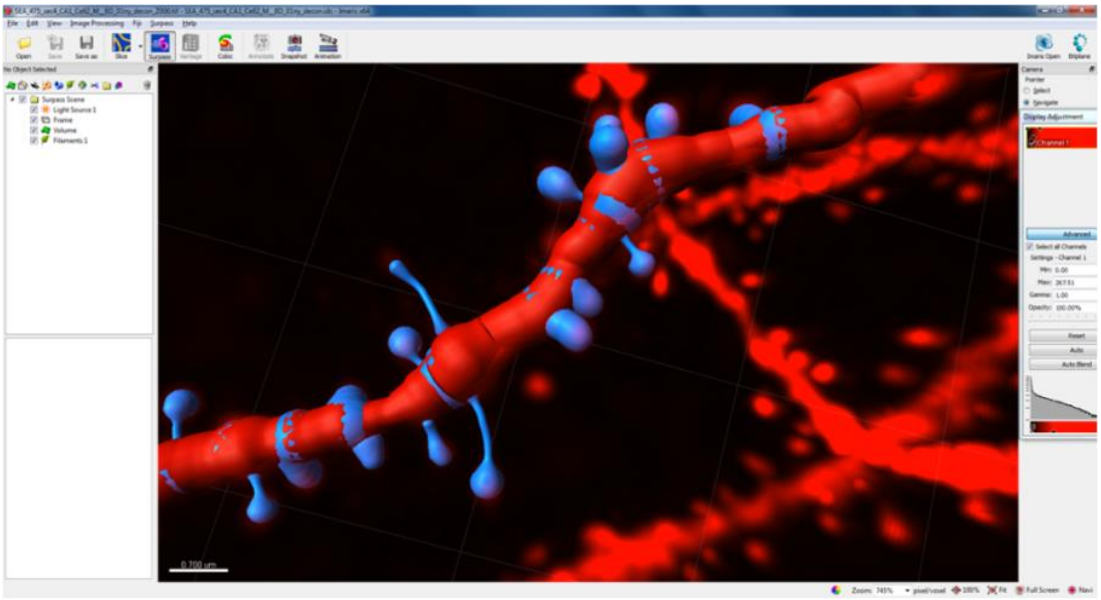

Figure 4-3. A representative figure showing a fully reconstructed dendrite and its dendritic spines.

After removing those unwanted dendrites in the image, the dendritic spines on the dendrite of interest were reconstructed by IMARIS at this stage. Manual trimming may still be required at this stage to remove any spines that were out of focus. Since the Z plane resolution (about 200 nm) of our confocal set-up is far worse than the X-Y plane, spines grew toward the Z planes were only used for density analysis and were excluded from further morphology characterisation.

4.2.5 Western blotting

Animals were sacrificed via neck dislocation, brains were then quickly removed and the region of interest (hippocampus and visual cortex) were dissected out from both hemispheres. All procedures were performed in a dissecting dish on ice and filled with ice-cold PBS with 10% sucrose. Dissected tissues were quickly

put into 1.5 ml Eppendorf tubes which were pre-cooled with dry ice to "snap-freeze" before stored in a −80°C freezer.

Tissues were homogenised with lysis buffer containing protease and phosphatase inhibitors (RIPA buffer: 50 mM Tris-HCl, 150 mM NaCl, 1% Triton X-100, 0.5% sodium deoxylcholate, 0.1% SDS, 1 mM EDTA, pH 7.4; protease inhibitor (EDTA free), Roche #11836170001; phosphatase inhibitor cocktail, Calbiochem #524625 (II) and #524628 (IV)). Protein concentration of homogenised tissues were checked by using a protein assay kit (Pierce™ BCA Protein Assay Kit, Thermo #23225, 23227) before running the Western blot. Briefly, for a microplate (96 wells), pipette 10 µl of each standard or unknown sample replicate into each well, and then add 200 µl of the BCA working reagent into each well. The microplate was then put on a plate shaker to mix thoroughly for 30 seconds. Plate was then covered with tin foil and left in 37°C for 30 min for incubation. Finally, the microplate was allowed to cool to room temperature prior plate reading. Several loading stocks were made based on the plate reading results of protein concentration of each sample. A 50 µl loading stock with a protein concentration of 0.5 µg/µl (containing 25 µl of 2X Laemmli buffer) was made for each sample and all loading stocks were stored in a −80°C freezer prior gel running. Details of buffers used and buffers recipes can be found in the Appendix section (Chapter 8) at the end of the thesis.

Pre-cast gels (Mini-PROTEAN® TGX gels, Bio-Rad #456-1046; 12%) were used for all Western blotting experiments in this Chapter. Those pre-made loading stocks were heated to 95°C on a heat plate for 5 min, and 2 pre-cast gels were put

into one cassette and then the cassette was put into a tank filled with running buffer. The first and last lane of each gel were loaded with 5 µl of 2X Laemmli buffer only, and one lane was loaded with 5 µl of protein ladder (PageRuler® Plus Prestained Protein Ladder, 10 to 250 kDa, Thermo #26619) of each gel. The remaining lanes was then loaded with 10 µl loading stock to make the final protein concentration of each lane equal to 5 µg. Gels were running for about 100 min with 100 V before transferring to nitrocellulose membranes. All components were equilibrated in transfer buffer to reduce the risk of air bubbles which would impede protein transfer.

The gels were transferred to nitrocellulose membranes for 1 hr with 100 mA, then membranes were washed thoroughly with PBS followed by incubating in the blocking buffer (Odyssey® blocking buffer, Li-COR #927-40000, Cambridge, UK) for 45 min at room temperature. Primary antibodies against ERK1/2 (or pERK1/2) and beta-actin were then added into the blocking buffer (with 0.1% Tween-20) at the desired concentration (ERK1/2: 1:2000, mouse anti-ERK1/2, Cell Signalling #4696S; pERK1/2: 1:2000, mouse anti-pERK1/2, Cell Signalling #9106S; β-actin: 1:2000, rabbit anti-β-actin, abcam #ab8227) and gels were incubated at 4°C overnight. Membranes were washed thoroughly with PBS the next day and incubated with secondary antibodies (goat anti-mouse Alexa Fluor® 680, Life Technologies #A-21057, 1:5000; goat anti-rabbit IRDye® 800, Li-COR #926-32211, 1:5000) for 1 hr at room temperature in a light-tight box to prevent fading. Membranes were then washed again with PBS for several times and were imaged with an Odyssey Infrared Imaging System (Li-COR Odyssey 9120, Cambridge, UK). Images of Western

results were then quantified with a freeware provided by Li-COR (Image Studio™ Lite, Li-COR).

Some membranes were blotted several times with different antibodies, in this case membranes were incubated in 1X stripping buffer (ReBlot Plus stripping solution (10X), Millipore #2504) for 10 – 15 min at room temperature and rinsed thoroughly with PBS. After incubating in blocking buffer for 1 hr, a new primary antibody can then be introduced to the membrane following the above process.

For Western blot results, images gathered via Li-COR Odyssey were processed and quantified by using their own software Image Studio™ Lite. Two channels were analysed separately. For each channel, multiple size-fixed user-defined region of interests (ROIs) were put on top of each individual lane where proteins were shown. Along that, a small area surrounding each ROI was used as the background noise value for further readout adjustment. An absolute value was then shown for each ROI after subtracting its own background noise value. The value of β-actin was used as a loading control and all values presented are shown as a ratio of protein : β-actin.

4.2.6 Statistics

Data were analysed with GraphPad Prism (version 6th, GraphPad Software, CA, USA), presented as mean ± SEM unless otherwise specified. Student's unpaired *t*-test, K-S test, or ANOVA were used for statistical analysis as appropriate. *p* values

were reported and significance was set when $p < 0.05$ (marked as *; ** when $p < 0.01$ and *** when $p < 0.001$, respectively.

4.3 Results

4.3.1 Dendritic spine density was unaltered between the *Fmr1*$^{-/y}$ and WT mice in CA1 and V1 after LOV treatment.

In this Chapter, I tested whether LOV treatment would affect dendritic spine density or morphology in the *Fmr1*$^{-/y}$ mice. Mice from both genotypes were given CON or LOV treatment for 10 days and dendritic spines from dye-filled neurons in the CA1 and V1 were analysed (Fig. 4-4 – 4-6).

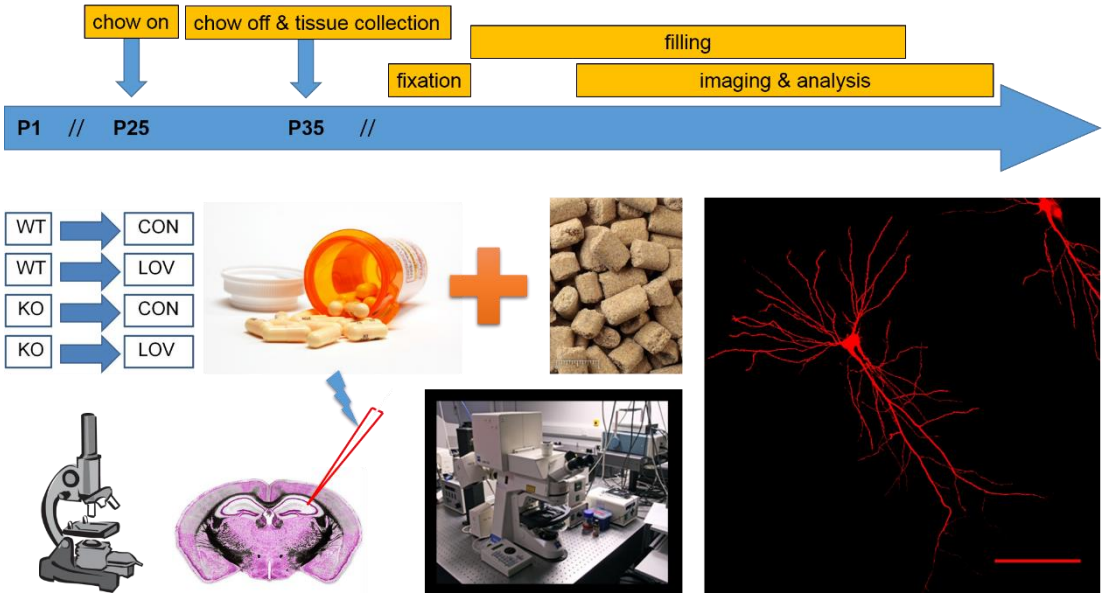

Figure 4-4. A diagram showing the general experimental design of this Chapter.

Both the *Fmr1*$^{-/y}$ mice and WT controls were assigned randomly to receive either CON or LOV treatment for 10 days from P25. At P35, all mice were sacrificed via transcardial perfusion and then I performed "stick and stain" on selected coronal sections containing the CA1 or V1 region. Dye-filled neurons were then imaged by a laser scanning confocal set-up in the IMPACT centre at HRB.

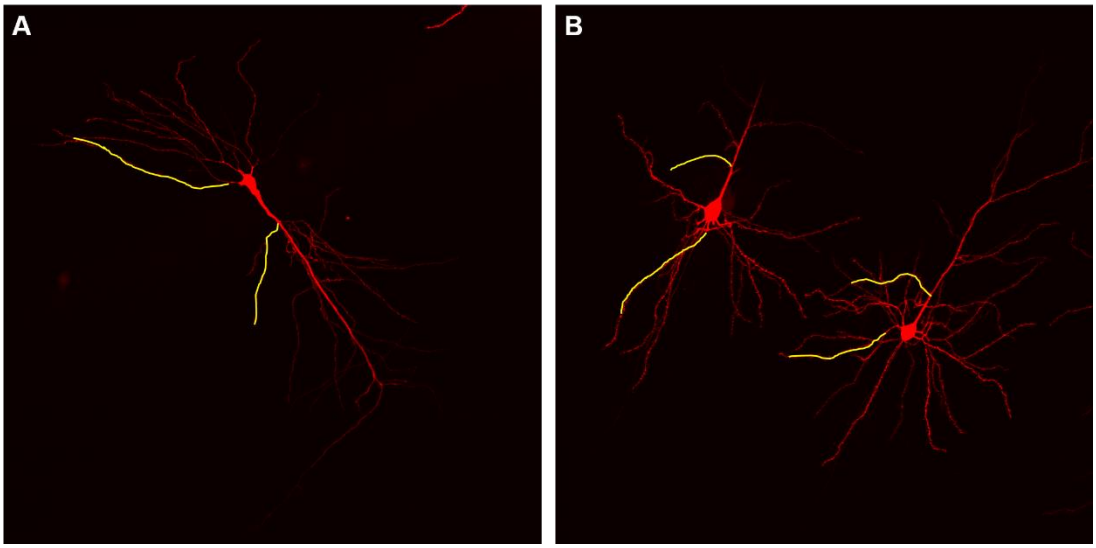

Figure 4-5. Representative figures of dye-filled neurons in the CA1 and V1 region.

A CA1 pyramidal cell is shown in (A), the apical and basal dendrites used for spine density and morphology analysis are marked in yellow. Two neurons from the V1 region are shown in (B).

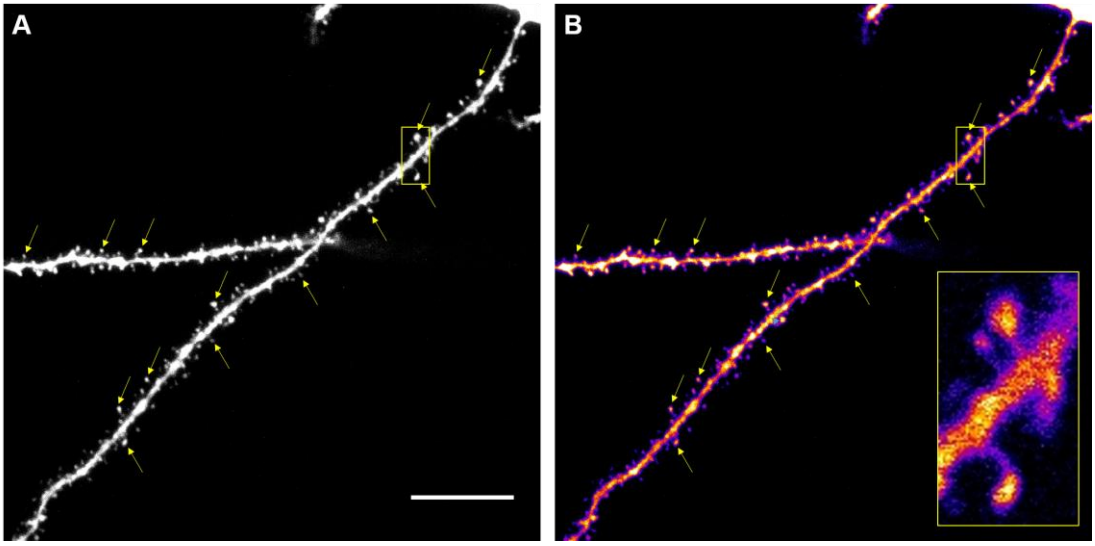

Figure 4-6. Representative figures of an apical dendrite from the CA1 region are shown to illustrate using colour-coding to assist image analysis.

An apical dendrite from the CA1 region is shown in (A), and the same dendrite was colour-coded in (B) using ImageJ to assist spine visualisation and analysis. A 300X zoomed-in spine section (the yellow box in the bottom right corner) was highlighted in (B). Dendritic spine samples were marked with the yellow arrow heads in both graphs. Scale bar: 10 µm.

I first looked into the overall dendritic spine density of the *Fmr1*$^{-/y}$ and WT mice and see if there were any changes after the lovastatin treatment. There was no interaction between genotypes and treatments across all regions examined (Fig. 4-7A, $F_{(1, 13)} = 0.1701$, $p = 0.6867$; Fig. 4-7B, $F_{(1, 14)} = 0.1151$, $p = 0.7394$; Fig. 4-7C, $F_{(1, 18)} = 1.515$, $p = 0.2342$; Fig. 4-7D, $F_{(1, 17)} = 0.08411$, $p = 0.7753$, Two-way ANOVA). Drug treatment did not have an effect on spine density in CA1 and V1 dendrites (Fig. 4-7A, $F_{(1, 13)} = 0.2166$, $p = 0.6493$; Fig. 4-7B, $F_{(1, 14)} = 0.4587$, $p = 0.5093$; Fig. 4-7C, $F_{(1, 18)} = 2.605$, $p = 0.1239$; Fig. 4-7D, $F_{(1, 17)} = 0.03133$, $p =$

0.8616, Two-way ANOVA). A genotype effect on spine density was only found in the V1 apical dendrites (Fig. 4-7A, $F_{(1, 13)} = 6.523$, $p = 0.0240$, Two-way ANOVA), and no effect was found on the rest of the regions examined (Fig. 4-7B, $F_{(1, 14)} = 2.727$, $p = 0.1209$; Fig. 4-7C, $F_{(1, 18)} = 0.09648$, $p = 0.7597$; Fig. 4-7D, $F_{(1, 17)} = 0.2972$, $p = 0.5927$, Two-way ANOVA).

However, a significant increase of spine density was noticed in the V1 apical dendrites of the *Fmr1*$^{-/y}$ mice compared to the WT mice (Fig. 4-7A, $p = 0.0315$, unpaired two-tailed Student's *t*-test; Power = 0.65, at least 7 WT and 5 *Fmr1*$^{-/y}$ mice will be needed if aiming to reach 0.8 in Power), when both of them receiving CON treatment (i.e., under normal condition). This increase of spine density in V1 of the *Fmr1*$^{-/y}$ mice was diminished after 10 days of LOV treatment compared to the WT controls (Fig. 4-7A, LOV WT vs. LOV *Fmr1*$^{-/y}$, $p = 0.2607$, unpaired two-tailed Student's *t*-test). However, this was likely due to the slight increase of spine density in the WT animals after LOV treatment (Fig. 4-7A, CON WT vs. LOV WT, $p = 0.5860$, unpaired two-tailed Student's *t*-test; mean of CON WT = 12.06 ± 0.97, mean of LOV WT = 13.15 ± 1.79), as spine density of the *Fmr1*$^{-/y}$ mice did not alter after LOV treatment (Fig. 4-7A, CON *Fmr1*$^{-/y}$ vs. LOV *Fmr1*$^{-/y}$, $p = 0.9668$, unpaired two-tailed Student's *t*-test; mean of CON *Fmr1*$^{-/y}$ = 15.76 ± 0.94, mean of LOV *Fmr1*$^{-/y}$ = 15.82 ± 1.20). Meanwhile, the spine density in the LOV *Fmr1*$^{-/y}$ group was still significantly increased compared to the CON WT group (Fig. 4-7A, $p = 0.0427$, unpaired two-tailed Student's *t*-test).

No differences in spine density were found in the CA1 region (both apical and basal dendrites) and basal dendrites in the V1 region. A slight but not significant

increase of spine density of the apical dendrites in the CA1 region was noticed in the *Fmr1*$^{-/y}$ mice after 10 days of lovastatin treatment (Fig. 4-7C, CON *Fmr1*$^{-/y}$ vs. LOV *Fmr1*$^{-/y}$, $p = 0.0630$, unpaired two-tailed Student's *t*-test).

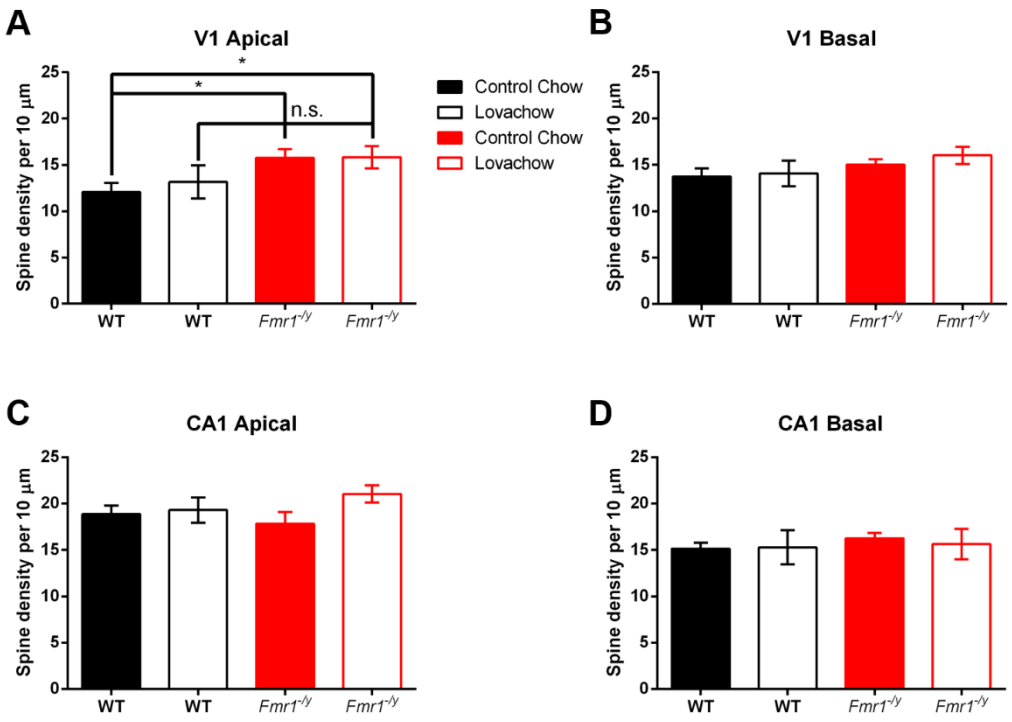

Figure 4-7. The effect of lovastatin treatment on dendritic spine density of the *Fmr1*$^{-/y}$ and WT mice are presented.

Dendritic spine density of the *Fmr1*$^{-/y}$ and WT mice from CA1 and V1 are shown before and after 10 days of CON/LOV treatment. Mean spine density per 10 µm along the dendrites from left to right in (A): 12.06, 13.15, 15.76, 15.82; (B): 13.75, 14.08, 15.03, 16.03; (C): 18.88, 19.31, 17.84, 21.05; (D) 15.13, 15.28, 16.27, 15.63. $n = 5$ in each group besides the LOV-*Fmr1*$^{-/y}$ group, where $n = 7$.

4.3.2 Dendritic spine morphologies were largely unaltered between the *Fmr1*$^{-/y}$ and WT mice before and after LOV treatment.

As a first attempt to identify differences in spine morphologies between genotypes, I attempted to categorise dendritic spines (long/thin, stubby, mushroom, etc.) based on their prominent features (e.g., neck length, head width) as previously reported (Arellano et al., 2007; Galvez and Greenough, 2005; Harris et al., 1992; Hering and Sheng, 2001). A detailed diagram of how spines were grouped is shown in Fig. 4-8 and different spine morphologies are shown in Fig. 4-9.

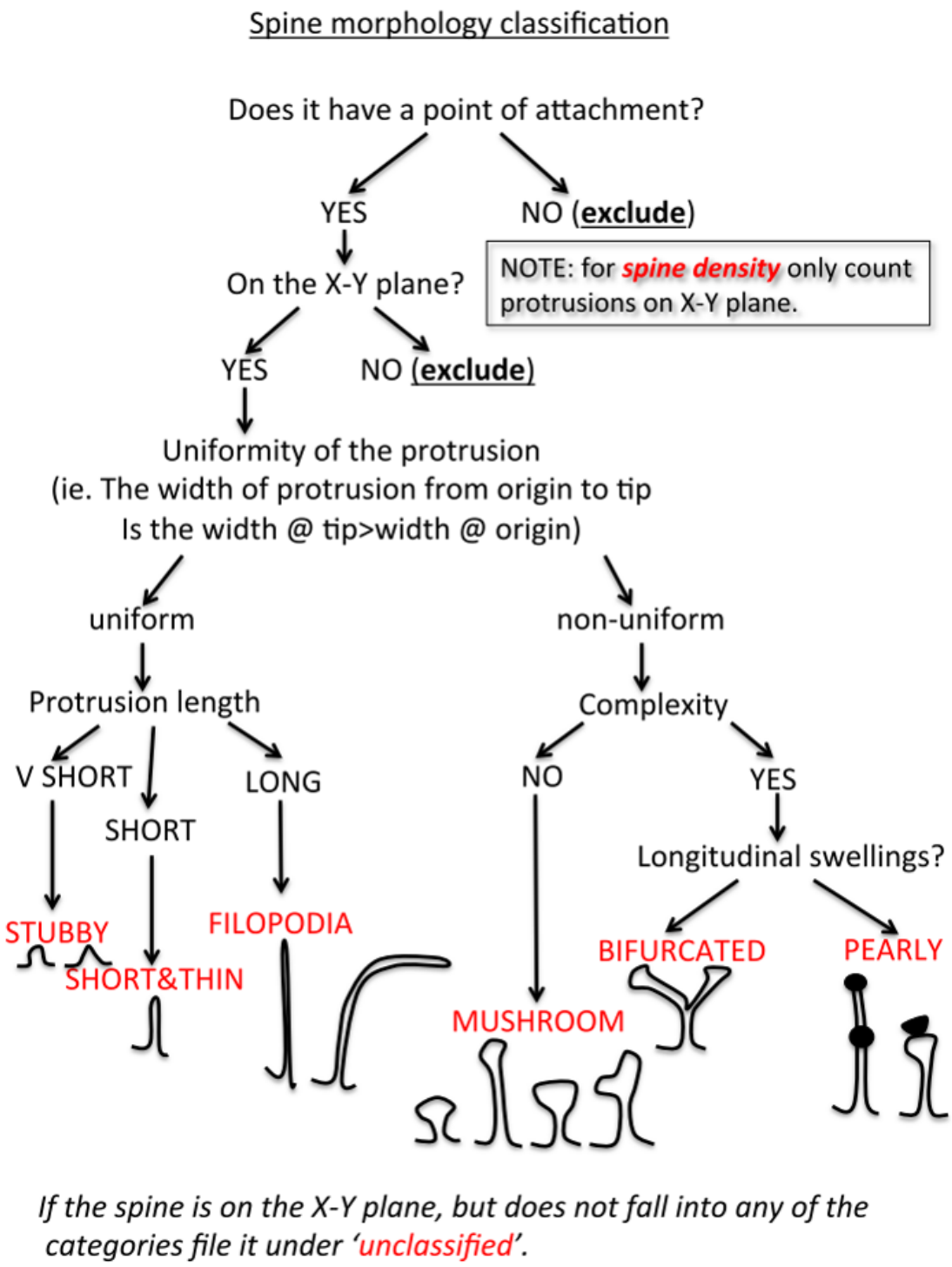

Figure 4-8. A detailed diagram showing how spines were grouped into different categories.

This diagram was drawn by Dr. Lasani Wijetunge based on a lab meeting about spine morphology characterisation. We first excluded all spines that did not have a clear attachment to the dendritic

shaft, as in this case we cannot conclude they are spines or some random artefacts. We next excluded those spines located on the Z plane, as the Z resolution of the confocal microscope was poor compared to the X-Y plane. The remaining spines were then categorised first by its uniformity, more precisely, with or without a clear spine "neck". Spines that are without a clear neck and are short were called "stubby" spines; short and thin spines were therefore categorised as "short & thin"; longer spines and without a prominent head were then named as "filopodia", which was consistent with previous literatures. Spines with a clear neck and a prominent head were then classified as "mushroom" spines, which then depending on the complexity some were further classified as "pearly" or "bifurcated" spines.

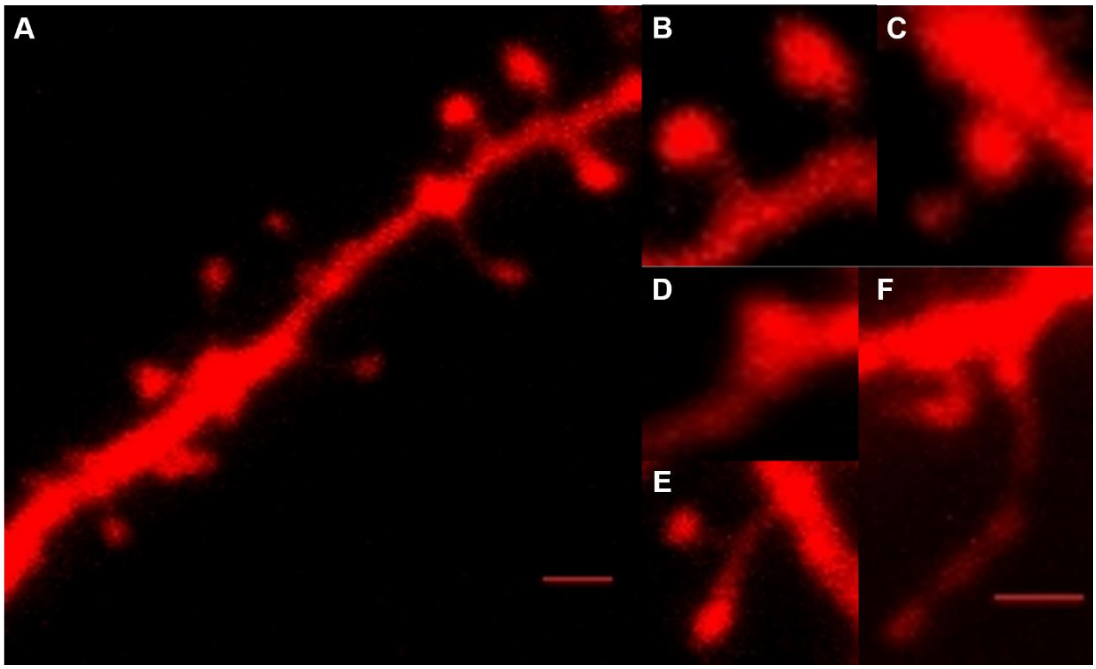

Figure 4-9. A representative figure showing spines with different morphologies.

Several dendritic spines along a dendrite are shown in (A). Two mushroom spines are shown in (B), one pearly spine (C), one stubby spine (D), one bifurcated spine (E), and one filopodia spine (F) is shown in the right panel of the figure, respectively. Scale bar: 1 µm.

Based on this categorisation procedure, I did not find any significant differences between the *Fmr1*$^{-/y}$ and WT mice on spine morphologies, and 80% of all the spines I have measured were mushroom-like spines (Fig. 4-10 and Fig. 4-11).

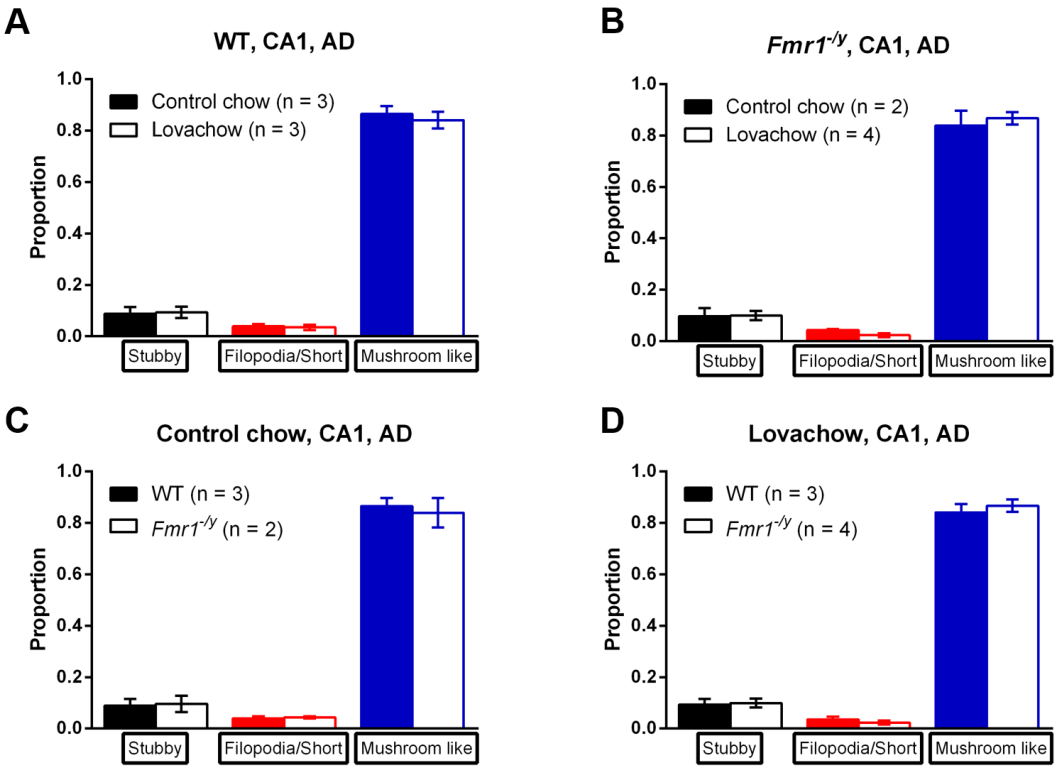

Figure 4-10. Dendritic spines with different morphologies from the CA1 region of the *Fmr1*$^{-/y}$ and WT mice are presented (apical dendrites).

Stubby, filopodia/short and thin, and mushroom spines were characterised from the apical dendrites in the CA1 region. The proportion of spines with different morphologies are shown here. WT animals treated with CON or LOV are shown in (A). *Fmr1*$^{-/y}$ mice treated with CON or LOV are shown in (B). In (C) and (D), WT and *Fmr1*$^{-/y}$ mice treated with either CON or LOV are shown, respectively. *n* equals number of animals.

There were no gross changes between the two genotypes (Fig. 4-10A and Fig. 4-10B), nor between the two different treatments (Fig. 4-10C and Fig. 4-10D) in spine morphology. Unpaired two-tailed Student's *t*-test was used to examine the difference between groups. Results in Fig. 4-10A: stubby: $p = 0.8991$, filopodia: $p = 0.7501$, mushroom: $p = 0.6212$; Fig. 4-10B: stubby: $p = 0.9376$, filopodia: $p = 0.1529$, mushroom: $p = 0.6104$; Fig. 4-10C: stubby: $p = 0.8621$, filopodia: $p = 0.7598$, mushroom: $p = 0.6884$; Fig. 4-10D: stubby: $p = 0.8419$, filopodia: $p = 0.3563$, mushroom: $p = 0.5394$. The statistical Power in this experiment was 0.28, at least 6 animals under the CON treatment and 12 animals for the LOV group will be needed if aiming to reach 0.8 in Power.

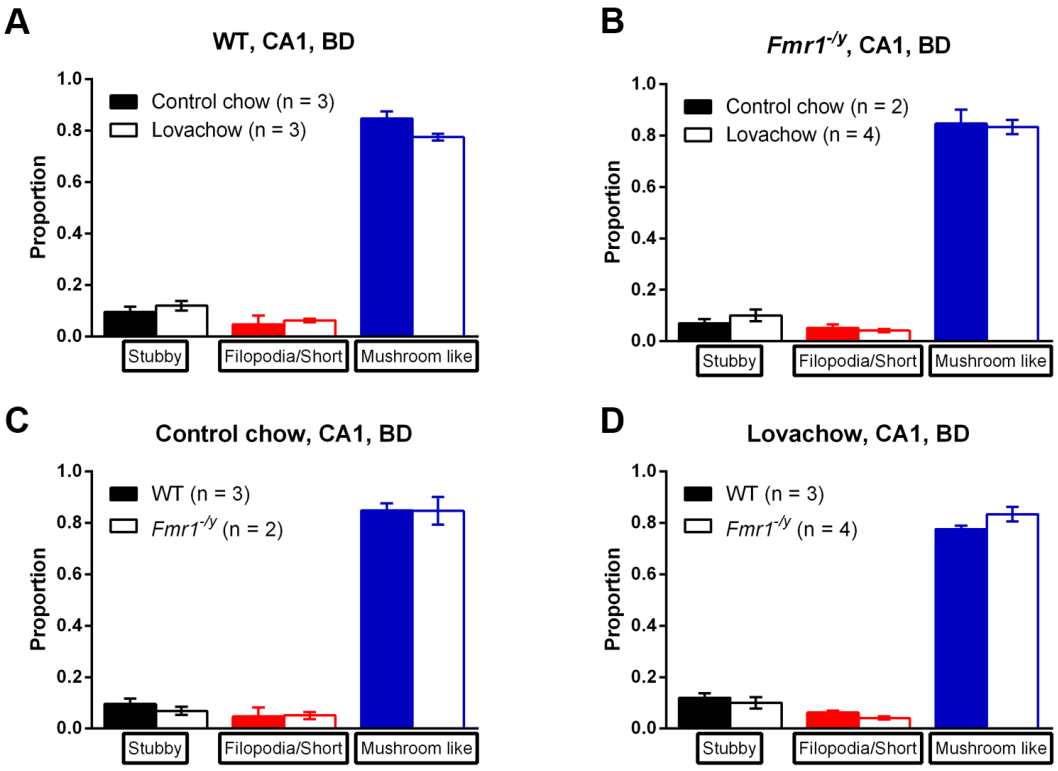

Figure 4-11. Dendritic spines with different morphologies from the CA1 region of the *Fmr1*$^{-/y}$ and WT mice are presented (basal dendrites).

Stubby, filopodia/short and thin, and mushroom spines were characterised from the basal dendrites in the CA1 region. The proportion of spines with different morphologies are shown here. WT animals treated with CON or LOV are shown in (A). *Fmr1*$^{-/y}$ mice treated with CON or LOV are shown in (B). In (C) and (D), WT and *Fmr1*$^{-/y}$ mice treated with either CON or LOV are shown, respectively. *n* equals number of animals.

There were no gross changes between the two genotypes (Fig. 4-11A and Fig. 4-11B), nor between the two different treatments (Fig. 4-11C and Fig. 4-11D). Unpaired two-tailed Student's *t*-test was used to examine the difference between

groups. Results in Fig. 4-11A: stubby: $p = 0.4355$, filopodia: $p = 0.6981$, mushroom: $p = 0.075$; Fig. 4-11B: stubby: $p = 0.4273$, filopodia: $p = 0.4726$, mushroom: $p = 0.8178$; Fig. 4-11C: stubby: $p = 0.446$, filopodia: $p = 0.9409$, mushroom: $p = 0.9793$; Fig. 4-11D: stubby: $p = 0.5495$, filopodia: $p = 0.0818$, mushroom: $p = 0.1525$. The statistical Power in this experiment was 0.13, at least 15 animals under the CON treatment and 31 animals for the LOV group will be needed if aiming to reach 0.8 in Power. These preliminary results indicated that the "morphological categorisation" approach was not effective and might not be able to detect the differences between the two genotypes (if there were any). Hence, I took another approach to examine spine morphology and it will be discussed in the following section.

4.3.3 Detailed spine morphology measurements indicated that the spine head diameter was increased in the *Fmr1*$^{-/y}$ mice.

It has recently been shown that dendritic spine categorisation is artificial and instead, spine morphology is a continuum (Tønnesen et al., 2014; Wijetunge et al., 2014). Hence, to get a more accurate estimate of spine morphology, I analysed spine head width and length with the commercial software IMARIS® alongside with a specific plugin called "FilamentTracer" (Bitplane, Zurich, Switzerland). I started with measuring the spine head diameter as an increased spine head diameter in the *Fmr1*$^{-/y}$ mice was reported previously (Wijetunge et al., 2014). Consistent with these previous studies, I found a significant increase in spine head diameter from CA1

apical dendrites in the *Fmr1*$^{-/y}$ mice compared to the WT controls (Fig. 4-12A). I also found a consistent increase of spine head diameter in the apical dendrites of the CA1 region and both apical and basal dendrites in the V1 region when the WT mice were given 10 days of LOV treatment (Fig. 4-12C, 4-14C, and 4-15C).

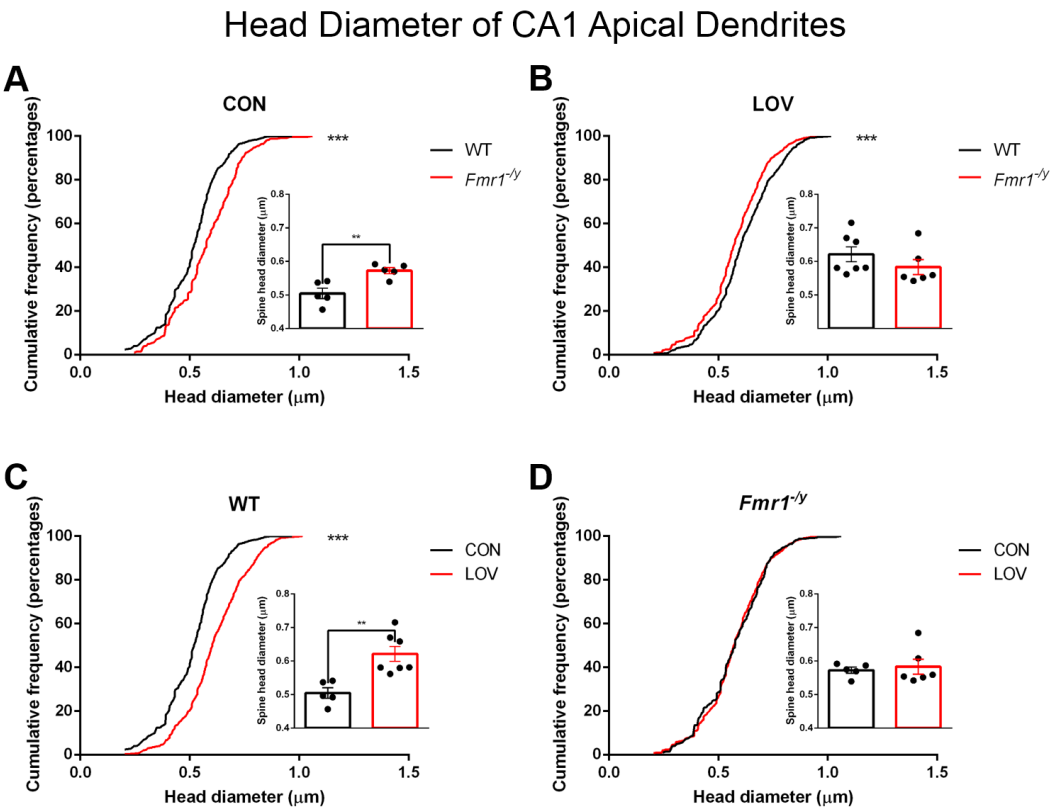

Figure 4-12. LOV treatment rescued the increased spine head diameter of CA1 apical dendrites in the *Fmr1*$^{-/y}$ mice.

For all four figures, the left panel showed the cumulative frequency distribution of spine head diameter and the mean for each individual animal was plotted in the right panel. Control chow treated animals are shown in (A), where *Fmr1*$^{-/y}$ mice and WT mice are marked with red and black, respectively. LOV treated animals are shown in (B), where *Fmr1*$^{-/y}$ mice and WT mice are marked with red and black, respectively. In (C), WT animals treated with CON or LOV are shown in black or red, respectively. In (D), *Fmr1*$^{-/y}$ animals treated with CON or LOV are shown in black or red, respectively. The dots in the right small panel represent each individual animal. CON-WT: n = 5; LOV-WT: n = 7; CON-*Fmr1*$^{-/y}$: n = 5; LOV-*Fmr1*$^{-/y}$: n = 6.

Spine head diameter of CA1 apical dendrites was significantly increased in the *Fmr1*$^{-/y}$ mice compared to WT controls under CON treatment (Fig. 4-12A, cumulative frequency was tested with K-S test, $p < 0.0001$; overall mean difference was tested via unpaired two-tailed Student's *t*-test, $p = 0.0057$; Power = 0.90). The increased spine head diameter in the *Fmr1*$^{-/y}$ mice was diminished after 10 days of LOV treatment (Fig. 4-12B, cumulative frequency was tested with K-S test, $p < 0.0001$; overall mean difference was tested via unpaired two-tailed Student's *t*-test, $p = 0.258$). The difference of spine head diameter on WT animals between two treatments was shown in Fig. 4-12C, where animals receiving LOV treatment for 10 days had bigger spine head compared to the animals under CON treatment (cumulative frequency was tested with K-S test, $p < 0.0001$; overall mean difference was tested via unpaired two-tailed Student's *t*-test, $p = 0.003$; Power = 0.97). There was no difference in spine head diameter between the two treatment groups of the *Fmr1*$^{-/y}$ mice (Fig. 4-12D, cumulative frequency was tested with K-S test, $p = 0.2370$; overall mean difference was tested via unpaired two-tailed Student's *t*-test, $p = 0.6939$).

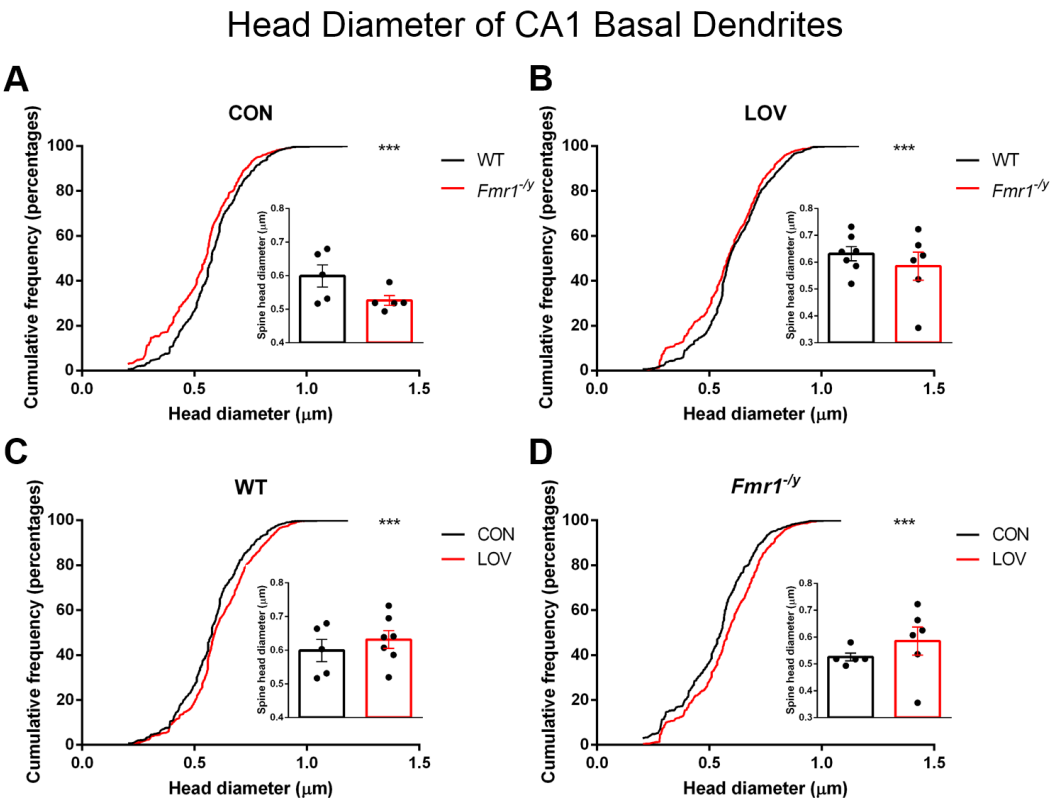

Figure 4-13. Mean spine head diameter of basal dendrites in the CA1 region were not altered.

Statistics and figure compositions are the same as shown in Fig. 4-12. Control chow treated animals are shown in (A), where *Fmr1*$^{-/y}$ mice and WT mice are marked with red and black, respectively. LOV treated animals are shown in (B), where *Fmr1*$^{-/y}$ mice and WT mice are marked with red and black, respectively. In (C), WT animals treated with CON or LOV are shown in black or red, respectively. In (D), *Fmr1*$^{-/y}$ animals treated with CON or LOV are shown in black or red, respectively. The dots in the right small panel represent each individual animal. CON-WT: n = 5; LOV-WT: n = 7; CON-*Fmr1*$^{-/y}$: n = 5; LOV-*Fmr1*$^{-/y}$: n = 6.

The mean spine head diameter of CA1 basal dendrites were not altered between the two genotypes or between the two treatments in both regions examined. In Fig. 4-13A, the overall cumulative distribution of spine head diameter of the *Fmr1*$^{-/y}$ mice was significantly smaller than the WT mice ($p < 0.0001$, K-S test). But the mean spine head diameter remained unaltered ($p = 0.0788$, unpaired two-tailed Student's *t*-test). LOV treatment did not have a significant effect on overall mean spine head diameter of the two genotypes (Fig. 4-13B, $p = 0.4279$, unpaired two-tailed Student's *t*-test). However, the cumulative frequency distribution suggested that after LOV treatment, the WT animals' spine head diameter was increased compared to the *Fmr1*$^{-/y}$ mice (Fig. 4-13B, $p < 0.0001$, K-S test). The spine head diameter of WT animals receiving either the LOV or the CON treatment are shown in Fig. 4-13C. The overall mean was not altered (Fig. 4-13C, $p = 0.4568$, unpaired two-tailed Student's *t*-test), but the cumulative distribution of the spine head diameter in the LOV treated mice was significantly increased compared to the CON group (Fig. 4-13C, $p < 0.0001$, K-S test). A similar pattern was also noticed in Fig. 4-13D, while no gross changes were noticed when comparing the overall mean of the spine head diameter between the *Fmr1*$^{-/y}$ and WT mice (Fig. 4-13D, $p = 0.3448$, unpaired two-tailed Student's *t*-test). A significant increase of the cumulative distribution of spine diameter was noticed in the LOV group compared to the CON group (Fig 4-13D, $p < 0.0001$, K-S test).

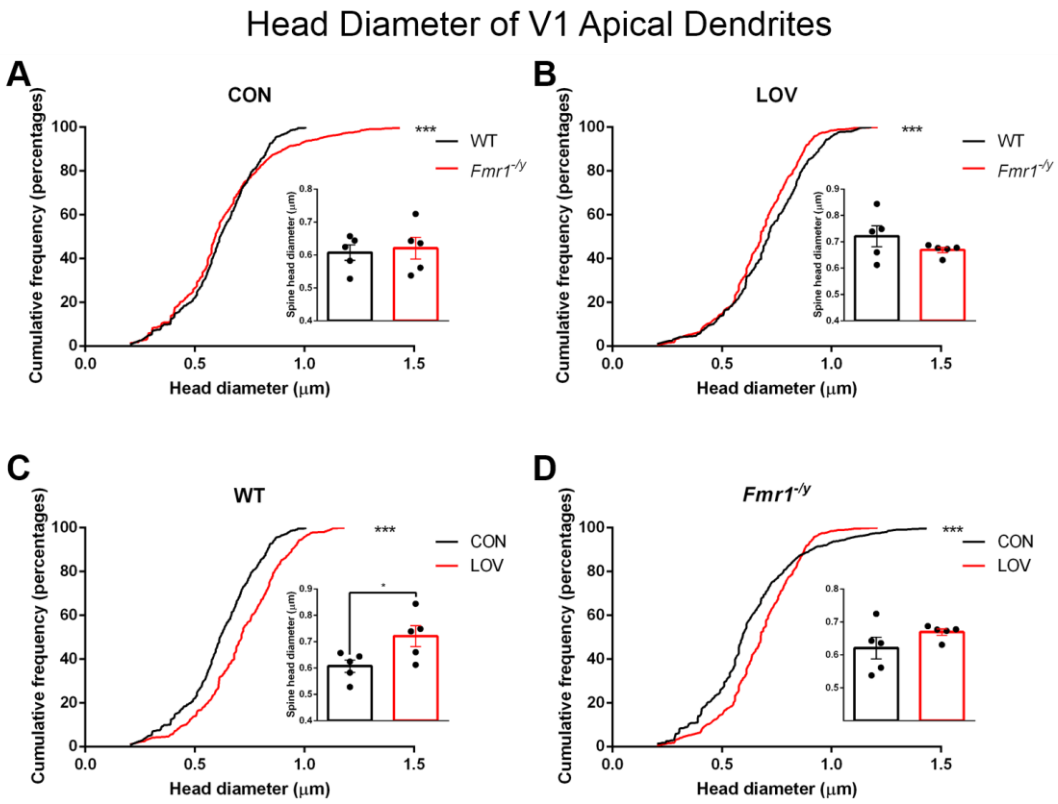

Figure 4-14. LOV treatment increased the spine head diameter of the apical dendrites from the V1 region of the WT animals.

Statistics and figure compositions are the same as shown in Fig. 4-12. Control chow treated animals are shown in (A), where *Fmr1*$^{-/y}$ mice and WT mice are marked with red and black, respectively. LOV treated animals are shown in (B), where *Fmr1*$^{-/y}$ mice and WT mice are marked with red and black, respectively. In (C), WT animals treated with CON or LOV are shown in black or red, respectively. In (D), *Fmr1*$^{-/y}$ animals treated with CON or LOV are shown in black or red, respectively. The dots in the right small panel represent each individual animal. CON-WT: n = 5; LOV-WT: n = 5; CON-*Fmr1*$^{-/y}$: n = 5; LOV-*Fmr1*$^{-/y}$: n = 5.

The mean spine head diameter of V1 apical dendrites were not altered between the two genotypes. However, WT animals treated with LOV showed an increased spine head diameter compared with the *Fmr1*$^{-/y}$ mice (Fig. 4-14C). In Fig. 4-14A, the overall cumulative distribution of spine head diameter of the *Fmr1*$^{-/y}$ mice was significantly larger than the WT mice ($p < 0.0001$, K-S test). But the mean spine head diameter remained unaltered ($p = 0.7519$, unpaired two-tailed Student's *t*-test). LOV treatment did not have a significant effect on overall mean spine head diameter of the two genotypes (Fig. 4-14B, $p = 0.2424$, unpaired two-tailed Student's *t*-test). However, the cumulative frequency distribution suggested that after LOV treatment, the WT animals' spine head diameter was increased compared to the *Fmr1*$^{-/y}$ mice (Fig 4-14B, $p < 0.0001$, K-S test). The spine head diameter of WT animals receiving either the LOV or the CON treatment were shown in Fig. 4-14C. The overall mean was increased in the LOV group (Fig. 4-14C, $p = 0.0394$, unpaired two-tailed Student's *t*-test; Power = 0.58, at least 8 animals per group will be needed if aiming to reach 0.8 in Power), and the cumulative distribution of the spine head diameter in the LOV treated mice was significantly increased compared to the CON group (Fig. 4-14C, $p < 0.0001$, K-S test). A similar pattern was also noticed in Fig. 4-14D, while no gross changes were noticed when comparing the overall mean of the spine head diameter between the *Fmr1*$^{-/y}$ and WT mice (Fig. 4-14D, $p = 0.1977$, unpaired two-tailed Student's *t*-test). A significant increase of the cumulative distribution of spine diameter was noticed in the LOV group compared to the CON group (Fig. 4-14D, $p < 0.0001$, K-S test).

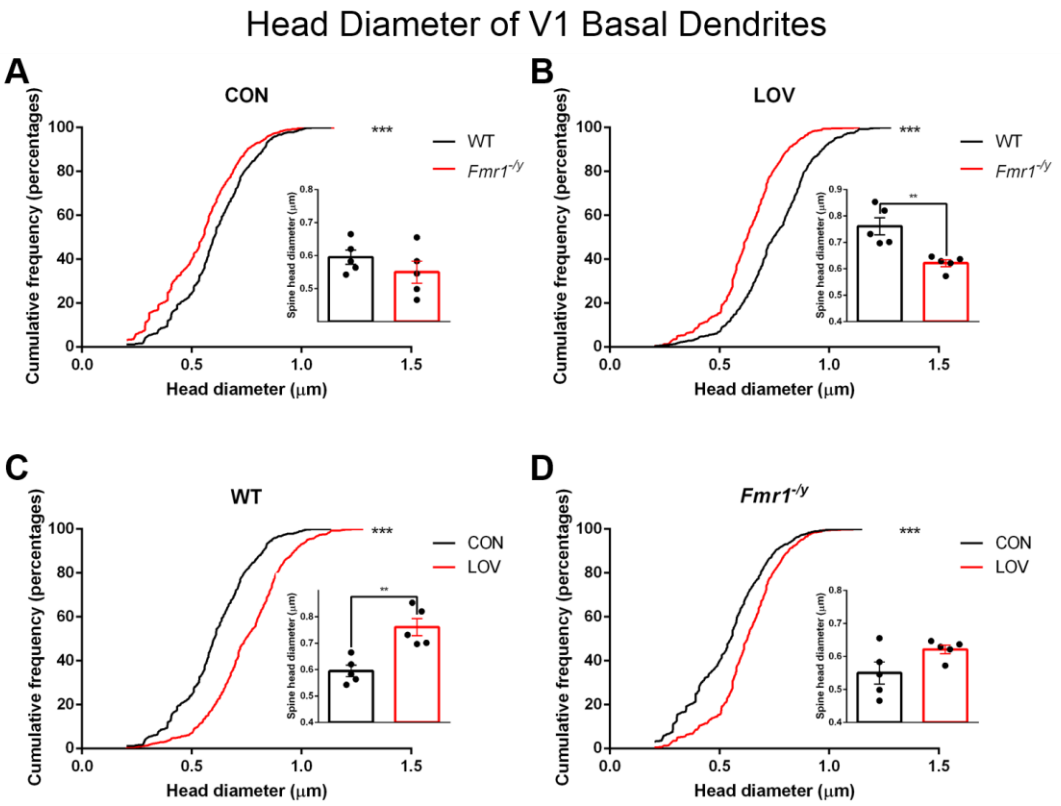

Figure 4-15. Mean spine head diameter of the V1 basal dendrites were significantly increased in the WT mice after LOV treatment.

Statistics and figure compositions are the same as shown in Fig. 4-12. Control chow treated animals are shown in (A), where *Fmr1*$^{-/y}$ mice and WT mice are marked with red and black, respectively. LOV treated animals are shown in (B), where *Fmr1*$^{-/y}$ mice and WT mice are marked with red and black, respectively. In (C), WT animals treated with CON or LOV are shown in black or red, respectively. In (D), *Fmr1*$^{-/y}$ animals treated with CON or LOV are shown in black or red, respectively. The dots in the right small panel represent each individual animal. CON-WT: n = 5; LOV-WT: n = 5; CON-*Fmr1*$^{-/y}$: n = 5; LOV-*Fmr1*$^{-/y}$: n = 5.

The overall mean spine head diameter of V1 basal dendrites were not altered between the two genotypes as shown in Fig. 4-15A ($p = 0.2861$, unpaired two-tailed Student's *t*-test). But the cumulative distribution indicated that WT animals had significantly larger spine heads compared to the *Fmr1*$^{-/y}$ mice (Fig. 4-15A, $p < 0.0001$, K-S test). The LOV treatment boosted the mean spine head diameter even further in WT mice (Fig. 4-15B, $p = 0.2861$, unpaired two-tailed Student's *t*-test; Power = 0.94). The same effect was also noticed when analysing the overall cumulative frequency distribution from the same animals (Fig. 4-15B, $p < 0.0001$, K-S test). An increase of spine head diameter was noticed in WT mice when LOV treatment was given for 10 days (Fig. 4-15C, $p = 0.0027$, unpaired two-tailed Student's *t*-test; $p < 0.0001$, K-S test; Power = 0.96). A similar trend of increasing spine head diameter was also shown in the *Fmr1*$^{-/y}$ mice after 10 days of LOV treatment, however only indicated in the cumulative frequency distribution (Fig. 4-15D, $p = 0.0785$, unpaired two-tailed Student's *t*-test; $p < 0.0001$, K-S test).

I next asked whether the spine length was altered between the *Fmr1*$^{-/y}$ mice and WT controls before and after the LOV treatment. A similar analysis was then performed on the same mice I used for the spine head diameter analysis (Fig. 4-16 – 19).

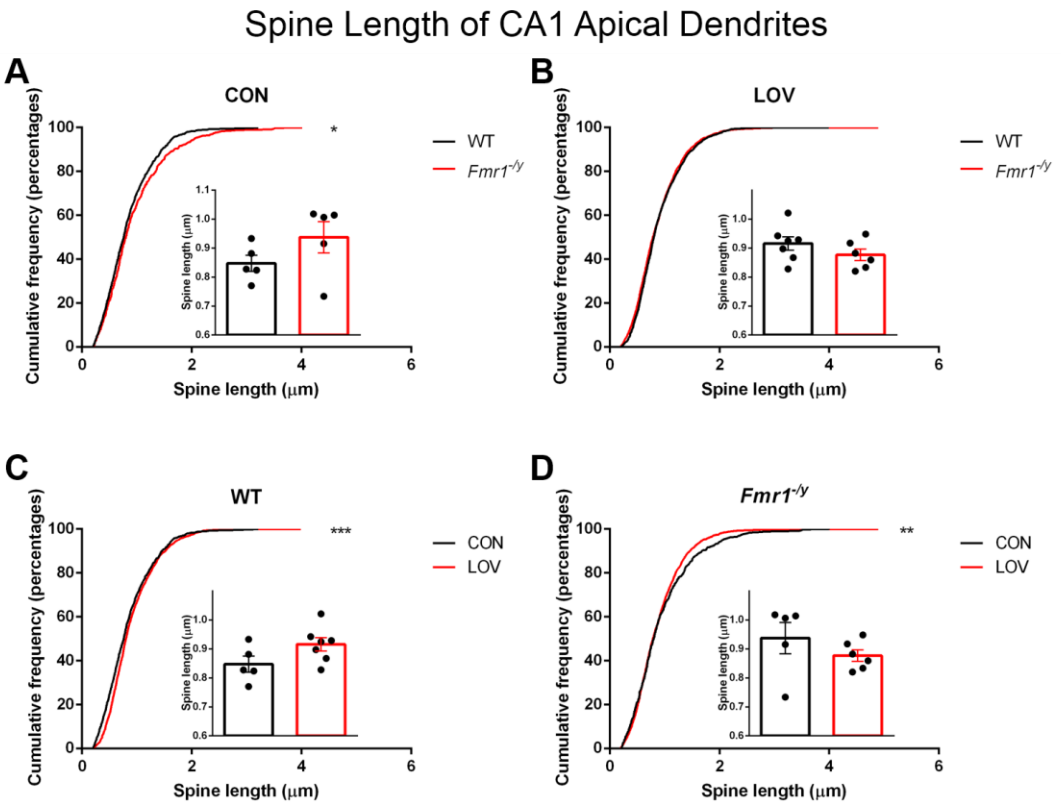

Figure 4-16. Dendritic spine length did not alter when sampling from the CA1 apical dendrites from the *Fmr1*$^{-/y}$ mice and WT controls.

Statistics and figure compositions are the same as shown in Fig. 4-12. Control chow treated animals are shown in (A), where *Fmr1*$^{-/y}$ mice and WT mice are marked with red and black, respectively. LOV treated animals are shown in (B), where *Fmr1*$^{-/y}$ mice and WT mice are marked with red and black, respectively. In (C), WT animals treated with CON or LOV are shown in black or red, respectively. In (D), *Fmr1*$^{-/y}$ animals treated with CON or LOV are shown in black or red, respectively. The dots in the right small panel represent each individual animal. CON-WT: n = 5; LOV-WT: n = 7; CON-*Fmr1*$^{-/y}$: n = 5; LOV-*Fmr1*$^{-/y}$: n = 6.

No gross spine length changes were noticed in the CA1 apical dendrites from both genotypes before nor after LOV treatment. Detailed cumulative frequency analysis showed an increased spine length in the *Fmr1*$^{-/y}$ mice compared to the WT controls under CON treatment (Fig. 4-16A, $p = 0.02$, K-S test; $p = 0.1780$, unpaired two-tailed Student's *t*-test). This difference between the two genotypes was diminished after 10 days of LOV treatment (Fig. 4-16B, $p = 0.12$, K-S test; $p = 0.2393$, unpaired two-tailed Student's *t*-test). LOV treatment induced a significant increase of spine length in the WT controls (Fig. 4-16C, $p < 0.0001$, K-S test; $p = 0.0869$, unpaired two-tailed Student's *t*-test), but caused an opposite effect when applied to the *Fmr1*$^{-/y}$ mice (Fig. 4-16D, $p = 0.0078$, K-S test; $p = 0.2901$, unpaired two-tailed Student's *t*-test).

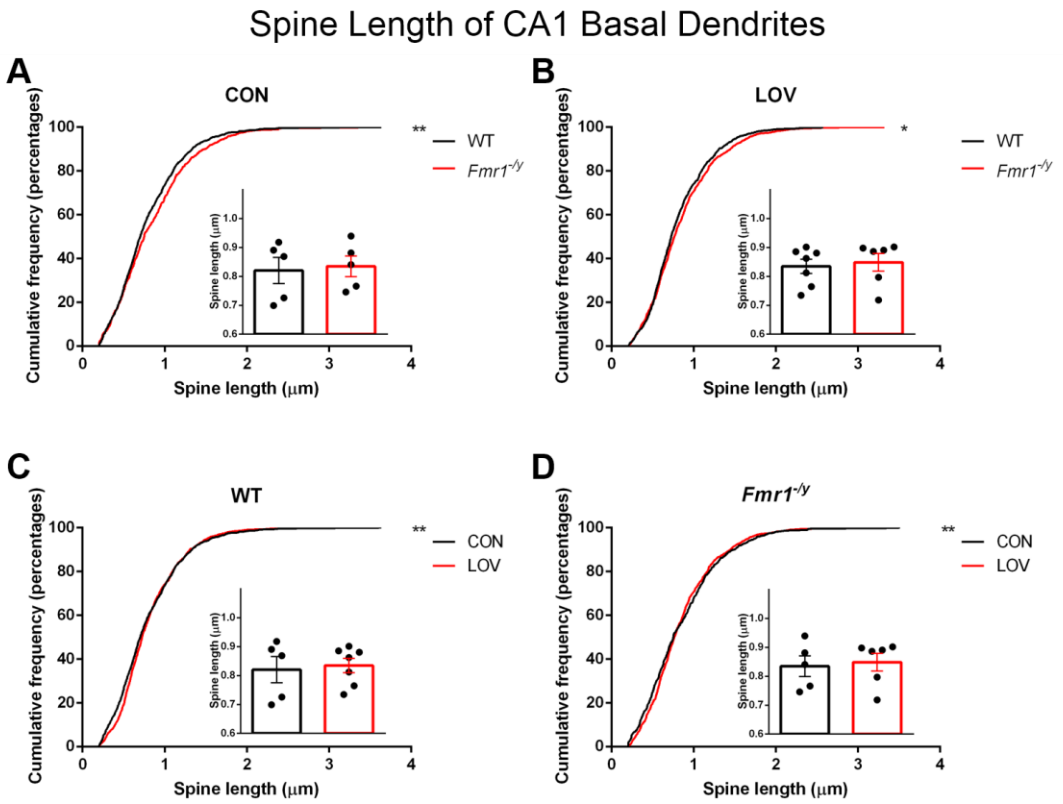

Figure 4-17. No gross changes of spine length were noticed in the CA1 basal dendrites from the two genotypes before or after LOV treatment.

Statistics and figure compositions are the same as shown in Fig. 4-12. Control chow treated animals are shown in (A), where *Fmr1*$^{-/y}$ mice and WT mice are marked with red and black, respectively. LOV treated animals are shown in (B), where *Fmr1*$^{-/y}$ mice and WT mice are marked with red and black, respectively. In (C), WT animals treated with CON or LOV are shown in black or red, respectively. In (D), *Fmr1*$^{-/y}$ animals treated with CON or LOV are shown in black or red, respectively. The dots in the right small panel represent each individual animal. CON-WT: n = 5; LOV-WT: n = 7; CON-*Fmr1*$^{-/y}$: n = 5; LOV-*Fmr1*$^{-/y}$: n = 6.

There were no overall mean spine length changes in the CA1 basal dendrites throughout the experiment. Under normal conditions (i.e., animals receiving CON

treatment), the spine length in the *Fmr1*$^{-/y}$ mice was significantly increased compared to the WT controls when looking at the cumulative frequency distributions (Fig. 4-17A, $p = 0.007$, K-S test; $p = 0.8107$, unpaired two-tailed Student's *t*-test). The increase of spine length in the *Fmr1*$^{-/y}$ mice persisted after 10 days of LOV treatment (Fig. 4-17B, $p = 0.04$, K-S test; $p = 0.7243$, unpaired two-tailed Student's *t*-test). LOV treatment induced a subtle but significant increase in spine length in both genotypes, although the overall mean spine length remained unaltered (Fig. 4-17C, $p = 0.0024$, K-S test, $p = 0.7731$, unpaired two-tailed Student's *t*-test; Fig. 4-17D, $p = 0.0054$, K-S test; $p = 0.7737$, unpaired two-tailed Student's *t*-test).

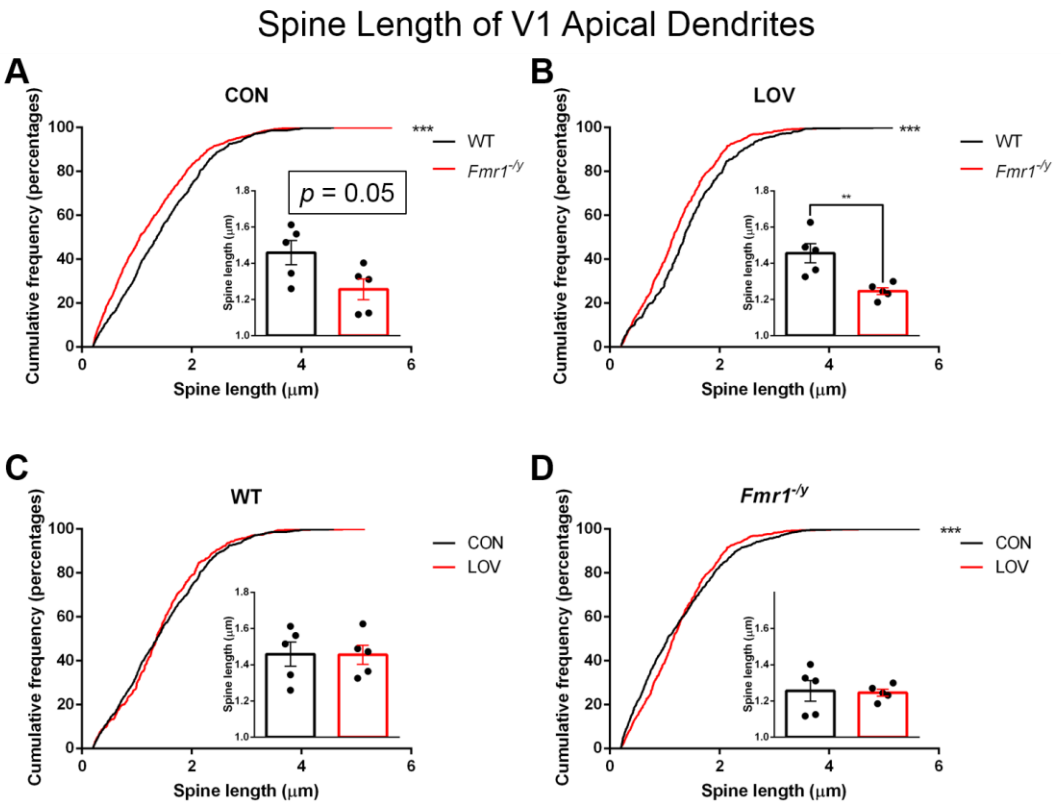

Figure 4-18. A significant increase of spine length in the V1 apical dendrites of the WT mice was noticed compared to the *Fmr1*$^{-/y}$ mice after 10 days of LOV treatment.

Statistics and figure compositions are the same as shown in Fig. 4-12. Control chow treated animals are shown in (A), where *Fmr1*$^{-/y}$ mice and WT mice are marked with red and black, respectively. LOV treated animals are shown in (B), where *Fmr1*$^{-/y}$ mice and WT mice are marked with red and black, respectively. In (C), WT animals treated with CON or LOV are shown in black or red, respectively. In (D), *Fmr1*$^{-/y}$ animals treated with CON or LOV are shown in black or red, respectively. The dots in the right small panel represent each individual animal. CON-WT: $n = 5$; LOV-WT: $n = 5$; CON-*Fmr1*$^{-/y}$: $n = 5$; LOV-*Fmr1*$^{-/y}$: $n = 5$.

The dendritic spine length in the V1 apical dendrites was significantly reduced in the *Fmr1*$^{-/y}$ mice under both CON and LOV treatment when comparing to their WT littermates (Fig. 4-18A, $p < 0.0001$, K-S test; $p = 0.0510$, unpaired two-tailed Student's *t*-test; Power = 0.53, at least 9 animals per group will be needed if aiming to reach 0.8 in Power; Fig. 4-18B, $p < 0.0001$, K-S test; $p = 0.0058$, unpaired two-tailed Student's *t*-test; Power = 0.90). Unlike CA1 apical dendrites, LOV treatment did not cause any gross changes on spine length of the V1 apical dendrites of the WT mice (Fig. 4-18C, $p = 0.13$, K-S test; $p = 0.9704$, unpaired two-tailed Student's *t*-test). However, LOV treatment caused a mild but significant increase in spine length in the V1 apical dendrites of the *Fmr1*$^{-/y}$ mice (Fig. 4-18D, $p < 0.0001$, K-S test; $p = 0.8702$, unpaired two-tailed Student's *t*-test).

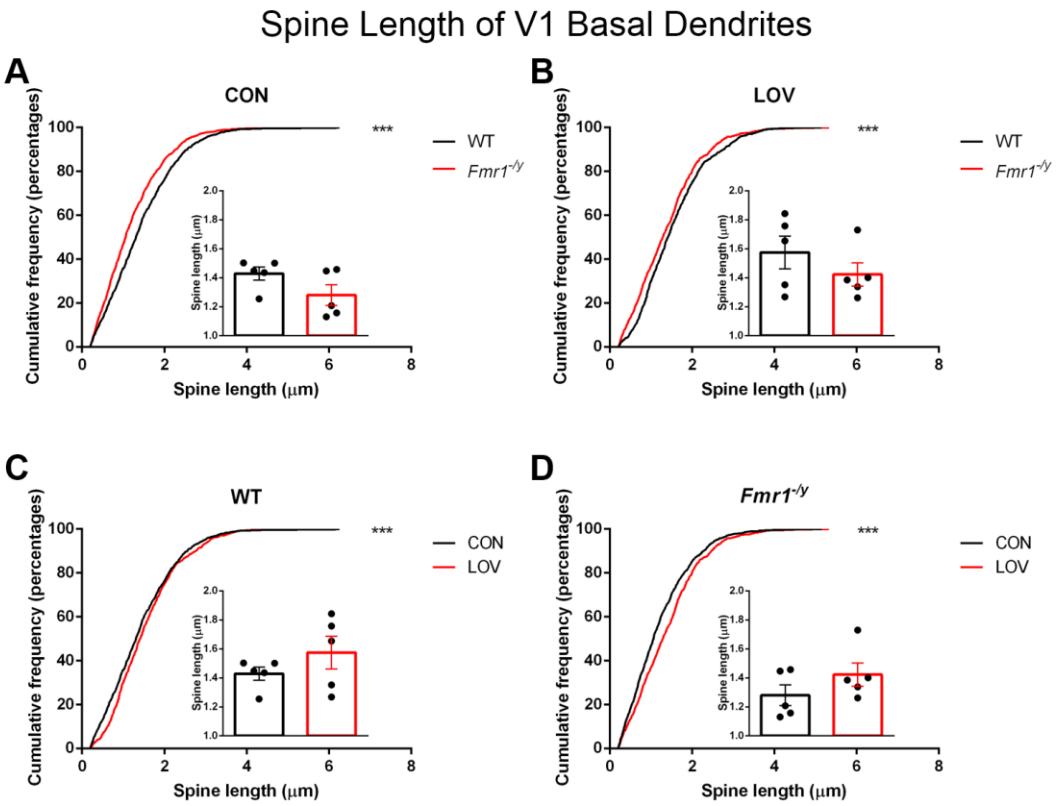

Figure 4-19. The spine length of the V1 basal dendrites was significantly reduced in the *Fmr1*$^{-/y}$ mice.

Statistics and figure compositions are the same as shown in Fig. 4-12. Control chow treated animals are shown in (A), where *Fmr1*$^{-/y}$ mice and WT mice are marked with red and black, respectively. LOV treated animals are shown in (B), where *Fmr1*$^{-/y}$ mice and WT mice are marked with red and black, respectively. In (C), WT animals treated with CON or LOV are shown in black or red, respectively. In (D), *Fmr1*$^{-/y}$ animals treated with CON or LOV are shown in black or red, respectively. The dots in the right small panel represent each individual animal. CON-WT: n = 5; LOV-WT: n = 5; CON-*Fmr1*$^{-/y}$: n = 5; LOV-*Fmr1*$^{-/y}$: n = 5.

The spine length of the V1 basal dendrites was significantly reduced in the *Fmr1*$^{-/y}$ mice under either CON or LOV treatment when comparing to the WT controls (Fig. 4-19A, $p < 0.0001$, K-S test; $p = 0.1174$, unpaired two-tailed Student's *t*-test; Fig. 4-19B, $p < 0.0001$, K-S test; $p = 0.3053$, unpaired two-tailed Student's *t*-test). LOV treatment for 10 days induced a slightly increased spine length in the V1 basal dendrites in both genotypes (Fig. 4-19C, $p = 0.0003$, K-S test; $p = 0.2644$, unpaired two-tailed Student's *t*-test; Fig. 4-19D, $p < 0.0001$, K-S test; $p = 0.2203$, unpaired two-tailed Student's *t*-test).

In summary, my quantitative analysis of spine morphology suggests that 1) dendritic spine head size was increased in CA1 apical dendrites of the *Fmr1*$^{-/y}$ mice compared to WT controls (Fig. 4-12A); 2) LOV treatment increased spine head diameter of the CA1 apical dendrites of the WT mice to a similar size found in the *Fmr1*$^{-/y}$ mice (Fig. 4-12B and 4-12C). A similar effect was found for V1 apical and basal dendrites, where an increase of spine head diameter in the LOV treated WT animals were noticed (Fig. 4-14C and 4-15C). 3) LOV treatment did not significantly alter the size of dendritic spines in the *Fmr1*$^{-/y}$ mice (Fig. 4-12D, 4-13D, 4-14D, and 4-15D). 4) Dendritic spine length was largely unaffected by genotype and treatment; an increase of spine length was noticed in the CA1 apical dendrites of the *Fmr1*$^{-/y}$ mice compared to the WT controls under CON treatment (Fig. 4-16A). However, an opposite effect was also noticed when sampling from the V1 apical dendrites, where the WT controls had longer spines than the *Fmr1*$^{-/y}$ mice (Fig. 4-18A and 4-18B).

4.3.4 LOV treatment did not alter the basal protein expression of ERK and pERK in WT and *Fmr1*$^{-/y}$ mice.

A similar study published by Osterweil *et al*. found that the LOV treatment reduced the excessive protein synthesis in the *Fmr1*$^{-/y}$ mice to WT levels (Osterweil et al., 2013). This was specifically due to the inhibition of the Ras-ERK pathway, as both lovastatin and a Ras antagonist farnesylthiosalicylic acid (FTS) reduced the excessive protein synthesis in the *Fmr1*$^{-/y}$ mice (Osterweil et al., 2013). Meanwhile, Osterweil *et al*. also reported that no difference was found in basal levels of Ras, ERK1/2, and pERK1/2 in hippocampal slices from the *Fmr1*$^{-/y}$ mice. Acute application of lovastatin significantly reduced ERK1/2 activation in both WT and *Fmr1*$^{-/y}$ slices (Osterweil et al., 2013). Thus, I examined ERK1/2 and pERK1/2 levels under the current LOV treatment by Western blotting. Hippocampi and visual cortices from both hemispheres were used for Western blotting in regard to where dendritic spines were analysed previously. No interactions were found between the genotype and treatment among all groups (Fig. 4-20A, $F_{(1, 14)} = 0.2557$, $p = 0.6210$; Fig. 4-20B, $F_{(1, 14)} = 0.4690$, $p = 0.5046$; Fig. 4-20C, $F_{(1, 12)} = 0.5622$, $p = 0.4678$; Fig. 4-20D, $F_{(1, 12)} = 1.110$, $p = 0.3128$). LOV treatment did not affect the ERK1/2 and pERK1/2 expression among all regions examined (Fig. 4-20A, $F_{(1, 14)} = 0.5442$, $p = 0.4729$; Fig. 4-20B, $F_{(1, 14)} = 0.08089$, $p = 0.7803$; Fig. 4-20C, $F_{(1, 12)} = 0.0005485$, $p = 0.9817$; Fig. 4-20D, $F_{(1, 12)} = 1.139$, $p = 0.3068$). Similarly, genotype did not cause an effect on both the ERK1/2 and pERK1/2 expression in CA1 and V1 (Fig. 4-20A, $F_{(1, 14)} = 0.2043$, $p = 0.6582$; Fig. 4-20B, $F_{(1, 14)} = 0.01990$, $p = 0.8898$; Fig. 4-20C, $F_{(1, 12)} = 0.1564$, $p = 0.6994$; Fig. 4-20D, $F_{(1, 12)} = 0.4403$, $p = 0.5195$).

My results suggest that no difference in basal levels of ERK1/2 and pERK1/2 are found between the *Fmr1*$^{-/y}$ mice and WT controls, which agreed well with previous findings. Moreover, 10 days of lovastatin treatment does not alter the ERK1/2 and pERK1/2 levels in both the *Fmr1*$^{-/y}$ mice and WT controls.

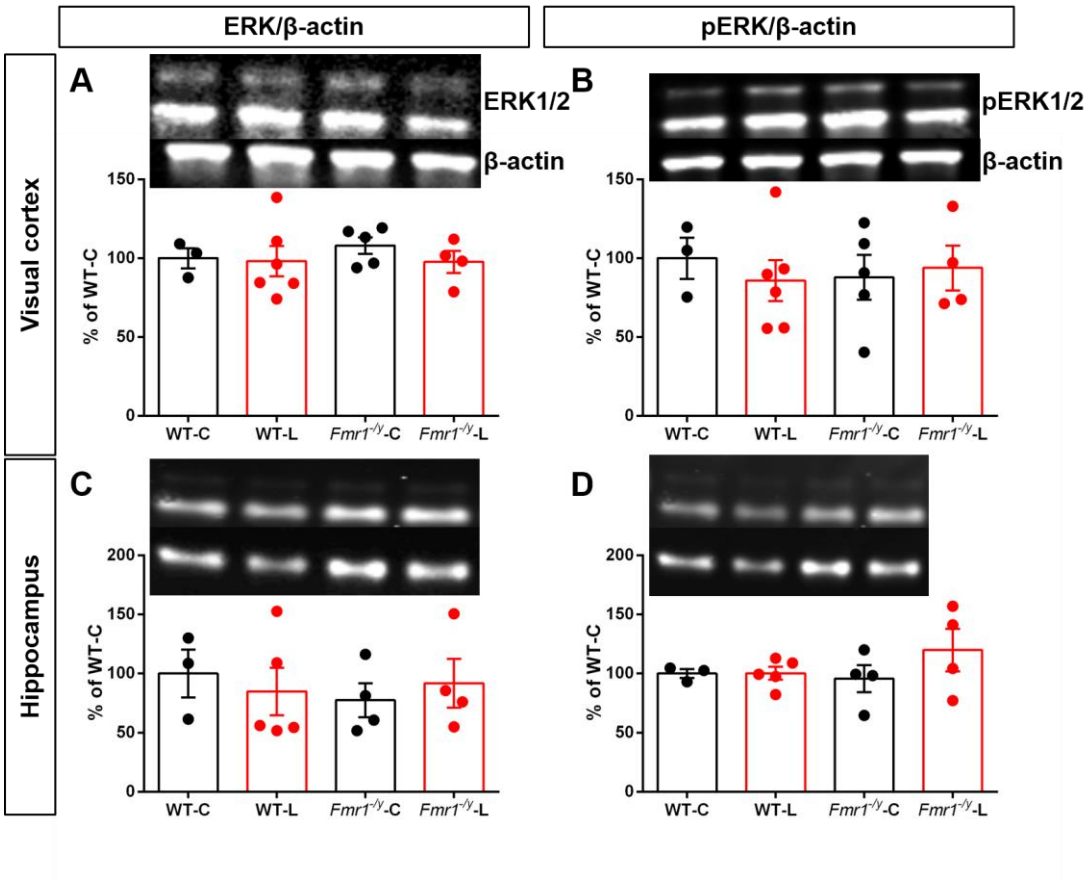

Figure 4-20. Downstream protein markers were unaltered after LOV treatment in both genotypes.

Two protein markers downstream the mGluR-signalling were analysed by Western blotting. Representative Western blot images are shown on top and their relative quantification are shown at the bottom of each figure. ERK1/2 and pERK1/2 protein levels remains unaltered before and after the LOV treatment for 10 days. Data were analysed by using Two-way ANOVA. Number of dots of each bar represents the number of animals used. WT-C: $n = 3$; WT-L: $n = 5$; *Fmr1*$^{-/y}$-C: $n = 4$; *Fmr1*$^{-/y}$-L: $n = 4$.

4.4 Discussion

My findings suggest that LOV treatment for 10 days did not alter the dendritic spine density in CA1 and layer II/III of the visual cortex from both of the *Fmr1*$^{-/y}$ mice and WT controls. Instead, an elevation of spine density was noticed in layer II/III apical dendrites of the visual cortex of the *Fmr1*$^{-/y}$ mice under the basal condition, which agreed with previous findings in the same region (Dölen et al., 2007). In contrast, a profound effect of lovastatin on spine morphology is noticed. Specifically, the spine head diameter was significantly enlarged in CA1 apical dendrites and both apical and basal dendrites in V1 of the WT animals treated with lovastatin. The *Fmr1*$^{-/y}$ mice exhibited an increase of spine head diameter in CA1 apical dendrites compared to WT animals under the basal condition (i.e., CON treatment), and LOV treatment failed to restore the enlarged spines of the *Fmr1*$^{-/y}$ mice to the WT level. Intriguingly, LOV treatment increases the spine head diameter of the CA1 apical dendrites of the WT mice to a similar size found in the *Fmr1*$^{-/y}$ mice, without altering the size of spine in the *Fmr1*$^{-/y}$ mice.

Dendritic spine length remains largely unaltered between the *Fmr1*$^{-/y}$ mice and WT animals. An increase of spine length is noticed in the CA1 apical dendrite of the *Fmr1*$^{-/y}$ mice. On the contrary, a decrease in spine length is noticed in both apical and basal dendrites in the V1 of the *Fmr1*$^{-/y}$ mice. Unlike the profound effect of increasing spine head diameter of the WT mice, spine length remains largely unaltered with regard to LOV treatment in both the *Fmr1*$^{-/y}$ mice and WT controls. Finally, ERK1/2 and pERK1/2 expression are not altered between the *Fmr1*$^{-/y}$ mice

and WT controls under basal conditions, and LOV treatment does not alter either protein expression as examined with Western blotting.

4.4.1 How does lovastatin regulate the Ras-ERK pathway?

As one of the members of the statin family, lovastatin was originally used as an antihyperlipidemic drug back in 1980s, which successfully reduced LDL cholesterol in healthy volunteers without any severe side effects (Tobert et al., 1982a, 1982b). Similar to other members of the statin family, lovastatin reduces cholesterol synthesis by inhibiting its key enzyme HMG-CoA reductase, causing a reduction of mevalonate, which is a precursor for cholesterol (Endo et al., 1977; Maron et al., 2000). However, two isoprenoid intermediates are also reduced during this process; the geranylgeranyl pyrophosphate (GGPP) and the farnesyl pyrophosphate (FPP) (Edwards, 1999). These two pyrophosphates not only participate in the cholesterol synthesis pathway but also are essential in the post-translational modification of proteins. Certain G-proteins such as Ras will only be activated after associating to the cell membrane, and this requires addition of lipid moieties by either farnesylation or geranylgeranylation (Higgins and Casey, 1996; Whyte et al., 1997).

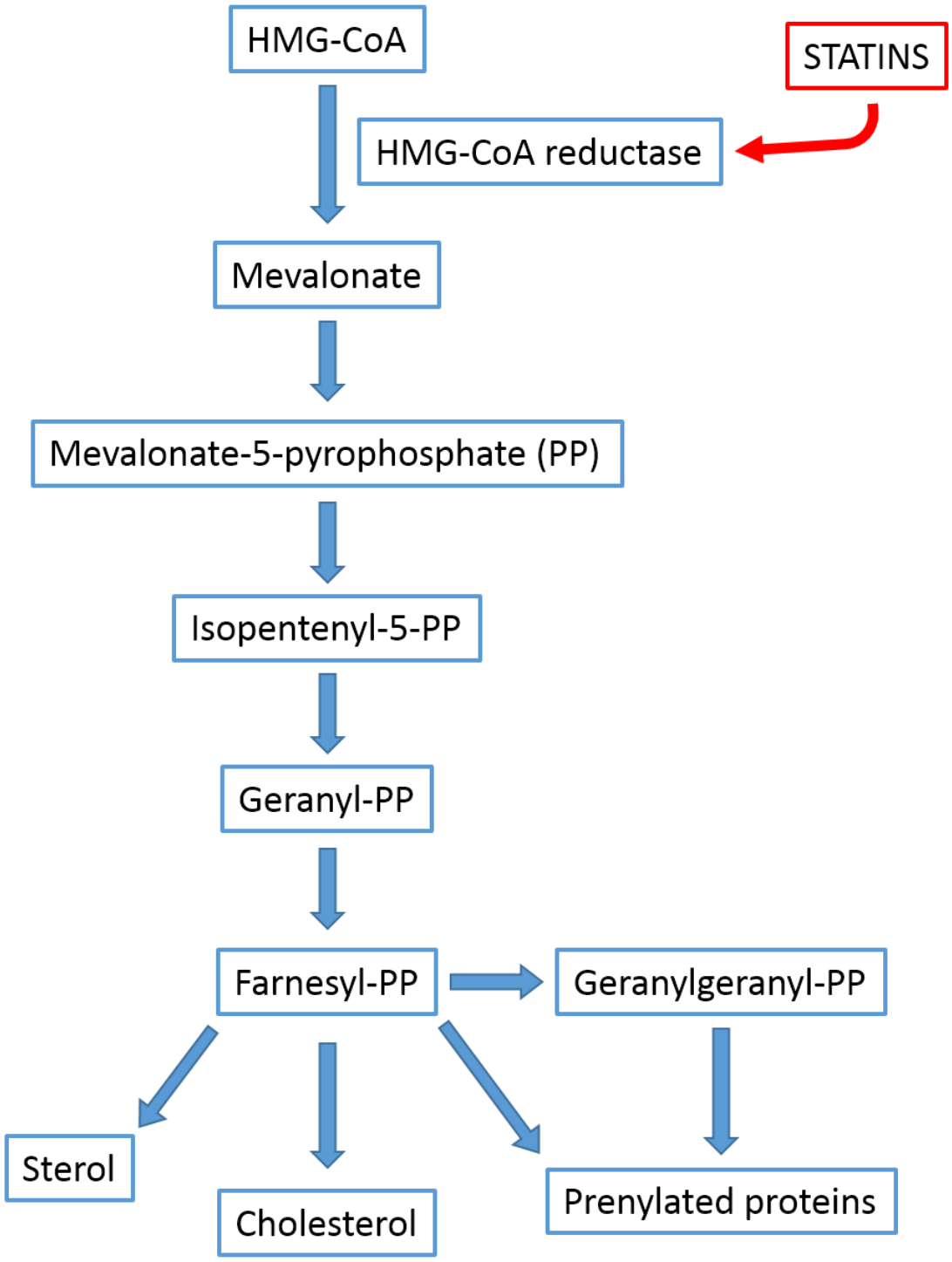

Figure 4-21. A simplified diagram of the cholesterol synthesise pathway.

HMG-CoA is the precursor of cholesterol synthesis. HMG-CoA reductase catalyses the production of mevalonate from HMG-CoA and acts as a rate-limiting enzyme for cholesterol synthesis. Statins

occupy the active site of HMG-CoA reductase, hence prevent HMG-CoA from binding to HMG-CoA reductase (Istvan and Deisenhofer, 2001). Mevalonate is then metabolised to farnesyl-PP by a series of enzymes along with some intermediates, including the mevalonate-5-PP, isopentenyl-5-PP, and geranyl-PP.

4.4.2 The possible therapeutic effects of lovastatin beyond lowering blood cholesterol.

An approach of using statins as a treatment for certain types of cancer has emerged in the early ’90s. Among that, Li *et al*. also started to use lovastatin as a treatment of NF1 (Li et al., 2005). The underlying mechanism of NF1 is an exaggerated Ras activity and eventually leads to an impairment of LTP, causing hyperactivity, learning disability and cognitive impairment in human patients and animal models (Costa et al., 2002; Koth et al., 2000; Ozonoff, 1999). More recently, another study was reported using lovastatin to successfully rescue some key phenotypes of the *Fmr1*$^{-/y}$ mice (Osterweil et al., 2013). However, the dendritic spine abnormalities found in the *Fmr1*$^{-/y}$ mice were not addressed in that study. Thus, in the current study I focused on the effect of lovastatin on rescuing dendritic spine abnormalities in *Fmr1*$^{-/y}$ mice.

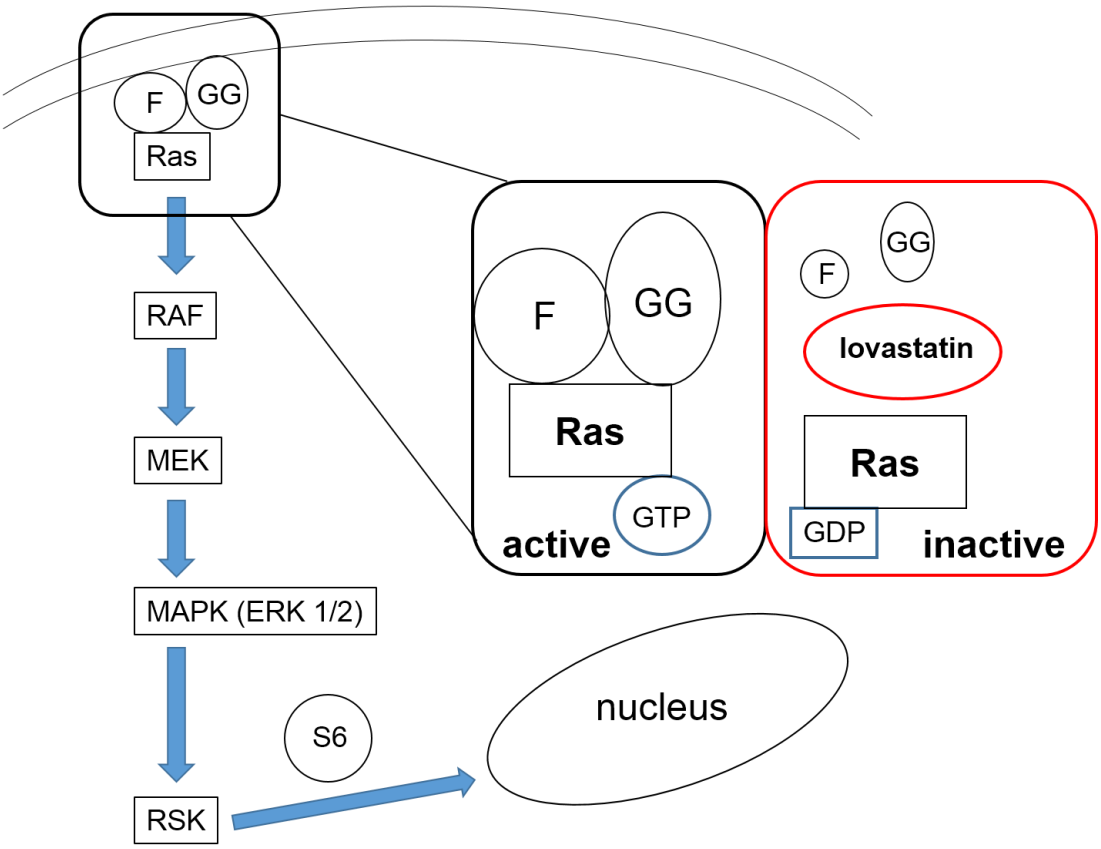

Figure 4-22. A simplified diagram showing how lovastatin reduces the activity of Ras-MAPK pathway.

Lovastatin reduces Ras activation through reducing intracellular levels of farnesyl-pyrophosphate (F) and geranylgeranyl- pyrophosphate (GG), which are both required for Ras anchoring to the plasma membrane in order to initiate its downstream signalling. The presence of lovastatin switches Ras from an active GTP-binding state to an inactive GDP-binding state through reducing the levels of F and GG, hence inhibits Ras-MAPK signalling. The Ras-MAPK signalling initiates when active Ras activates RAF, RAF then activates MEK, which in turn phorsphorylates and activates ERK. RSK is then activated by ERK, and in turn activates S6 which regulates mRNA translation and protein synthesis in an mTOR independent manner (Dhillon et al., 2007; Roux et al., 2007). Abbreviations: GDP: guanosine diphosphate; GTP: guanosine-5'-triphosphate; MAPK: mitogen-activated protein kinase; MEK: MAPK kinase; mTOR: mammalian target of rapamycin; RAF: rapidly accelerated fibrosarcoma; RSK: p90 ribosomal S6 kinase; S6: ribosomal protein S6

Table 4-1. A summary of dendritic spine abnormalities in different cortical layers and the hippocampus reported previously in *Fmr1*$^{-/y}$ mice.

	Age	Methods	Strains	Regions	Notes
Layer II/III					
1	P7 – P21	2P, *in vivo*	C57BL/6	Barrel Cx	D: normal L: normal High turnover at P10 – P12 Immature ↑
2	P14	2P, acute slices	C57	PFC	D: normal L: longer
3	P30	Golgi, fixed	C57	Visual Cx	D: higher
4	Adult	Golgi, fixed	C57	Temporal Cx	D: higher L: normal
5	Adult	Golgi, fixed	FVB	mPFC	D: higher L: longer
Layer IV					
6	P7, P14	Golgi, fixed	C57	Barrel Cx	D: normal
Layer V					
7	P7 – P21	2P, fixed	FVB	Barrel Cx	D: higher at P7; normal at P14 & P30 L: longer at P7 & P14; normal at P30
8	P2 + 5 DIV	2P, cultured slices	FVB	Barrel Cx	D: normal L: normal

					Motility: normal
9	Adult	Golgi, fixed	C57	Visual Cx	D: higher L: longer Immature ↑
10	Adult	Golgi, fixed	FVB	Visual Cx	D: normal Immature ↑
11	Adult	Golgi, fixed	C57	Visual Cx	D: higher Immature ↑
12	Adult	Golgi, fixed	C57	Visual Cx	D: normal Filopodia ↑; mushroom ↓
13	P25; Adult	Golgi, fixed	C57	Barrel Cx	D: higher in adults; normal at P25 L: longer in adults; normal at P25 Immature ↑
Hippocampus					
14	P0 + 7 DIV or 21 DIV	DiI, fixed	FVB	Dissociated	D: lower Length: normal
15	P0 + 16 DIV	FITC-phalloidin, fixed	C57	Dissociated	D: higher Immature ↑
16	E15/16 + 14 DIV; P7	*In vitro* GFP, fixed	FVB	CA1 & CA3	L: longer at P7 Immature ↑
17	P6/7 + 4 – 5 DIV	2P, cultured slices, fixed	C57		D: normal
18	E18 + 21 DIV	mCherry, fixed	C57	Dissociated	D: normal Filopodia ↑

19	P60 – P90	Golgi, fixed	C57	CA1	D: higher Immature ↑

Cx: cortex; D: spine density; DIV: days *in vitro*; EM: electron microscopy; FITC: fluorescein isothiocyanate; GFP: green fluorescent protein; L: spine length. Adopted from (Portera-Cailliau, 2012). Ref. 1): (Cruz-Martín et al., 2010); 2): (Meredith et al., 2007); 3): (Dölen et al., 2007); 4): (Hayashi et al., 2007); 5): (Liu et al., 2011); 6): (Harlow et al., 2010); 7) & 8): (Nimchinsky et al., 2001); 9): (Comery et al., 1997); 10): (Irwin et al., 2002); 11): (McKinney et al., 2005); 12): (Restivo et al., 2005); 13): (Galvez and Greenough, 2005); 14): (Braun and Segal, 2000; Segal et al., 2003); 15): (Antar et al., 2006); 16): (Bilousova et al., 2009); 17): (Pfeiffer and Huber, 2007); 18): (de Vrij et al., 2008); 19): (Grossman et al., 2006)

4.4.3 Dendritic spine abnormalities in *Fmr1*$^{-/y}$ mice.

The current findings regarding the changes of spine density and morphology in the *Fmr1*$^{-/y}$ mice are controversial (Table 4-1). Depending on different brain regions and various cortical layers composition, loss of FMRP can lead to very different outcomes. The results may also vary depending on how the tissues were sampled (i.e., fixed or unfixed), methodologies used (e.g., Golgi staining, fluorescent labelling), and the developmental stages chosen.

Consistent with some previous findings, the dendritic spine density in the apical dendrites of the visual cortex was significantly increased in the *Fmr1*$^{-/y}$ mice compared to the WT littermates (Comery et al., 1997; Dölen et al., 2007; McKinney et al., 2005). LOV treatments failed to rescue this phenotype; however, through increasing the spine density in the WT by about 12% with changing only 1% in the *Fmr1*$^{-/y}$ mice, the increased spine density in the *Fmr1*$^{-/y}$ mice was diminished.

I noticed a significant increase of spine head diameter in the CA1 apical dendrites of the *Fmr1*$^{-/y}$ mice compared to WT controls under CON treatment, and this difference was diminished when both groups were treated with lovastatin. Meanwhile, LOV treatment showed a dramatic impact on increasing spine head diameter in the WT mice in various regions, including the CA1 apical, V1 apical, and V1 basal dendrites. On the contrary, LOV treatment did not show significant changes of the mean spine head diameter in the *Fmr1*$^{-/y}$ mice in the same regions where significant changes were shown in the WT mice.

4.4.4 The possible mechanism of how lovastatin regulates spine morphology in mice.

The fact that LOV treatment seems to have a profound effect on spine morphology is surprising; however, this effect is limited to the WT animals only and no gross alterations have been found in the *Fmr1*$^{-/y}$ mice treated with lovastatin. One possible explanation of how lovastatin regulates dendritic spine morphology is that statins are known to suppress the expression of CSPGs (Holmberg et al., 2008), which suppress spine formation in cortical neurons (Kurihara and Yamashita, 2012). This might explain the slight increase of spine density in the V1 apical dendrites of the WT mice after LOV treatment, but why spine density remained unaltered after LOV treatment in the *Fmr1*$^{-/y}$ mice is still unclear. The relationship between CSPGs and FXS is poorly understood, and further evidence will be needed to elucidate the different response to LOV treatment in the *Fmr1*$^{-/y}$ mice and WT controls.

4.4.5 The relationship between spine morphology and synapse compartmentalisation.

As spine morphology is closely related to synapse compartmentalisation (Svoboda et al., 1996; Wijetunge et al., 2014; Yuste, 2013), the morphological changes of spines after LOV treatment may imply an overall change in local signal propagation in the designated brain regions.

In a detailed review by Rafael Yuste in 2013, he described spine compartmentalisation as follows:

"…spines can behave as separate electrical compartments, by demonstrating that the somatic amplitude of the potentials generated by activating a spine was inversely proportional to the length of its spine neck (Araya et al., 2006). Thus, whereas spines with short necks generated larger somatic potentials, those with long necks generated smaller, or even undetectable, depolarisations" (Yuste, 2013).

However, due to the limit of resolution of the confocal microscopy (roughly 180 nm in the X-Y plane), I do not have a precise measurement of the dendritic spine neck width, which is the most crucial factor regarding compartmentalisation (Tønnesen et al., 2014). In addition, spine neck length has also been proved to be essential to electrical compartmentalisation. A reverse linear relationship of spine neck length and the amplitude of uncaging potentials at the soma has been reported, and it is independent of the size of the spine head (Araya et al., 2006). Thus, the reduced spine length in the visual cortex of the *Fmr1*$^{-/y}$ mice may suggest an increase

in electrical compartmentalisation compared to the WT mice. Given the fact that the size of spine head in the visual cortex was not significantly altered between the two genotypes, the increased spine length was likely to be attributed mainly to the neck length. To elucidate our speculation on spine neck changes after LOV treatment, a higher power microscopy such as STED will be needed in the future.

One possibility that LOV treatment had a more profound impact on the WT mice might be that the dosage of lovastatin given was not sufficient to cause any effects in the *Fmr1*$^{-/y}$ mice. However, the dose of lovastatin we chose was consistent with previous literature and it has been shown that this dosage can rescue audio-genic seizure after only 48 hr of oral administration (Osterweil et al., 2013). To further verify the effectiveness of the LOV treatment, I performed several Western blot experiments to examine specifically the MAPK activity in the *Fmr1*$^{-/y}$ and WT mice. Unlike previous *in vitro* findings, where lovastatin treatment reduces the MAPK activity in the WT mice by about 15% and causes a 20% reduction in the *Fmr1*$^{-/y}$ mice (Osterweil et al., 2013), my data suggested that LOV treatment did not show a profound reduction of MAPK activity *in vivo*. Similar experimental design using the *NF1*$^{+/-}$ mice suggested that consecutive administration of lovastatin (10 mg/kg, SC) for four days can reduce MAPK activity to the WT level. And oral administration of lovastatin (0.15 mg lovastatin into 200 mg pellets) can rescue the cognitive deficits of the *NF1*$^{+/-}$ mice when assessed with the lateralized reaction-time task (Li et al., 2005). However, despite the difference of lovastatin dosages used across studies, none of these experiments have examined the MAPK activity after

lovastatin administration “orally”, suggesting that the reduction of MAPK activity might not be easily observable when lovastatin was administered orally.

Another possibility why the current LOV treatment did not alter the MAPK activity was that I used a 10-day consecutive treatment, instead of a short-term drug administration. I chose to use a chronic lovastatin treatment as this mimicked the actual drug usage in humans. It would be beneficial to re-examine the MAPK activity after an acute oral administration of lovastatin for 48 hr, as this can provide us a better understanding of how lovastatin regulate the MAPK activity *in vivo*.

Chapter 5: The Intrinsic Inhibitory Network Difference in Two C57BL/6 Substrains of Mice

5.1 Introduction

Animal models are valuable for scientific research. Various animals ranging from *Drosophila* to chimpanzees contribute to the understanding of human diseases and facilitate our knowledge of the underlying mechanisms of the diseases. Mice are one of the most widely used animal models for studying human diseases for several reasons: highly reproductive, short life span, genetic manipulations are well-established, and as mammals they share many common anatomical and physiological traits with humans. More importantly, some of the symptoms we observed in human patients are reproducible in mouse models of the same disease, both behaviourally and physiologically.

The first inbred mouse strain was developed by a Harvard biologist Clarence Cook Little in 1909. This strain was known as DBA, which stands for the coat colour alleles dilute (D), brown (B), and non-agouti (A). Since then many mouse strains have been developed to suit specific research interests, such that there are currently more than 450 mouse strains available worldwide (Beck et al., 2000). Most of the mice used in scientific research are inbred (at least over 20 generations) to ensure they are genetically identical, thus each mouse from the same strain can be treated as an identical "replicate". Despite the fact that the diversity of mouse strains brings the opportunity to tackle particular questions, the phenotypic differences

between strains should be carefully considered before starting the experiment. For example, the C3H mouse strain suffers from retinal degeneration around P28 and therefore is not suitable for any experiments that requires vision-related tasks (Dunn, 1954; Sidman and Green, 1965). Thus, it is critical that researchers are aware of the phenotypical characteristics of the mouse strain that is used for their experiments, to avoid drawing any incorrect conclusions from their findings.

5.1.1 The origin of the two C57BL/6 substrains used in this Chapter

The C57BL/6 strain is considered as one of the most widely used inbred mouse strains in scientific research (Crawley et al., 1997). I focused on two popular substrains, the C57BL/6JOla and the C57BL/6J, to study their *in vivo* responses toward a specific visual stimulus. The C57BL/6JOla substrain mentioned in this thesis was originated from the Jackson Labs in 1948, later imported into UK by OLAC in 1974 and then acquired by Harlan Labs in 1985. Both OLAC and Harlan Labs kept this line inbred since it first separated from the Jackson Labs. Forty years of inbred breeding have led to some genetic deletions in this substrain, notably the gene encoding α-synuclein (*Scna*) (Specht and Schoepfer, 2001) and the gene encoding multimerin 1 (*Mmrn1*) (Reheman et al., 2010; Specht and Schoepfer, 2004). On the other hand, the C57BL/6J substrain has been distributed by Charles River UK since 1981, and they continually replenished their stock mice with the Jackson Labs. One genetic deletion has been noticed so far of the C57BL/6J substrain, the gene

encoding for the nicotinamide nucleotide transhydrogenase (*Nnt*) was found missing in mice originated from the Jackson Labs (Mekada et al., 2009). A detailed timeline of how the C57BL/6 substrains were distributed and maintained is listed below (Fig. 5-1).

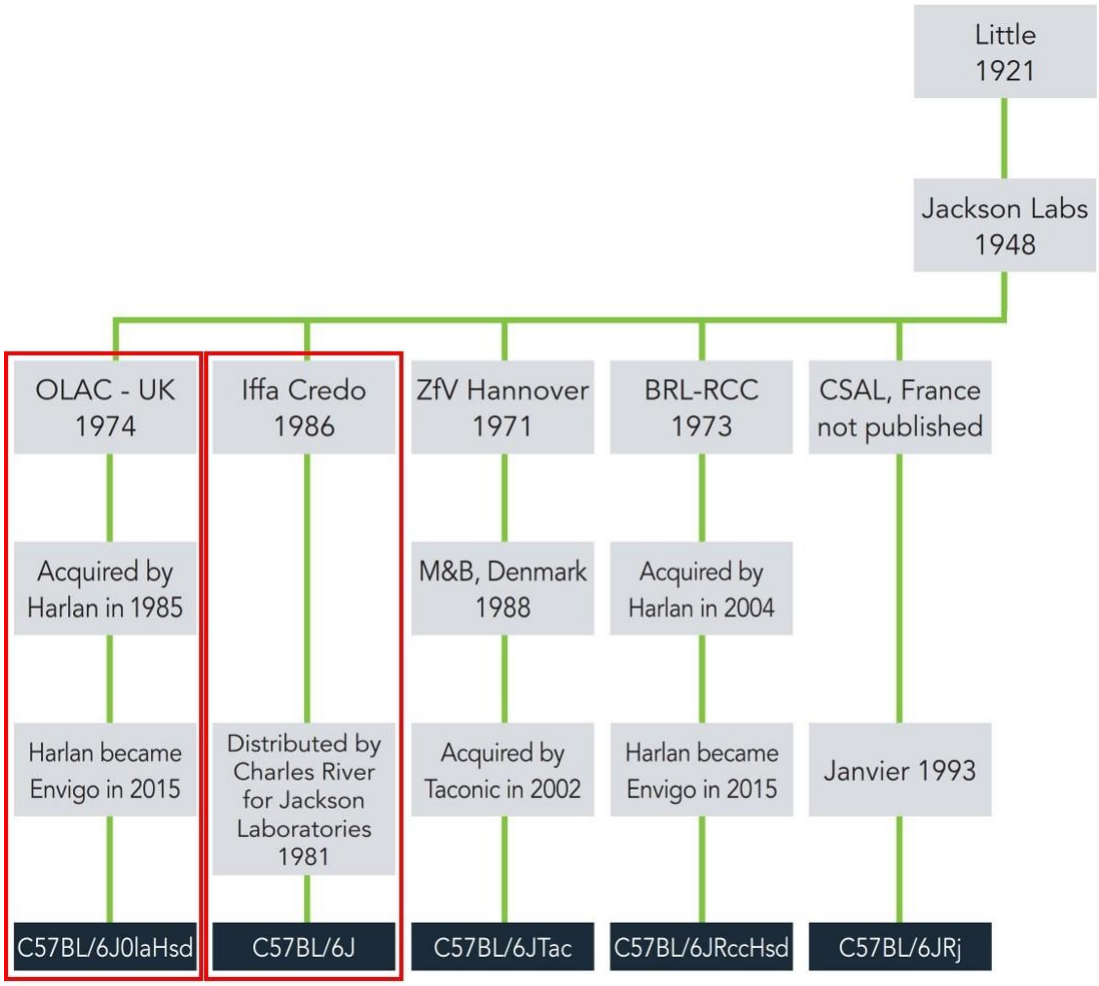

Figure 5-1. The origin of the two C57BL/6 substrains I used in this thesis.

This figure summarises the timeline and origin of the commonly used C57BL/6 substrains. The C57BL/6JOla (C57BL/6JOlaHsd as shown in the figure) and C57BL/6J substrains are marked with red boxes as they were used to study the stimulus-selective visual potentiation in this Chapter. Figure credit: Envigo UK. Available from: http://www.envigo.com/resources/data-sheets/envigo-68-c57bl6-enhanced-technical-data-sheet-a4_screen-eu.pdf

5.1.2 The loss of α-Synuclein in the C57BL/6JOla substrain

The work published by Ranson et al. indicated that the C57BL/6JOla mice lacked the open-eye potentiation response after being monocularly deprived for 5 – 6 days during the critical period, a phenomenon that can be seen in the C57BL/6J (Ranson et al., 2012). A lack of homeostatic plasticity in the C57BL/6JOla was then been proposed, while the intrinsic signal response and retinotopic map remained unaltered (Ranson et al., 2012). Thus, it is intriguing that the subtle background substrain difference can lead to such a distinct physiological response difference. In the work of Specht and Schoepfer they indicated that both the mRNA and the protein product of α-synuclein were not found in the C57BL/6JOla mice throughout their lifespan. Thus, a chromosomal deletion of the α-synuclein gene locus (*Scna*) was then suggested. Interestingly, the amount of another form of synuclein (β-synuclein) which is also abundant in the brain did not seem to compensate the loss of α-synuclein, as the authors did not find any alterations of its protein level through postnatal development (Specht and Schoepfer, 2001).

α-Synuclein is a protein initially recognised as a precursor for the non-β amyloid component of Alzheimer's disease (AD) amyloid plaques (Polymeropoulos et al., 1997; Uéda et al., 1993). It is mostly found located in the presynaptic terminals and while its precise function is still unknown, it is thought to facilitate amyloid plaques formation and aggregation and therefore accelerate the progression of AD (Han et al., 1995; Iwai et al., 1995; Jensen et al., 1997). α-Synuclein then was proposed to be essential as one of the known genetic mutations related to Parkinson's

disease (PD). A mutation within the α-synuclein gene was found in one large Italian kindred and three other independent Greek origin families with autosomal dominant inheritance for the PD phenotype (Polymeropoulos et al., 1997). Despite the fact that α-synuclein is involved in neurodegenerative disorders such as AD and PD, complete removal of either the mRNA or the protein product of α-synuclein gene in mouse does not show gross anatomical or physiological alterations (Abeliovich et al., 2000), which might be due to the compensation effect from another brain-rich isoform, β-synuclein, although the precise compensatory mechanism remains unclear.

It is intriguing that α-synuclein knockout C57BL/6JOla mice did not show homeostatic plasticity. Interestingly the loss of α-synuclein did not cause the loss of homeostatic plasticity as α-synuclein knock-out mice showed normal homeostatic plasticity after monocular deprivation (MD) (Ranson et al., 2012). To further our understanding of the differences in C57BL/6 substrains, I examined whether the C57BL/6JOla substrain has defects in another form of experience-dependent potentiation, namely stimulus-selective response potentiation (SRP). SRP is an experience-dependent visual plasticity that according to Frenkel *et al*. it is based on NMDA and α-amino-3-hydroxy-5-methyl-4-isoxazolepropionic acid (AMPA) receptors trafficking (Frenkel et al., 2006). This may not only uncover some unknown substrain characteristics of the C57BL/6JOla mice, but also help to shed some light on the underlying mechanism of the absence of homeostatic plasticity in this substrain.

In this Chapter, I examined the physiological responses within the primary visual cortex to a given visual stimulus in three different substrains of the C57BL/6

mice; C57BL/6J, C57BL/6JOla, and a mixture of these two substrains by crossing them for more than three generations (C57BL/6JaxOla). I focused on the C57BL/6J and the C57BL/6JOla substrains as these are the two most prevalent substrains used in the USA and Europe, respectively, and these strains have been the most commonly used models for neurodevelopmental disorders, including FXS. Furthermore, *Syngap*$^{+/-}$ mice will not breed on the C57BL/6J background but will breed effectively on the C57BL/6JOla background. Therefore prior to examining SRP in our models of FXS (on the C57BL/6J background) and *SYNGAP1* haploinsufficiency (on the C57BL/6JOla background), it was first necessary to characterise SRP on these two backgrounds to allow comparison between models of neurodevelopmental disorders.

5.2 Materials and methods

5.2.1 Animals

Two different backgrounds of C57BL/6 mice were used, C57BL/6JOla mice were purchased from Harlan Labs (Bicester, UK) and C57BL/6J were purchased from Charles River (Charles River UK, Ltd.). All mice were then backcrossed at least for 20 generations before use. A mixed background of these two substrains were created by crossing them for three generations. To be specific, F1 hybrid mice (i.e., the mixed background) were produced by crossing mice of these two different inbred strains (i.e., the C57BL/6J and the C57BL/6JOla). F1 males and females were then set up for inbreeding to get F2 animals, and F3 animals were acquired by

crossing F2 littermates. All mice have *ad libitum* access to food and water at all times through the experiment. Animals were kept in the animal unit located in the Hugh Robson Building (BRR-HRB, The University of Edinburgh) and kept under a 12 hr/12 hr light/dark cycle.

5.2.2 Stereotaxic surgery and electrode implantation

Mice were anesthetized by inhalation of isoflurane (1.5 – 2% in pure O_2). Depth of anaesthesia was carefully monitored throughout the whole surgery procedure via monitoring the respiration rate and hind-limb pinch withdrawal. A heating plate connected to a thermometer was used at all times during surgery to maintain the animal's body temperature. A subcutaneous injection of Buprenorphine (Vetergesic®; 0.05 mg/kg) was given prior to surgery. Surgical area was first cleaned with iodine and 70% ethanol, then the skull was exposed by removing the hair and skin above. For future head restraint purposes, a steel headpost was affixed to the skull at a position anterior to bregma with cyanoacrylate glue. Two small burr holes were drilled in the skull just anterior to bregma and overlaying the prefrontal cortex, and another two burr holes were drilled overlaying the binocular visual cortex (3.2 mm lateral of lambda; 3 mm was used for animals at P28). Two reference electrodes were implanted into the two burr holes anterior to bregma. Each one of the reference electrodes was custom made by soldering a silver wire with a gold wire contact (FST #19003-00). Two tungsten recording electrodes (FHC Tungsten Microelectrode, UEWSECSEBN1C, Ext. 2 mm/Epoxy 2 mm/7 mm Exp. w/ male pin, impedance within 0.4 – 0.5 MΩ) were implanted into the two burr holes overlaying the

binocular visual cortex at a depth of 470 μm (450 μm was used for animals at P28) below the cortical surface. All four electrodes were secured using cyanoacrylate glue and then reinforced with dental cement. Finally, the remaining skull was covered with dental cement to form a stable "head cap". Animals were put back in their home cages and kept warm with a thermal blanket to accelerate recovery and avoid death caused by loss of body heat. Jellies containing 0.5 mg/kg of Buprenorphine were given to animals for post-operative pain relief. Animals were monitored frequently for signs of discomfort or infection and allowed at least 24 hr recovery before proceeding habituation and further training. Animals showing signs of infection or significant weight loss after surgery would be removed from further experiment and humanely culled.

5.2.3 VEP recording

5.2.3.1 Visual stimulus

All visual stimuli were generated by a ViSaGe stimulus generator (ViSaGe MKII, Cambridge Research Systems, Kent, UK). Stimuli used in this experiment were full-field sine-wave gratings of 100% contrast (for the grey screen contrast was set to 0%), square reversing at 1 Hz and with a spatial frequency set at 0.05 cycles/degree. The display CRT monitor was positioned 20 cm in front of the mouse and aligned to the midline, in this case 92° × 66° of the visual field was covered.

5.2.3.2 SRP recording procedure

Animals were allowed to habituate to the head restraint apparatus for 30 min on the day prior to further chronic VEP recordings. To fit the animal into the restraint apparatus, its headpost was screwed tight with the apparatus and thus the head of the animal remained still but its body could move freely inside the holding cylinder (3.7 cm in diameter, close to the size of a toilet paper roll). The animal and the apparatus were then put in front of a CRT monitor at a distance of 20 cm. Animals remained still but alert at all times during the recording procedure. An isolated room was used for the VEP recording to minimize the background noise, and all room lights were turned off during recording.

During the habituation process a grey screen was first presented to the animal for 100 phase reversals, followed by 300 phase reversals using 0° sine-wave gratings of 100% contrast. Animals showing signs of distress (e.g., squeak, running) were first checked and if the distress signs continued animals were returned to their home cages temporarily and tested later. The next day, animals received 300 phase reversals at a random orientation of 100% contrast. Animals were then presented with the same stimuli for another four days. At Day 5, animals were first presented with the same stimuli then a novel orientation (orthogonal to the familiar stimulus used for previous recordings) was introduced to each animal six hours after the first session (D5N). According to the literature, SRP can induce robust and long-lasting VEP responses for the familiar stimulus after 5 days of training. Introducing a novel stimulus at the end of the SRP protocol would induce a VEP response similar to D1,

which indicates that SRP is stimulus-specific and mice are capable of discriminating different visual stimuli (Cooke and Bear, 2012; Frenkel et al., 2006).

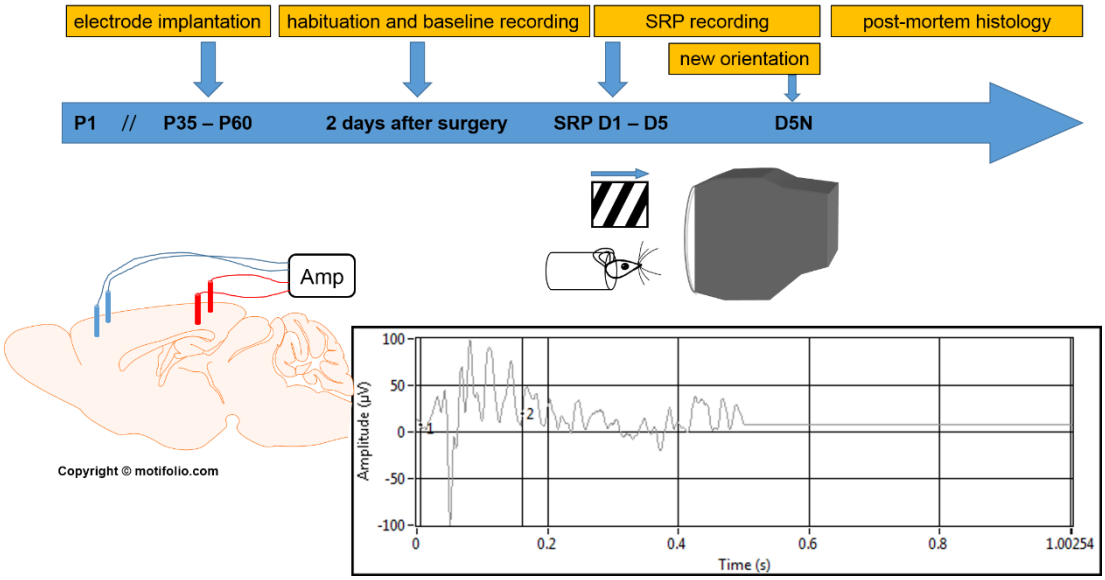

Figure 5-2. A representative diagram of experimental design and timeline for chronic VEP recording in mice.

The top panel of this diagram indicates the experimental timeline for this experiment. Young adult mice at the age around P40 – P60 were implanted with recording electrodes and then returned to their home cages. Animals were then habituated to the head restraint apparatus and a series of VEP recordings were performed once daily for 5 consecutive days. At Day 5, a novel orientation was introduced to each animal and the VEP responses were recorded accordingly.

5.2.4 Data acquisition and analysis

Electrical signals were amplified (1000×) and acquired via a USB board (NI USB-6251, National Instruments, TX, US). Data were first acquired and analysed using a custom software written in LabView (National Instruments, TX, US)

provided courtesy of the Maffei Lab (Pisa, Italy) and with the assistance of the Bear Lab (MIT, MA, US). Individual traces were then re-analysed and plotted with MATLAB with a script provided by Dr. Aleksander Domanski.

The amplitude of VEP was quantified by measuring the trough – peak response amplitude, as described previously (Frenkel and Bear, 2004; Sawtell et al., 2003). In general, animals were presented around 300 – 500 phase reversals of each oriented stimulus per day. The number of trials (1 trial contained 100 phase reversals of a given contrast and orientation) varied depending on animals' response to the presentation. If VEP responses varied over 15% between trials then additional trials were performed until at least 3 successful trials were acquired for each animal.

5.2.5 Histology

In order to mark the recording sites, animals were humanely culled via cervical dislocation followed by electrolytic lesions near the implantation sites. Electrolytic lesions were then conducted using a 9-V battery (MN1604, Duracell®, 2.1A) for roughly 1 – 2 sec. Brains were quickly removed and stored in ice-cold 4% PFA overnight. Brains were sliced into 50 µm coronal sections and rinsed thoroughly with PBS. Slices were then put on pre-coated slides and left in room temperature overnight. Next day, slides were rinsed with ddH_2O several times and then put into Nissl staining solution for 5 – 15 min followed by several rinses with 70% ethanol. Slides were then rinsed with 95% ethanol containing 0.1% glacial acetic acid, then dehydrated with 100% ethanol for 10 min. Finally, slides were

rinsed with xylene and then coverslipped with DPX (Sigma-Aldrich). A Leica upright microscope (DM5500 Capture) with an image acquisition software (AF6000 E) was then used for image acquisition.

5.3 Results

5.3.1 SRP was only inducible on the C57BL/6J substrain.

After electrode implantation, three groups of mice with different background substrains were chronically recorded for five days using the SRP protocol. As previously mentioned, the SRP protocol contained five consecutive recordings using the same visual stimulus over five days, and on Day 5 a novel stimulus was introduced around six hours after the previous recording session (D5N). The summarised results are shown in Fig. 5-3, where only mice on the C57BL/6J background showed a significantly potentiated VEP response through chronic recordings over five days (Fig. 5-3A, D1 vs. D5, $p = 0.0003$, unpaired two-tailed Student's *t*-test) and both the C57BL/6JOla group and the mix group were failed (Fig. 5-3B, D1 vs. D5, $p = 0.1554$; and Fig. 5-3C, D1 vs. D5, $p = 0.1314$, unpaired two-tailed Student's *t*-test). The potentiated response of the C57BL/6J mice was then diminished when animals were presented with a novel stimulus (D5N), which then drove the VEP response back to baseline (Fig. 5-3A, D5 vs. D5N, $p = 0.0018$; D1 vs D5N, $p = 0.0647$, unpaired two-tailed Student's *t*-test). This phenomenon is well established and recognised as the feature of SRP, which suggests the potentiated response is only related to the same familiar stimulus that we presented to the

animals chronically. I failed to induce SRP in the C57BL/6JOla substrain, and surprisingly, the mixed background also failed to show SRP after 3 generations of crossing (i.e., F3 animals).

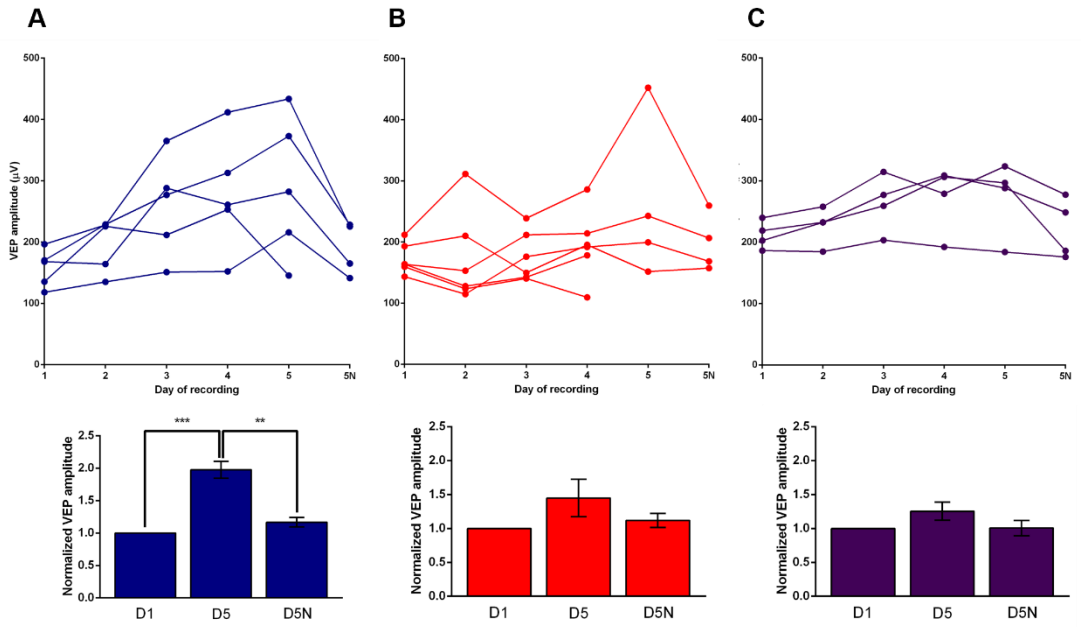

Figure 5-3. SRP cannot be established in the C57BL/6JOla or the mixed background mice.

Three different background substrains of mice were chronically recorded for 5 days using the SRP protocol. The C57BL/6J mice (A) showed clear SRP as the VEP amplitude gradually increased from Day 1 to Day 5. And then the VEP amplitude dropped back to baseline when a novel stimulus was presented on Day 5 six hours after the previous session (D5N). In contrast, only one C57BL/6JOla mouse showed SRP while all the remaining C57BL/6JOla (B) and mixed background mice (C) failed to show SRP after five days of training. VEP responses were first normalised to baseline (D1) and then quantified using unpaired two-tailed Student's *t*-test and the results are presented beneath each graph.

5.3.2 A distinct LFP power peak in the frequency ranges between 60 – 80 Hz was noticed in the C57BL/6JOla mice.

The failure to induce SRP in the C57BL/6JOla substrain along with the lack of homeostatic plasticity reported previously by Ranson *et al*. made me wonder if the basal cortical response of this substrain was different from the C57BL/6J substrain (Ranson et al., 2012). To characterise the cortical response to visual stimuli, I next examined the local field potential (LFP) and frequency power spectrum during the SRP protocols. By converting the raw VEP data with a customised MATLAB script (using multi-taper Fast Fourier Transform), I was able to analyse the LFP power and frequency of these animals. An example of transformed VEP data is presented in Figure 5-4, where the LFP power over frequency is shown combined with the original VEP amplitude distribution, to provide a better overview of the *in vivo* responses to the given visual stimuli (Fig. 5-4).

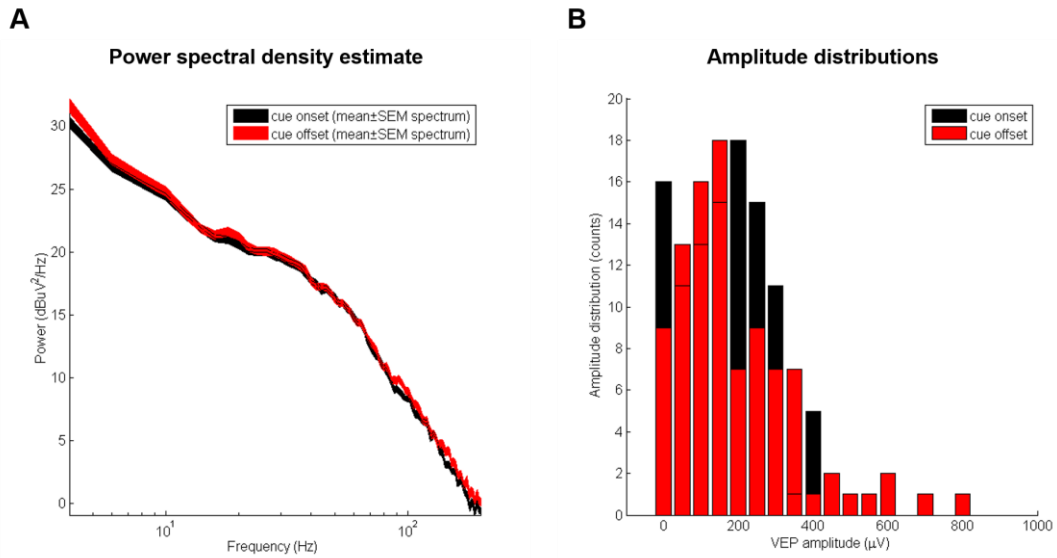

Figure 5-4. Representative figures of VEP power density estimate and amplitude distribution.

In (A), VEP responses were analysed as LFP and presented as its estimated power against its frequency. Total VEP amplitude distribution from the same trial is presented in (B). Black line and bars are VEP responses during the cue "on-set" phase, and cue "off-set" phase is indicated in red. "On-set" and "off-set" was used to indicate the phase reversal of the given visual stimuli.

Surprisingly while the general profile was very similar between the two substrains, there was a significant increase of LFP power in the gamma frequency of the C57BL/6JOla mice compared to the C57BL/6J mice. An example is shown in Figure 5-5, where an obvious elevation of LFP power in the gamma frequency was noticed in the C57BL/6JOla mice.

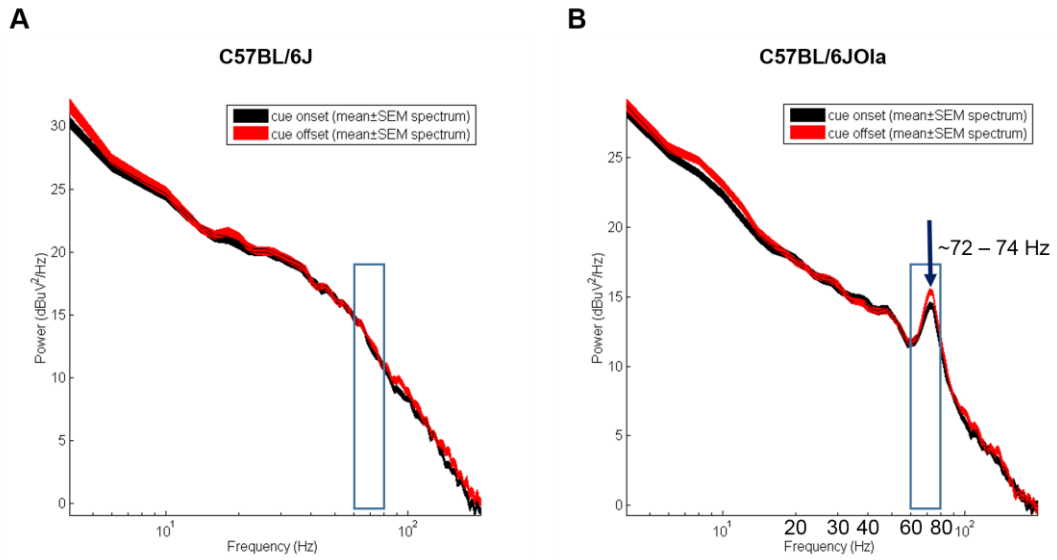

Figure 5-5. An example of the mean gamma power distribution between two substrains of the C57BL/6 mice.

The C57BL/6JOla mice showed a clear increased in LFP power near the frequency of 70 Hz with a noticeable peak at 72 – 74 Hz, which was inside the gamma range. On the contrary, the C57BL/6J mice did not show any peak in LFP power in the gamma range. The blue boxes indicate the frequency range between 60 – 80 Hz. VEP responses during the cue "on-set" phase and cue "off-set" phase are indicated in black and red, respectively.

With the data transformation tool my next goal was to compare the differences between the two C57BL/6 substrains. I therefore listed all experimental animals' data first to examine the individual difference then the group differences between the two substrains. All mice on the C57BL/6JOla background are shown in Figure 5-6, and a distinct LFP power peak was noticed during recordings from D1 of the SRP recording across all animals in the frequency range between 60 – 80 Hz (Fig. 5-6). On the contrary, no LFP power peak was observed when analysing the mice on

the C57BL/6J background (Fig. 5-7). A substrain phenotype was clearly noticed, thus we wanted to examine if the same phenomenon still existed if we crossed the substrains. Strikingly, after three generations of crossing the C57BL/6J and the C57BL/6JOla mice, the C57BL/6JaxOla mice showed a "reduced" LFP power peak in the gamma frequency compared to the C57BL/6JOla mice (Fig. 5-8).

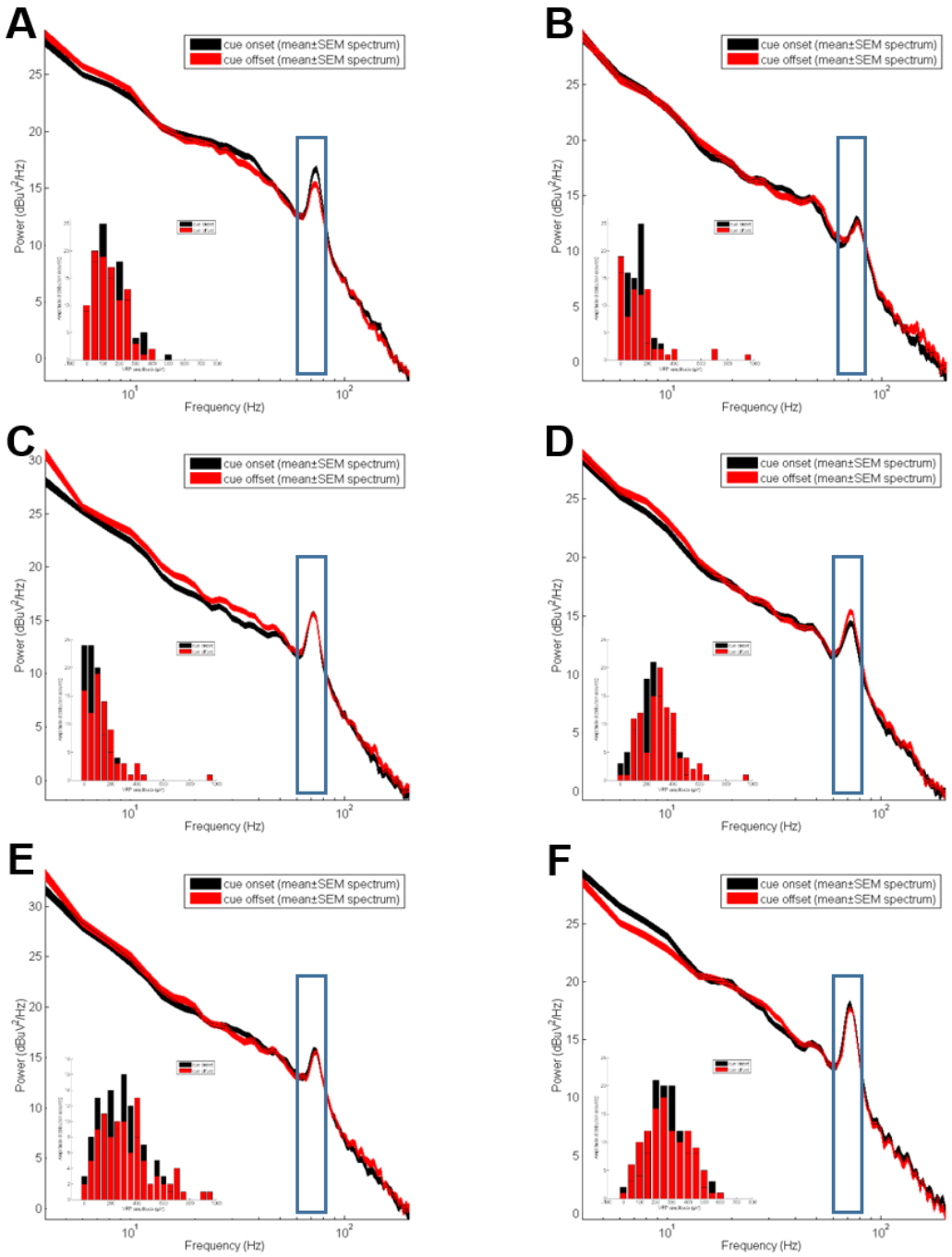

Figure 5-6. The gamma power distribution recorded from six C57BL/6JOla animals.

VEP amplitudes and LFP power recorded from six C57BL/6JOla mice of their first day of SRP are presented here (A – F). Mean gamma power recorded during cue on-set and off-set is shown in black and red, respectively. The overall VEP amplitudes for each animal during that session is also

presented in the bottom left corner of each individual animal. The blue boxes indicate the frequency range between 60 – 80 Hz. Data layout is identical as previously shown in Fig. 5-4.

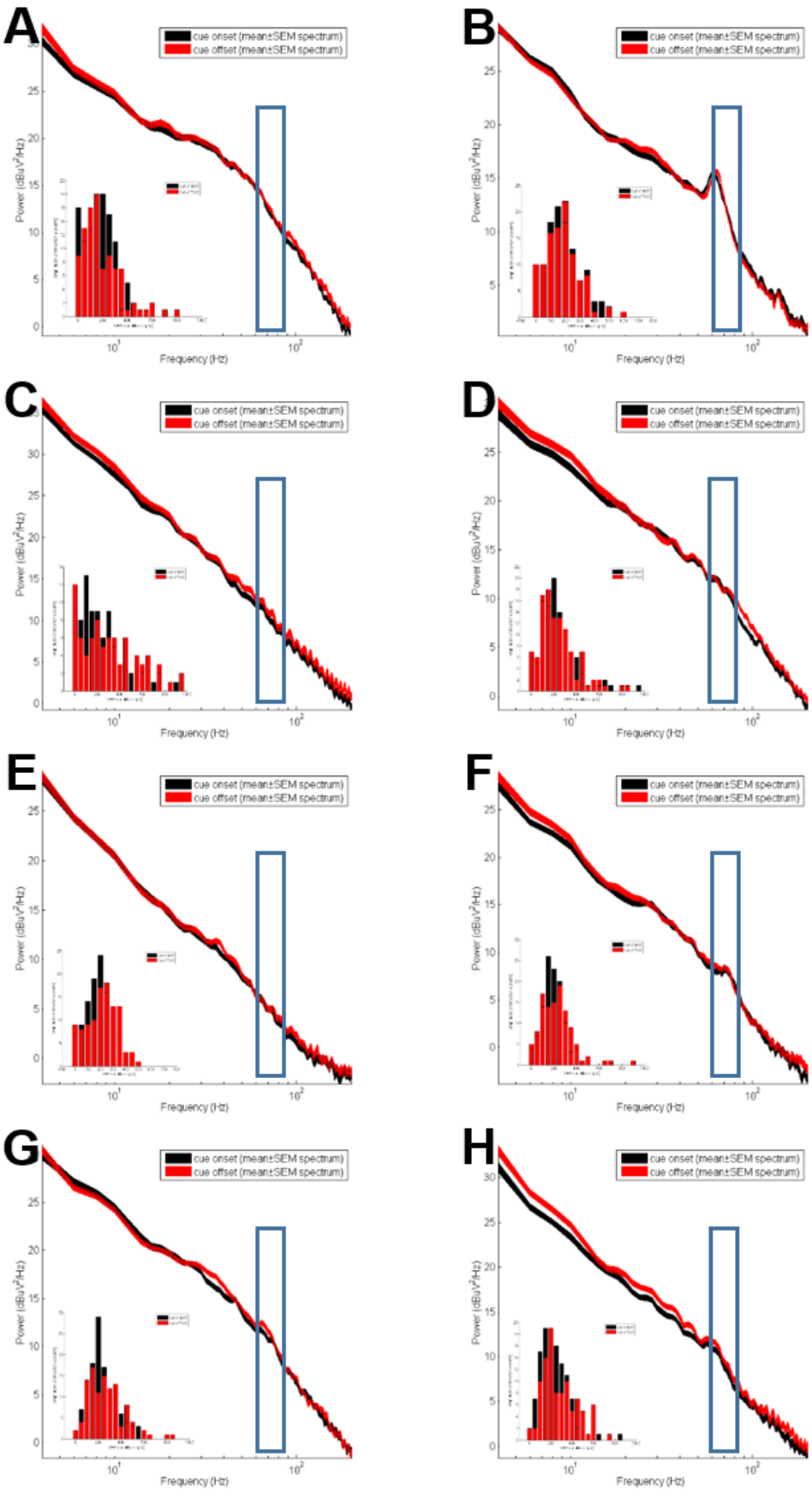
A
B
C
D
E
F
G
H
cue onset (mean±SEM spectrum)
cue offset (mean±SEM spectrum)
Power (dBuV²/Hz)
Frequency (Hz)

Figure 5-7. The gamma power distribution recorded from eight C57BL/6J animals.

Mean gamma power of SRP D1 recording session from eight C57BL/6J mice are presented here (A – H). Mean gamma power recorded during cue on-set and off-set is shown in black and red, respectively. The overall VEP amplitudes for each animal during that session is also presented in the bottom left corner of each individual animal. A lack of the LFP power peak in the high gamma frequency range (60 – 80 Hz) is noticed in all of the C57BL/6J mice compared to the C57BL/6JOla mice.

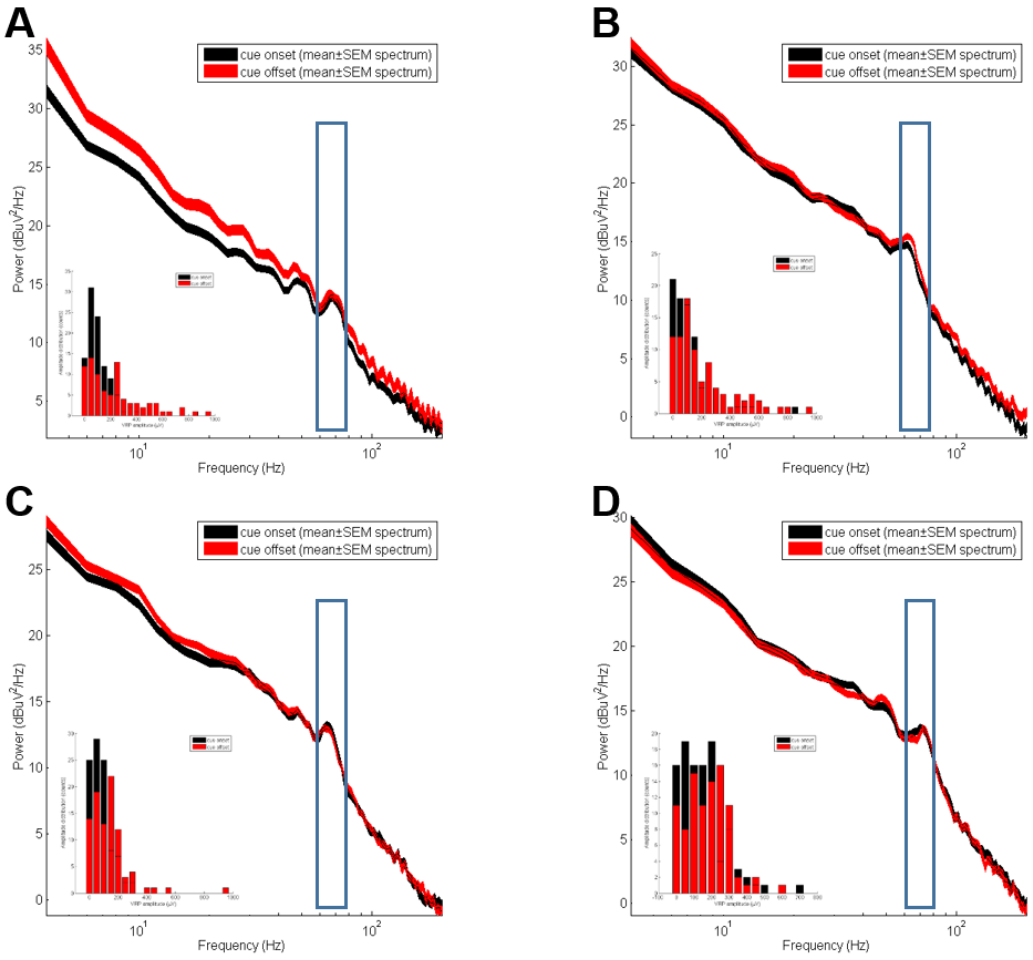

Figure 5-8. The gamma power distribution recorded from four C57BL/6JaxOla animals.

Similar to the findings reported previously in the C57BL/6J mice, four mice with the mix backgrounds are shown here and no obvious LFP power in the gamma frequency is noticed (A – D). Mean gamma power recorded during cue on-set and off-set is shown in black and red, respectively. The overall VEP amplitudes for each animal during that session is also presented in the bottom left corner of each individual animal.

5.3.3 Five days of SRP reduced the LFP power peak within the high gamma frequency range especially in the C57BL/6JOla mice.

I then examined the LFP power peak after 5 days of SRP experiment. Intriguingly, the power peak of the C57BL/6JOla mice was dramatically reduced compared to SRP D1 (Fig. 5-9 and 5-13). For the C57BL/6J and the C57BL/6JaxOla mice, due to their initial LFP power peaks being small they did not show any significant changes after 5 days of SRP (Fig. 5-10, 5-11, and 5-13). LFP power spectrum and VEP amplitudes of each individual animal are presented in Fig. 5-9 – 5-11, and detailed quantification and comparison between groups is presented in Fig. 5-13.

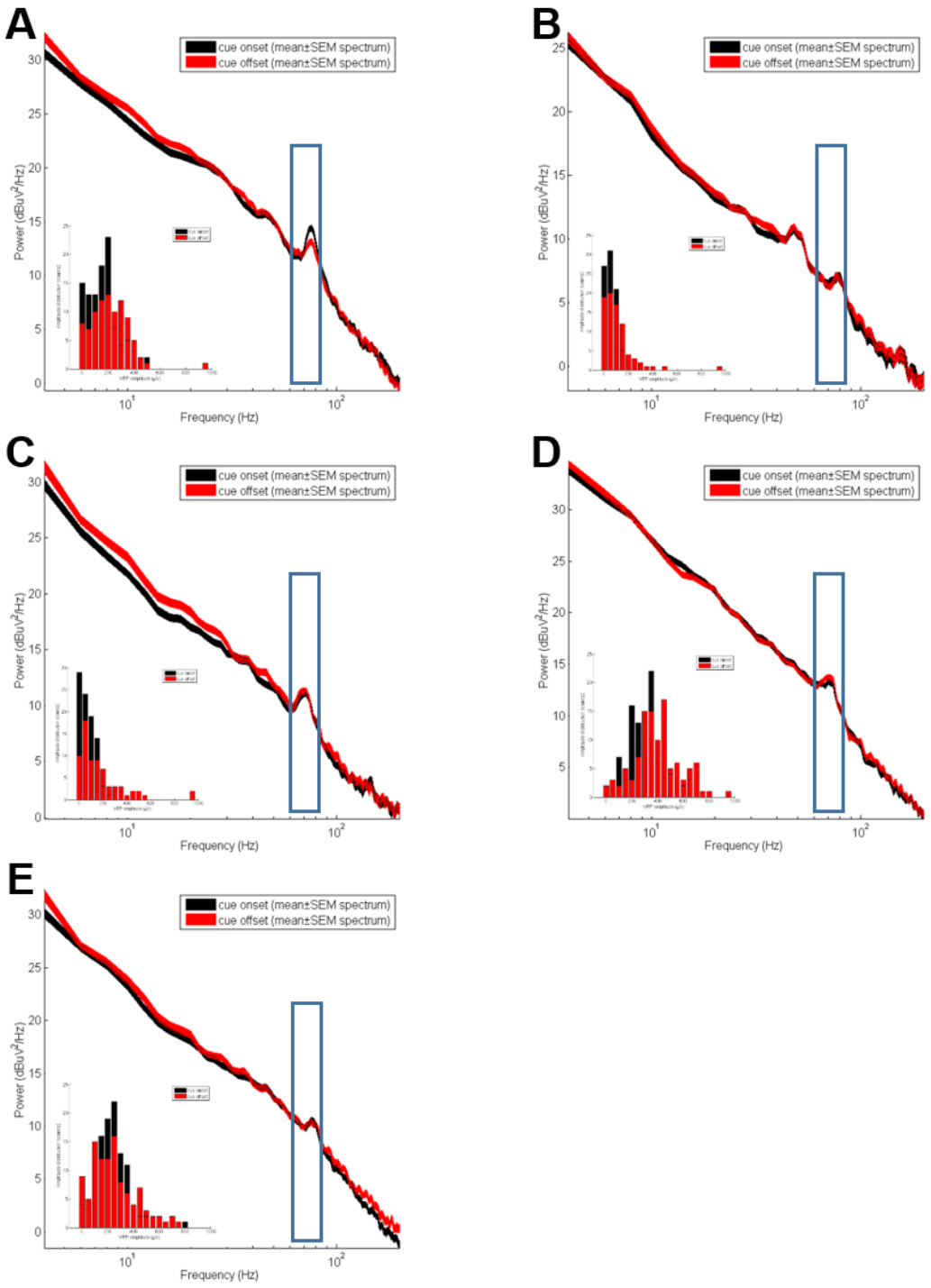

Figure 5-9. The gamma power distribution recorded from the same C57BL/6JOla animals after 5 days of SRP.

The LFP power peak in the gamma frequency was greatly reduced compared to the recordings done on D1. For better comparison, (A – E) represents the same animals presented in Fig. 5-6A to 5-6E, respectively. The animal presented in Fig. 5-6F is removed from the current figure as its headpost was detached during recordings. Mean gamma power recorded during cue on-set and off-set is shown in black and red, respectively. The overall VEP amplitudes for each animal during that session is also presented in the bottom left corner of each individual animal.

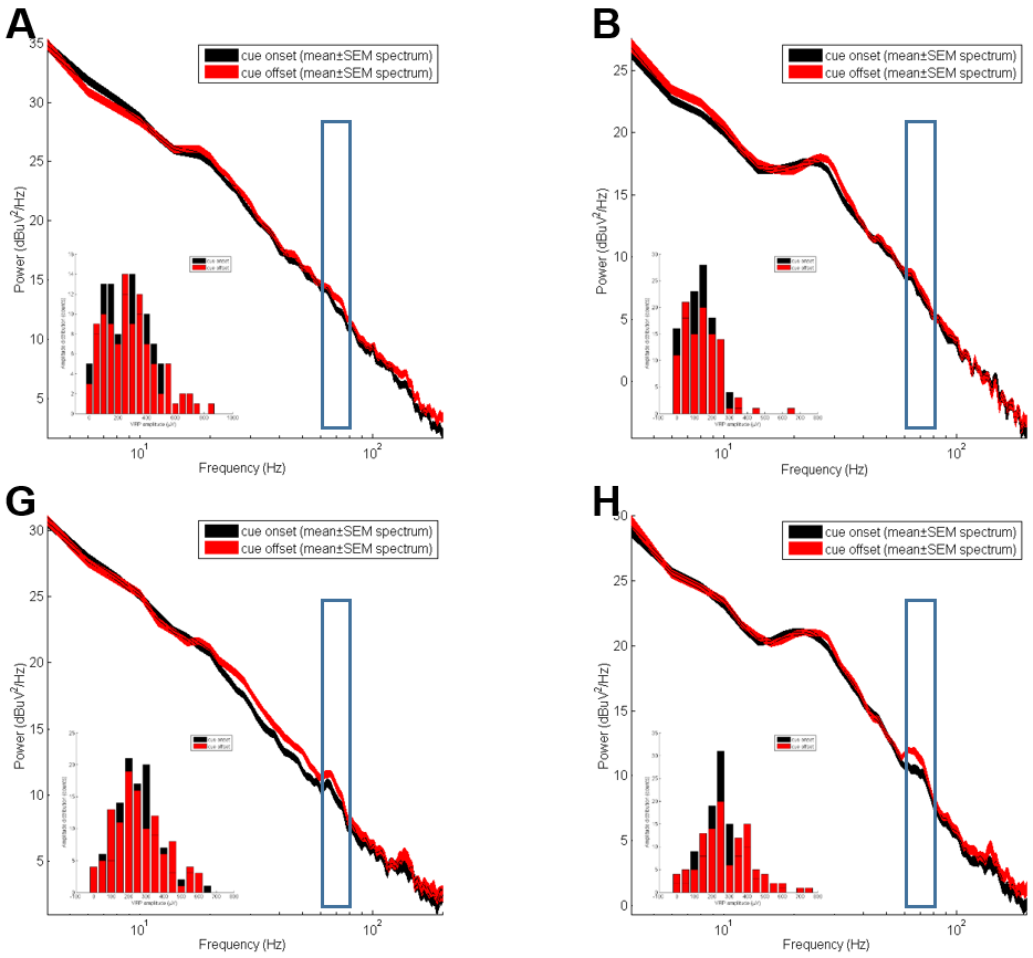

Figure 5-10. The gamma power distribution recorded from the same C57BL/6J animals after 5 days of SRP.

As shown previously, LFP power spectrum and VEP amplitudes from the same batch of C57BL/6J mice presented in Fig. 5-7A to 5-7H are presented here with their recordings on D5 of the SRP protocol (A, B, G, and H). Mean gamma power recorded during cue on-set and off-set is shown in black and red, respectively. The overall VEP amplitudes for each animal during that session is also presented in the bottom left corner of each individual animal. Two animals (C and F) suffered from headpost detachment thus were excluded from the current experiment; another two animals (D and E) were excluded due to showing stress signs (e.g., squeak, running) during recordings and therefore I was unable to proceed but put them back to their home cages.

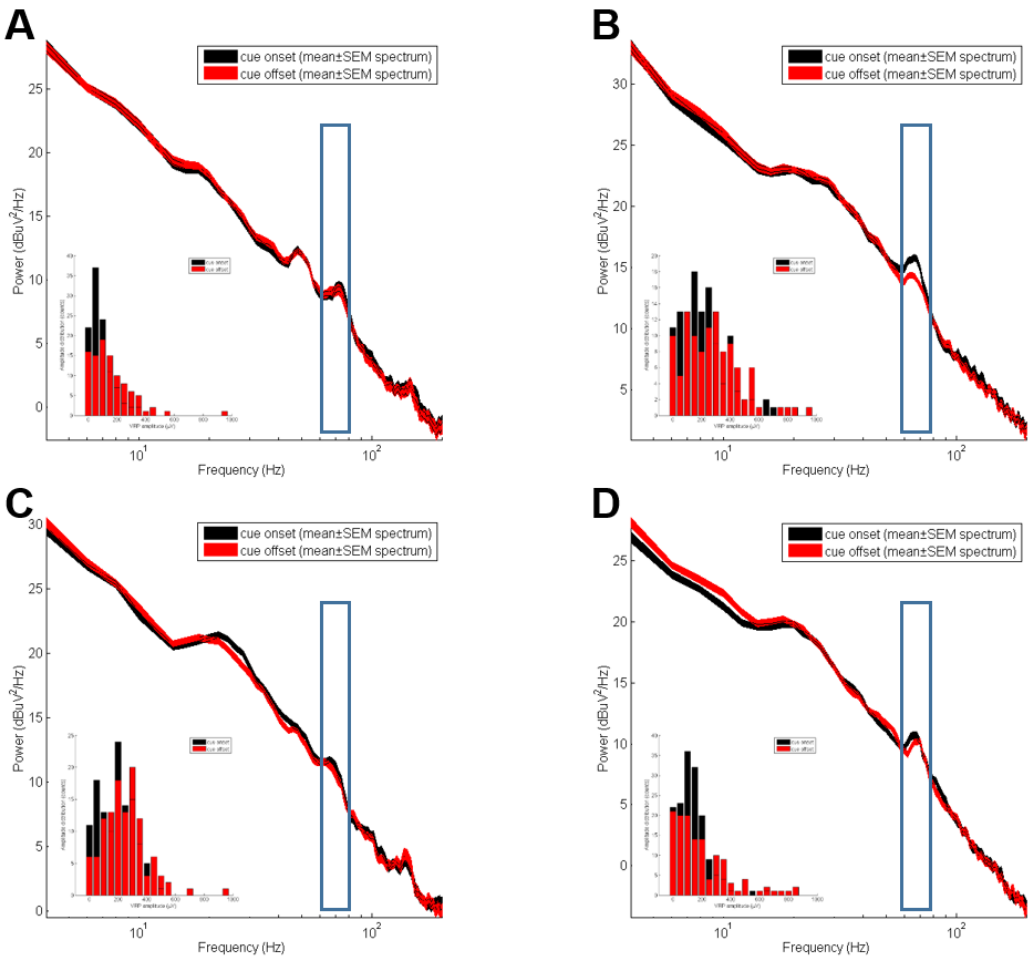

Figure 5-11. The gamma power distribution of four C57BL/6JaxOla animals after SRP.

Same animals with the mix backgrounds presented in Fig. 5-8A to 5-8D are shown here (A – D). Five days of SRP did not cause a profound effect on gamma power, most likely due to the lack of LFP power peak in the gamma frequency in the first place as presented in Fig. 5-8. Mean gamma power recorded during cue on-set and off-set is shown in black and red, respectively. The overall VEP amplitudes for each animal during that session is also presented in the bottom left corner of each individual animal.

To statistically quantify the LFP peak in the gamma range, I first analysed the overall LFP power distribution of the C57BL/6JOla mice. The overall LFP power peak fell in the frequency range between 70 – 76 Hz for the six C57BL/6JOla mice (Fig. 5-12). Thus, all mice were re-analysed and the LFP power peaks in the frequency range between 70 – 76 Hz were isolated and plotted in Fig. 5-13. A significant reduction of the LFP power after 5 days of SRP was noted in the C57BL/6JOla (Fig. 5-13A, D1 vs. D5, $p = 0.013$; Fig. 5-13B, $p = 0.0118$, unpaired two-tailed Student's *t*-test). The novel stimulus introduced in the D5N session did not induce a significant LFP power change in the C57BL/6JOla mice compared with their response at D5 (Fig. 5-13A, D5 vs. D5N, $p = 0.2442$; Fig. 5-13B, $p = 0.4165$). No changes in LFP power after 5 days of SRP was seen in either the C57BL/6J mice (Fig. 5-13A, D1 vs. D5, $p = 0.9915$; Fig. 5-13B, $p = 0.8403$) or the C57BL/6JaxOla mice (Fig. 5-13A, D1 vs. D5, $p = 0.3958$; Fig. 5-13B, $p = 0.1923$).

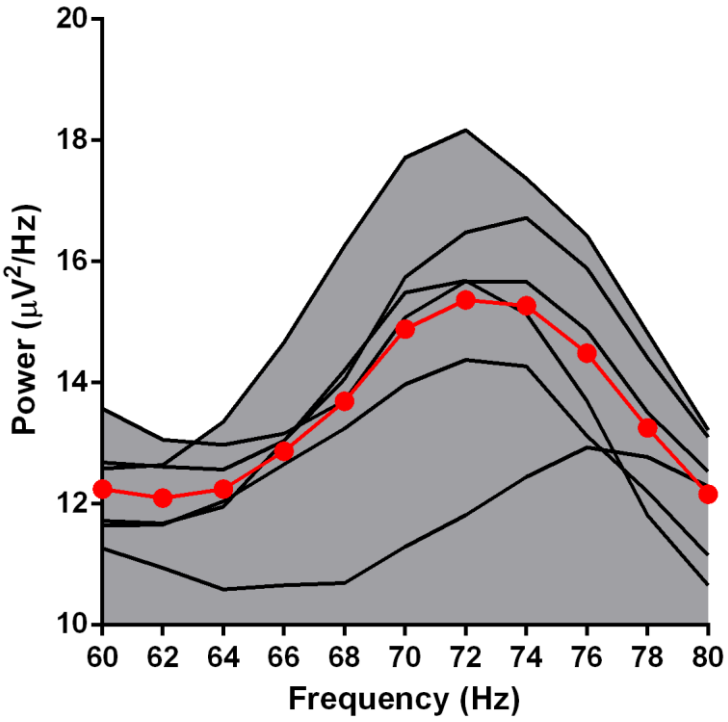

Figure 5-12. LFP power frequency distribution of six C57BL/6JOla mice.

Each individual trace represents one C57BL/6JOla mouse, and the overall mean of these six mice is presented in red. The overall mean peak of the LFP power spectrum fell between 70 – 76 Hz and were not shifted to other frequency ranges among these six mice.

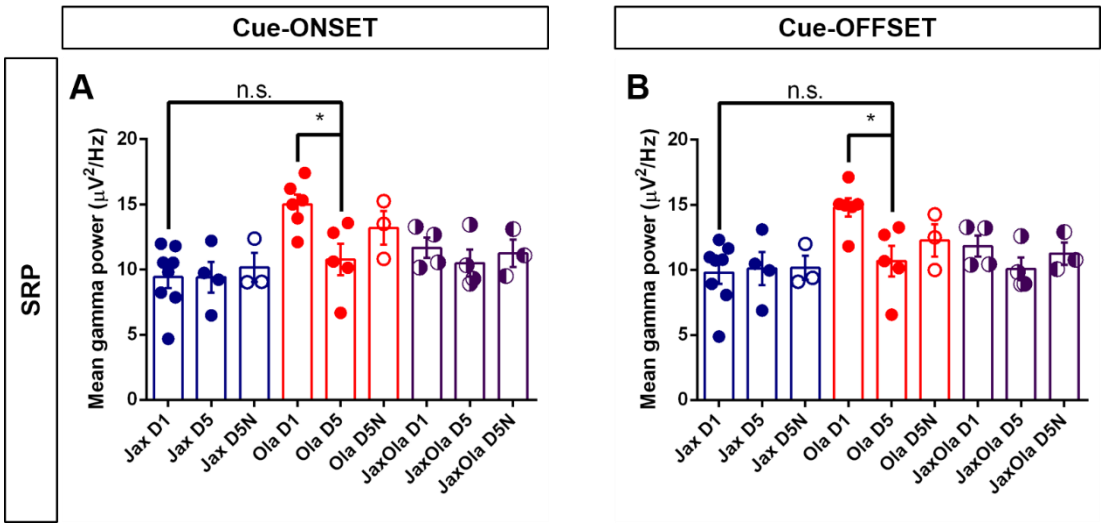

Figure 5-13. The LFP power peak in the gamma range was reduced after 5 days of SRP in the C57BL/6JOla mice.

The LFP power in the gamma range (70 – 76 Hz) from three different background substrains are presented here. A significant reduction of the LFP power after 5 days of SRP was noted in the C57BL/6JOla mice during both cue on-set (A) and cue off-set (B) conditions. However, the C57BL/6J and the C57BL/6JaxOla mice did not show any significant differences of the LFP power in the designated frequency range either before or after SRP. Substrains are simplified as follows: Jax = C57BL/6J; Ola = C57BL/6JOla; JaxOla = C57BL/6JaxOla; D1 and D5 represented the day of SRP, where D5N represented a novel stimulus was introduced on D5 after SRP.

5.3.4 The LFP power peak in the gamma range was significantly reduced when animals were recorded during the critical period.

A critical period of visual plasticity is well defined in the mice, and it is within the range between postnatal day 19 (P19) to 32 (P32) (Gordon and Stryker,

1996). The LFP power peak in the gamma range in adult C57BL/6JOla mice was reduced after 5 days of SRP training suggested it can be regulated through repeated exposure to a familiar stimulus chronically. Beyond this, whether the increased LFP power would affect homeostatic plasticity within the visual cortex is unknown. Moreover, it is not clear if the increased gamma power in the C57BL/6JOla substrain exists during the critical period. Thus, mice from the two different C57BL/6 substrains were recorded at postnatal day 28 (P28) to examine the LFP power during the critical period. I first listed all the individual animal's LFP power spectrum and VEP amplitudes for a clear comparison between groups. Juvenile mice on the C57BL/6JOla background and the C57BL/6J background are presented in Figure 5-14 and 5-15, respectively. A prominent reduction of LFP power peak in the gamma frequency was noticed in the C57BL/6JOla mice when comparing to adult animals on the same background (Fig. 5-14). On the contrary, the LFP power spectrum in the juvenile C57BL/6J mice was almost identical to adult mice on the same background (Fig. 5-15). A summarised figure highlighting the difference between adult and juvenile animals on both backgrounds is presented for better comparison (Fig. 5-16).

I noticed that in some animals there was a clear power peak around the 50 Hz range which is often considered as a result of contamination, usually known as the power-line noise which come from the equipment used in the recording environment. These noises might dampen the LFP power spectrum in the gamma range, as 3 out of 7 C57BL/6JOla mice that showed the 50 Hz noise also failed to show a clear gamma power peak (Fig. 5-14C, 5-14D, and 5-14F). Meanwhile, the remaining 4 C57BL/6JOla mice all showed clear gamma power peaks, although the size of the

peaks were smaller than in adult mice on the same background (Fig. 5-14A, 5-14B, 5-14E, and 5-14G).

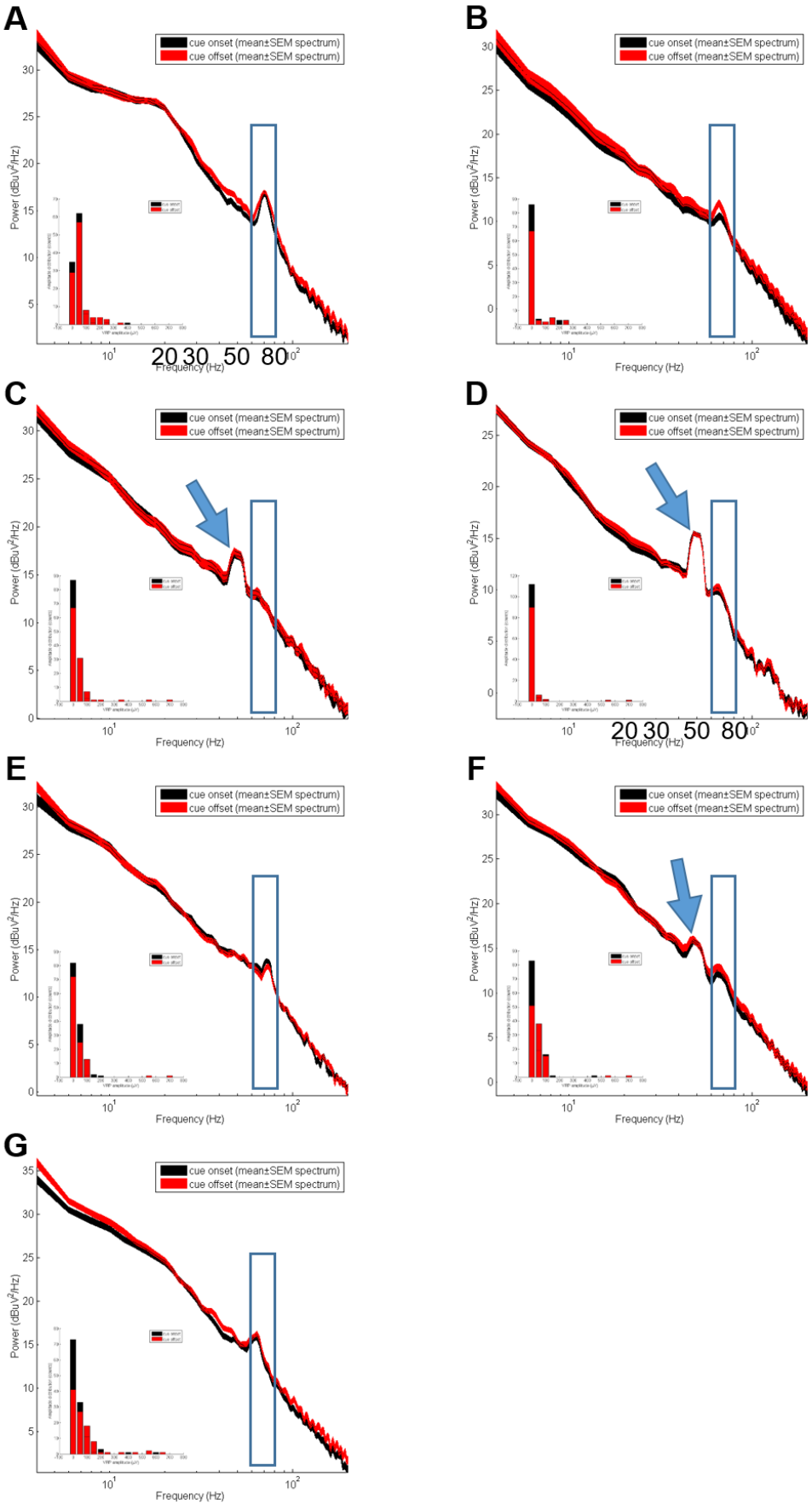
A
B
C
D
E
F
G
cue onset (mean±SEM spectrum)
cue offset (mean±SEM spectrum)
Power (dBu V²/Hz)
Frequency (Hz)
20 30 50 80

Figure 5-14. The gamma power peaks recorded from seven C57BL/6JOla animals during the critical period (P28) were decreased compared to adulthood.

Seven juvenile C57BL/6JOla mice are presented here along with their LFP power spectrum and VEP amplitudes (A – G). Mean gamma power recorded during cue on-set and off-set is shown in black and red, respectively. The overall VEP amplitudes for each animal during that session is also presented in the bottom left corner of each individual animal. Blue arrows indicate the 50 Hz noises.

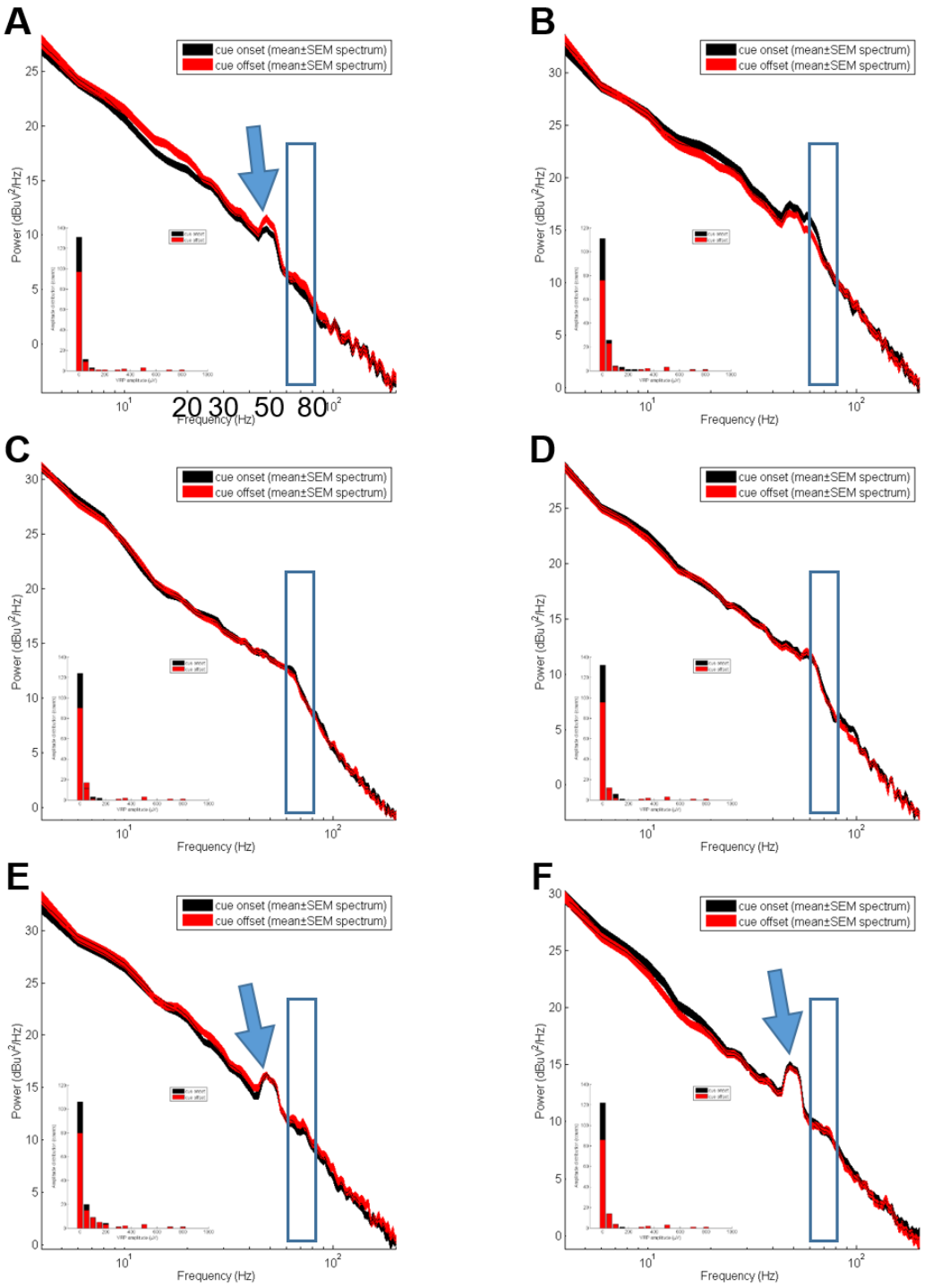

Figure 5-15. The gamma power distribution recorded from six C57BL/6J animals during the critical period (P28) was similar to adulthood.

Six juvenile C57BL/6J mice are presented here along with their LFP power spectrum and VEP amplitudes (A – F). Mean gamma power recorded during cue on-set and off-set is shown in black and red, respectively. The overall VEP amplitudes for each animal during that session is also presented in the bottom left corner of each individual animal. Blue arrows indicate the 50 Hz noises.

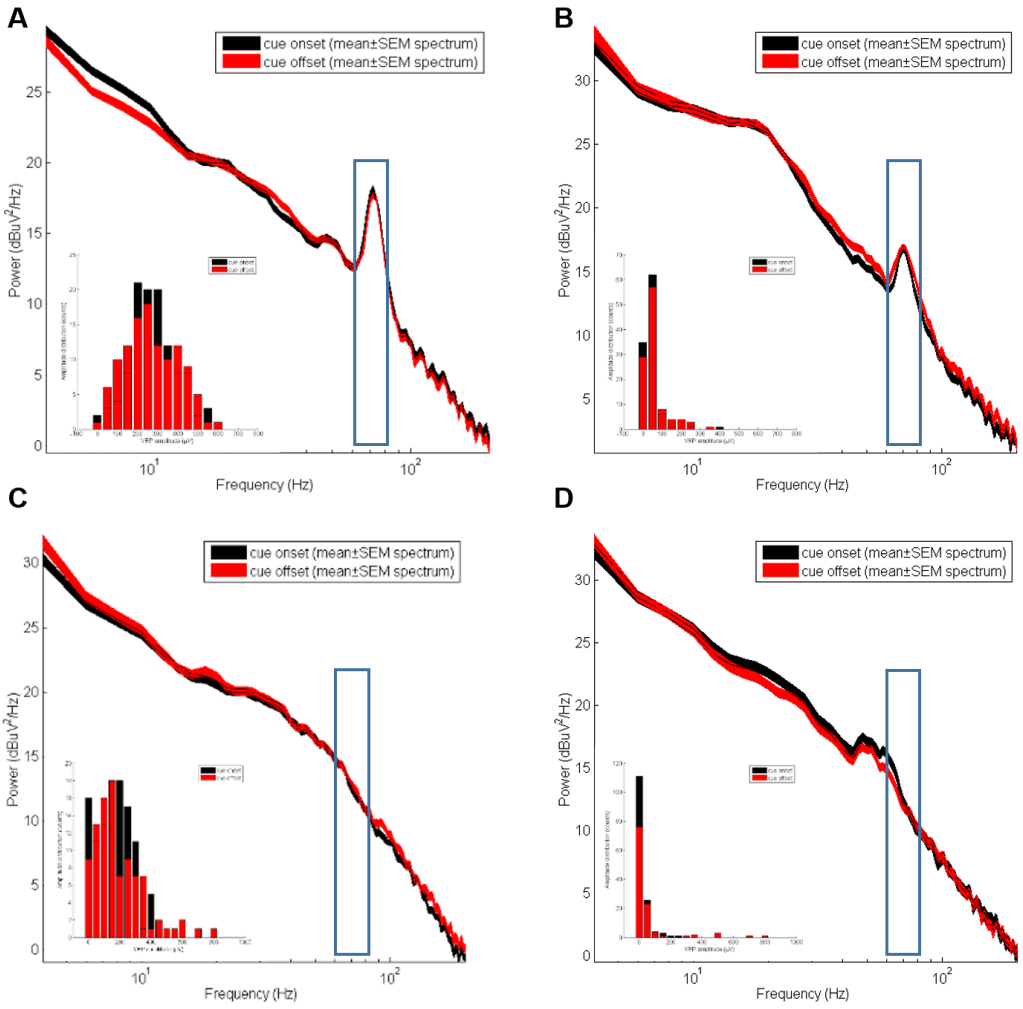

Figure 5-16. A representative figure shows the gamma power difference between adult and juvenile mice on both backgrounds.

Adult and juvenile animals on either the C57BL/6JOla or the C57BL/6J backgrounds are compared in this figure. One representative animal is chosen for each condition. Adult and juvenile (P28) C57BL/6JOla mice are shown in (A) and (B), respectively. Similarly, adult and juvenile (P28) mice on the C57BL/6J background are shown in (C) and (D), respectively. Mean gamma power recorded during cue on-set and off-set is shown in black and red, respectively. The overall VEP amplitudes for each animal during that session is also presented in the bottom left corner of each individual animal.

A significant reduction of the LFP power in the frequency range of 70 – 76 Hz was noticed in the adult C57BL/6JOla mice compared to the juvenile mice with

the same substrain (Fig. 5-17A, Ola vs. Ola 28, $p = 0.0214$; Power = 0.71, at least 7 adult animals and 9 juvenile mice will be needed if aiming to reach 0.8 in Power; Fig. 5-17B, $p = 0.0332$, unpaired two-tailed Student's *t*-test; Power = 0.63, at least 9 adult animals and 11 juvenile mice will be needed if aiming to reach 0.8 in Power). Meanwhile, the significant difference of LFP power in the gamma range between the C57BL/6JOla and C57BL/6J substrains (Fig. 5-17A, Jax vs. Ola, $p = 0.0005$; Fig. 5-17B, $p = 0.001$; Power = 0.99 in both experiments) was diminished when both were examined during the critical period (Fig. 5-17A, Jax 28 vs. Ola 28, $p = 0.0855$; Fig. 5-17B, $p = 0.0685$). Crossing the two substrains for more than three generations reduced the LFP power in the gamma range significantly (Fig. 5-17A, Ola vs. JaxOla, $p = 0.0178$; Power = 0.76, at least 7 Ola animals and 5 JaxOla animals will be needed if aiming to reach 0.8 in Power; Fig. 5-17B: $p = 0.0249$; Power = 0.68, at least 8 Ola mice and 6 JaxOla mice will be needed if aiming to reach 0.8 in Power; Fig. 5-17A, Jax vs. JaxOla, $p = 0.1269$; Fig. 5-17B, $p = 0.1632$).

To summarise, I found a distinct intrinsic feature of the C57BL/6JOla substrain that was present in both during the critical period and adulthood that was regulated by visual experience (Fig. 5-16). The increased LFP power peak within the gamma range was only present in the C57BL/6JOla substrain but not the C57BL/6J, and crossing the two substrains for three generations significantly reduced this difference (Fig. 5-17).

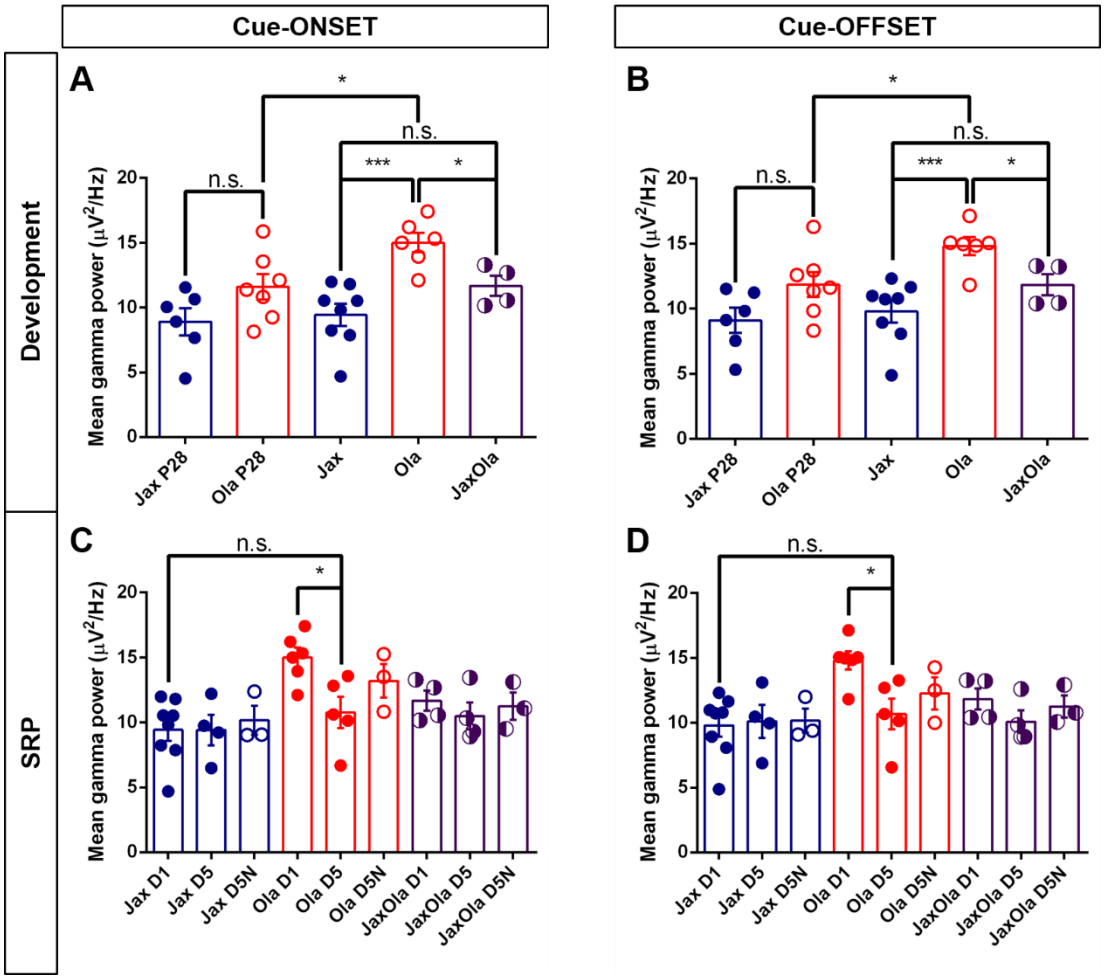

Figure 5-17. The mean gamma power change between the C57BL/6J and C57BL/6JOla mice during VEP recordings.

The mean gamma power in the frequency ranges between 70 – 76 Hz of each group is presented in this figure. Mean gamma power recorded at different developmental stages during the cue-onset and cue-offset phase is presented in (A) and (B), respectively. Mena gamma power recorded at different time points along the SRP protocol during the cue-onset and cue-offset phase is presented in (C) and (D), respectively. Animals from either the C57BL/6J (Jax) or the C57BL/6JOla (Ola) substrains were used and VEP recorded at P28 are presented as Jax P28 and Ola P28, respectively. An additional group of animals generated by crossing the C57BL/6J and C57BL/6JOla was also presented as the "JaxOla" group. SRP data are presented in the sequence of Day 1 (D1), Day 5 (D5), and Day 5 with a novel orientation (D5N). Unpaired two-tailed Student's *t*-test was used for statistical analysis among

groups. Number of animals used is marked upon each group as dots. Jax P28: n = 6; Ola P28: n = 7; Jax: n = 8; Ola: n = 6; JaxOla: n = 6; Jax D1: n = 8; Jax D5: n = 4; Jax D5N: n = 3; Ola D1: n = 6; Ola D5: n = 5; Ola D5N: n = 3; JaxOla D1: n = 4; JaxOla D5: n = 3; JaxOla D5N: n = 3.

5.4 Discussion

In this Chapter, I found a distinct LFP feature in the C57BL/6JOla mice substrain, which was a peak of LFP power isolated in the gamma frequency range between 60 – 80 Hz (more precisely, 70 – 76 Hz). This increased gamma power may be related to the apparent absence of SRP in this particular substrain, as SRP was normal in the commonly used C57BL/6J substrain. Crossing the two substrains together for three generations appeared to "rescue" this LFP power peak by reducing roughly 25% of the gamma power. Interestingly, this relative increase of gamma power in the C57BL/6JOla mice was less pronounced at P28, indicating an age-dependency to this substrain difference. Finally, the increased gamma power in the C57BL/6JOla mice reduced significantly when mice received a same visual stimulus daily chronically for 5 days, a protocol based on the experience-dependent learning (SRP). These findings suggest that an innate feature of increased cortical inhibition is found in the C57BL/6JOla mice, and this increased inhibition might underlie the loss of homeostatic plasticity and LTP-based visual responses observed in this substrain.

5.4.1 The origin of LFP power in the gamma frequency.

The increased LFP power peak in the gamma range might serve as one of the possible mechanisms of the failure of SRP induction in the C57BL/6JOla mice. In 1924, when Hens Berger first successfully recorded the brain wave activities from humans using EEG (Haas, 2003), scientists began to use such an approach to understand the relationship between these brain waves and our consciousness. One well known example is the different brain wave composition between awake and sleep, which in awake state tends to be more low-amplitude, high-frequency rhythms; on the contrary, large-amplitude but slow oscillations become the dominant wave form during sleep (Steriade and Deschenes, 1984; Steriade et al., 1993). Neuronal oscillations caught neuroscientists' attention as these oscillations with distinct features might serve as a fundamental mechanism of brain synchronisation (Buzsáki and Draguhn, 2004; Engel et al., 2001; Kahana et al., 2001; Llinás and Ribary, 1993; Varela et al., 2001; Whittington et al., 1995). Among them, gamma oscillations are defined between the frequency ranges of 30 – 80 Hz, typically at 40 Hz (Fries, 2009; Fries et al., 2007; Hermes et al., 2015; Jia and Kohn, 2011). Although the detailed mechanisms of how and where these oscillations originate remain elusive, current understanding suggest they are mainly originated from the fast-spiking, parvalbumin-positive (PV^+) GABAergic interneurons (Buzsáki and Wang, 2012; Freund, 2003; Fries, 2009; Sohal et al., 2009).

In the mammalian brain, about 80% of the neurons are excitatory (glutamatergic principal neurons), and GABAergic inhibitory interneurons constitute the remaining 20% (Aika et al., 1994; Freund and Buzsáki, 1996). For example,

GABAergic interneurons constitutes about 11% of all neurons in the CA1 region of the hippocampus. Among them, only 24% are PV^+. In other words, PV^+ interneurons only constitutes about 3% of all neurons in the brain (Bezaire and Soltesz, 2013). However, despite the relatively low concentration, GABAergic interneurons are essential in regulating the overall "balance" of the brain network. Losing the inhibitory control provided by these interneurons will render the whole system into a "hyperactive" state, and this imbalance of excitatory-inhibitory control will eventually lead to neurological diseases such as seizure (Kumar and Buckmaster, 2006).

LFP, by definition, is an electrical signal that sums the electric currents from all nearby neurons within a small volume of nervous tissue. It is mechanistically identical to the EEG and the electrocorticogram (ECoG), where EEG is recorded from the scalp and ECoG is recorded from the cortical surface, the LFP however, is recorded deep in the brain through a small metal/glass electrode (for review, see Buzsáki et al., 2012). Thus, LFP will capture all the excitable membrane (e.g., spine, dendrite, axon) or transmembrane currents that contribute to the extracellular field, disregarding the source of the signals (Buzsáki et al., 2012). The LFP signals (i.e., the VEPs) I recorded were gathered from the electrodes implanted in layer IV of the binocular region of the primary visual cortex, and according to Porciatti *et al*. and Frenkel *et al*.'s reports, recording at this depth can yield the maximum VEP responses (Frenkel et al., 2006; Porciatti et al., 1999).

In a detailed review written by Buzsáki and Wang at 2012, the cellular mechanisms of gamma oscillation in the brain was discussed (Buzsáki and Wang,

2012). The "cell assembly" theory offers a plausible explanation of how a group of neurons integrate their spiking synchronously. The functional role of this hypothesised assembly is described as *"to bring together sufficient numbers of peer neurons so that their collective spiking can discharge the postsynaptic neuron"*, as described by Buzsáki and Wang (Buzsáki and Wang, 2012; Harris et al., 2003). Hence, a precise time window that allows these peer neurons to fire simultaneously is therefore essential. For pyramidal neurons in the CA1 region, this time window is about 10 – 30 ms, which falls within a gamma cycle (Harris et al., 2003). Gamma oscillations have been seen in many regions of the brain, including the neocortex (Cardin et al., 2009; Siegle et al., 2014; Sohal et al., 2009), amygdala (Popescu et al., 2009), hippocampus (Mann et al., 2005; Whittington et al., 1995), striatum (Berke et al., 2004; Tort et al., 2008), and the visual cortex (Brunet et al., 2015; Hermes et al., 2014; Nase et al., 2003).

The first evidence of the involvement of fast-spiking interneurons in gamma oscillations was published in 1983. In that study, a correlation between spikes generated from fast-spiking interneurons and LFP gamma oscillations was found in the hippocampus of free-behaving rats (Buzsáki et al., 1983). Fast-spiking interneurons are considered as one of the most essential sources of gamma oscillations for several reasons. To begin with, the nature of how interneurons interact with surrounding pyramidal cells sets up a good model for generating neuronal oscillations. A typical basket cell can make contact to a large number of its neighbouring pyramidal cells (within ~100 μm), and those pyramidal cells in turn can make contacts to other local interneurons. Hence, an oscillation that involves a

large population of local neurons is emerged (Isaacson and Scanziani, 2011). Furthermore, inhibition of fast-spiking PV^+ interneurons suppresses gamma power *in vivo* (Sohal et al., 2009), and reversely, stimulating fast-spiking PV^+ interneurons can elicit gamma oscillations in downstream pyramidal cells (Cardin et al., 2009; Sohal et al., 2009). All these features of fast-spiking PV^+ interneurons make them an ideal candidate as the origin of gamma oscillations in the brain. To determine whether the increased gamma power in the C57BL/6JOla mice was due to a different profile of PV^+ interneurons in these two substrains, I therefore plan to first characterise the expression of PV^+ interneurons in animals on the C57BL/6J and the C57BL/6JOla background. It would also be very interesting to determine the profile of PV^+ interneurons in the C57BL/6JaxOla mice, as this could further elucidate the contribution of PV^+ interneurons toward the increased gamma power in the C57BL/6JOla mice.

5.4.2 A stimulus-specific gamma power in the C57BL/6J substrain was previously reported.

Neurons in the mouse visual cortex have been reported to fire synchronously at the gamma frequency in response to visual stimulation (Nase et al., 2003). In Nase *et al*.'s report, they found a stimulus-induced LFP power in the gamma frequency (~40 Hz) in the C57BL/6J substrain. Nevertheless, I did not notice a distinct LFP power peak in the gamma range in this substrain. One major difference may lead to the discrepancies between Nase *et al*.'s work and mine. That is, all

animals were alert and no anaesthesia was used during my recordings; where all recordings were done under mild general anaesthesia (~1% isoflurane or halothane) in their report (Nase et al., 2003). The use of isoflurane has been reported to reduce the optimal amplitudes of cortical neurons to a given visual stimulus, and it is even stronger than halothane under the same equipotent concentration (Villeneuve and Casanova, 2003).

5.4.3 What are the physiological consequences of increasing gamma power in the primary visual cortex?

As gamma oscillation is one of the dominant brain waves during arousal and alert state (Hasenstaub et al., 2005; Steriade et al., 1993), the increased gamma power in the visual cortex might imply an increase of attention and alertness. Several *in vivo* studies demonstrated that gamma oscillations in the visual cortex could increase up to tenfold in power when certain visual stimuli (but not noise) are presented (Henrie and Shapley, 2005; Hermes et al., 2015, 2014). Furthermore, the fact that gamma oscillations may largely originate from the PV^+ interneurons suggests that such an increase of gamma power might result in an elevated inhibitory network in the C57BL/6JOla mice. One hypothesis of the function of gamma oscillations in the brain (especially in the visual cortex) is to enhance the signal-to-noise ratio through suppressing the "noisy" inputs (Pritchett et al., 2015). I wonder whether the increased gamma power observed in the C57BL/6JOla substrain was too strong that it not only suppressed those noisy inputs but also the signal. If this is true,

then the reason behind the failure of eliciting SRP in the C57BL/6JOla mice would simply due to the animals cannot distinguish or recognise the visual stimulus presented every day during the SRP protocol.

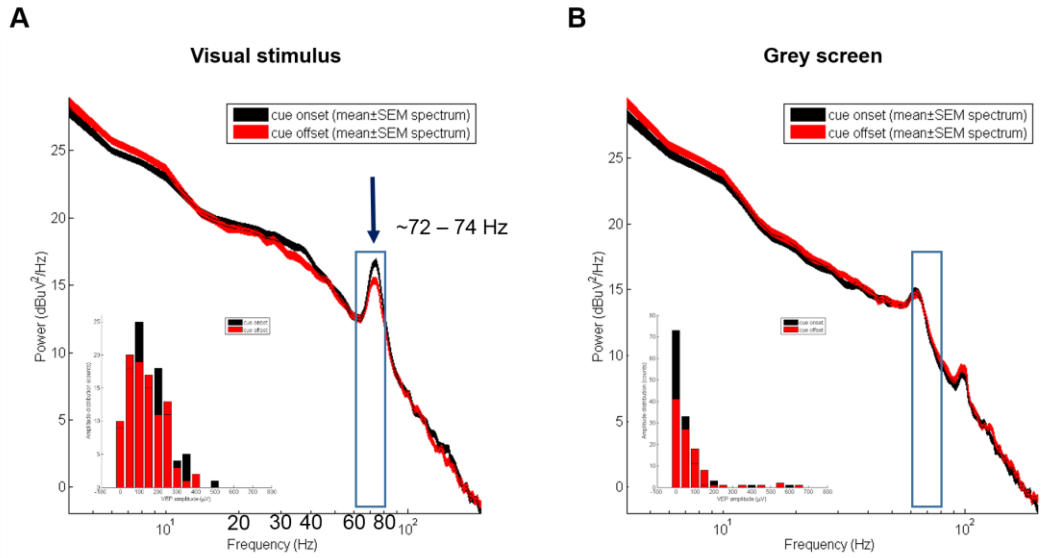

Figure 5-18. An example of the VEP responses and LFP power spectrum recorded from one C57BL/6JOla mouse during background (grey screen) and visual stimulus.

The C57BL/6JOla mouse showed a clear increased LFP power near the frequency around 70 Hz with a noticeable peak at 72 – 74 Hz, which was inside the gamma range (A). On the contrary, the same mouse did not show a clear peak LFP power in the gamma range when a grey screen was presented (B). Furthermore, the VEP amplitudes during the grey screen session was reduced compared to the stimulus session as indicated in the bar-chart at the bottom left corner of each figure. These data indicate that the increased gamma power does not affect the ability to discriminate a visual stimulus from the background in the C57BL/6JOla mice. The blue boxes indicate the frequency range between 60 – 80 Hz. VEP amplitudes and LFP power spectrum during the cue on-set and off-set phase is indicated in black and red, respectively.

However, the gamma power was clearly different between the visual stimulus session and grey screen session as the figure shown above (Fig. 5-18), thus the C57BL/6JOla mice still can distinguish the visual stimulus from the background. This also suggest that the increased gamma power we noticed in these mice are stimulus-specific, as reported previously by other groups (Henrie and Shapley, 2005; Nase et al., 2003). It is intriguing that when a given visual stimulus which can stimulate strong VEP responses is presented to the C57BL/6JOla mice, a distinct gamma power with the frequency within 60 – 80 Hz is seen; however, a grey screen which failed to elicit strong VEP responses also failed to stimulate the gamma power in this substrain. A mutual compensatory mechanism between the cortical inhibitory and excitatory network might underlie this phenomenon.

5.4.4 Stimulus-selective response potentiation.

SRP is an experience-dependent visual plasticity that according to Frenkel *et al*. it is based on NMDA and AMPA receptors trafficking (Frenkel et al., 2006). LTP plays an essential role in regulating synaptic plasticity (Bear and Malenka, 1994; Malenka, 1994; Malinow et al., 2000), and can be induced either *in vivo* or *in vitro*. Similar to the findings that long-term stimulation of dorsal lateral geniculate nucleus (dLGN) induces LTP in the primary visual cortex in rats *in vivo* (Heynen and Bear, 2001), and the fact that LTP is responsible for adult open-eye potentiation after MD (Sawtell et al., 2003). LTP has also been validated that it is required to establish SRP in mice (Frenkel et al., 2006). Chemical blockade of the NMDA receptors by systemically administering its antagonist 3-(2-Carboxypiperazin-4-yl)propyl-1-

phosphonic acid (CPP) abolishes SRP induction in mice (Frenkel et al., 2006). Similar results are also noted when the NR1 subunit of the NMDA receptor is genetically removed in layers II – IV of the mice visual cortex (Sawtell et al., 2003, unpublished data).

Moreover, the increase of AMPA receptors onto the "silent" synapses is known to be one of the consequences after LTP induction (see Malinow et al., 2000 for a complete review), and this is believed to be mediated through an interaction between AMPA receptor and the carboxy-tail of its GluR1 subunit (Hayashi et al., 2000). Blockade of new AMPA receptors insertion during LTP induction through viral transfection of the GluR1 subunit's C-terminal domain (GluR1-CT) has been shown to be effective either *in vitro* (Shi et al., 2001) or *in vivo* (Takahashi et al., 2003). Thus, SRP would likely be abolished if GluR1-CT vector is locally injected in the primary visual cortex, and this was proved by Frenkel *et al*. in his original SRP study (Frenkel et al., 2006). Therefore, one possible explanation that SRP was diminished in the C57BL/6JOla mice might be due to defect of LTP, through the malfunctioning of either NMDA or AMPA receptors, or both. However, none of these have been reported previously, making it difficult to interpret the deficit in SRP we observed in this substrain.

5.4.5 Loss of homeostatic plasticity in the C57BL/6JOla substrain.

Ranson and his colleagues' work in 2012 indicated that there was a deficit of homeostatic plasticity in the C57BL/6JOla mice (Ranson et al., 2012). In this particular substrain, no open-eye potentiation was noticed after 5 – 6 days of MD during the critical period; synaptic scaling after dark exposure was also diminished during that period in this substrain. Strikingly, the open-eye potentiation in adult C57BL/6JOla mice after 7 days of MD was identical to the C57BL/6J mice. These data suggest that juvenile and adult open-eye potentiation after MD may be regulated via different mechanisms.

Homeostatic plasticity is essential in regulating cellular and network activity, as it maintains the activity at a set point level (Feldman, 2009; Turrigiano and Nelson, 2004). Monocular deprivation in juvenile mice (specifically during the critical period) for 3 days induced a rapid reduction of visual responses of the deprived eye, longer deprivation (4 – 5 days) would then lead to a slower potentiation of responses of the opened eye accompanied with the recovery of responses of the deprived eye (Kaneko et al., 2008; Mrsic-Flogel et al., 2007; Sato and Stryker, 2008). A similar phenomenon was noticed when the same experiment was conducted in adulthood. A longer deprivation (7 days) period was necessary for adult mice to show any ocular dominance shift. Although adult mice showed a weaker reduction of responses following MD compared to juvenile mice, a potentiated response of the non-deprived eye after MD was still seen in adult mice (Frenkel et al., 2006; Sato and Stryker, 2008). Evidence suggested that both the reduction and potentiation of responses

were based on a homeostatic mechanism (Kaneko et al., 2008; Mrsic-Flogel et al., 2007). Moreover, Kaneko *et al*. dissociated these into two distinct processes, where the potentiation of responses after MD (specifically during the critical period) was a homeostatic increase of responses mediated via the tumour necrosis factor-α (TNFα) signalling (Kaneko et al., 2008). However, adult open-eye potentiation seems to be independent of TNFα signalling, as adult TNFα knockout mice showed normal open-eye potentiation after MD (Ranson et al., 2012). Meanwhile, Ca^{2+}/calmodulin-dependent protein kinase IIα (αCaMKII) was shown to be essential in LTP induction and maintenance (for review, see Lisman et al., 2012). A clear deficit of LTP in the visual cortex was reported in adult αCaMKII mutant mice, and this phenomenon was age-dependent as an absence of adult-LTP was reported while synaptic potentiation can still be observed in the juvenile mutant animals (Kirkwood et al., 1997). Moreover, open-eye potentiation after 7 days of MD was completely abolished in adult αCaMKII mutant mice (Ranson et al., 2012), suggesting that adult open-eye potentiation was LTP-dependent while a homeostatic increase of responses was responsible for juvenile open-eye potentiation.

5.4.6 The loss of α-synuclein in the C57BL/6JOla mice.

Previous studies of the C57BL/6JOla mice did not reveal any significant differences compared to other substrains despite the fact that α-synuclein was absent in this substrain (Specht and Schoepfer, 2001). Nevertheless, the absence of α-synuclein did not account for the lack of homeostatic plasticity in the C57BL/6JOla mice as the α-synuclein knock-out mice showed intact open-eye potentiation like WT

animals after MD (Ranson et al., 2012). Since SRP is mostly, if not all, based upon on LTP mechanism, the role of α-synuclein in LTP is therefore essential to elucidate. α-Synuclein is a protein that mainly expresses in neurons and is heavily involves in some neurodegenerative disorders such as PD and AD. The precise physiological role of α-synuclein in these diseases remains elusive, however, it is generally believed that α-synuclein aggravates these diseases' progression. Loss of α-synuclein in the C57BL/6JOla substrain did not cause major physiological abnormalities, and its spatial learning and memory performance tested with the water maze remained unaffected (Chen et al., 2002). α-Synuclein is a protein that known to form dimers, oligomers, and fibrillar structures under certain conditions (Conway et al., 2000). Among that, oligomeric forms was suggested to impair LTP and increase basal synaptic transmission in a NMDA receptor mediated fashion (Diogenes et al., 2012). A further experiment to test whether SRP is inducible in the α-synuclein knock-out mice could give us a better understanding of whether the loss of α-synuclein dampens the SRP induction in the C57BL/6JOla mice.

5.4.7 Age-dependent gamma power profile in the C57BL/6JOla mice.

Intriguingly, the lack of homeostatic plasticity after short-term MD in the C57BL/6JOla mice during the critical period was diminished with aging. As adult C57BL/6JOla mice showed normal open-eye potentiation after MD (Ranson et al., 2012), suggesting that there were distinct mechanisms involved in juvenile and adult

visual plasticity in this substrain. We did not test if SRP was inducible in the juvenile C57BL/6JOla mice, but the increased LFP power peak within the gamma range was reduced in the juvenile mice compared to adults. If the visual cortical responsiveness remained largely unaltered after puberty, a greater chance of inducing SRP in the juvenile C57BL/6JOla mice is therefore expected as the gamma power is greatly reduced at this period. Hence, despite the current preliminary findings, future works focusing on eliciting SRP in the juvenile C57BL/6JOla mice would shed some light on the dynamic equilibrium in visual plasticity.

My findings that the mix background mice showed a "reduced" gamma power comparing to the C57BL/6JOla substrain indicated that there could be a potential genetic "dose-response" relationship between gamma power and the C57BL/6JOla background. A 66% increase of gamma power was noticed in the C57BL/6JOla background compared to the C57BL/6Jax mice, and after only 3 crossings the mixed background mice showed a roughly 20% reduction in gamma power compared to the C57BL/6JOla mice (Fig. 5-17A and 5-17B). It would be very interesting to re-examine the result if I backcross the F1 hybrid from the mixed background mice with the C57BL/6Jax mice, rather than using the F1 × F1 from the mixed background mice to acquire the F2 and F3. In the former case, F1b (F1 backcrossing) litters will have 75% genetic traits of the C57BL/6Jax mice; however, in the latter case I will continuously get litters that have 50% genetic traits of the C57BL/6Jax mice for my F2 and F3 crossing. A F1b crossing could therefore provide valuable information about the relationships between gamma power and the substrain effect.

One possibility that the gamma power was decreased in the juvenile C57BL/6JOla mice might be the fact that some of our animals did not show stable VEP recordings during that time, as most of the VEP amplitudes were below 100 µV. This could be a result from inaccurate electrodes implantation or electrodes dislocation during recording. However, apart from two animals excluded from the experiment due to the detachment of headposts, my *post hoc* histological examination did not reveal any significant differences between animals and the sites of implantation were located around layer IV of the primary visual cortex (Fig. 5-19).

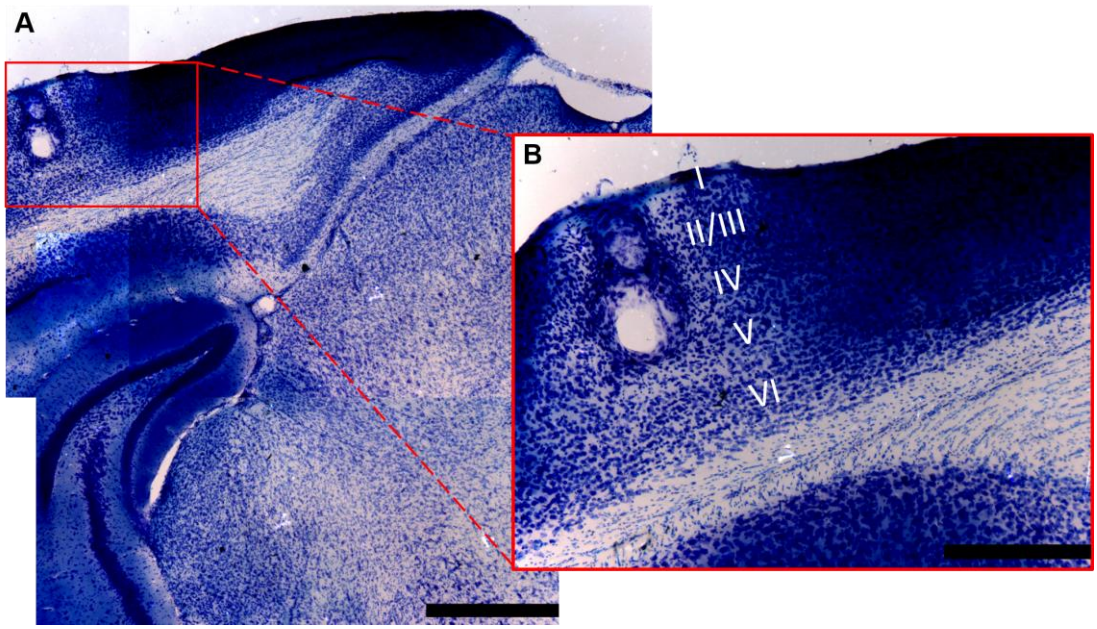

Figure 5-19. Post-mortem histological examination of the electrode implantation sites.

Post-mortem electrolytic lesions were made right after the final recording session of each animal. Brain sections were stained with Nissl solution for better visualisation of different cortical layers as presented in (A). To better distinguish different cortical layers in order to verify the site of electrode implantation, a 5X zoom-in image of (A) is presented in (B). Cortical layers are indicated using Roman numerals. The "hole" located around layer IV indicates the site of electrode implantation. Scale bar in (A): 344 µm; (B): 68.8 µm.

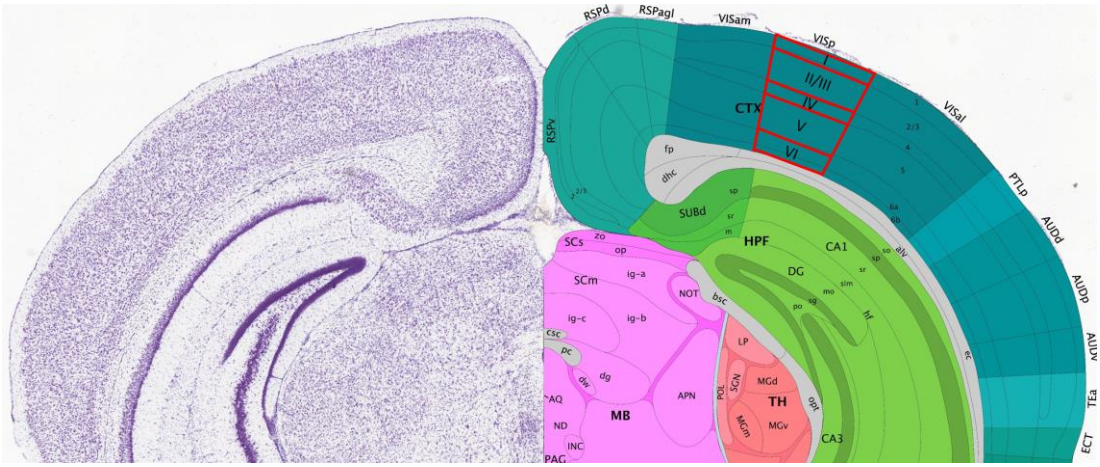

Figure 5-20. Precision of the implantation sites were verified using a mouse brain atlas.

To verify the sites of electrode implantation, I used the Allen Mouse Brain Atlas to further confirm the implantation sites were located in layer IV of the primary visual cortex. The primary visual cortex is marked with the red box, and individual cortical layers are indicated in Roman numerals. Image credit: Allen Institute for Brain Science. Primary publication: (Lein et al., 2007). Website: © 2015 Allen Institute for Brain Science. Allen Mouse Brain Atlas [Internet]. Available from: http://atlas.brain-map.org/#atlas=1&plate=100960057&structure=549&x=5596.000027126736&y=3357.037082248263 7&zoom=-3&resolution=9.31&z=5

In summary, we identified a novel mechanism that may explain the failure of SRP induction in the C57BL/6JOla mice via an exaggerated LFP power peak in the gamma range. We found that through experience-based learning, the increased gamma power in the C57BL/6JOla mice was significantly reduced to the level present in the C57BL/6J substrain. However, once a novel stimulus was presented there was a trend of increase of gamma power in the C57BL/6JOla mice, suggesting

that the failure of SRP induction was not caused by the deficit of visual discrimination. This robust increase of gamma power was only noticed in the adult C57BL/6JOla substrain, as no differences were noticed in juvenile mice between the two substrains.

Chapter 6: Conclusions & Future Perspectives

FXS is the leading inherited cause of human intellectual disability. Moreover, among 30% of male FXS patients will meet the diagnosis criteria for autism in their later lives. The cause of FXS is an expansion of the CGG trinucleotide repeat in the 5' UTR region of the *FMR1* gene, causing hypermethylation of the gene and eventually lead to a reduction or absence of the protein product FMRP.

Previous findings suggested that no gross pathological abnormalities were found in the brains of individuals with FXS and the *Fmr1*$^{-/y}$ mice (Ellegood et al., 2010; Reyniers et al., 1999; The Dutch-Belgian Fragile X Consortium, 1994). However, some minute differences between the FXS individuals and healthy controls were reported using MRI and DTI, including the CC (Villalon-Reina et al., 2013). Therefore, I looked into the white matter abnormalities of the CC by using EM. Among all parameters I have examined there were no significant differences between the *Fmr1*$^{-/y}$ mice and WT controls, consistent with previous literatures. The only difference I found was an increased axon diameter of the *Fmr1*$^{-/y}$ mice, which agreed well with previous studies that no gross white matter abnormalities were identified in the *Fmr1*$^{-/y}$ mice. Based on this finding I speculated that the conduction velocity and the latency of conduction might also be altered in the *Fmr1*$^{-/y}$ mice. We then found that the conduction latency was significantly reduced and a trend of increased conduction velocity was noticed in the *Fmr1*$^{-/y}$ mice through our computer simulation model.

One of the best interpretations of Hebbian theory is that *"cells that fire together, wire together"*—from Carla J Shatz (Shatz, 1992). The precise "timing" of cell firing has been recognised as a crucial factor of how neuronal network being propagated. In other words, the temporal order of cell firing was essential for information processing in the neuronal network. This idea first came out in the mid-1990s and was soon recognised as a novel form of neuronal plasticity—STDP (Gerstner et al., 1996; Markram et al., 1997). As STDP can be down to a millisecond precision, the shortened conduction latency we observed in the *Fmr1*$^{-/y}$ mice could impact information processing dramatically. As a matter of fact, defects in STDP of the *Fmr1*$^{-/y}$ mice have already been reported in previous studies (Desai et al., 2006; Meredith et al., 2007). Our data suggested that an increased axon diameter in the *Fmr1*$^{-/y}$ mice might offer a new insight in how STDP was disrupted by the loss of FMRP. To better understand the effect of an increased axon diameter in axonal conduction velocity, I propose to perform some *in vitro* electrophysiological recordings focusing on the CC region in the near future. Our goal will be to measure the latency between the stimulation and the elicited afferent fibre volley, and with the known distance between the stimulation site and recording site (marked with biocytin) we would be able to estimate the conduction velocity of the CC in the *Fmr1*$^{-/y}$ mice.

The abnormalities of dendritic spines were reported in early post-mortem findings of individuals with FXS, including an increase of spine density in certain areas and excessive long/thin immature spines (Hinton et al., 1991; Irwin et al., 2001; Rudelli et al., 1985; Wisniewski et al., 1991). However, the small sample size in

some studies and various developmental stages and brain areas of sampling made the results hard to interpret. Animal studies initially showed similar findings as previously found in individuals with FXS, an excessively long and immature dendritic spine morphology appeared in the *Fmr1*$^{-/y}$ mice compared to WT controls (Comery et al., 1997; Irwin et al., 2002; Nimchinsky et al., 2001). Increased spine density across different neocortical layers in a various brain regions have also been reported in the *Fmr1*$^{-/y}$ mice (Dölen et al., 2007; Hayashi et al., 2007; Liu et al., 2011). However, recent studies using the state-of-the-art microscopy techniques often failed to replicate these findings in the *Fmr1*$^{-/y}$ mice (for review, see He and Portera-Cailliau, 2013). At least two discrepancies were noticed between the earlier and more recent studies; previous studies often focused on adult stages and used the Golgi method as a way of staining, whereas more and more recent studies tend to focus on early developmental stages and used 2-photon microscopy or super-resolution microscopy such as stimulated emission depletion microscopy (STED) (Cruz-Martín et al., 2010; Meredith et al., 2007; Wijetunge et al., 2014).

Dendritic spines development is a dynamic process. In mice, new spines are formed rapidly during early development, and then a dramatic "pruning" of spines happened around P16 to P25, causing a net loss of spines (Holtmaat et al., 2005). Survival spines also help stabilise the dendritic branches and eventually the majority of spines (66%) are stable when entering adulthood (P80 – P120). We chose to start the lovastatin treatment right after weaning, and examined the spine morphology and density at a time when most of the spines were stable and overall network connectivity was established. Our experiment agreed with those recent studies that

the vast majority of spines of the *Fmr1*$^{-/y}$ mice remained unaltered regarding their morphology. In addition, we found that the spine density was elevated in layer II/III of the visual cortex of the *Fmr1*$^{-/y}$ mice, which was consistent with previous findings (Dölen et al., 2007). Our results showed no gross abnormalities in spine morphology between the *Fmr1*$^{-/y}$ mice and WT controls, however, an increase of spine head diameter was noticed in the CA1 apical dendrites of the *Fmr1*$^{-/y}$ mice compared to WT controls. This agreed well with our previous findings using STED microscopy at the same developmental stage, suggesting an increase of immature spine population in the *Fmr1*$^{-/y}$ mice (Wijetunge et al., 2014). The lovastatin treatment failed to rescue the increased spine head diameter in the *Fmr1*$^{-/y}$ mice. Surprisingly, all our data suggested that lovastatin treatment had a profound effect on spine morphology (specifically on spine head diameter), but only limited to the WT mice. As our data indicated that the LOV-WT group showed a significant increase of spine head diameter over the CON-WT in both CA1 and V1. Details of how lovastatin treatment altered spine morphology in the WT mice remain unknown. However, the fact that lovastatin treatment successfully rescued some key phenotypes in the *Fmr1*$^{-/y}$ mice (Osterweil et al., 2013) but not the spine morphology might indicate that different underlying mechanisms were involved in the loss of FMRP; and some of them could be rescued by lovastatin while others did not.

Since ASDs/ID are developmental disorders that result from both genetic and environmental influences, I next studied the mechanism by which genetic predisposition affects experience-dependent brain development. I compared two commonly used C57BL/6 substrains of mice by recording their electrophysiological

responses to visual stimuli *in vivo*. My results suggest that the C57BL/6JOla substrain has a significant stronger overall inhibitory network activity in the visual cortex than the C57BL/6J substrain. This is in good agreement with previous findings showing a lack of open-eye potentiation to MD in this substrain (Ranson et al., 2012), and highlights the need for appropriate choice of mouse strains when studying neurodevelopmental models. They also give valuable insight into the genetic mechanisms that permit experience-dependent developmental plasticity.

Gamma oscillations have been described in many brain regions including the visual cortex (Fries et al., 2001; Gray et al., 1989). We speculated that the increase of LFP power in the gamma range was closely related to the alterations of PV^+, fast-spiking basket cells as these cells were essential in generating gamma oscillations (Cardin et al., 2009; Sohal et al., 2009). Therefore, we are keen on examining the inhibitory network in the visual cortex by two strategies: first to understand the composition of the subpopulation of PV^+ interneurons within this region through immunohistochemistry, follow by sophisticated single-cell patching to understand the electrophysiological profiles of the PV^+ interneurons in the C57BL/6JOla mice.

In summary, I discovered some fine structure abnormalities in the *Fmr1*$^{-/y}$ mice compared to WT controls. However, my data also suggested that these differences were minute and no gross alterations were found in the loss of FMRP. I believe that instead of an abrupt change, the axon and spine abnormalities were largely remained unaltered with only some deviations in the *Fmr1*$^{-/y}$ mice. Moreover, these differences would be tightly regulated by development. Re-examination of these changes in adulthood would help to validate this assumption.

Finally, my data also suggested that an innate feature of stronger inhibitory network was noticed in one of the commonly used C57BL/6 substrains, and therefore highlighted the importance of choosing the appropriate animal model for experiment.

Chapter 7: References

Abeliovich, A., Schmitz, Y., Fariñas, I., Choi-Lundberg, D., Ho, W.-H., Castillo, P.E., Shinsky, N., Verdugo, J.M.G., Armanini, M., Ryan, A., Hynes, M., Phillips, H., Sulzer, D., Rosenthal, A., 2000. Mice lacking α-synuclein display functional deficits in the nigrostriatal dopamine system. Neuron 25, 239–252. doi:10.1016/S0896-6273(00)80886-7

Abitbol, M., Menini, C., Delezoide, A.-L., Rhyner, T., Vekemans, M., Mallet, J., 1993. Nucleus basalis magnocellularis and hippocampus are the major sites of FMR-1 expression in the human fetal brain. Nat. Genet. 4, 147–153.

Aboitiz, F., Montiel, J., 2003. One hundred million years of interhemispheric communication: the history of the corpus callosum. Brazilian J. Med. Biol. Res. 36, 409–420.

Aboitiz, F., Scheibel, A.B., Fisher, R.S., Zaidel, E., 1992. Fiber composition of the human corpus callosum. Brain Res. 598, 143–153. doi:0006-8993(92)90178-C [pii]

Aika, Y., Ren, J.Q., Kosaka, K., Kosaka, T., 1994. Quantitative analysis of GABA-like-immunoreactive and parvalbumin-containing neurons in the CA1 region of the rat hippocampus using a stereological method, the disector. Exp. Brain Res. 99, 267–276. doi:10.1007/BF00239593

Alexander, A.L., Lee, J.E., Lazar, M., Boudos, R., DuBray, M.B., Oakes, T.R., Miller, J.N., Lu, J., Jeong, E.-K., McMahon, W.M., Bigler, E.D., Lainhart, J.E., 2007. Diffusion tensor imaging of the corpus callosum in Autism. Neuroimage

34, 61–73.

Amaral, D.G., Schumann, C.M., Nordahl, C.W., 2008. Neuroanatomy of autism. Trends Neurosci. 31, 137–145. doi:10.1016/j.tins.2007.12.005

American Psychiatric Association, 2013. Diagnostic and Statistical Manual of Mental Disorders, 5th ed. American Psychiatric Association, Arlington, VA.

American Psychiatric Association, 2000. Diagnostic and Statistical Manual of Mental Disorders, 4th ed. American Psychiatric Association, Washington, DC.

Amir, R.E., Van den Veyver, I.B., Wan, M., Tran, C.Q., Francke, U., Zoghbi, H.Y., 1999. Rett syndrome is caused by mutations in X-linked MECP2, encoding methyl-CpG-binding protein 2. Nat. Genet. 23, 185–188. doi:10.1038/13810

Antar, L.N., Li, C., Zhang, H., Carroll, R.C., Bassell, G.J., 2006. Local functions for FMRP in axon growth cone motility and activity-dependent regulation of filopodia and spine synapses. Mol. Cell. Neurosci. 32, 37–48. doi:10.1016/j.mcn.2006.02.001

Araya, R., Jiang, J., Eisenthal, K.B., Yuste, R., 2006. The spine neck filters membrane potentials. Proc. Natl. Acad. Sci. U. S. A. 103, 17961–17966. doi:10.1073/pnas.0608755103

Arellano, J.I., Benavides-Piccione, R., DeFelipe, J., Yuste, R., 2007. Ultrastructure of dendritic spines: correlation between synaptic and spine morphologies. Front. Neurosci. 1, 131–143.

Asperger, H., 1944. Die autistischen psychopathen im kindesalter. Arch. Psychiatr. Nervenkr. 117, 76–136.

Auerbach, B.D., Osterweil, E.K., Bear, M.F., 2011. Mutations causing syndromic autism define an axis of synaptic pathophysiology. Nature 480, 63–68. doi:10.1038/nature10658

Bagni, C., Greenough, W.T., 2005. From mRNP trafficking to spine dysmorphogenesis: the roots of fragile X syndrome. Nat. Rev. Neurosci. 6, 376–387.

Bailey, D.B., Hatton, D.D., Skinner, M., Mesibov, G., 2001. Autistic behavior, FMR1 protein, and developmental trajectories in young males with fragile X syndrome. J. Autism Dev. Disord. 31, 165–174. doi:10.1023/A:1010747131386

Bailey, D.B., Raspa, M., Bishop, E., Holiday, D., 2009. No change in the age of diagnosis for fragile X syndrome: findings from a national parent survey. Pediatrics 124, 527–533. doi:10.1542/peds.2008-2992

Baird, G., Simonoff, E., Pickles, A., Chandler, S., Loucas, T., Meldrum, D., Charman, T., 2006. Prevalence of disorders of the autism spectrum in a population cohort of children in South Thames: the Special Needs and Autism Project (SNAP). Lancet 368, 210–215. doi:10.1016/S0140-6736(06)69041-7

Baker, J.P., 2013. Autism at 70 -- redrawing the boundaries. N. Engl. J. Med. 369, 1089–1091. doi:10.1056/NEJMp1304681

Banko, J.L., Hou, L., Poulin, F., Sonenberg, N., Klann, E., 2006. Regulation of eukaryotic initiation factor 4E by converging signaling pathways during metabotropic glutamate receptor-dependent long-term depression. J. Neurosci. 26, 2167–2173. doi:10.1523/JNEUROSCI.5196-05.2006

Barnea-Goraly, N., Eliez, S., Hedeus, M., Menon, V., White, C.D., Moseley, M., Reiss, A.L., 2003. White matter tract alterations in fragile X syndrome: preliminary evidence from diffusion tensor imaging. Am. J. Med. Genet. Part B 118, 81–88.

Barnea-Goraly, N., Kwon, H., Menon, V., Eliez, S., Lotspeich, L., Reiss, A.L., 2004. White matter structure in autism: preliminary evidence from diffusion tensor imaging. Biol. Psychiatry 55, 323–326. doi:10.1016/j.biopsych.2003.10.022

Basu, T.N., Gutmann, D.H., Fletcher, J.A., Glover, T.W., Collins, F.S., Downward, J., 1992. Aberrant regulation of ras proteins in malignant tumour cells from type 1 neurofibromatosis patients. Nature 356, 713–715. doi:10.1038/356713a0

Bear, M.F., Huber, K.M., Warren, S.T., 2004. The mGluR theory of fragile X mental retardation. Trends Neurosci. 27, 370–377.

Bear, M.F., Malenka, R.C., 1994. Synaptic plasticity: LTP and LTD. Curr. Opin. Neurobiol. 4, 389–399.

Beck, J.A., Lloyd, S., Hafezparast, M., Lennon-Pierce, M., Eppig, J.T., Festing, M.F.W., Fisher, E.M.C., 2000. Genealogies of mouse inbred strains. Nat. Genet. 24, 23–25. doi:10.1038/71641

Belmonte, M.K., Bourgeron, T., 2006. Fragile X syndrome and autism at the intersection of genetic and neural networks. Nat. Neurosci. 9, 1221–1225. doi:10.1038/nn1765

Berke, J.D., Okatan, M., Skurski, J., Eichenbaum, H.B., 2004. Oscillatory entrainment of striatal neurons in freely moving rats. Neuron 43, 883–896.

doi:10.1016/j.neuron.2004.08.035

Berry-Kravis, E., Hessl, D., Coffey, S., Hervey, C., Schneider, A., Yuhas, J., Hutchison, J., Snape, M., Tranfaglia, M., Nguyen, D. V, Hagerman, R., 2009. A pilot open label, single dose trial of fenobam in adults with fragile X syndrome. J. Med. Genet. 46, 266–271. doi:10.1136/jmg.2008.063701

Berry-Kravis, E.M., Hessl, D.H., Rathmell, B., Zarevics, P., Cherubini, M., Walton-Bowen, K., Mu, Y., Nguyen, D. V, Gonzalez-Heydrich, J., Wang, P.P., Carpenter, R.L., Bear, M.F., Hagerman, R.J., 2012. Effects of STX209 (arbaclofen) on neurobehavioral function in children and adults with fragile X syndrome: a randomized, controlled, phase 2 trial. Sci. Transl. Med. 4, 152ra127. doi:10.1126/scitranslmed.3004214

Bezaire, M.J., Soltesz, I., 2013. Quantitative assessment of CA1 local circuits: knowledge base for interneuron-pyramidal cell connectivity. Hippocampus 23, 751–785. doi:10.1002/hipo.22141

Bhatt, D.H., Zhang, S., Gan, W.-B., 2009. Dendritic spine dynamics. Annu. Rev. Physiol. 71, 261–282. doi:10.1146/annurev.physiol.010908.163140

Bhattacharya, A., Kaphzan, H., Alvarez-Dieppa, A.C., Murphy, J.P., Pierre, P., Klann, E., 2012. Genetic removal of p70 S6 kinase 1 corrects molecular, synaptic, and behavioral phenotypes in fragile X syndrome mice. Neuron 76, 325–337. doi:10.1016/j.neuron.2012.07.022

Bian, W.-J., Miao, W.-Y., He, S.-J., Qiu, Z., Yu, X., 2015. Coordinated spine pruning and maturation mediated by inter-spine competition for

cadherin/catenin complexes. Cell 162, 808–822. doi:10.1016/j.cell.2015.07.018

Bilousova, T. V, Dansie, L., Ngo, M., Aye, J., Charles, J.R., Ethell, D.W., Ethell, I.M., 2009. Minocycline promotes dendritic spine maturation and improves behavioural performance in the fragile X mouse model. J. Med. Genet. 46, 94–102. doi:10.1136/jmg.2008.061796

Boellaard, R., O'Doherty, M.J., Weber, W.A., Mottaghy, F.M., Lonsdale, M.N., Stroobants, S.G., Oyen, W.J.G., Kotzerke, J., Hoekstra, O.S., Pruim, J., Marsden, P.K., Tatsch, K., Hoekstra, C.J., Visser, E.P., Arends, B., Verzijlbergen, F.J., Zijlstra, J.M., Comans, E.F.I., Lammertsma, A.A., Paans, A.M., Willemsen, A.T., Beyer, T., Bockisch, A., Schaefer-Prokop, C., Delbeke, D., Baum, R.P., Chiti, A., Krause, B.J., 2010. FDG PET and PET/CT: EANM procedure guidelines for tumour PET imaging: version 1.0. Eur. J. Nucl. Med. Mol. Imaging 37, 181–200. doi:10.1007/s00259-009-1297-4

Bontekoe, C.J.M., Bakker, C.E., Nieuwenhuizen, I.M., van der Linde, H., Lans, H., de Lange, D., Hirst, M.C., Oostra, B.A., 2001. Instability of a (CGG)98 repeat in the Fmr1 promoter. Hum. Mol. Genet. 10, 1693–1699.

Bos, J.L., 2003. Epac: a new cAMP target and new avenues in cAMP research. Nat. Rev. Mol. Cell Biol. 4, 733–738. doi:10.1038/nrm1197

Bowen, P., Biederman, B., Swallow, K.A., 1978. The X-linked syndrome of macroorchidism and mental retardation: further observations. Am. J. Med. Genet. 2, 409–414.

Braun, K., Segal, M., 2000. FMRP involvement in formation of synapses among

cultured hippocampal neurons. Cereb. Cortex 10, 1045–1052. doi:10.1093/cercor/10.10.1045

Bregman, J.D., Leckman, J.F., Ort, S.I., 1988. Fragile X syndrome: genetic predisposition to psychopathology. J. Autism Dev. Disord. 18, 343–354.

Brouwer, J.R., Mientjes, E.J., Bakker, C.E., Nieuwenhuizen, I.M., Severijnen, L.A., Van der Linde, H.C., Nelson, D.L., Oostra, B.A., Willemsen, R., 2007. Elevated Fmr1 mRNA levels and reduced protein expression in a mouse model with an unmethylated Fragile X full mutation. Exp. Cell Res. 313, 244–253. doi:10.1016/j.yexcr.2006.10.002

Brown, V., Small, K., Lakkis, L., Feng, Y., Gunter, C., Wilkinson, K.D., Warren, S.T., 1998. Purified recombinant Fmrp exhibits selective RNA binding as an intrinsic property of the fragile X mental retardation protein. J. Biol. Chem. 273, 15521–15527.

Brunet, N., Bosman, C.A., Roberts, M., Oostenveld, R., Womelsdorf, T., De Weerd, P., Fries, P., 2015. Visual cortical gamma-band activity during free viewing of natural images. Cereb. Cortex 25, 918–926. doi:10.1093/cercor/bht280

Buell, S.J., 1982. Golgi-Cox and rapid Golgi methods as applied to autopsied human brain tissue: widely disparate results. J. Neuropathol. Exp. Neurol. 41, 500–507.

Bureau, I., Shepherd, G.M.G., Svoboda, K., 2008. Circuit and plasticity defects in the developing somatosensory cortex of FMR1 knock-out mice. J. Neurosci. 28, 5178–5188. doi:10.1523/JNEUROSCI.1076-08.2008

Busquets-Garcia, A., Gomis-González, M., Guegan, T., Agustín-Pavón, C., Pastor,

A., Mato, S., Pérez-Samartín, A., Matute, C., de la Torre, R., Dierssen, M., Maldonado, R., Ozaita, A., 2013. Targeting the endocannabinoid system in the treatment of fragile X syndrome. Nat. Med. 19, 603–607. doi:10.1038/nm.3127

Buzsáki, G., Anastassiou, C.A., Koch, C., 2012. The origin of extracellular fields and currents--EEG, ECoG, LFP and spikes. Nat. Rev. Neurosci. 13, 407–420. doi:10.1038/nrn3241

Buzsáki, G., Draguhn, A., 2004. Neuronal oscillations in cortical networks. Science (80-.). 304, 1926–1929. doi:10.1126/science.1099745

Buzsáki, G., Leung, L.-W.S., Vanderwolf, C.H., 1983. Cellular bases of hippocampal EEG in the behaving rat. Brain Res. Rev. 6, 139–171. doi:10.1016/0165-0173(83)90037-1

Buzsáki, G., Wang, X.-J., 2012. Mechanisms of gamma oscillations. Annu. Rev. Neurosci. 35, 203–225. doi:10.1146/annurev-neuro-062111-150444

Caku, A., Pellerin, D., Bouvier, P., Riou, E., Corbin, F., 2014. Effect of lovastatin on behavior in children and adults with fragile X syndrome: an open-label study. Am. J. Med. Genet. A 164A, 2834–2842. doi:10.1002/ajmg.a.36750

Cardin, J.A., Carlén, M., Meletis, K., Knoblich, U., Zhang, F., Deisseroth, K., Tsai, L.-H., Moore, C.I., 2009. Driving fast-spiking cells induces gamma rhythm and controls sensory responses. Nature 459, 663–667. doi:10.1038/nature08002

Carpenter, L.A., Soorya, L., Halpern, D., 2009. Asperger's syndrome and high-functioning autism. Pediatr. Ann. 38, 30–35.

Chakrabarti, S., Fombonne, E., 2001. Pervasive developmental disorders in

preschool children. JAMA 285, 3093–3099.

Chen, P.E., Specht, C.G., Morris, R.G.M., Schoepfer, R., 2002. Spatial learning is unimpaired in mice containing a deletion of the alpha-synuclein locus. Eur. J. Neurosci. 16, 154–158. doi:10.1046/j.1460-9568.2002.02062.x

Chess, S., 1971. Autism in children with congenital rubella. J. Autism Child. Schizophr. 1, 33–47.

Collins, S.C., Bray, S.M., Suhl, J.A., Cutler, D.J., Coffee, B., Zwick, M.E., Warren, S.T., 2010. Identification of novel FMR1 variants by massively parallel sequencing in developmentally delayed males. Am. J. Med. Genet. A 152, 2512–2520. doi:10.1002/ajmg.a.33626

Comery, T.A., Harris, J.B., Willems, P.J., Oostra, B.A., Irwin, S.A., Weiler, I.J., Greenough, W.T., 1997. Abnormal dendritic spines in fragile X knockout mice: maturation and pruning deficits. Proc. Natl. Acad. Sci. U. S. A. 94, 5401–5404.

Conway, K.A., Harper, J.D., Lansbury, P.T.J., 2000. Fibrils formed in vitro from α-synuclein and two mutant forms linked to Parkinson's disease are typical amyloid. Biochemistry 39, 2552–2563. doi:10.1021/bi991447r

Cooke, S.F., Bear, M.F., 2012. Stimulus-selective response plasticity in the visual cortex: an assay for the assessment of pathophysiology and treatment of cognitive impairment associated with psychiatric disorders. Biol. Psychiatry 71, 487–495. doi:10.1016/j.biopsych.2011.09.006

Costa, R.M., Federov, N.B., Kogan, J.H., Murphy, G.G., Stern, J., Ohno, M., Kucherlapati, R., Jacks, T., Silva, A.J., 2002. Mechanism for the learning

deficits in a mouse model of Neurofibromatosis Type 1. Nature 415, 526–530. doi:10.1038/nature711

Courchesne, E., 1997. Brainstem, cerebellar and limbic neuroanatomical abnormalities in autism. Curr. Opin. Neurobiol. 7, 269–278. doi:10.1016/S0959-4388(97)80016-5

Courchesne, E., Carper, R., Akshoomoff, N., 2003. Evidence of brain overgrowth in the first year of life in autism. JAMA 290, 337–344. doi:10.1001/jama.290.3.337

Courchesne, E., Karns, C.M., Davis, H.R., Ziccardi, R., Carper, R.A., Tigue, Z.D., Chisum, H.J., Moses, P., Pierce, K., Lord, C., Lincoln, A.J., Pizzo, S., Schreibman, L., Haas, R.H., Akshoomoff, N.A., Courchesne, R.Y., 2001. Unusual brain growth patterns in early life in patients with autistic disorder: an MRI study. Neurology 57, 245–254. doi:10.1212/WNL.57.2.245

Crawford, D.C., Acuña, J.M., Sherman, S.L., 2001. FMR1 and the fragile X syndrome: human genome epidemiology review. Genet. Med. 3, 359–371.

Crawley, J.N., Belknap, J.K., Collins, A., Crabbe, J.C., Frankel, W., Henderson, N., Hitzemann, R.J., Maxson, S.C., Miner, L.L., Silva, A.J., Wehner, J.M., Wynshaw-Boris, A., Paylor, R., 1997. Behavioral phenotypes of inbred mouse strains: implications and recommendations for molecular studies. Psychopharmacology (Berl). 132, 107–124.

Cruz-Martín, A., Crespo, M., Portera-Cailliau, C., 2010. Delayed stabilization of dendritic spines in fragile X mice. J. Neurosci. 30, 7793–7803.

doi:10.1523/JNEUROSCI.0577-10.2010

D'Hulst, C., Kooy, R.F., 2007. The GABAA receptor: a novel target for treatment of fragile X? Trends Neurosci. 30, 425–431. doi:10.1016/j.tins.2007.06.003

Darby, J.K., 1976. Neuropathologic aspects of psychosis in children. J. Autism Child. Schizophr. 6, 339–352. doi:10.1007/BF01537911

Darnell, J.C., Klann, E., 2013. The translation of translational control by FMRP: therapeutic targets for FXS. Nat. Neurosci. 16, 1530–1536. doi:10.1038/nn.3379

Daston, M.M., Scrable, H., Nordlund, M., Sturbaum, A.K., Nissen, L.M., Ratner, N., 1992. The protein product of the neurofibromatosis type 1 gene is expressed at highest abundance in neurons, Schwann cells, and oligodendrocytes. Neuron 8, 415–428. doi:10.1016/0896-6273(92)90270-N

Davis, M.I., Ronesi, J., Lovinger, D.M., 2003. A predominant role for inhibition of the adenylate cyclase/protein kinase A pathway in ERK activation by cannabinoid receptor 1 in N1E-115 neuroblastoma cells. J. Biol. Chem. 278, 48973–48980. doi:10.1074/jbc.M305697200

Dawson, G., Munson, J., Webb, S.J., Nalty, T., Abbott, R., Toth, K., 2007. Rate of head growth decelerates and symptoms worsen in the second year of life in autism. Biol. Psychiatry 61, 458–464. doi:10.1016/j.biopsych.2006.07.016

Dawson, G., Osterling, J., Meltzoff, A.N., Kuhl, P., 2000. Case study of the development of an infant with autism from birth to two years of age. J. Appl. Dev. Psychol. 21, 299–313. doi:10.1016/S0193-3973(99)00042-8

de Vrij, F.M.S., Levenga, J., van der Linde, H.C., Koekkoek, S.K., De Zeeuw, C.I.,

Nelson, D.L., Oostra, B.A., Willemsen, R., 2008. Rescue of behavioral phenotype and neuronal protrusion morphology in Fmr1 KO mice. Neurobiol. Dis. 31, 127–132. doi:10.1016/j.nbd.2008.04.002

DeClue, J.E., Papageorge, A.G., Fletcher, J.A., Diehl, S.R., Ratner, N., Vass, W.C., Lowy, D.R., 1992. Abnormal regulation of mammalian p21ras contributes to malignant tumor growth in von Recklinghausen (type 1) neurofibromatosis. Cell 69, 265–273. doi:10.1136/jmg.29.9.678-c

Deelen, W., Bakker, C., Halley, D.J.J., Oostra, B.A., 1994. Conservation of CGG region in FMR1 gene in mammals. Am. J. Med. Genet. 51, 513–516.

Dementieva, Y.A., Vance, D.D., Donnelly, S.L., Elston, L.A., Wolpert, C.M., Ravan, S.A., DeLong, G.R., Abramson, R.K., Wright, H.H., Cuccaro, M.L., 2005. Accelerated head growth in early development of individuals with autism. Pediatr. Neurol. 32, 102–108. doi:10.1016/j.pediatrneurol.2004.08.005

den Broeder, M.J., van der Linde, H., Brouwer, J.R., Oostra, B.A., Willemsen, R., Ketting, R.F., 2009. Generation and characterization of Fmr1 knockout zebrafish. PLoS One 4, e7910. doi:10.1371/journal.pone.0007910

Deng, P.-Y., Sojka, D., Klyachko, V.A., 2011. Abnormal presynaptic short-term plasticity and information processing in a mouse model of fragile X syndrome. J. Neurosci. 31, 10971–10982. doi:10.1523/JNEUROSCI.2021-11.2011

Desai, N.S., Casimiro, T.M., Gruber, S.M., Vanderklish, P.W., 2006. Early postnatal plasticity in neocortex of Fmr1 knockout mice. J. Neurophysiol. 96, 1734–1745. doi:10.1152/jn.00221.2006

Descamps, O.S., Tenoutasse, S., Stephenne, X., Gies, I., Beauloye, V., Lebrethon, M.C., De Beaufort, C., De Waele, K., Scheen, A., Rietzschel, E., Mangano, A., Panier, J.P., Ducobu, J., Langlois, M., Balligand, J.L., Legat, P., Blaton, V., Muls, E., Van Gaal, L., Sokal, E., Rooman, R., Carpentier, Y., De Backer, G., Heller, F.R., 2011. Management of familial hypercholesterolemia in children and young adults: Consensus paper developed by a panel of lipidologists, cardiologists, paediatricians, nutritionists, gastroenterologists, general practitioners and a patient organization. Atherosclerosis 218, 272–280. doi:10.1016/j.atherosclerosis.2011.06.016

Desmond, M.M., Wilson, G.S., Melnick, J.L., Singer, D.B., Zion, T.E., Rudolph, A.J., Pineda, R.G., Ziai, M.-H., Battner, R.J., 1967. Congenital rubella encephalitis: course and early sequelae. J. Pediatr. 71, 311–331.

Dhillon, A.S., Hagan, S., Rath, O., Kolch, W., 2007. MAP kinase signalling pathways in cancer. Oncogene 26, 3279–3290. doi:10.1038/sj.onc.1210421

Di Nuovo, S.F., Buono, S., 2007. Psychiatric syndromes comorbid with mental retardation: differences in cognitive and adaptive skills. J. Psychiatr. Res. 41, 795–800. doi:10.1016/j.jpsychires.2006.02.011

Ding, Q., Sethna, F., Wang, H., 2014. Behavioral analysis of male and female Fmr1 knockout mice on C57BL/6 background. Behav. Brain Res. 271, 72–78. doi:10.1016/j.bbr.2014.05.046

Diogenes, M.J., Dias, R.B., Rombo, D.M., Vicente Miranda, H., Maiolino, F., Guerreiro, P., Nasstrom, T., Franquelim, H.G., Oliveira, L.M.A., Castanho, M.A.R.B., Lannfelt, L., Bergstrom, J., Ingelsson, M., Quintas, A., Sebastiao,

A.M., Lopes, L. V, Outeiro, T.F., 2012. Extracellular alpha-synuclein oligomers modulate synaptic transmission and impair LTP via NMDA-receptor activation. J. Neurosci. 32, 11750–11762. doi:10.1523/JNEUROSCI.0234-12.2012

Dölen, G., Osterweil, E.K., Rao, B.S.S., Smith, G.B., Auerbach, B.D., Chattarji, S., Bear, M.F., 2007. Correction of fragile X syndrome in mice. Neuron 56, 955–962. doi:10.1016/j.neuron.2007.12.001

Downward, J., 2003. Targeting RAS signalling pathways in cancer therapy. Nat. Rev. Cancer 3, 11–22. doi:10.1038/nrc969

Dunn, T.B., 1954. The importance of differences in morphology in inbred strains. J. Natl. Cancer Inst. 15, 573–591.

Eberhart, D.E., Malter, H.E., Feng, Y., Warren, S.T., 1996. The fragile X mental retardation protein is a ribonucleoprotein containing both nuclear localization and nuclear export signals. Hum. Mol. Genet. 5, 1083–1091.

Edwards, P.A., 1999. Sterols and isoprenoids: signaling molecules derived from the cholesterol biosynthetic pathway. Annu. Rev. Biochem. 68, 157–185. doi:10.1146/annurev.pharmtox.46.120604.141053

Einfeld, S.L., Ellis, L.A., Emerson, E., 2011. Comorbidity of intellectual disability and mental disorder in children and adolescents: a systematic review. J. Intellect. Dev. Disabil. 36, 137–143. doi:10.1080/13668250.2011.572548

Ellegood, J., Pacey, L.K.K., Hampson, D.R., Lerch, J.P., Henkelman, R.M., 2010. Anatomical phenotyping in a mouse model of fragile X syndrome with magnetic resonance imaging. Neuroimage 53, 1023–1029.

doi:10.1016/j.neuroimage.2010.03.038

Elsabbagh, M., Divan, G., Koh, Y.-J., Kim, Y.S., Kauchali, S., Marcín, C., Montiel-Nava, C., Patel, V., Paula, C.S., Wang, C., Yasamy, M.T., Fombonne, E., 2012. Global prevalence of autism and other pervasive developmental disorders. Autism Res. 5, 160–179. doi:10.1002/aur.239

Emerson, E., Hatton, C., 2007. Mental health of children and adolescents with intellectual disabilities in Britain. Br. J. Psychiatry 191, 493–499. doi:10.1192/bjp.bp.107.038729

Endo, A., Tsujita, Y., Kuroda, M., Tanzawa, K., 1977. Inhibition of cholesterol synthesis in vitro and in vivo by ML-236A and ML-236B, competitive inhibitors of 3-hydroxy-3-methylglutaryl-coenzyme A reductase. Eur. J. Biochem. 77, 31–36. doi:10.1111/j.1432-1033.1977.tb11637.x

Engel, A.K., Fries, P., Singer, W., 2001. Dynamic predictions: oscillations and synchrony in top-down processing. Nat. Rev. Neurosci. 2, 704–716. doi:10.1038/35094565

Faul, F., Erdfelder, E., Lang, A.-G., Buchner, A., 2007. G*Power 3: a flexible statistical power analysis program for the social, behavioral, and biomedical sciences. Behav. Res. Methods 39, 175–191. doi:10.3758/BF03193146

Feldman, D.E., 2009. Synaptic mechanisms for plasticity in neocortex. Annu. Rev. Neurosci. 32, 33–55. doi:10.1146/annurev.neuro.051508.135516

Fields, R.D., 2008. White matter in learning, cognition and psychiatric disorders. Trends Neurosci. 31, 361–370. doi:10.1016/j.tins.2008.04.001

Folstein, S.E., Rosen-Sheidley, B., 2001. Genetics of autism: complex aetiology for a heterogeneous disorder. Nat. Rev. Genet. 2, 943–955. doi:10.1038/35103559

Fombonne, É., 2003. Epidemiological surveys of autism and other pervasive developmental disorders: an update. J. Autism Dev. Disord. 33, 365–382.

Fombonne, E., Du Mazaubrun, C., Cans, C., Grandjean, H., 1997. Autism and associated medical disorders in a French epidemiological survey. J. Am. Acad. Child Adolesc. Psychiatry 36, 1561–1569.

Frankland, P.W., Wang, Y., Rosner, B., Shimizu, T., Balleine, B.W., Dykens, E.M., Ornitz, E.M., Silva, A.J., 2004. Sensorimotor gating abnormalities in young males with fragile X syndrome and Fmr1-knockout mice. Mol. Psychiatry 9, 417–425. doi:10.1038/sj.mp.4001432

Frenkel, M.Y., Bear, M.F., 2004. How monocular deprivation shifts ocular dominance in visual cortex of young mice. Neuron 44, 917–923.

Frenkel, M.Y., Sawtell, N.B., Diogo, A.C.M., Yoon, B., Neve, R.L., Bear, M.F., 2006. Instructive effect of visual experience in mouse visual cortex. Neuron 51, 339–349. doi:10.1016/j.neuron.2006.06.026

Freund, T.F., 2003. Interneuron Diversity series: rhythm and mood in perisomatic inhibition. Trends Neurosci. 26, 489–495. doi:10.1016/S0166-2236(03)00227-3

Freund, T.F., Buzsáki, G., 1996. Interneurons of the hippocampus. Hippocampus 6, 347–470. doi:10.1002/(SICI)1098-1063(1996)6:4<347::AID-HIPO1>3.0.CO;2-I

Fridell, R.A., Benson, R.E., Hua, J., Bogerd, H.P., Cullen, B.R., 1996. A nuclear role

for the Fragile X mental retardation protein. EMBO J. 15, 5408–5414.

Fries, P., 2009. Neuronal gamma-band synchronization as a fundamental process in cortical computation. Annu. Rev. Neurosci. 32, 209–224. doi:10.1146/annurev.neuro.051508.135603

Fries, P., Nikolic, D., Singer, W., 2007. The gamma cycle. Trends Neurosci. 30, 309–316. doi:10.1016/j.tins.2007.05.005

Fries, P., Reynolds, J.H., Rorie, A.E., Desimone, R., 2001. Modulation of oscillatory neuronal synchronization by selective visual attention. Science (80-.). 291, 1560–1563. doi:10.1126/science.1055465

Gallagher, S.M., Daly, C.A., Bear, M.F., Huber, K.M., 2004. Extracellular signal-regulated protein kinase activation is required for metabotropic glutamate receptor-dependent long-term depression in hippocampal area CA1. J. Neurosci. 24, 4859–4864. doi:10.1523/JNEUROSCI.5407-03.2004

Galvez, R., Greenough, W.T., 2005. Sequence of abnormal dendritic spine development in primary somatosensory cortex of a mouse model of the fragile X mental retardation syndrome. Am. J. Med. Genet. 135A, 155–160. doi:10.1002/ajmg.a.30709

Gandhi, R.M., Kogan, C.S., Messier, C., 2014. 2-Methyl-6-(phenylethynyl) pyridine (MPEP) reverses maze learning and PSD-95 deficits in Fmr1 knock-out mice. Front. Cell. Neurosci. 8, 70. doi:10.3389/fncel.2014.00070

Gantois, I., Pop, A.S., de Esch, C.E.F., Buijsen, R.A.M., Pooters, T., Gomez-Mancilla, B., Gasparini, F., Oostra, B.A., D'Hooge, R., Willemsen, R., 2013.

Chronic administration of AFQ056/Mavoglurant restores social behaviour in Fmr1 knockout mice. Behav. Brain Res. 239, 72–79. doi:10.1016/j.bbr.2012.10.059

Gerstner, W., Kempter, R., van Hemmen, J.L., Wagner, H., 1996. A neuronal learning rule for sub-millisecond temporal coding. Nature 383, 76–78.

Ghabriel, M.N., Allt, G., 1981. Incisures of Schmidt-Lanterman. Prog. Neurobiol. 17, 25–58. doi:10.1016/0301-0082(81)90003-4

Ghanizadeh, A., Sahraeizadeh, A., Berk, M., 2014. A head-to-head comparison of aripiprazole and risperidone for safety and treating autistic disorders, a randomized double blind clinical trial. Child Psychiatry Hum. Dev. 45, 185–192.

Giampetruzzi, A., Carson, J.H., Barbarese, E., 2013. FMRP and myelin protein expression in oligodendrocytes. Mol. Cell. Neurosci. 56, 333–341. doi:10.1016/j.mcn.2013.07.009

Gillberg, C., Wing, L., 1999. Autism: not an extremely rare disorder. Acta Psychiatr. Scand. 99, 399–406. doi:10.1111/j.1600-0447.1999.tb00984.x

Girirajan, S., Rosenfeld, J.A., Coe, B.P., Parikh, S., Friedman, N., Goldstein, A., Filipink, R.A., McConnell, J.S., Angle, B., Meschino, W.S., Nezarati, M.M., Asamoah, A., Jackson, K.E., Gowans, G.C., Martin, J.A., Carmany, E.P., Stockton, D.W., Schnur, R.E., Penney, L.S., Martin, D.M., Raskin, S., Leppig, K., Thiese, H., Smith, R., Aberg, E., Niyazov, D.M., Escobar, L.F., El-Khechen, D., Johnson, K.D., Lebel, R.R., Siefkas, K., Ball, S., Shur, N., McGuire, M.,

Brasington, C.K., Spence, J.E., Martin, L.S., Clericuzio, C., Ballif, B.C., Shaffer, L.G., Eichler, E.E., 2012. Phenotypic heterogeneity of genomic disorders and rare copy-number variants. N. Engl. J. Med. 367, 1321–1331. doi:10.1056/NEJMoa1200395

Goldstein, J.L., Brown, M.S., 1990. Regulation of the mevalonate pathway. Nature 343, 425–430.

Gordon, J.A., Stryker, M.P., 1996. Experience-dependent plasticity of binocular responses in the primary visual cortex of the mouse. J. Neurosci. 16, 3274–3286.

Gray, C.M., Konig, P., Engel, A.K., Singer, W., 1989. Oscillatory responses in cat visual cortex exhibit inter-columnar synchronization which reflects global stimulus properties. Nature 338, 334–337.

Green, T., Barnea-Goraly, N., Raman, M., Hall, S.S., Lightbody, A.A., Bruno, J.L., Quintin, E.-M., Reiss, A.L., 2015. Specific effect of the fragile-X mental retardation-1 gene (FMR1) on white matter microstructure. Br. J. Psychiatry 207, 143–148. doi:10.1192/bjp.bp.114.151654

Grossman, A.W., Elisseou, N.M., McKinney, B.C., Greenough, W.T., 2006. Hippocampal pyramidal cells in adult Fmr1 knockout mice exhibit an immature-appearing profile of dendritic spines. Brain Res. 1084, 158–164. doi:10.1016/j.brainres.2006.02.044

Haas, B.W., Barnea-Goraly, N., Lightbody, A.A., Patnaik, S.S., Hoeft, F., Hazlett, H.C., Piven, J., Reiss, A.L., 2009. Early white-matter abnormalities of the

ventral frontostriatal pathway in fragile X syndrome. Dev. Med. Child Neurol. 51, 593–599.

Haas, L.F., 2003. Hans Berger (1873-1941), Richard Caton (1842-1926), and electroencephalography. J. Neurolology, Neurosurgery, Psychiatry 74, 9.

Hagerman, R.J., Polussa, J., 2015. Treatment of the psychiatric problems associated with fragile X syndrome. Curr. Opin. Psychiatry 28, 107–112. doi:10.1097/YCO.0000000000000131

Hall, S.S., Jiang, H., Reiss, A.L., Greicius, M.D., 2013. Identifying large-scale brain networks in fragile X syndrome. JAMA Psychiatry 70, 1215–1223. doi:10.1001/jamapsychiatry.2013.247

Hamdan, F.F., Daoud, H., Piton, A., Gauthier, J., Dobrzeniecka, S., Krebs, M.-O., Joober, R., Lacaille, J.-C., Nadeau, A., Milunsky, J.M., Wang, Z., Carmant, L., Mottron, L., Beauchamp, M.H., Rouleau, G.A., Michaud, J.L., 2011a. De novo SYNGAP1 mutations in nonsyndromic intellectual disability and autism. Biol. Psychiatry 69, 898–901. doi:10.1016/j.biopsych.2010.11.015

Hamdan, F.F., Gauthier, J., Araki, Y., Lin, D.-T., Yoshizawa, Y., Higashi, K., Park, A.-R., Spiegelman, D., Dobrzeniecka, S., Piton, A., Tomitori, H., Daoud, H., Massicotte, C., Henrion, E., Diallo, O., Shekarabi, M., Marineau, C., Shevell, M., Maranda, B., Mitchell, G., Nadeau, A., D'Anjou, G., Vanasse, M., Srour, M., Lafrenière, R.G., Drapeau, P., Lacaille, J.C., Kim, E., Lee, J.-R., Igarashi, K., Huganir, R.L., Rouleau, G.A., Michaud, J.L., 2011b. Excess of de novo deleterious mutations in genes associated with glutamatergic systems in nonsyndromic intellectual disability. Am. J. Hum. Genet. 88, 306–316.

doi:10.1016/j.ajhg.2011.02.001

Hamdan, F.F., Gauthier, J., Spiegelman, D., Noreau, A., Yang, Y., Pellerin, S., Dobrzeniecka, S., Cote, M., Perreau-Linck, E., Carmant, L., D'Anjou, G., Fombonne, E., Addington, A.M., Rapport, J.L., Delisi, L.E., Krebs, M.-O., Mouaffak, F., Joober, R., Mottron, L., Drapeau, P., Marineau, C., Lafreniere, R.G., Lacaille, J.C., Rouleau, G.A., Michaud, J.L., 2009. Mutations in SYNGAP1 in autosomal nonsyndromic mental retardation. N. Engl. J. Med. 360, 599–605.

Hamilton, S.M., Green, J.R., Veeraragavan, S., Yuva, L., McCoy, A., Wu, Y., Warren, J., Little, L., Ji, D., Cui, X., Weinstein, E., Paylor, R., 2014. Fmr1 and Nlgn3 knockout rats: novel tools for investigating autism spectrum disorders. Behav. Neurosci. 128, 103–109. doi:10.1037/a0035988

Han, H., Weinreb, P.H., Lansbury, P.T.J., 1995. The core Alzheimer's peptide NAC forms amyloid fibrils which seed and are seeded by beta-amyloid: is NAC a common trigger or target in neurodegenerative disease? Chem. Biol. 2, 163–169. doi:10.1016/1074-5521(95)90071-3

Hardan, A.Y., Minshew, N.J., S, K.M., 2000. Corpus callosum size in autism. Neurology 55, 1033–1036. doi:10.1159/000101293

Harlow, E.G., Till, S.M., Russell, T.A., Wijetunge, L.S., Kind, P.C., Contractor, A., 2010. Critical period plasticity is disrupted in the barrel cortex of Fmr1 knockout mice. Neuron 65, 385–398. doi:10.1016/j.neuron.2010.01.024

Harris, J.C., 2006. Intellectual Disability: Understanding Its Development, Causes,

Classification, Evaluation, and Treatment. Oxford University Press, New York, NY.

Harris, K.D., Csicsvari, J., Hirase, H., Dragoi, G., Buzsáki, G., 2003. Organization of cell assemblies in the hippocampus. Nature 424, 552–556. doi:10.1038/nature01765.1.

Harris, K.M., Jensen, F.E., Tsao, B., 1992. Three-dimensional structure of dendritic spines and synapses in rat hippocampus (CA1) at postnatal day 15 and adult ages: implications for the maturation of synaptic physiology and long-term potentiation. J. Neurosci. 12, 2685–2705.

Harrison, C.J., Jack, E.M., Allen, T.D., Harris, R., 1983. The fragile X: a scanning electron microscope study. J. Med. Genet. 20, 280–285.

Hasenstaub, A., Shu, Y., Haider, B., Kraushaar, U., Duque, A., McCormick, D.A., 2005. Inhibitory postsynaptic potentials carry synchronized frequency information in active cortical networks. Neuron 47, 423–435. doi:10.1016/j.neuron.2005.06.016

Hatton, D.D., Sideris, J., Skinner, M., Mankowski, J., Jr, D.B.B., Roberts, J., Mirrett, P., 2006. Autistic behavior in children with fragile X syndrome: prevalence, stability, and the impact of FMRP. Am. J. Med. Genet. A 140A, 1804–1813. doi:10.1002/ajmg.a

Hayashi, M.L., Rao, B.S.S., Seo, J.-S., Choi, H.-S., Dolan, B.M., Choi, S.-Y., Chattarji, S., Tonegawa, S., 2007. Inhibition of p21-activated kinase rescues symptoms of fragile X syndrome in mice. Proc. Natl. Acad. Sci. U. S. A. 104,

11489–11494. doi:10.1073/pnas.0705003104

Hayashi, Y., Shi, S.-H., Esteban, J.A., Piccini, A., Poncer, J.-C., Malinow, R., 2000. Driving AMPA receptors into synapses by LTP and CaMKII: requirement for GluR1 and PDZ domain interaction. Science (80-.). 287, 2262–2267. doi:10.1126/science.287.5461.2262

Hazlett, H.C., Poe, M., Gerig, G., Smith, R.G., Provenzale, J., Ross, A., Gilmore, J., Piven, J., 2005. Magnetic resonance imaging and head circumference study of brain size in autism: birth through age 2 years. Arch. Gen. Psychiatry 62, 1366–1376. doi:10.1016/S0098-1672(08)70087-0

He, C.X., Portera-Cailliau, C., 2013. The trouble with spines in fragile X syndrome: density, maturity and plasticity. Neuroscience 251, 120–128. doi:10.1016/j.neuroscience.2012.03.049

Henderson, C., Wijetunge, L., Kinoshita, M.N., Shumway, M., Hammond, R.S., Postma, F.R., Brynczka, C., Rush, R., Thomas, A., Paylor, R., Warren, S.T., Vanderklish, P.W., Kind, P.C., Carpenter, R.L., Bear, M.F., Healy, A.M., 2012. Reversal of disease-related pathologies in the fragile X mouse model by selective activation of GABAB receptors with arbaclofen. Sci. Transl. Med. 4, 152ra128. doi:10.1126/scitranslmed.3004218

Henrie, J.A., Shapley, R., 2005. LFP power spectra in V1 cortex: the graded effect of stimulus contrast. J. Neurophysiol. 94, 479–490. doi:10.1152/jn.00919.2004

Hering, H., Sheng, M., 2001. Dendritic spines: structure, dynamics and regulation. Nat. Rev. Neurosci. 2, 880–888. doi:10.1038/35104061

Hermes, D., Miller, K.J., Wandell, B.A., Winawer, J., 2015. Gamma oscillations in visual cortex: the stimulus matters. Trends Cogn. Sci. 19, 57–58. doi:10.1016/j.tics.2014.12.009

Hermes, D., Miller, K.J., Wandell, B.A., Winawer, J., 2014. Stimulus dependence of gamma oscillations in human visual cortex. Cereb. Cortex 25, 2951–2959. doi:10.1093/cercor/bhu091

Heulens, I., Suttie, M., Postnov, A., De Clerck, N., Perrotta, C.S., Mattina, T., Faravelli, F., Forzano, F., Kooy, R.F., Hammond, P., 2013. Craniofacial characteristics of fragile X syndrome in mouse and man. Eur. J. Hum. Genet. 21, 816–823. doi:10.1038/ejhg.2012.265

Heynen, A.J., Bear, M.F., 2001. Long-term potentiation of thalamocortical transmission in the adult visual cortex in vivo. J. Neurosci. 21, 9801–9813. doi:21/24/9801 [pii]

Higgins, J.B., Casey, P.J., 1996. The role of prenylation in G-protein assembly and function. Cell. Signal. 8, 433–437. doi:10.1016/S0898-6568(96)00071-X

Hildebrand, C., Remahl, S., Persson, H., Bjartmar, C., 1993. Myelinated nerve fibres in the CNS. Prog. Neurobiol. 40, 319–384.

Hinds, H.L., Ashley, C.T., Sutcliffe, J.S., Nelson, D.L., Warren, S.T., Housman, D.E., Schalling, M., 1993. Tissue specific expression of FMR-1 provides evidence for a functional role in fragile X syndrome. Nat. Genet. 3, 36–43.

Hinton, V.J., Brown, W.T., Wisniewski, K., Rudelli, R.D., 1991. Analysis of neocortex in three males with the fragile X syndrome. Am. J. Med. Genet. 41,

289–294.

Hoeffer, C.A., Sanchez, E., Hagerman, R.J., Mu, Y., Nguyen, D. V, Wong, H., Whelan, A.M., Zukin, R.S., Klann, E., Tassone, F., 2012. Altered mTOR signaling and enhanced CYFIP2 expression levels in subjects with fragile X syndrome. Genes, Brain Behav. 11, 332–341. doi:10.1111/j.1601-183X.2012.00768.x

Hoeft, F., Carter, J.C., Lightbody, A.A., Cody Hazlett, H., Piven, J., Reiss, A.R., 2010. Region-specific alterations in brain development in one- to three-year-old boys with fragile X syndrome. Proc. Natl. Acad. Sci. U. S. A. 107, 9335–9339. doi:10.1073/pnas.1002762107

Holmberg, E., Zhang, S., Sarmiere, P.D., Kluge, B.R., White, J.T., Doolen, S., 2008. Statins decrease chondroitin sulfate proteoglycan expression and acute astrocyte activation in central nervous system injury. Exp. Neurol. 214, 78–86. doi:10.1016/j.expneurol.2008.07.020

Holtmaat, A.J.G.D., Trachtenberg, J.T., Wilbrecht, L., Shepherd, G.M., Zhang, X., Knott, G.W., Svoboda, K., 2005. Transient and persistent dendritic spines in the neocortex in vivo. Neuron 45, 279–291. doi:10.1016/j.neuron.2005.01.003

Howlin, P., 2003. Outcome in high-functioning adults with autism with and without early language delays: implications for the differentiation between autism and Asperger syndrome. J. Autism Dev. Disord. 33, 3–13. doi:10.1023/A:1022270118899

Huber, K.M., Gallagher, S.M., Warren, S.T., Bear, M.F., 2002. Altered synaptic

plasticity in a mouse model of fragile X mental retardation. Proc. Natl. Acad. Sci. U. S. A. 99, 7746–7750. doi:10.1073/pnas.122205699

Hursh, J.B., 1939. Conduction velocity and diameter of nerve fibers. Am. J. Physiol. 127, 131–139.

Innocenti, G.M., Aggoun-Zouaoui, D., Lehmann, P., 1995. Cellular aspects of callosal connections and their development. Neuropsychologia 33, 961–987.

Iossifov, I., Ronemus, M., Levy, D., Wang, Z., Hakker, I., Rosenbaum, J., Yamrom, B., Lee, Y., Narzisi, G., Leotta, A., Kendall, J., Grabowska, E., Ma, B., Marks, S., Rodgers, L., Stepansky, A., Troge, J., Andrews, P., Bekritsky, M., Pradhan, K., Ghiban, E., Kramer, M., Parla, J., Demeter, R., Fulton, L.L., Fulton, R.S., Magrini, V.J., Ye, K., Darnell, J.C., Darnell, R.B., Mardis, E.R., Wilson, R.K., Schatz, M.C., McCombie, W.R., Wigler, M., 2012. De novo gene disruptions in children on the autistic spectrum. Neuron 74, 285–299. doi:10.1016/j.neuron.2012.04.009

Irwin, S.A., Galvez, R., Greenough, W.T., 2000. Dendritic spine structural anomalies in fragile-X mental retardation syndrome. Cereb. Cortex 10, 1038–1044.

Irwin, S.A., Idupulapati, M., Gilbert, M.E., Harris, J.B., Chakravarti, A.B., Rogers, E.J., Crisostomo, R.A., Larsen, B.P., Mehta, A., Alcantara, C.J., Patel, B., Swain, R.A., Weiler, I.J., Oostra, B.A., Greenough, W.T., 2002. Dendritic spine and dendritic field characteristics of layer V pyramidal neurons in the visual cortex of fragile-X knockout mice. Am. J. Med. Genet. 111, 140–146. doi:10.1002/ajmg.10500

Irwin, S.A., Patel, B., Idupulapati, M., Harris, J.B., Crisostomo, R.A., Larsen, B.P., Kooy, R.F., Willems, P.J., Cras, P., Kozlowski, P.B., Swain, R.A., Weiler, I.J., Greenough, W.T., 2001. Abnormal dendritic spine characteristics in the temporal and visual cortices of patients with fragile-X syndrome: a quantitative examination. Am. J. Med. Genet. 98, 161–167.

Isaacson, J.S., Scanziani, M., 2011. How inhibition shapes cortical activity. Neuron 72, 231–243. doi:10.1016/j.neuron.2011.09.027

Istvan, E.S., Deisenhofer, J., 2001. Structural mechansim for statin inhibition of HMG-CoA reductase. Science (80-.). 292, 1160–1164. doi:10.1126/science.1059344

Iwai, A., Yoshimoto, M., Masliah, E., Saitoh, T., 1995. Non-Aβ component of Alzheimer's disease amyloid (NAC) is amyloidogenic. Biochemistry 34, 10139–10145.

Jacquemont, S., Hagerman, R.J., Hagerman, P.J., Leehey, M.A., 2007. Fragile-X syndrome and fragile X-associated tremor/ataxia syndrome: two faces of FMR1. Lancet Neurol. 6, 45–55. doi:10.1016/S1474-4422(06)70676-7

Janusz, A., Milek, J., Perycz, M., Pacini, L., Bagni, C., Kaczmarek, L., Dziembowska, M., 2013. The fragile X mental retardation protein regulates matrix metalloproteinase 9 mRNA at synapses. J. Neurosci. 33, 18234–18241. doi:10.1523/JNEUROSCI.2207-13.2013

Jensen, P.H., Højrup, P., Hager, H., Nielsen, M.S., Jacobsen, L., Olesen, O.F., Gliemann, J., Jakes, R., 1997. Binding of Aβ to α-synuclein and β-synucleins:

identification of segments in α-synuclein/NAC precursor that bind Aβ and NAC. Biochem. J. 323, 539–546.

Ji, N.Y., Findling, R.L., 2015. An update on pharmacotherapy for autism spectrum disorder in children and adolescents. Curr. Opin. Psychiatry 28, 91–101. doi:10.1097/YCO.0000000000000132

Jia, X., Kohn, A., 2011. Gamma rhythms in the brain. PLoS Biol. 9, e1001045. doi:10.1371/journal.pbio.1001045

Jin, P., Warren, S.T., 2000. Understanding the molecular basis of fragile X syndrome. Hum. Mol. Genet. 9, 901–908.

Johnson, M.D., Woodard, A., Okediji, E.J., Toms, S.A., Allen, G.S., 2002. Lovastatin is a potent inhibitor of meningioma cell proliferation: evidence for inhibition of a mitogen associated protein kinase. J. Neurooncol. 56, 133–142.

Kahana, M.J., Seelig, D., Madsen, J.R., 2001. Theta returns. Curr. Opin. Neurobiol. 11, 739–744.

Kaneko, M., Stellwagen, D., Malenka, R.C., Stryker, M.P., 2008. Tumor necrosis factor-α mediates one component of competitive, experience-dependent plasticity in developing visual cortex. Neuron 58, 673–680. doi:10.1016/j.neuron.2008.04.023

Kanner, L., 1943. Autistic disturbances of affective contact. Nerv. Child 2, 217–250.

Kelleher, R.J.I., Bear, M.F., 2008. The autistic neuron: troubled translation? Cell 135, 401–406. doi:10.1016/j.cell.2008.10.017

Kemper, T.L., Bauman, M.L., 1993. The contribution of neuropathologic studies to

the understanding of autism. Neurol. Clin. 11, 175–187.

Kerby, D.S., Dawson, B.L., 1994. Autistic features, personality, and adaptive behavior in males with the fragile X syndrome and no autism. Am. J. Ment. Retard. 998, 455–462.

Kim, J.A., Szatmari, P., Bryson, S.E., Streiner, D.L., Wilson, F.J., 2000. The prevalence of anxiety and mood problems among children with autism and Asperger syndrome. Autism 4, 117–132. doi:10.1177/1362361300004002002

Kim, Y.S., Leventhal, B.L., Koh, Y.-J., Fombonne, E., Laska, E., Lim, E.-C., Cheon, K.-A., Kim, S.-J., Kim, Y.-K., Lee, H., Song, D.-H., Grinker, R.R., 2011. Prevalence of autism spectrum disorders in a total populaiton sample. Am. J. Psychiatry 168, 904–912.

King, B.H., Toth, K.E., Hodapp, R.M., Dykens, E.M., 2009. Intellectual disability, in: Sadock, B.J., Sadock, V.A., Ruiz, P. (Eds.), Comprehensive Textbook of Psychiatry. Lippincott Williams & Wilkins, Philadelphia, pp. 3444–3474.

Kirkwood, A., Silva, A., Bear, M.F., 1997. Age-dependent decrease of synaptic plasticity in the neocortex of alphaCaMKII mutant mice. Proc. Natl. Acad. Sci. U. S. A. 94, 3380–3383. doi:10.1073/pnas.94.7.3380

Klann, E., Dever, T.E., 2004. Biochemical mechanisms for translational regulation in synaptic plasticity. Nat. Rev. Neurosci. 5, 931–942. doi:10.1038/nrn1557

Knafo, S., Ariav, G., Barkai, E., Libersat, F., 2004. Olfactory learning-induced increase in spine density along the apical dendrites of CA1 hippocampal neurons. Hippocampus 14, 819–825. doi:10.1002/hipo.10219

Kogan, M.D., Blumberg, S.J., Schieve, L.A., Boyle, C.A., Perrin, J.M., Ghandour, R.M., Singh, G.K., Strickland, B.B., Trevathan, E., van Dyck, P.C., 2009. Prevalence of parent-reported diagnosis of autism spectrum disorder among children in the US, 2007. Pediatrics 124, 1395–1403. doi:10.1542/peds.2009-1522

Kooy, R.F., 2003. Of mice and the fragile X syndrome. Trends Genet. 19, 148–154.

Koth, C.W., Cutting, L.E., Denckla, M.B., 2000. The association of Neurofibromatosis Type 1 and attention deficit hyperactivity disorder. Child Neuropsychol. 6, 185–194. doi:10.1076/chin.6.3.185.3155

Krueger, D.D., Bear, M.F., 2011. Toward fulfilling the promise of molecular medicine in fragile X syndrome. Annu. Rev. Med. 62, 411–429.

Kuddo, T., Nelson, K., 2003. How common are gastrointestinal disorders in children with autism? Curr. Opin. Pediatr. 15, 339–343.

Kumar, S.S., Buckmaster, P.S., 2006. Hyperexcitability, interneurons, and loss of GABAergic synapses in entorhinal cortex in a model of temporal lobe epilepsy. J. Neurosci. 26, 4613–4623. doi:10.1523/JNEUROSCI.0064-06.2006

Kurihara, D., Yamashita, T., 2012. Chondroitin sulfate proteoglycans down-regulate spine formation in cortical neurons by targeting tropomyosin-related kinase B (TrkB) protein. J. Biol. Chem. 287, 13822–13828. doi:10.1074/jbc.M111.314070

Lachiewicz, A.M., Dawson, D. V, 1994. Do young boys with fragile X syndrome have macroorchidism? Pediatrics 93, 992–995.

Laggerbauer, B., Ostareck, D., Keidel, E.-M., Ostareck-Lederer, A., Fischer, U., 2001. Evidence that fragile X mental retardation protein is a negative regulator of translation. Hum. Mol. Genet. 10, 329–338. doi:10.1093/hmg/10.4.329

Lauritsen, M.B., Ewald, H., 2001. The genetics of autism. Acta Psychiatr. Scand. 103, 411–427. doi:10.1016/j.spen.2004.07.003

Lavedan, C., Grabczyk, E., Usdin, K., Nussbaum, R.L., 1998. Long uninterrupted CGG repeats within the first exon of the human FMR1 gene are not intrinsically unstable in transgenic mice. Genomics 50, 229–240. doi:10.1006/geno.1998.5299

Lavedan, C.N., Garrett, L., Nussbaum, R.L., 1997. Trinucleotide repeats (CGG)22TGG(CGG)43TGG(CGG)21 from the fragile X gene remain stable in transgenic mice. Hum. Genet. 100, 407–414.

Lee, A., Li, W., Xu, K., Bogert, B.A., Su, K., Gao, F.-B., 2003. Control of dendritic development by the Drosophila fragile X-related gene involves the small GTPase Rac1. Development 130, 5543–5552. doi:10.1242/dev.00792

Lein, E.S., Hawrylycz, M.J., Ao, N., Ayres, M., Bensinger, A., Bernard, A., Boe, A.F., Boguski, M.S., Brockway, K.S., Byrnes, E.J., Chen, L., Chen, L., Chen, T.-M., Chi Chin, M., Chong, J., Crook, B.E., Czaplinska, A., Dang, C.N., Datta, S., Dee, N.R., Desaki, A.L., Desta, T., Diep, E., Dolbeare, T.A., Donelan, M.J., Dong, H.-W., Dougherty, J.G., Duncan, B.J., Ebbert, A.J., Eichele, G., Estin, L.K., Faber, C., Facer, B.A., Fields, R., Fischer, S.R., Fliss, T.P., Frensley, C., Gates, S.N., Glattfelder, K.J., Halverson, K.R., Hart, M.R., Hohmann, J.G., Howell, M.P., Jeung, D.P., Johnson, R.A., Karr, P.T., Kawal, R., Kidney, J.M.,

Knapik, R.H., Kuan, C.L., Lake, J.H., Laramee, A.R., Larsen, K.D., Lau, C., Lemon, T.A., Liang, A.J., Liu, Y., Luong, L.T., Michaels, J., Morgan, J.J., Morgan, R.J., Mortrud, M.T., Mosqueda, N.F., Ng, L.L., Ng, R., Orta, G.J., Overly, C.C., Pak, T.H., Parry, S.E., Pathak, S.D., Pearson, O.C., Puchalski, R.B., Riley, Z.L., Rockett, H.R., Rowland, S.A., Royall, J.J., Ruiz, M.J., Sarno, N.R., Schaffnit, K., Shapovalova, N. V, Sivisay, T., Slaughterbeck, C.R., Smith, S.C., Smith, K.A., Smith, B.I., Sodt, A.J., Stewart, N.N., Stumpf, K.-R., Sunkin, S.M., Sutram, M., Tam, A., Teemer, C.D., Thaller, C., Thompson, C.L., Varnam, L.R., Visel, A., Whitlock, R.M., Wohnoutka, P.E., Wolkey, C.K., Wong, V.Y., Wood, M., Yaylaoglu, M.B., Young, R.C., Youngstrom, B.L., Feng Yuan, X., Zhang, B., Zwingman, T.A., Jones, A.R., 2007. Genome-wide atlas of gene expression in the adult mouse brain. Nature 445, 168–176. doi:10.1038/nature05453

Leonard, H., Wen, X., 2002. The epidemiology of mental retardation: challenges and opportunities in the new millennium. Ment. Retard. Dev. Disabil. Res. Rev. 8, 117–134. doi:10.1002/mrdd.10031

Levy, S.E., Mandell, D.S., Schultz, R.T., 2009. Autism. Lancet 374, 1627–1638. doi:10.1016/S0140-6736(09)61376-3

Leyfer, O.T., Folstein, S.E., Bacalman, S., Davis, N.O., Dinh, E., Morgan, J., Tager-Flusberg, H., Lainhart, J.E., 2006. Comorbid psychiatric disorders in children with autism: interview development and rates of disorders. J. Autism Dev. Disord. 36, 849–861. doi:10.1007/s10803-006-0123-0

Li, W., Cui, Y., Kushner, S.A., Brown, R.A.M., Jentsch, J.D., Frankland, P.W.,

Cannon, T.D., Silva, A.J., 2005. The HMG-CoA reductase inhibitor lovastatin reverses the learning and attention deficits in a mouse model of Neurofibromatosis Type 1. Curr. Biol. 15, 1961–1967. doi:10.1016/j.cub.2005.09.043

Li, Z., Zhang, Y., Ku, L., Wilkinson, K.D., Warren, S.T., Feng, Y., 2001. The fragile X mental retardation protein inhibits translation via interacting with mRNA. Nucleic Acids Res. 29, 2276–2283.

Lisman, J., Yasuda, R., Raghavachari, S., 2012. Mechanisms of CaMKII action in long-term potentiation. Nat. Rev. Neurosci. 13, 169–182. doi:10.1038/nrn3192

Liu, Z.-H., Chuang, D.-M., Smith, C.B., 2011. Lithium ameliorates phenotypic deficits in a mouse model of fragile X syndrome. Int. J. Neuropsychopharmacol. 14, 618–630. doi:10.1017/S1461145710000520

Llinás, R., Ribary, U., 1993. Coherent 40-Hz oscillation characterizes dream state in humans. Proc. Natl. Acad. Sci. U. S. A. 90, 2078–2081. doi:10.1073/pnas.90.5.2078

Lubs, H.A., 1969. A marker X chromosome. Am. J. Hum. Genet. 21, 231–244.

Lubs, H.A., Stevenson, R.E., Schwartz, C.E., 2012. Fragile X and X-linked intellectual disability: four decades of discovery. Am. J. Hum. Genet. 90, 579–590. doi:10.1016/j.ajhg.2012.02.018

Ludwig, A.L., Espinal, G.M., Pretto, D.I., Jamal, A.L., Arque, G., Tassone, F., Berman, R.F., Hagerman, P.J., 2014. CNS expression of murine fragile X protein (FMRP) as a function of CGG-repeat size. Hum. Mol. Genet. 23, 3228–

3238. doi:10.1093/hmg/ddu032

Maestro, S., Muratori, F., Cavallaro, M.C., Pei, F., Stern, D., Golse, B., Palacio-Espasa, F., 2002. Attentional skills during the first 6 months of age in autism spectrum disorder. J. Am. Acad. Child Adolesc. Psychiatry 41, 1239–1245.

Malenka, R.C., 1994. Synaptic plasticity in the hippocampus: LTP and LTD. Cell 78, 535–538.

Maletic-Savatic, M., Malinow, R., Svoboda, K., 1999. Rapid dendritic morphogenesis in CA1 hippocampal dendrites induced by synaptic activity. Science (80-.). 283, 1923–1927. doi:10.1126/science.283.5409.1923

Malinow, R., Mainen, Z.F., Hayashi, Y., 2000. LTP mechanisms: from silence to four-lane traffic. Curr. Opin. Neurobiol. 10, 352–357. doi:10.1016/S0959-4388(00)00099-4

Mancuso, J.J., Chen, Y., Li, X., Xue, Z., Wong, S.T.C., 2013. Methods of dendritic spine detection: from Golgi to high-resolution optical imaging. Neuroscience 251, 129–140. doi:10.1016/j.neuroscience.2012.04.010

Mann, E.O., Suckling, J.M., Hajos, N., Greenfield, S.A., Paulsen, O., 2005. Perisomatic feedback inhibition underlies cholinergically induced fast network oscillations in the rat hippocampus in vitro. Neuron 45, 105–117. doi:10.1016/j.neuron.2004.12.016

Markram, H., Lubke, J., Frotscher, M., Sakmann, B., 1997. Regulation of synaptic efficacy by coincidence of postysnaptic APs and EPSPs. Science (80-.). 275, 213–215. doi:10.1126/science.275.5297.213

Maron, D.J., Fazio, S., Linton, M.F., 2000. Current perspectives on statins. Circulation 101, 207–213. doi:10.1007/978-94-017-9585-2

Martin, J.P., Bell, J., 1943. A pedigree of mental defect showing sex-linkage. J. Neurol. Psychiatry 6, 154–157. doi:10.1136/jnnp.6.3-4.154

Matson, J.L., Cervantes, P.E., 2013. Comorbidity among persons with intellectual disabilities. Res. Autism Spectr. Disord. 7, 1318–1322. doi:10.1016/j.rasd.2013.07.018

Matson, J.L., Neal, D., 2009. Seizures and epilepsy and their relationship to autism spectrum disorders. Res. Autism Spectr. Disord. 3, 999–1005. doi:10.1016/j.rasd.2009.06.003

Matson, J.L., Nebel-Schwalm, M.S., 2007. Comorbid psychopathology with autism spectrum disorder in children: an overview. Res. Dev. Disabil. 28, 341–352. doi:10.1016/j.ridd.2005.12.004

Maulik, P.K., Mascarenhas, M.N., Mathers, C.D., Dua, T., Saxena, S., 2011. Prevalence of intellectual disability: a meta-analysis of population-based studies. Res. Dev. Disabil. 32, 419–436. doi:10.1016/j.ridd.2010.12.018

McBride, S.M.J., Choi, C.H., Wang, Y., Liebelt, D., Braunstein, E., Ferreiro, D., Sehgal, A., Siwicki, K.K., Dockendorff, T.C., Nguyen, H.T., McDonald, T. V, Jongens, T.A., 2005. Pharmacological rescue of synaptic plasticity, courtship behavior, and mushroom body defects in a Drosophila model of fragile X syndrome. Neuron 45, 753–764. doi:10.1016/j.neuron.2005.01.038

McKinney, B.C., Grossman, A.W., Elisseou, N.M., Greenough, W.T., 2005.

Dendritic spine abnormalities in the occipital cortex of C57BL/6 Fmr1 knockout mice. Am. J. Med. Genet. Part B 136B, 98–102. doi:10.1002/ajmg.b.30183

McLaren, J., Bryson, S.E., 1987. Review of recent epidemiological studies of mental retardation: prevalence, associated disorders, and etiology. Am. J. Ment. Retard. 92, 243–254.

Mekada, K., Abe, K., Murakami, A., Nakamura, S., Nakata, H., Moriwaki, K., Obata, Y., Yoshiki, A., 2009. Genetic differences among C57BL/6 substrains. Exp. Anim. 58, 141–149.

Meredith, R.M., Holmgren, C.D., Weidum, M., Burnashev, N., Mansvelder, H.D., 2007. Increased threshold for spike-timing-dependent plasticity is caused by unreliable calcium signaling in mice lacking fragile X gene Fmr1. Neuron 54, 627–638. doi:10.1016/j.neuron.2007.04.028

Michalon, A., Sidorov, M., Ballard, T.M., Ozmen, L., Spooren, W., Wettstein, J.G., Jaeschke, G., Bear, M.F., Lindemann, L., 2012. Chronic pharmacological mGlu5 inhibition corrects fragile X in adult mice. Neuron 74, 49–56. doi:10.1016/j.neuron.2012.03.009

Michel, C.I., Kraft, R., Restifo, L.L., 2004. Defective neuronal development in the mushroom bodies of Drosophila fragile X mental retardation 1 mutants. J. Neurosci. 24, 5798–5809. doi:10.1523/JNEUROSCI.1102-04.2004

Middleton, F.A., Strick, P.L., 1994. Anatomical evidence for cerebellar and basal ganglia involvement in higher cognitive function. Science (80-.). 266, 458–461. doi:10.1126/science.7939688

Miles, J.H., 2011. Autism spectrum disorders--a genetics review. Genet. Med. 13, 278–294. doi:10.1097/GIM.0b013e3181ff67ba

Morales, J., Hiesinger, P.R., Schroeder, A.J., Kume, K., Verstreken, P., Jackson, F.R., Nelson, D.L., Hassan, B.A., 2002. Drosophila fragile X protein, DFXR, regulates neuronal morphology and function in the brain. Neuron 34, 961–972. doi:10.1016/S0896-6273(02)00731-6

Morgan, V.A., Croft, M.L., Valuri, G.M., Zubrick, S.R., Bower, C., McNeil, T.F., Jablensky, A. V, 2012. Intellectual disability and other neuropsychiatric outcomes in high-risk children of mothers with schizophrenia, bipolar disorder and unipolar major depression. Br. J. Psychiatry 200, 282–289. doi:10.1192/bjp.bp.111.093070

Morgan, V.A., Leonard, H., Bourke, J., Jablensky, A., 2008. Intellectual disability co-occurring with schizophrenia and other psychiatric illness: population-based study. Br. J. Psychiatry 193, 364–372. doi:10.1192/bjp.bp.107.044461

Moseley, R.L., Ypma, R.J.F., Holt, R.J., Floris, D., Chura, L.R., Spencer, M.D., Baron-Cohen, S., Suckling, J., Bullmore, E., Rubinov, M., 2015. Whole-brain functional hypoconnectivity as an endophenotype of autism in adolescents. NeuroImage Clin. 9, 140–152. doi:10.1016/j.nicl.2015.07.015

Moser, M.-B., Trommald, M., Andersen, P., 1994. An increase in dendritic spine density on hippocampal CA1 pyramidal cells following spatial learning in adult rats suggests the formation of new synapses. Proc. Natl. Acad. Sci. U. S. A. 91, 12673–12675.

Mostofsky, S.H., Mazzocco, M.M.M., Aakalu, G., Warsofsky, I.S., Denckla, M.B., Reiss, A.L., 1998. Decreased cerebellar posterior vermis size in fragile X syndrome: correlation with neurocognitive performance. Neurology 50, 121–130. doi:10.1212/WNL.50.1.121

Mrsic-Flogel, T.D., Hofer, S.B., Ohki, K., Reid, R.C., Bonhoeffer, T., Hübener, M., 2007. Homeostatic regulation of eye-specific responses in visual cortex during ocular dominance plasticity. Neuron 54, 961–972. doi:10.1016/j.neuron.2007.05.028

Musumeci, S.A., Bosco, P., Calabrese, G., Bakker, C., De Sarro, G.B., Elia, M., Ferri, R., Oostra, B.A., 2000. Audiogenic seizures susceptibility in transgenic mice with fragile X syndrome. Epilepsia 41, 19–23.

Musumeci, S.A., Ferri, R., Elia, M., Colognola, R.M., Bergonzi, P., Tassinari, C.A., 1991. Epilepsy and fragile X syndrome: a follow-up study. Am. J. Med. Genet. 38, 511–513.

Nase, G., Singer, W., Monyer, H., Engel, A.K., 2003. Features of neuronal synchrony in mouse visual cortex. J. Neurophysiol. 90, 1115–1123. doi:10.1152/jn.00480.2002

Newschaffer, C.J., Croen, L.A., Daniels, J., Giarelli, E., Grether, J.K., Levy, S.E., Mandell, D.S., Miller, L.A., Pinto-Martin, J., Reaven, J., Reynolds, A.M., Rice, C.E., Schendel, D., Windham, G.C., 2007. The epidemiology of autism spectrum disorders. Annu. Rev. Public Health 28, 235–258. doi:10.1146/annurev.publhealth.28.021406.144007

Nimchinsky, E.A., Oberlander, A.M., Svoboda, K., 2001. Abnormal development of dendritic spines in FMR1 knock-out mice. J. Neurosci. 21, 5139–5146.

Nosyreva, E.D., Huber, K.M., 2006. Metabotropic receptor-dependent long-term depression persists in the absence of protein synthesis in the mouse model of fragile X syndrome. J. Neurophysiol. 95, 3291–3295. doi:10.1152/jn.01316.2005

O'Donnell, W.T., Warren, S.T., 2002. A decade of molecular studies of fragile X syndrome. Annu. Rev. Neurosci. 25, 315–338. doi:10.1146/annurev.neuro.25.112701.142909

O'Roak, B.J., Deriziotis, P., Lee, C., Vives, L., Schwartz, J.J., Girirajan, S., Karakoc, E., MacKenzie, A.P., Ng, S.B., Baker, C., Rieder, M.J., Nickerson, D.A., Bernier, R., Fisher, S.E., Shendure, J., Eichler, E.E., 2011. Exome sequencing in sporadic autism spectrum disorders identifies severe de novo mutations. Nat. Genet. 43, 585–589. doi:10.1038/ng.835

O'Roak, B.J., State, M.W., 2008. Autism genetics: strategies, challenges, and opportunities. Autism Res. 1, 4–17. doi:10.1002/aur.3

O'Roak, B.J., Vives, L., Girirajan, S., Karakoc, E., Krumm, N., Coe, B.P., Levy, R., Ko, A., Lee, C., Smith, J.D., Turner, E.H., Stanaway, I.B., Vernot, B., Malig, M., Baker, C., Reilly, B., Akey, J.M., Borenstein, E., Rieder, M.J., Nickerson, D.A., Bernier, R., Shendure, J., Eichler, E.E., 2012. Sporadic autism exomes reveal a highly interconnected protein network of de novo mutations. Nature 485, 246–250. doi:10.1038/nature10989

Ogawa, S., Tank, D.W., Menon, R., Ellermann, J.M., Kim, S.-G., Merkle, H., Ugurbil, K., 1992. Intrinsic signal changes accompanying sensory stimulation: functional brain mapping with magnetic resonance imaging. Proc. Natl. Acad. Sci. U. S. A. 89, 5951–5955.

Olivares, R., Montiel, J., Aboitiz, F., 2001. Species differences and similarities in the fine structure of the mammalian corpus callosum. Brain. Behav. Evol. 57, 98–105.

Olmos-Serrano, J.L., Paluszkiewicz, S.M., Martin, B.S., Kaufmann, W.E., Corbin, J.G., Huntsman, M.M., 2010. Defective GABAergic neurotransmission and pharmacological rescue of neuronal hyperexcitability in the amygdala in a mouse model of fragile X syndrome. J. Neurosci. 30, 9929–9938. doi:10.1523/JNEUROSCI.1714-10.2010

Osterweil, E.K., Chuang, S.-C., Chubykin, A.A., Sidorov, M., Bianchi, R., Wong, R.K.S., Bear, M.F., 2013. Lovastatin corrects excess protein synthesis and prevents epileptogenesis in a mouse model of fragile X syndrome. Neuron 77, 243–250. doi:10.1016/j.neuron.2012.01.034

Osterweil, E.K., Krueger, D.D., Reinhold, K., Bear, M.F., 2010. Hypersensitivity to mGluR5 and ERK1/2 leads to excessive protein synthesis in the hippocampus of a mouse model of fragile X syndrome. J. Neurosci. 30, 15616–15627. doi:10.1523/JNEUROSCI.3888-10.2010

Ozonoff, S., 1999. Cognitive impairment in Neurofibromatosis Type 1. Am. J. Med. Genet. 89, 45–52. doi:10.1002/(SICI)1096-8628(19990326)89:1<45::AID-AJMG9>3.0.CO;2-J

Pacey, L.K.K., Xuan, I.C.Y., Guan, S., Sussman, D., Henkelman, R.M., Chen, Y., Thomsen, C., Hampson, D.R., 2013. Delayed myelination in a mouse model of fragile X syndrome. Hum. Mol. Genet. 22, 3920–3920. doi:10.1093/hmg/ddt246

Palman, S.J.M.C., Van Engeland, H., Hof, P.R., Schmitz, C., 2004. Neuropathological findings in autism. Brain 127, 2572–2583. doi:10.1016/j.cdip.2004.01.005

Partington, M.W., 1984. The fragile X syndrome II: preliminary data on growth and development in males. Am. J. Med. Genet. 17, 175–194.

Paul, R., Grieve, S.M., Chaudary, B., Gordon, N., Lawrence, J., Cooper, N., Clark, C.R., Kukla, M., Mulligan, R., Gordon, E., 2009. Relative contributions of the cerebellar vermis and prefrontal lobe volumes on cognitive function across the adult lifespan. Neurobiol. Aging 30, 457–465. doi:10.1016/j.neurobiolaging.2007.07.017

Penagarikano, O., Mulle, J.G., Warren, S.T., 2007. The pathophysiology of fragile X syndrome. Annu. Rev. Genomics Hum. Genet. 8, 109–129. doi:10.1146/annurev.genom.8.080706.092249

Peters, S.U., Beaudet, A.L., Madduri, N., Bacino, C.A., 2004. Autism in Angelman syndrome: implications for autism research. Clin. Genet. 66, 530–536. doi:10.1111/j.1399-0004.2004.00362.x

Pfeiffer, B.E., Huber, K.M., 2007. Fragile X mental retardation protein induces synapse loss through acute postsynaptic translational regulation. J. Neurosci. 27, 3120–3130. doi:10.1523/JNEUROSCI.0054-07.2007

Pieretti, M., Zhang, F., Fu, Y.-H., Warren, S.T., Oostra, B.A., Caskey, C.T., Nelson, D.L., 1991. Absence of expression of the FMR-1 gene in fragile X syndrome. Cell 66, 817–822. doi:10.1016/0092-8674(91)90125-I

Polimeni, M.A., Richdale, A.L., Francis, A.J.P., 2005. A survey of sleep problems in autism, Asperger's disorder and typically developing children. J. Intellect. Disabil. Res. 49, 260–268. doi:10.1111/j.1365-2788.2005.00642.x

Polymeropoulos, M.H., Lavedan, C., Leroy, E., Ide, S.E., Dehejia, A., Dutra, A., Pike, B., Root, H., Rubenstein, J., Boyer, R., Stenroos, E.S., Chandrasekharappa, S., Athanassiadou, A., Papapetropoulos, T., Johnson, W.G., Lazzarini, A.M., Duvoisin, R.C., Iorio, G. Di, Golbe, L.I., Nussbaum, R.L., 1997. Mutation in the α-synuclein gene identified in families with Parkinson ' s disease. Science (80-.). 276, 2045–2047. doi:10.1126/science.276.5321.2045

Pop, A.S., Levenga, J., de Esch, C.E.F., Buijsen, R.A.M., Nieuwenhuizen, I.M., Li, T., Isaacs, A., Gasparini, F., Oostra, B.A., Willemsen, R., 2014. Rescue of dendritic spine phenotype in Fmr1 KO mice with the mGluR5 antagonist AFQ056/Mavoglurant. Psychopharmacology (Berl). 231, 1227–1235. doi:10.1007/s00213-012-2947-y

Popescu, A.T., Popa, D., Paré, D., 2009. Coherent gamma oscillations couple the amygdala and striatum during learning. Nat. Neurosci. 12, 801–807. doi:10.1038/nn.2305

Porciatti, V., Pizzorusso, T., Maffei, L., 1999. The visual physiology of the wild type mouse determined with pattern VEPs. Vision Res. 39, 3071–3081.

Portera-Cailliau, C., 2012. Which comes first in fragile X syndrome, dendritic spine dysgenesis or defects in circuit plasticity? Neurosci. 18, 28–44. doi:10.1177/1073858410395322

Pritchett, D.L., Siegle, J.H., Deister, C.A., Moore, C.I., 2015. For things needing your attention: the role of neocortical gamma in sensory perception. Curr. Opin. Neurobiol. 31, 254–263. doi:10.1016/j.conb.2015.02.004

Qin, M., Kang, J., Burlin, T. V, Jiang, C., Smith, C.B., 2005. Postadolescent changes in regional cerebral protein synthesis: an in vivo study in the Fmr1 null mouse. J. Neurosci. 25, 5087–5095. doi:10.1523/JNEUROSCI.0093-05.2005

Raichle, M.E., 2003. Functional brain imaging and human brain function. J. Neurosci. 23, 3959–3962.

Ranson, A., Cheetham, C.E.J., Fox, K., Sengpiel, F., 2012. Homeostatic plasticity mechanisms are required for juvenile, but not adult, ocular dominance plasticity. Proc. Natl. Acad. Sci. U. S. A. 109, 1311–1316. doi:10.1073/pnas.1112204109

Rauch, A., Hoyer, J., Guth, S., Zweier, C., Kraus, C., Becker, C., Zenker, M., Huffmeier, U., Thiel, C., Ruschendorf, F., Nurnberg, P., Reis, A., Trautmann, U., 2006. Diagnostic yield of various genetic approaches in patients with unexplained developmental delay or mental retardation. Am. J. Med. Genet. A 140A, 2063–2074. doi:10.1002/ajmg.a

Reheman, A., Tasneem, S., Ni, H., Hayward, C.P.M., 2010. Mice with deleted multimerin 1 and alpha-synuclein genes have impaired platelet adhesion and impaired thrombus formation that is corrected by multimerin 1. Thromb. Res.

125, e177–e183.

Restivo, L., Ferrari, F., Passino, E., Sgobio, C., Bock, J., Oostra, B.A., Bagni, C., Ammassari-Teule, M., 2005. Enriched environment promotes behavioral and morphological recovery in a mouse model for the fragile X syndrome. Proc. Natl. Acad. Sci. U. S. A. 102, 11557–11562. doi:10.1073/pnas.0504984102

Reyniers, E., Martin, J.J., Cras, P., Van Marck, E., Handig, I., Jorens, H.Z.J., Oostra, B.A., Kooy, R.F., Willems, P.J., 1999. Postmortem examination of two fragile X brothers with an FMR1 full mutation. Am. J. Med. Genet. 84, 245–249. doi:10.1002/(SICI)1096-8628(19990528)84:3<245::AID-AJMG16>3.0.CO;2-U

Richards, R.I., Sutherland, G.R., 1997. Dynamic mutation: possible mechanisms and significance in human disease. Trends Biochem. Sci. 22, 432–436. doi:10.1016/S0968-0004(97)01108-0

Ritvo, E.R., Freeman, B.J., Mason-Brothers, A., Mo, A., Ritvo, A.M., 1985. Concordance for the syndrome of autism in 40 pairs of afflicted twins. Am. J. Psychiatry 142, 74–77.

Ritvo, E.R., Freeman, B.J., Scheibel, A.B., Duong, T., Robinson, H., Guthrie, D., Ritvo, A., 1986. Lower Purkinje cell counts in the cerebella of four autistic subjects: initial findings of the UCLA-NSAC Autopsy Research Report. Am. J. Psychiatry 143, 862–866.

Roberson, E.D., English, J.D., Adams, J.P., Selcher, J.C., Kondratick, C., Sweatt, J.D., 1999. The mitogen-activated protein kinase cascade couples PKA and PKC to cAMP response element binding protein phosphorylation in area CA1

of hippocampus. J. Neurosci. 19, 4337–4348. doi:10341237

Robu, M.E., Larson, J.D., Nasevicius, A., Beiraghi, S., Brenner, C., Farber, S.A., Ekker, S.C., 2007. P53 activation by knockdown technologies. PLoS Genet. 3, e78. doi:10.1371/journal.pgen.0030078

Rogers, S.J., Wehner, E.A., Hagerman, R.J., 2001. The behavioral phenotype in fragile X: symptoms of autism in very young children with fragile X syndrome, idiopathic autism, and other developmental disorders. Dev. Behav. Pediatr. 22, 409–417.

Ronemus, M., Iossifov, I., Levy, D., Wigler, M., 2014. The role of de novo mutations in the genetics of autism spectrum disorders. Nat. Rev. Genet. 15, 133–141. doi:10.1038/nrg3585

Rosoklija, G., Mancevski, B., Ilievski, B., Perera, T., Lisanby, S.H., Coplan, J.D., Duma, A., Serafimova, T., Dwork, A.J., 2003. Optimization of Golgi methods for impregnation of brain tissue from humans and monkeys. J. Neurosci. Methods 131, 1–7. doi:10.1016/j.jneumeth.2003.06.001

Roux, P.P., Shahbazian, D., Vu, H., Holz, M.K., Cohen, M.S., Taunton, J., Sonenberg, N., Blenis, J., 2007. RAS/ERK signaling promotes site-specific ribosomal protein S6 phosphorylation via RSK and stimulates cap-dependent translation. J. Biol. Chem. 282, 14056–14064. doi:10.1074/jbc.M700906200

Rudelli, R.D., Brown, W.T., Wisniewski, K., Jenkins, E.C., Laure-Kamionowska, M., Connell, F., Wisniewski, H.M., 1985. Adult fragile X syndrome. Clinico-neuropathologic findings. Acta Neuropathol. 67, 289–295.

Rushton, W.A.H., 1951. A theory of the effects of fibre size in medullated nerve. J. Physiol. 115, 101–122.

Rutter, M., Silberg, J., O'Connor, T., Simonoff, E., 1999. Genetics and child psychiatry: II empirical research findings. J. Child Psychol. Psychiatry, Appl. Discip. 40, 19–55. doi:10.1111/1469-7610.00423

Sanders, S.J., Murtha, M.T., Gupta, A.R., Murdoch, J.D., Raubeson, M.J., Willsey, A.J., Ercan-Sencicek, A.G., DiLullo, N.M., Parikshak, N.N., Stein, J.L., Walker, M.F., Ober, G.T., Teran, N.A., Song, Y., El-Fishawy, P., Murtha, R.C., Choi, M., Overton, J.D., Bjornson, R.D., Carriero, N.J., Meyer, K.A., Bilguvar, K., Mane, S.M., Šestan, N., Lifton, R.P., Günel, M., Roeder, K., Geschwind, D.H., Devlin, B., State, M.W., 2012. De novo mutations revealed by whole-exome sequencing are strongly associated with autism. Nature 485, 237–241. doi:10.1038/nature10945

Sato, M., Stryker, M.P., 2008. Distinctive features of adult ocular dominance plasticity. J. Neurosci. 28, 10278–10286. doi:10.1523/JNEUROSCI.2451-08.2008

Sawtell, N.B., Frenkel, M.Y., Philpot, B.D., Nakazawa, K., Tonegawa, S., Bear, M.F., 2003. NMDA receptor-dependent ocular dominance plasticity in adult visual cortex. Neuron 38, 977–985.

Schaeffer, C., Beaulande, M., Ehresmann, C., Ehresmann, B., Moine, H., 2003. The RNA binding protein FMRP: new connections and missing links. Biol. Cell 95, 221–228. doi:10.1016/S0248-4900(03)00037-6

Schneider, A., Leigh, M.J., Adams, P., Nanakul, R., Chechi, T., Olichney, J., Hagerman, R., Hessl, D., 2013. Electrocortical changes associated with minocycline treatment in fragile X syndrome. J. Psychopharmacol. 27, 956–963. doi:10.1177/0269881113494105

Schumann, C.M., Barnes, C.C., Lord, C., Courchesne, E., 2009. Amygdala enlargement in toddlers with autism related to severity of social and communication impairments. Biol. Psychiatry 66, 942–949. doi:10.1016/j.biopsych.2009.07.007

Schumann, C.M., Hamstra, J., Goodlin-Jones, B.L., Lotspeich, L.J., Kwon, H., Buonocore, M.H., Lammers, C.R., Reiss, A.L., Amaral, D.G., 2004. The amygdala is enlarged in children but not adolescents with autism; the hippocampus is enlarged at all ages. J. Neurosci. 24, 6392–6401. doi:10.1523/JNEUROSCI.1297-04.2004

Segal, M., 2005. Dendritic spines and long-term plasticity. Nat. Rev. Neurosci. 6, 277–284. doi:10.1038/nrn1649

Segal, M., Kreher, U., Greenberger, V., Braun, K., 2003. Is fragile X mental retardation protein involved in activity-induced plasticity of dendritic spines? Brain Res. 972, 9–15. doi:10.1016/S0006-8993(03)02410-7

Sekine, T., Yamaguchi, T., Hamano, K., Siomi, H., Saez, L., Ishida, N., Shimoda, M., 2008. Circadian phenotypes of Drosophila fragile x mutants in alternative genetic backgrounds. Zoolog. Sci. 25, 561–571. doi:0289-0003-25-6-561 [pii] 10.2108/zsj.25.561

Sharma, A., Hoeffer, C.A., Takayasu, Y., Miyawaki, T., McBride, S.M., Klann, E., Zukin, R.S., 2010. Dysregulation of mTOR signaling in fragile X syndrome. J. Neurosci. 30, 694–702. doi:10.1523/JNEUROSCI.3696-09.2010

Sharma, S., Woolfson, L.M., Hunter, S.C., 2011. Confusion and inconsistency in diagnosis of Asperger syndrome: a review of studies from 1981 to 2010. Autism 16, 465–486. doi:10.1177/1362361311411935

Shatz, C.J., 1992. The developing brain. Sci. Am. 267, 60–67.

Shi, S.-H., Hayashi, Y., Esteban, J.A., Malinow, R., 2001. Subunit-specific rules governing AMPA receptor trafficking to synapses in hippocampal pyramidal neurons. Cell 105, 331–343. doi:10.1126/science.284.5421.1811

Sidhu, H., Dansie, L.E., Hickmott, P.W., Ethell, D.W., Ethell, I.M., 2014. Genetic removal of matrix metalloproteinase 9 rescues the symptoms of fragile X syndrome in a mouse model. J. Neurosci. 34, 9867–9879. doi:10.1523/JNEUROSCI.1162-14.2014

Sidman, R.L., Green, M.C., 1965. Retinal degeneration in the mouse: location of the rd locus in linkage group XVII. J. Hered. 56, 23–29.

Siegle, J.H., Pritchett, D.L., Moore, C.I., 2014. Gamma-range synchronization of fast-spiking interneurons can enhance detection of tactile stimuli. Nat. Neurosci. 17, 1371–1379. doi:10.1038/nn.3797

Simonoff, E., Pickles, A., Charman, T., Chandler, S., Loucas, T., Baird, G., 2008. Psychiatric disorders in children with autism spectrum disorders: prevalence, comorbidity, and associated factors in a population-derived sample. J. Am.

Acad. Child Adolesc. Psychiatry 47, 921–929.

Sohal, V.S., Zhang, F., Yizhar, O., Deisseroth, K., 2009. Parvalbumin neurons and gamma rhythms enhance cortical circuit performance. Nature 459, 698–702. doi:10.1038/nature07991

Sparks, B.F., Friedman, S.D., Shaw, D.W., Aylward, E.H., Echelard, D., Artru, A.A., Maravilla, K.R., Giedd, J.N., Munson, J., Dawson, G., Dager, S.R., 2002. Brain structural abnormalities in young children with autism spectrum disorder. Neurology 59, 184–192. doi:10.1212/WNL.59.2.184

Specht, C.G., Schoepfer, R., 2004. Deletion of multimerin-1 in α-synuclein-deficient mice. Genomics 83, 1176–1178.

Specht, C.G., Schoepfer, R., 2001. Deletion of the alpha-synuclein locus in a subpopulation of C57BL/6J inbred mice. BMC Neurosci. 2, 11.

Spencer, C.M., Alekseyenko, O., Hamilton, S.M., Thomas, A.M., Serysheva, E., Yuva-Paylor, L.A., Paylor, R., 2011. Modifying behavioral phenotypes in Fmr1 KO mice: genetic background differences reveal autistic-like responses. Autism Res. 4, 40–56. doi:10.1002/aur.168

Spencer, C.M., Alekseyenko, O., Serysheva, E., Yuva-Paylor, L.A., Paylor, R., 2005. Altered anxiety-related and social behaviors in the Fmr1 knockout mouse model of fragile X syndrome. Genes, Brain Behav. 4, 420–430. doi:10.1111/j.1601-183X.2005.00123.x

Splawski, I., Timothy, K.W., Sharpe, L.M., Decher, N., Kumar, P., Bloise, R., Napolitano, C., Schwartz, P.J., Joseph, R.M., Condouris, K., Tager-Flusberg,

H., Priori, S.G., Sanguinetti, M.C., Keating, M.T., 2004. CaV1.2 calcium channel dysfunction causes a multisystem disorder including arrhythmia and autism. Cell 119, 19–31. doi:10.1016/j.cell.2004.09.011

Steffenburg, S., Gillberg, C., Hellgren, L., Andersson, L., Gillberg, I.C., Jakobsson, G., Bohman, M., 1989. A twin study of autism in Denmark, Finland, Iceland, Norway and Sweden. J. Child Psychol. Psychiatry, Appl. Discip. 30, 405–416.

Steriade, M., Deschenes, M., 1984. The thalamus as a neuronal oscillator. Brain Res. Rev. 8, 1–63.

Steriade, M., McCormick, D.A., Sejnowski, T.J., 1993. Thalamocortical oscillations in the sleeping and aroused brain. Science (80-.). 262, 679–685. doi:10.1126/science.8235588

Sullivan, K., Hatton, D., Hammer, J., Sideris, J., Hooper, S., Ornstein, P., Bailey, D.J., 2006. ADHD symptoms in children with FXS. Am. J. Med. Genet. A 140, 2275–2288. doi:10.1002/ajmg.a

Sundaram, S.K., Kumar, A., Makki, M.I., Behen, M.E., Chugani, H.T., Chugani, D.C., 2008. Diffusion tensor imaging of frontal lobe in autism spectrum disorder. Cereb. Cortex 18, 2659–2665. doi:10.1093/cercor/bhn031

Sutherland, G.R., 1977. Fragile sites on human chromosomes: demonstration of their dependence on the type of tissue culture medium. Science (80-.). 197, 265–266.

Svizenska, I., Dubovy, P., Sulcova, A., 2008. Cannabinoid receptors 1 and 2 (CB1 and CB2), their distribution, ligands and functional involvement in nervous system structures — A short review. Pharmacol. Biochem. Behav. 90, 501–511.

doi:10.1016/j.pbb.2008.05.010

Svoboda, K., Tank, D.W., Denk, W., 1996. Direct measurement of coupling between dendritic spines and shafts. Science (80-.). 272, 716–719. doi:10.1126/science.272.5262.716

Takahashi, T., Svoboda, K., Malinow, R., 2003. Experience strengthening transmission by driving AMPA receptors into synapses. Science (80-.). 299, 1585–1589. doi:10.1126/science.1079886

Tassone, F., Hagerman, R.J., Taylor, A.K., Gane, L.W., Godfrey, T.E., Hagerman, P.J., 2000. Elevated levels of FMR1 mRNA in carrier males: a new mechanism of involvement in the fragile-X syndrome. Am. J. Hum. Genet. 66, 6–15. doi:10.1086/302720

Terracciano, A., Chiurazzi, P., Neri, G., 2005. Fragile X syndrome. Am. J. Med. Genet. Part C Semin. Med. Genet. 137, 32–37. doi:10.1002/ajmg.c.30062

Tessier, C.R., Broadie, K., 2008. Drosophila fragile X mental retardation protein developmentally regulates activity-dependent axon pruning. Development 135, 1547–1557. doi:10.1242/dev.015867

The Deciphering Developmental Disorders Study, 2015. Large-scale discovery of novel genetic causes of developmental disorders. Nature 519, 223–228. doi:10.1038/nature14135

The Dutch-Belgian Fragile X Consortium, 1994. Fmrl knockout mice: a model to study fragile X mental retardation. Cell 78, 23–33.

The WHO World Mental Health Survey Consortium, 2004. Prevalence, severity, and

unmet need for treatment of mental disorders in the World Health Organization World Mental Health Surveys. JAMA 291, 2581–2590.

Till, S.M., Asiminas, A., Jackson, A.D., Katsanevaki, D., Barnes, S.A., Osterweil, E.K., Bear, M.F., Chattarji, S., Wood, E., Wyllie, D.J.A., Kind, P.C., 2015. Conserved hippocampal cellular pathophysiology but distinct behavioral deficits in a new rat model of FXS. Hum. Mol. Genet. 24, 5977–5984. doi:10.1093/hmg/ddv299

Till, S.M., Wijetunge, L.S., Seidel, V.G., Harlow, E.G., Wright, A.K., Bagni, C., Contractor, A., Gillingwater, T.H., Kind, P.C., 2012. Altered maturation of the primary somatosensory cortex in a mouse model of fragile X syndrome. Hum. Mol. Genet. 21, 2143–2156. doi:10.1093/hmg/dds030

Tobert, J.A., 1988. Efficacy and long-term adverse effect pattern of lovastatin. Am. J. Cardiol. 62, 28J–34J. doi:10.1016/0002-9149(88)90004-5

Tobert, J.A., Bell, G.D., Birtwell, J., James, I., Kukovetz, W.R., Pryor, J.S., Buntinx, A., Holmes, I.B., Chao, Y.S., Bolognese, J.A., 1982a. Cholesterol-lowering effect of mevinolin, an inhibitor of 3-hydroxy-3-methylglutaryl-coenzyme A reductase, in healthy volunteers. J. Clin. Invest. 69, 913–919. doi:10.1172/JCI110530

Tobert, J.A., Hitzenberger, G., Kukovetz, W.R., Holmes, I.B., Jones, K.H., 1982b. Rapid and substantial lowering of human serum cholesterol by mevinolin (MK-803), an inhibitor of hydroxymethylglutaryl-coenzyme A reductase. Atherosclerosis 41, 61–65.

Tønnesen, J., Katona, G., Rózsa, B., Nägerl, U.V., 2014. Spine neck plasticity regulates compartmentalization of synapses. Nat. Neurosci. 17, 678–685. doi:10.1038/nn.3682

Tort, A.B.L., Kramer, M.A., Thorn, C., Gibson, D.J., Kubota, Y., Graybiel, A.M., Kopell, N.J., 2008. Dynamic cross-frequency couplings of local field potential oscillations in rat striatum and hippocampus during performance of a T-maze task. Proc. Natl. Acad. Sci. U. S. A. 105, 20517–20522. doi:10.1073/pnas.0810524105

Travers, B.G., Bigler, E.D., Tromp, D.P.M., Adluru, N., Destiche, D., Samsin, D., Froehlich, A., Prigge, M.D.B., Duffield, T.C., Lange, N., Alexander, A.L., Lainhart, J.E., 2015. Brainstem white matter predicts individual differences in manual motor difficulties and symptom severity in autism. J. Autism Dev. Disord. doi:10.1007/s10803-015-2467-9

Trommald, M., Jensen, V., Andersen, P., 1995. Analysis of dendritic spines in rat CA1 pyramidal cells intracellularly filled with a fluorescent dye. J. Comp. Neurol. 353, 260–274. doi:10.1002/cne.903530208

Tuchman, R., Cuccaro, M., Alessandri, M., 2010. Autism and epilepsy: historical perspective. Brain Dev. 32, 709–718. doi:10.1016/j.braindev.2010.04.008

Tuchman, R., Rapin, I., 2002. Epilepsy in autism. Lancet Neurol. 1, 352–358.

Tucker, B., Richards, R.I., Lardelli, M., 2006. Contribution of mGluR and Fmr1 functional pathways to neurite morphogenesis, craniofacial development and fragile X syndrome. Hum. Mol. Genet. 15, 3446–3458. doi:10.1093/hmg/ddl422

Turner, G., Eastman, C., Casey, J., McLeay, A., Procopis, P., Turner, B., 1975. X-linked mental retardation associated with macro-orchidism. J. Med. Genet. 12, 367–371. doi:10.1136/jmg.12.4.367

Turner, G., Webb, T., Wake, S., Robinson, H., 1996. Prevalence of fragile X syndrome. Am. J. Med. Genet. 64, 196–197. doi:10.1002/(SICI)1096-8628(19960712)64:1<196::AID-AJMG35>3.0.CO;2-G

Turrigiano, G.G., Nelson, S.B., 2004. Homeostatic plasticity in the developing nervous system. Nat. Rev. Neurosci. 5, 97–107. doi:10.1038/nrn1327

Turu, G., Hunyady, L., 2010. Signal transduction of the CB1 cannabinoid receptor. J. Mol. Endocrinol. 44, 75–85. doi:10.1677/JME-08-0190

U.S. Centers for Disease Control and Prevention, 2014. Prevalence of autism spectrum disorder among children aged 8 years - autism and developmental disabilities monitoring network, 11 sites, United States, 2010. Morb. Mortal. Wkly. Report. Surveill. Summ. 63, 1–21.

Uéda, K., Fukushima, H., Masliah, E., Xia, Y., Iwai, A., Yoshimoto, M., Otero, D.A.C., Kondo, J., Ihara, Y., Saitoh, T., 1993. Molecular cloning of cDNA encoding an unrecognized component of amyloid in Alzheimer disease. Proc. Natl. Acad. Sci. U. S. A. 90, 11282–11286. doi:10.1073/pnas.90.23.11282

Van Dam, D., Errijgers, V., Kooy, R.F., Willemsen, R., Mientjes, E., Oostra, B.A., De Deyn, P.P., 2005. Cognitive decline, neuromotor and behavioural disturbances in a mouse model for fragile-X-associated tremor/ataxia syndrome (FXTAS). Behav. Brain Res. 162, 233–239. doi:10.1016/j.bbr.2005.03.007

Varela, F., Lachaux, J.-P., Rodriguez, E., Martinerie, J., 2001. The brainweb: phase synchronization and large-scale integration. Nat. Rev. Neurosci. 2, 229–239.

Verkerk, A.J.M.H., Pieretti, M., Sutcliffe, J.S., Fu, Y.-H., Kuhl, D.P.A., Pizzuti, A., Reiner, O., Richards, S., Victoria, M.F., Zhang, F., Eussen, B.E., van Ommen, G.-J.B., Blonden, L.A.J., Riggins, G.J., Chastain, J.L., Kunst, C.B., Gaijaard, H., Caskey, C.T., Nelson, D.L., Oostra, B.A., Warren, S.T., 1991. Identification of a gene (FMR-1) containing a CGG repeat coincident with a breakpoint cluster region exhibiting length variation in fragile X syndrome. Cell 65, 905–914.

Villalon-Reina, J., Jahanshad, N., Beaton, E., Toga, A.W., Thompson, P.M., Simon, T.J., 2013. White matter microstructural abnormalities in girls with chromosome 22q11.2 deletion syndrome, Fragile X or Turner syndrome as evidenced by diffusion tensor imaging. Neuroimage 81, 441–454. doi:10.1016/j.neuroimage.2013.04.028

Villeneuve, M.Y., Casanova, C., 2003. On the use of isoflurane versus halothane in the study of visual response properties of single cells in the primary visual cortex. J. Neurosci. Methods 129, 19–31. doi:10.1016/S0165-0270(03)00198-5

Vincze, A., Mázló, M., Seress, L., Komoly, S., Abrahám, H., 2008. A correlative light and electron microscopic study of postnatal myelination in the murine corpus callosum. Int. J. Dev. Neurosci. 26, 575–584. doi:10.1016/j.ijdevneu.2008.05.003

Viscidi, E.W., Triche, E.W., Pescosolido, M.F., McLean, R.L., Joseph, R.M., Spence, S.J., Morrow, E.M., 2013. Clinical characteristics of children with

autism spectrum disorder and co-occurring epilepsy. PLoS One 8, e67797. doi:10.1371/journal.pone.0067797

Vissers, L.E.L.M., de Ligt, J., Gilissen, C., Janssen, I., Steehouwer, M., de Vries, P., van Lier, B., Arts, P., Wieskamp, N., del Rosario, M., van Bon, B.W.M., Hoischen, A., de Vries, B.B.A., Brunner, H.G., Veltman, J.A., 2010. A de novo paradigm for mental retardation. Nat. Genet. 42, 1109–1112. doi:10.1038/ng.712

Vissers, L.E.L.M., Gilissen, C., Veltman, J.A., 2015. Genetic studies in intellectual disability and related disorders. Nat. Rev. Genet. 17, 9–18. doi:10.1038/nrg3999

Volkert, V.M., Vaz, P.C.M., 2010. Recent studies on feeding problems in children with autism. J. Appl. Behav. Anal. 43, 155–159. doi:10.1901/jaba.2010.43-155

Volkmar, F.R., Chawarska, K., 2008. Autism in infants: an update. World Psychiatry 7, 19–21.

Walker, D.R., Thompson, A.P., Zwaigenbaum, L., Goldberg, J., Bryson, S.E., Mahoney, W.J., Strawbridge, C.P., Szatmari, P., 2004. Specifying PDD-NOS: a comparison of PDD-NOS, Asperger syndrome, and autism. J. Am. Acad. Child Adolesc. Psychiatry 43, 172–180.

Wallace, M.R., Marchuk, D.A., Andersen, L.B., Letcher, R., Odeh, H.M., Saulino, A.M., Fountain, J.W., Brereton, A., Nicholson, J., Mitchell, A.L., Brownstein, B.H., Collins, F.S., 1990. Type 1 neurofibromatosis gene: identification of a large transcript disrupted in three NF1 patients. Science (80-.). 249, 181–186. doi:10.1126/science.2134734

Wan, L., Dockendorff, T.C., Jongens, T.A., Dreyfuss, G., 2000. Characterization of dFMR1, a Drosophila melanogaster homolog of the fragile X mental retardation protein. Mol. Cell. Biol. 20, 8536–8547. doi:10.1128/MCB.20.22.8536-8547.2000

Wang, H., Ku, L., Osterhout, D.J., Li, W., Ahmadian, A., Liang, Z., Feng, Y., 2004. Developmentally-programmed FMRP expression in oligodendrocytes: a potential role of FMRP in regulating translation in oligodendroglia progenitors. Hum. Mol. Genet. 13, 79–89. doi:10.1093/hmg/ddh009

Wang, X., Snape, M., Klann, E., Stone, J.G., Singh, A., Petersen, R.B., Castellani, R.J., Casadesus, G., Smith, M.A., Zhu, X., 2012. Activation of the extracellular signal-regulated kinase pathway contributes to the behavioral deficit of fragile x-syndrome. J. Neurochem. 121, 672–679. doi:10.1111/j.1471-4159.2012.07722.x

Warren, R.P., Singh, V.K., Averett, R.E., Odell, J.D., Maciulis, A., Burger, R.A., Daniels, W.W., Warren, W.L., 1996. Immunogenetic studies in autism and related disorders. Mol. Chem. Neuropathol. 28, 77–81.

Waxman, S.G., 1980. Determinants of conduction velocity in myelinated nerve fibers. Muscle Nerve 3, 141–150. doi:10.1002/mus.880030207

Weiler, I.J., Greenough, W.T., 1999. Synaptic synthesis of the Fragile X protein: possible involvement in synapse maturation and elimination. Am. J. Med. Genet. 83, 248–252. doi:10.1002/(SICI)1096-8628(19990402)83:4<248::AID-AJMG3>3.0.CO;2-1

Whittington, M.A., Traub, R.D., Jefferys, J.G.R., 1995. Synchronized oscillations in interneuron networks driven by metabotropic glutamate receptor activation. Nature 373, 612–615.

Whyte, D.B., Kirschmeier, P., Hockenberry, T.N., Nunez-Oliva, I., James, L., Catino, J.J., Bishop, W.R., Pai, J.K., 1997. K- and N-Ras are geranylgeranylated in cells treated with farnesyl protein transferase inhibitors. J. Biol. Chem. 272, 14459–14464. doi:10.1074/jbc.272.22.14459

Wijetunge, L.S., Angibaud, J., Frick, A., Kind, P.C., Nägerl, U.V., 2014. Stimulated emission depletion (STED) microscopy reveals nanoscale defects in the developmental trajectory of dendritic spine morphogenesis in a mouse model of fragile X syndrome. J. Neurosci. 34, 6405–6412. doi:10.1523/JNEUROSCI.5302-13.2014

Williams, R.S., Hauser, S.L., Purpura, D.P., DeLong, G.R., Swisher, C.N., 1980. Autism and mental retardation: neuropathologic studies performed in four retarded persons with autistic behavior. Arch. Neurol. 37, 749–753. doi:10.1001/archneur.1980.00500610029003

Wisniewski, K.E., Segan, S.M., Miezejeski, C.M., Sersen, E.A., Rudelli, R.D., 1991. The fra(X) syndrome: neurological, electrophysiological, and neuropathological abnormalities. Am. J. Med. Genet. 38, 476–480.

World Health Organization, 1993. The ICD-10 Classification of Mental and Behavioral Disorders: Diagnostic Criteria for Research. World Health Organization, Geneva.

Yamada, T., Shinnoh, N., Taniwaki, T., Ohyagi, Y., Asahara, H., Horiuchi, I., Kira, J., Horiuchi, Kira, J., 2000. Lovastatin does not correct the accumulation of very long-chain fatty acids in tissues of adrenoleukodystrophy protein-deficient mice. J. Inherit. Metab. Dis. 23, 607–614.

Yeargin-Allsopp, M., Rice, C., Karapurkar, T., Doernberg, N., Boyle, C., Murphy, C., 2003. Prevalence of autism in a US metropolitan area. JAMA 289, 49–55. doi:10.1001/jama.289.1.49

Yiu, G., He, Z., 2006. Glial inhibition of CNS axon regeneration. Nat. Rev. Neurosci. 7, 617–627. doi:10.1038/nrn1956

Yuste, R., 2013. Electrical compartmentalization in dendritic spines. Annu. Rev. Neurosci. 36, 429–449. doi:10.1146/annurev-neuro-062111-150455

Yuste, R., Bonhoeffer, T., 2004. Genesis of dendritic spines: insights from ultrastructural and imaging studies. Nat. Rev. Neurosci. 5, 24–34. doi:10.1038/nrn1300

Yuste, R., Bonhoeffer, T., 2001. Morphological changes in dendritic spines associated with long-term synaptic plasticity. Annu. Rev. Neurosci. 24, 1071–1089.

Zhang, Y.Q., Bailey, A.M., Matthies, H.J.G., Renden, R.B., Smith, M.A., Speese, S.D., Rubin, G.M., Broadie, K., 2001. Drosophila fragile x-related gene regulates the MAP1B homolog Futsch to control synaptic structure and function. Cell 107, 591–603. doi:10.1016/S0092-8674(01)00589-X

Zhu, Y., Ghosh, P., Charnay, P., Burns, D.K., Parada, L.F., 2002. Neurofibromas in

NF1: Schwann cell origin and role of tumor environment. Science (80-.). 296, 920–922. doi:10.1126/science.1068452

Ziv, N.E., Smith, S.J., 1996. Evidence for a role of dendritic filopodia in synaptogenesis and spine formation. Neuron 17, 91–102.

Chapter 8: Appendix

8.1 Recipes

Buffer for genotyping	**Ingredients**
tail buffer	100 mM Tris, pH 8.5 200 mM NaCl 0.2% SDS 5 mM EDTA
Buffer for Nissl staining	**Ingredients**
Nissl solution	Solution A: 1 g thionin in 100 ml ddH_2O Solution B: 6 ml glacial acetic acid (98 – 100%) with 994 ml ddH_2O Solution C: 0.1 M sodium acetate solution ($NaC_2H_3O_2$-$3H_2O$) Nissl solution: mix 90 ml B with 10 ml C and 2.5 ml A

Abbreviations: EDTA: ethylenediaminetetraacetic acid; ddH_2O: double-distilled water; SDS: sodium dodecyl sulfate

8.2 Thermocycling conditions for genotyping

	Cycling Conditions	
Step	***Fmr1***	
	Temperature	Duration
1	94°C	3 min
2	94°C	30 sec
3	63°C	30 sec
4	72°C	1 min
5		Go to step 2, 35 times
6	72°C	2 min
7	10°C	5 min
8		Samples can now be stored in 4°C before gel running

8.3 Materials for Western blotting

Materials	Ingredients/Source	Concentration
RIPA buffer	50 mM Tris-HCl, pH 7.4 150 mM NaCl 1% Triton X-100 0.5% sodium deoxylcholate 0.1% SDS 1 mM EDTA	
Laemmli buffer (2X)	Bio-Rad #161-0737	
protease inhibitor (EDTA free)	Roche #11836170001	1 tablet in 10 ml lysis buffer
phosphatase inhibitor cocktail	Calbiochem #524625 (II), #524628 (IV)	1:100
Pierce™ BCA protein assay kit	Thermo #23225, #23227	
Mini-PROTEAN® TGX™ gels	Bio-Rad #456-1046	
pERK1/2 1˚**Ab**	Cell Signaling #9106S (from mouse) Cell Signaling #4370 (from rabbit)	1:2000
ERK1/2 1˚**Ab**	Cell Signaling #4696 (from mouse) Cell Signaling #4695 (from rabbit)	1:2000 1:1000
β-actin 1˚**Ab**	abcam #ab8226 (from mouse) abcam #ab8227 (from rabbit)	1:2000
IRDye® 800CW Goat anti-Rabbit 2˚**Ab**	Li-COR #926-32211	1:5000
Alexa Fluor 680® Goat	Life Technologies #A-21057	1:5000

anti-Mouse 2˚Ab		
Odyssey blocking buffer	Li-COR #927-40000	
ReBlot Plus stripping solution (10X)	Millipore #2504	dilute to 1X
running buffer	25 mM Tris 190 mM glycine 0.1% SDS adjust pH to 8.3	
transfer buffer	25 mM Tris 190 mM glycine 0.1% SDS (for proteins larger than 80 kDa) 20% methanol adjust pH to 8.3	
nitrocellulose membrane	Bio-Rad #162-0112	
PageRuler Plus prestained protein ladder, 10 to 250 kDa	Thermo #26619	

Abbreviations: 1˚Ab: primary antibody; 2˚Ab: secondary antibody; kDa: kilo Dalton; RIPA: radio-immunoprecipitation assay; SDS: sodium dodecyl sulfate;